Applications of Novel Imaging Protocols and Devices in Interventional Neuroradiology



Mudassar Kamran

Magdalen College

Thesis Submitted for the Degree of Doctor of Philosophy in Surgery

Oxford Neurovascular and Neuroradiology Research Unit

Nuffield Department of Surgery

Medical Sciences Division

University of Oxford

Supervisor: Professor James V. Byrne

Hilary Term 2015

Acknowledgements

I would first like to thank my supervisor, Professor James V Byrne, for his support, guidance, and patience throughout the completion of this work. It was an invaluable learning experience and an absolute pleasure to work with him. His profound clinical insight remains a source of inspiration for me. The Rhodes Trust provided me the opportunity to come to Oxford, for which I will forever be grateful. Thanks to the Magdalen College for being my home in Oxford.

A special thanks to the Oxford Neurovascular and Neuroradiology team: Julia Yarnold, Alison Clarke, and Mary Sneade. I would like to thank the department of neuroradiology, particularly the angio-room and MRI teams as well the consultants: Dr Corkill, Dr Cellerini, Dr Kueker, Dr Pretorius, and Dr Sheerin for their help in the recruitment and scanning of the patients. Thanks to the patients who volunteered to be part of this research. I am deeply grateful to Dr Strother, Dr Grunwald, Dr Neelavali, and Dr Struffert for their invaluable input and help in my research.

Deepest thanks to my parents and my family; without their support, completion of this thesis would not have been possible. Finally, thanks to my friends who made my Oxford stay truly memorable.

Dedications

For my parents

Abstract

The historical development, current practice, and the future of interventional neuroradiology are intricately linked to the advancements in the imaging and devices used for neuroendovascular treatments. This thesis explores the advanced imaging potential of the C-arm imaging systems used in the neurointerventional suite and investigates the initial clinical experience with a new flow diverter device to treat the intracranial aneurysms.

A cohort of aneurysmal SAH patients who developed delayed cerebral ischaemia (DCI) were prospectively studied with a new *parenchymal blood volume (PBV) research protocol C-arm CT examination* concurrent with a *magnetic resonance (MR) imaging examination* that included perfusion and diffusion weighted sequences. Using a robust quantitative volume-of-interest analysis, it was demonstrated that C-arm CT PBV measurements are in agreement with MR-PWI CBV and CBF, and the PBV represents a composite perfusion parameter with both blood-flow (≈60%) and blood-volume (≈40%) weightings. Subsequently, using a voxel-wise ROC curve analysis and MR-DWI, it was shown that using optimal thresholds, C-arm CT PBV measurements allow reliable demarcation of the irreversibly infarcted parenchyma. For evaluation of ischaemic parenchyma, the PBV measurements were reliable for moderate-to-severe ischaemia but were prone to underestimate the mild-to-moderate ischaemia. A catalogue of reference mean PBV measurements was then created for various anatomical regions

encompassing the whole brain after excluding any locations with ongoing ischaemia or infarction. Next, using an ROI-based analysis of the C-arm CT projection data, *steady-state contrast concentration assumption* underlying the PBV calculations was investigated. It was demonstrated that for clinical scans, the ideal steady-state assumption is not fully met, however, for a large majority of C-arm CT examinations the temporal characteristics of TDCs closely approximate the expected ideal steady-state. The degree to which the TDC of a C-arm CT scan approximates the ideal steady-state was found to influence the resulting PBV measurements and their agreement to MR-CBV. Moreover, the temporal characteristics of TDCs showed inter-subject variation. Finally, the C-arm CT cross-sectional soft tissue images were demonstrated to be of adequate quality for the assessment of ventricles and for the detection of procedural vessel rupture. These findings advance the understanding of the nature of PBV parameter, establish the optimal PBV thresholds for infarction, provide reference PBV measurements, and highlight the limitations of C-arm CT PBV imaging. The work is of considerable clinical significance and has implications for implementation of C-arm CT PBV imaging in the interventional suite for management of patients with acute brain ischaemia.

In regards to the initial clinical experience with the *flow diversion treatment of intracranial aneurysms*, the procedural, angiographic, and clinical outcomes were studied. Several pertinent technical and clinical issues were highlighted for this new treatment approach. Based on the observations made during this work, *a new grading schema* was then developed to monitor the angiographic outcomes after flow diversion

treatment. Using the angiographic data for patients treated with FD, the new grading schema was demonstrated to be sufficiently sensitive to register gradual aneurysm occlusion and evaluate parent artery patency, with an excellent inter-rater reliability and applicability to various aneurysm morphologies. This work (largest multi-centre series at the time of its publication) informed the interventional neuroradiology community about the safety, efficacy, and outcomes of flow diversion treatment. Additionally, it provided a sensitive and reliable scale to evaluate the angiographic outcomes after flow diversion treatment, in both research and clinical practice.

List of Publications during DPhil

(a) Original manuscripts contributing to DPhil thesis

1. **Kamran M**, Byrne JV. C-arm flat detector computed tomography parenchymal blood volume imaging: the nature of parenchymal blood volume parameter and the feasibility of parenchymal blood volume imaging in aneurysmal subarachnoid haemorrhage patients. Neuroradiology. 2015; 1–13. doi:10.1007/s00234-015-1545-1

2. **Kamran M**, Byrne JV. C-Arm Flat Detector CT Parenchymal Blood Volume Thresholds for Identification of Infarcted Parenchyma in the Neurointerventional Suite. AJNR Am J Neuroradiol. 2015; doi:10.3174/ajnr.A4339

3. **Kamran M**, Downer J, Corkill R, Byrne JV. Non-invasive assessment of vasospasm following aneurysmal SAH using C-arm FDCT parenchymal blood volume measurement in the neuro-interventional suite: Technical feasibility. Interv Neuroradiol. 2015; 1591019915582376. doi:10.1177/1591019915582376

4. **Kamran M**, Yarnold J, Grunwald IQ, Byrne JV. Assessment of angiographic outcomes after flow diversion treatment of intracranial aneurysms: a new grading schema. Neuroradiology. 2011;53: 501–508. doi:10.1007/s00234-010-0767-5

5. **Kamran M**, Nagaraja S, Byrne JV. C-arm flat detector computed tomography: the technique and its applications in interventional neuro-radiology. Neuroradiology. 2010;52: 319–327. doi:10.1007/s00234-009-0609-5

6. Byrne JV, Beltechi R, Yarnold JA, Birks J, **Kamran M**. Early Experience in the Treatment of Intra-Cranial Aneurysms by Endovascular Flow Diversion: A Multicentre Prospective Study. PLoS ONE. 2010;5: e12492. doi:10.1371/journal.pone.0012492

(b) Other manuscripts

1. Rafiei P, Kim SK, **Kamran M**, Saad NE. Retrospective Study in 40 Patients of Utility of C-arm FDCT as an Adjunctive Modality in Technically Challenging Image-Guided Percutaneous Drainage Procedures. Cardiovasc Intervent Radiol. 2015; doi:10.1007/s00270-015-1091-6

2. **Kamran M**, Hacker CD, Allen MG, Mitchell TJ, Leuthardt EC, Snyder AZ, et al. Resting-State Blood Oxygen Level–Dependent Functional Magnetic Resonance Imaging for Presurgical Planning. Neuroimaging Clinics of North America. 2014;24: 655–669. doi:10.1016/j.nic.2014.07.009

3. Grunwald IQ, **Kamran M**, Corkill RA, Kühn AL, Choi IS, Turnbull S, et al. Simple Measurement of Aneurysm Residual after Treatment: the SMART scale for evaluation of intracranial aneurysms treated with flow diverters. Acta Neurochir. 2012;154: 21–26. doi:10.1007/s00701-011-1177-0

4. Orlowski P, Mahmud I, **Kamran M**, Summers P, Noble A, Ventikos Y, et al. An approach to the symbolic representation of brain arteriovenous malformations for management and treatment planning. Neuroradiology. 2014;56: 195–209. doi:10.1007/s00234-013-1307-x

5. Grunwald IQ, Walter S, Fassbender K, Kühn AL, Hartmann KM, Wilson N, Sievert H, **Kamran M**, Hopkins LN, Wakhloo AK. Ischaemic stroke in children: new aspects of treatment. J Pediatr. 2011;159: 366–370. doi:10.1016/j.jpeds.2011.03.051

6. Wallace AN, Vyhmeister R, **Kamran M**, Teefey SA. Submandibular venous hemangioma: Case report and review of the literature. J Clin Ultrasound. 2014; doi:10.1002/jcu.22258

List of Abstracts and Conference Presentations during DPhil

Oral presentations

1. **Kamran M**, Schweder P. Deuerling-Zheng Y, Mueller-Allissat B, Byrne JV. (2011, May). *Comprehensive Noninvasive Assessment of Vasospasm following Aneurysmal Subarachnoid Hemorrhage Using Dyna-CT Cerebral Blood Volume Measurements in the Neurointerventional Suite: a feasible method for Neurointensive Treatment Unit patient*. 49th Annual Meeting of ASNR (American Society of Neuroradiology); Seattle, MA.

2. **Kamran M**, Schweder PM, Byrne JV. (2010, June) Mapping Perfusion of the Human Orbitofrontal Cortex: A Reference for Functional Imaging Studies. 49th Annual Meeting of ASNR (American Society of Neuroradiology); Seattle, MA.

3. Byrne JV, Beltechi R, Yarnold J, **Kamran M**. (2009, October). *Audit of the SILK registry of patients treated for intracranial aneurysm with a flow diverter*. Annual Scientific Meeting of BSNR (British Society of Neuroradiologists); Nottingham, United Kingdom.

4. **Kamran M**, Stedman J, Byrne JV, Kuker W, Cellerini M, Corkill R. (2010, September). *Morphological, clinical, and flow dynamic characteristics of anterior communicating artery aneurysms: a predictive model for endovascular treatment outcomes*. Annual Scientific Meeting of BSNR (British Society of Neuroradiologists); Glasgow, United Kingdom.

5. **Kamran M**, Deuerling-Zheng Y, Grunwald IQ, Yarnold J, Byrne JV. (2010, October). *Assessing the severity of vasospasm after SAH using Dyna-CT to measure cerebral blood volume: a feasible method for the neuro-ITU patient*. XIX Symposium Neuroradiologicum; Bologna, Italy.

6. **Kamran M**, Deuerling-Zheng Y, Mueller-Allissat B, Grunwald IQ, Yarnold J, Byrne JV. (2010, September). *Measurement of cerebral blood volume using Dyna-CT: a feasible method for assessment of vasospasm severity following aneurysmal SAH*. Annual Scientific Meeting of BSNR (British Society of Neuroradiologists); Glasgow, United Kingdom.

7. **Kamran M**, Deuerling-Zheng Y, Mueller-Allissat B, Grunwald IQ, Yarnold J, Byrne JV. (2010, September). *Measurement of cerebral blood volume using Dyna-CT in the neuro-interventional suite: a validation study*. Annual Scientific Meeting of BSNR (British Society of Neuroradiologists); Glasgow, United Kingdom.

8. **Kamran M**, Rane N, Holland E, Ventikos Y, Byrne JV. (2009, October). *Correlation of posterior communicating artery aneurysm growth patterns, arterial environment, and clinical presentation*. Annual Scientific Meeting of BSNR (British Society of Neuroradiologists); Nottingham, United Kingdom.

9. **Kamran M**, Tomassini V, Johansen-Berg H. (2008, May). *Assessment of brain plasticity in multiple sclerosis using behavioral and fMRI measures of motor learning*. Annual Oxford Neuroscience Day; Oxford, United Kingdom.

10. **Kamran M**, Jokerst C, Siegel MJ, Hildebolt C, Ramirez-Giraldo JC, Bradley D. (April, 2013). Dose Reduction using Automated Kilovoltage and Iterative Reconstruction Technologies in Pediatric CT: Pilot Data. Annual Meeting of American Roentgen Ray Socitey (ARRS), Washington DC.

11. Rafiei P, **Kamran M**, Kim SK; Saad N. (2014, May) C-arm FDCT imaging in

technically challenging image-guided percutaneous drainage procedures. Journal of Vascular and Interventional Radiology. 39th Annual Scientific Meeting of Society of Interventional Radiology, San Diego, CA.

Poster Presentations

1. **Kamran M**, Deuerling-Zheng Y, Mueller-Allissat B, Grunwald IQ, Yarnold J, Byrne JV. (2010, November). *Evaluation of the haemodynamic significance of vasospasm after aneurysmal SAH using Dyna-CT CBV and its comparison with MR-PWI*. Poster presented at: 96th Scientific Assembly and Annual Meeting of RSNA (Radiological Society of North America); Chicago, IL.

2. **Kamran M**, Deuerling-Zheng Y, Neelavali J, Grunwald IQ, Yarnold J, Byrne JV. (2010, May). *Assessing the severity of vasospasm after subarachnoid haemorrhage using Dyna-CT to measure cerebral blood volume: a feasible method for neuro-ITU patient*. Poster presented at: 48th Annual Meeting of ASNR (American Society of Neuroradiology); Boston, MA.

3. **Kamran M**, Nagaraja S, Corkill R, Kuker W, Lalloo S, Byrne JV. (2008, October). *Advantages of C- arm flat detector CT in interventional neuroradiology*. Poster presented at: Annual Scientific Meeting of BSNR (British Society of Neuroradiologists); Manchester, United Kingdom.

4. Neelavalli J, Cheng Y-C N, **Kamran M**, Byrne JV, Haacke EM. (2010, May). *Accurate susceptibility quantification from MR phase data through the least squares fit method: phantom validation*. Poster presented at: 17th annual meeting of ISMRM (International Society of Magnetic Resonance in Medicine); Stockholm, Sweden.

5. **Kamran M**, Schweder PM, Deuerling-Zheng Y, Byrne JV. Perfusion Mapping of the Human Orbitofrontal Cortex using C-arm FDCT and MR-PWI. Poster presented at: 17th

Annual Meeting of the Organization on Human Brain Mapping Centre des Congrès de Québec June 26-30, 2011.

6. **Kamran M**, Schweder PM, Deuerling-Zheng Y, Byrne JV. Cerebral Perfusion Imaging with C-arm Flat Detector Computed Tomography. Poster presented at: 17th Annual Meeting of the Organization on Human Brain Mapping Centre des Congrès de Québec June 26-30, 2011.

7. **Kamran M**, Purdy H, Miller-Thomas M. (2013, November). Imaging Review of the Causes of Ataxia. Poster presented at: 99th Scientific Assembly and Annual Meeting of RSNA (Radiological Society of North America); Chicago, IL.

9. Purdy H, Miller-Thomas M., **Kamran M**. Eyes Half Shut: A Pictorial Review of the Causes of Horner Syndrome. Poster presented at: 99th Scientific Assembly and Annual Meeting of RSNA (Radiological Society of North America); Chicago, IL.

Table of contents

Acknowledgements i
Dedications ii
Abstract iii
List of publications during DPhil vi
List of abstracts and conference presentations during DPhil ix
Table of contents xiii
List of figures xix
List of tables xxiii
List of abbreviations xxvi

Chapter 1

Preamble

1.1 Background 01
1.2 Thesis Structure and Organization 09

Chapter 2

C-arm FDCT: the Technique and its Applications in Interventional Neuroradiology

2.1 Abstract 13
2.2 Introduction 15
2.3 Physics of C-arm FDCT 16
2.4 Applications of FDCT in the Angiography Suite 21
2.4.1 Evaluation of Intracranial Stents Used in the Treatment of Stenotic Arterial Disease 21
2.4.2 Evaluation of Stents Used in the Treatment of Intracranial Aneurysms 25
2.4.3 Angio-room Availability of CT-like Soft Tissue Images 27
2.4.4 FDCT Angiography 33
2.4.5 FDCT Perfusion 34
2.5 Conclusion 35

Chapter 3

C-arm FDCT Parenchymal Blood Volume Imaging: Historical Perspective and Introduction to the Technique

3.1 Historical Background 37

3.1.1 Relevance of Parenchymal and Perfusion Imaging in Neuro-interventional Suite 40

3.2 Theoretical Background 44

3.2.1 Contrast Material Injection Protocol 48

3.2.2 C arm CT PBV Scan Protocol 49

3.2.3 Post-processing of the C-arm Scan Projectional Data 50

Chapter 4

C-arm FDCT PBV Imaging in Delayed Cerebral Ischaemia following Aneurysmal Subarachnoid Haemorrhage

4.1 Abstract 56

4.2 Introduction 58

4.3 Materials and Methods 59

4.3.1 C-arm Flat Detector Computed Tomography (FDCT) Imaging 61

4.3.2 Magnetic Resonance (MR) Imaging 62

4.3.3 Further Post-processing and Quantitative VOI Analysis 64

4.3.4 Statistical Analysis 74

4.4 Results 75

4.4.1 Study Population Characteristics 75

4.4.2 Quantitative Image Analysis 76

4.5 Discussion 87

4.6 Conclusion 97

Chapter 5

C-arm FDCT PBV Thresholds for Identification of Infarcted Parenchyma

5.1 Abstract 100

5.2 Introduction 102

5.3 Materials and Methods 103

5.3.1 C-arm FDCT Imaging 104

5.3.2 MR Imaging 106
5.3.3 Further Post-processing and Quantitative VOI Analysis 107
5.3.4 Statistical Analysis 111
5.4 Results 112
5.4.1 Study Population Characteristics 112
5.4.2 Quantitative Image Analysis 113
5.5 Discussion 119
5.6 Conclusion 125

Chapter 6

Whole Brain C-arm FDCT PBV: Reference Measurements

6.1 Abstract 128
6.2 Introduction 130
6.3 Materials and Methods 132
6.3.1 C-arm FDCT Imaging 133
6.3.2 MR Imaging 135
6.3.3 Further Post-processing and Quantitative VOI Analysis 136
6.4 Results 141
6.5 Discussion 148
6.6 Conclusion 152

Chapter 7

Time Density Curve Analysis of C-arm FDCT PBV Imaging

7.1 Abstract 154
7.2 Introduction 156
7.3 Materials and Methods 158
7.3.1 C-arm FDCT Imaging 159
7.3.2 Time Density Curve (TDC) Analysis 160
7.3.3 Statistical Analysis 164
7.4 Results 165
7.4.1 Patient Characteristics 165
7.4.2 Statistical Analysis 166
7.5 Discussion 173

7.6 Conclusion 179

Chapter 8

Utility of Parenchymal C-arm FDCT Imaging in the Neurointerventional Suite

8.1 Abstract 181

8.2 Introduction 183

8.3 Materials and Methods 185

8.3.1 FDCT Data Acquisition and Post-processing 186

8.3.2 FDCT Image Evaluation 186

8.4 Results 188

8.4.1 Procedural Rupture 189

8.4.2 Hydrocephalus 190

8.4.3 Illustrative Cases 193

8.5 Discussion 194

8.6 Conclusion 199

Chapter 9

Flow Diversion: A New Endovascular Treatment Technique for Intracranial Aneurysms

9.1 Intracranial Aneurysms and their Treatment 201

9.1.1 Flow Diversion – a New Endovascular Treatment Approach 203

9.1.2 Clinical Experience with Flow Diverter Devices 207

9.2 Conclusion 214

Chapter 10

Early Experience in the Treatment of Intra-Cranial Aneurysms by Endovascular Flow Diversion: A Multicenter Prospective Study

10.1 Abstract 217

10.2 Introduction 219

10.3 Materials and Methods 220

10.3.1 Methods 220

10.3.2 Materials 222

10.4 Results 225

10.4.1 Procedures 225

10.4.2 Untoward Procedural Events (UPEs) 225
10.4.3 Procedural Morbidity 229
10.4.4 Delayed Morbidity 229
10.4.5 Angiographic Outcomes 231
10.4.6 Statistical Analysis 232
10.5 Discussion 236
10.6 Conclusion 240
10.7 Reception of the Work 240

Chapter 11
Assessment of Angiographic Outcomes after Flow Diversion Treatment of Intracranial Aneurysms: A New Grading Schema
11.1 Abstract 243
11.2 Introduction 245
11.3 Materials and Methods 247
11.3.1 Grading Schema for the Assessment of Angiographic Outcomes Following Endovascular FD Deployment 249
11.3.2 Statistical Analysis 253
11.4 Results 253
11.5 Discussion 257
11.6 Conclusion 261
11.7 Reception of the grading schema 262

Chapter 12
Conclusions
12.1 Conclusions 265
12.2 Future directions 269

Bibliography 272

Appendices i
(a) C-arm FDCT PBV project protcol: ii
(b) Risk Assessment for Research involving Ionising Radiation xxvi

(c) Evaluation of Statistical Methods by Centre for Statistics in Medicine xxviii
(d) Participant information sheet for C-arm FDCT PBV project xxx
(e) Consultee information sheet for C-arm FDCT PBV project xxxv
(f) Consent form for participants for C-arm FDCT PBV project xl
(g) Consent form for consultees for C-arm FDCT PBV project xlii

List of Figures

Chapter 1

1.1 Coil embolisation treatment for intracranial aneurysms ---------- 05

1.2 Flow diversion principle for treatment of intracranial aneurysms ---------- 05

1.3 'One-stop-shop' neurointerventional suite with diagnostic and interventional capabilities ---------- 08

1.4 An illustrative overview of the thesis chapters and their central themes ------ 10

Chapter 2

2.1 Schematic illustration of a flat panel detector used in currently available biplane C-arm angiographic systems ---------- 18

2.2 C-arm FDCT evaluation of intracranial stents ---------- 23

2.3 Evaluation of brain parenchyma with C-arm FDCT ---------- 31

2.4 Evaluation of intracranial vessels with C-arm FDCT ---------- 34

Chapter 3

3.1 A flat detector equipped biplane C-arm angiography system used in the neurointerventional suite ---------- 42

3.2 Tracer kinetics in the cerebral vasculature following its intravenous administration ---------- 46

3.3 C-arm FDCT scan protocol for PBV measurement ---------- 50

3.4 An overview of the post-processing steps for calculation of parametric PBV maps ---------- 51

3.5 Estimation of input function from the histogram analysis of subtraction volume ---------- 52

3.6 An overview of the C-arm FDCT PBV scan ---------- 53

Chapter 4

4.1 Harvard-Oxford structural brain atlas-based VOIs ---------- 65

4.2 A schematic overview of the image post-processing ---------- 66

4.3 MR-PWI analysis overview ---------- 68

4.4a Head motion (translation in mm) over time for an MR-PWI dataset ---------- 69

4.4b Head motion (rotation in degrees) over time for an MR-PWI dataset -------- 69

4.5 C-arm CT PBV dataset prior to post-processing ---------- 70

4.6 C-arm CT PBV dataset subsequent to brain extraction ---------- 70

4.7 Image histogram for a C-arm CT PBV dataset ---------- 71

4.8 Opacification of the major intracranial vascular structures in a C-arm CT PBV protocol scan ---------- 71

4.9 C-arm CT PBV dataset subsequent to vascular segmentation ---------- 72

4.10 C-arm CT PBV dataset subsequent to coregisteration ---------- 72

4.11 C-arm CT PBV dataset subsequent to coregisteration (axial recon.) ---------- 73

4.12 Agreement and correlation analysis plots for C-arm CT rPBV versus MR-PWI rCBV ---------- 81

4.13 Agreement and correlation analysis plots for C-arm CT rPBV versus MR-PWI rCBF ---------- 82

4.14 Agreement and correlation analysis plots for C-arm CT rPBV versus weighted mean of MR-PWI rCBV and rCBF ---------- 83

4.15 Illustrative case example 1 ---------- 86

4.16 Illustrative case example 2 ---------- 87

Chapter 5

5.1 Binary masks used for VOI analysis ---------- 109

5.2 A schematic overview of the image post-processing and analysis ---------- 110

5.3 Schematic illustration of the infarct and peri-infarct VOIs ---------- 115

5.4 Plot of mean PBV values for the infarct VOIs ---------- 116

5.5 Plot of mean PBV values for the moderate to severely ischemic, peri-infarct VOIs ---------- 116

5.6 Plot of mean PBV values for the mild to moderately ischemic, peri-infarct VOIs ---------- 117

5.7 ROC curves for absolute and normalized PBV ---------- 117

5.8 A theoretical understanding of C-arm CT PBV at various degrees of ischaemia ---------- 123

Chapter 6

6.1 A schematic overview of the image post-processing and analysis ---------- 138

6.2 Harvard-Oxford brain atlas-based volumes of interest (VOIs) ---------- 139

6.3 A volume rendered three-dimensional depiction of VOIs on surface shaded brain volume ---------- 140

6.4 Representative DWI images of patients showing areas of restricted diffusion. 140

6.5a C-arm CT PBV values (mean and standard deviation) for the VOIs 1-35 ----- 146

6.5b C-arm CT PBV values (mean and standard deviation) for the VOIs 36-58 --- 146

6.6 TDCs for C-arm FDCT datasets ---------- 147

Chapter 7

7.1 Illustration of ROI placement on the 2D C-arm FDCT rotational projections. - 162

7.2 Correction of IE differences for the differences in head diameter ---------- 162

7.3a Locally-weighted-scatterplot-smoothed (LOWESS) TDCs (aggregated) ----- 168

7.3b Locally-weighted-scatterplot-smoothed (LOWESS) TDCs in subgroups ----- 169

7.4 Steady-state model fitting for TDCs ---------- 170

Chapter 8

8.1 Illustrative cross-sectional C-arm FDCT images. ---------- 192

Chapter 9

9.1 Coil embolisation treatment of intracranial aneurysms ---------- 202

9.2 Flow diversion treatment principle for intracranial aneurysms ---------- 204

9.3 Silk and FRED FD devices ---------- 206

Chapter 10

10.1 Representative angiograms of aneurysms treated with the SFD ---------- 221

10.2 Partially thrombosed aneurysm after treatment with the flow diverter ----- 230

10.3 Timings and results of angiographic follow-up ---------- 234

Chapter 11

11.1 Axis I grading for saccular aneurysms ---------- 251

11.2 Axis II grading for fusiform aneurysms ---------- 252

11.3 Illustrative case 1 ---------- 255

11.4 Illustrative case 2 ---------- 255

11.5 Illustrative case 3 ---------- 256

11.6 Illustrative case 4 ---------- 256

List of Tables

Chapter 3

3.1 A comparison of CT and MR perfusion imaging techniques ---------- 39

3.2 Perfusion parameters used in routine clinical practice ---------- 40

Chapter 4

4.1 Harvard-Oxford structural brain atlas based volumes of interest (VOIs) used for analysis of C-arm CT PBV and MR perfusion maps ---------- 79

4.2 Demographics, clinical characteristics, and imaging and treatment details for the recruited patients ---------- 80

4.3 Results of Bland Altman analysis of agreement and Pearson correlation analysis ---------- 84

4.4: Results of Bland Altman agreement and Pearson correlation analysis for weighted MR-rCBF and rCBV ---------- 85

Chapter 5

5.1: Demographic, aneurysm, and clinical characteristics of the patients and the location of DWI lesions ---------- 118

Chapter 6

6.1: Demographic, aneurysm, and clinical characteristics of the patients and the details of DWI lesions ---------- 143

6.2a C-arm CT PBV measurements (ml/100ml) for the atlas-based predefined VOIs (1-35) ---------- 144

6.2b C-arm CT PBV measurements (ml/100ml) for the atlas-based predefined VOIs (36-58) ---------- 145

Chapter 7

7.1: Demographic, aneurysm, and clinical characteristics of the study population. 171

7.2: TDC descriptive statistics for the differences in image intensity between the mask and the contrast-enhanced runs' projections measured over time - 172

Chapter 8

8.1 Landis and Koch criteria for interpretation of the Cohen's kappa statistic ---- 188

8.2 Results of Fisher's exact test and contingency analysis for the evaluators A and B for the three-step FDCT images evaluation ---------- 191

Chapter 9

9.1 Morbidity, mortality, and occlusion rates for FDs in major case series, systemic reviews, and meta-analysis ---------- 215

Chapter 10

10.1 Aneurysm locations presented as maximum sac size, neck width, and morphology ---------- 227

10.2 Clinical complications observed in patients treated with SFD ---------- 228

10.3 Angiographic outcomes for the aneurysms treated with SFD ---------- 233

10.4 Effect of patient and procedure related variables on SFD deployment difficulty, flow disturbance, and delayed neurological complications -------- 235

Chapter 11

11.1 Axis I: Grading of the saccular occlusions following deployment of the FD devices ---------- 254

11.2 Axis II: Grading of the parent artery patency following deployment of the FD devices ---------- 254

List of Abbreviations

2D	Two-dimensional
3D	Three-dimensional
A	
ACA	Anterior cerebral artery
ADC	Apparent diffusion coefficient
AICA	Anterior inferior cerebellar artery
AIF	Arterial input function
ASL	Arterial spin labelling
AUC	Area under curve
AVMs	Arteriovenous malformations
B	
BA	Basilar artery
BBB	Blood brain barrier
BET	Brain extraction tool
C	
CBF	Cerebral blood flow
CBV	Cerebral blood volume
CE	Coil embolisation
CE’	Conformité Européenne
CI	Confidence interval

COA	Carotid ophthalmic artery
CRF	Case report form
CSF	Cerebrospinal fluid
CT	Computed tomography
CTA	Computer tomographic angiography
CTA-SI	Computer tomographic angiography source images
CTP	Computed tomographic perfusion

D

DCE	Dynamic contrast enhanced
DCI	Delayed cerebral ischaemia
DD	Deployment difficulty
DSA	Digital subtraction angiography
DSC	Dynamic susceptibility contrast
DWI	Diffusion weighted imaging

E

ECE	Endosaccular coil embolisation
EOT	End of treatment
ET	Echo time

F

FD	Flow diverter
FD	Flat detector
FDA	Food and Drug Administration
FDCT	Flat detector computer tomography

FLIRT	FMRIB linear image registration tool
FMRIB	Functional magnetic resonance imaging of brain
FOV	Field of view
FRED	Flow redirection endoluminal device
FSL	FMRIB software library

G

GCS	Glasgow coma scale
Gy	Gray

H

HU	Hounsfield units

I

ICA	Internal carotid artery
ICU	Intensive care unit
IE	Image intensity
INR	Interventional neuroradiology
ISAT	International Subarachnoid Aneurysm Trial

L

L	Length
LCD	Low contrast detectability
LOWESS	Locally weighted scatterplot smoothed
LUT	Look up table

M

MCA	Middle cerebral artery

MDCT	Multi detector computed tomography
MDCTA	Multi detector computed tomographic angiography
MIP	Maximum intensity projection
MR	Magnetic resonance
MRA	Magnetic resonance angiography
mRS	Modified Rankin score
MNI	Montreal neurological institute
MTT	Mean transit time

N

NCCT	Non-contrast computer tomography
NPV	Negative predictive value

O

OG	Occlusion grade
ONNRU	Oxford Neurovascular and Neuroradiology Research Unit

P

PACS	Picture archiving and communication system
PAO	Parent artery occlusion
PAT	Parent artery thrombosis
PBV	Parenchymal blood volume
PCA	Posterior cerebral artery
PCoA	Posterior communication artery
PED	Pipeline embolisation device
PET	Positron emission tomography

PICA	Posterior inferior cerebellar artery
PITA	Pipeline embolization device in the intracranial treatment of aneurysms
PPV	Positive predictive value
PWI	Perfusion weighted imaging

R

rCBF	Relative cerebral blood flow
rCBV	Relative cerebral blood volume
RIS	Radiology information system
ROC curve	Receiver operating characteristic curve
ROI	Region of interest
rPBV	Relative parenchymal blood volume

S

SAH	Subarachnoid haemorrhage
SCA	Superior cerebellar artery
SD	Standard deviation
SFD	Silk flow diverter
SVD	Singular value deconvolution

T

T	Tesla
TDC	Time density curve
TOF	Time of flight
TR	Repetition time
TTP	Time to peak

U

UPE	Untoward procedural events

V

VA	Vertebral artery
VOI	Volume of interest
VRT	Volumetric reconstruction technique

W

W	Width
WFNS	World federation of neurosurgical societies

1

Preamble

1.1 Background

Interventional neuroradiology (INR) is the branch of medicine that employs minimally invasive image-guided catheter-based techniques to diagnose and treat cerebrovascular, spine, and head and neck disorders (Lakhan et al., 2009). As a separate discipline dedicated to the treatment of disorders for which the traditional surgical procedures were deemed not feasible, INR owes its origin to the conceptual and technical contributions from a range of specialties including radiology, neurosurgery,

cardiology, neurology, and vascular surgery. It is of historical interest to note that Egas Moniz, a Portuguese neurologist, pioneered the first diagnostic cerebral angiogram in humans in 1927, by injecting strontium bromide through a surgically exposed common carotid artery (Wolpert, 1999). His technique, albeit with few modifications, remained in practice for the next three decades. It was not until 1960 that the possibility of minimally invasive treatment of cerebrovascular disorders was explored when an American neurosurgeon, Alfred Luesssenhop, first described endovascular embolisation of brain arteriovenous malformations (AVMs) by injecting silastic beads into the arteries of neck (Luessenhop AJ and Spence WT, 1960). Subsequently in 1971, Fedor Serbinenko, a Russian neurosurgeon, inspired by the children playing with Helium balloons at May day celebrations in Moscow's Red Square, described his technique for treating cerebral aneurysms and carotid cavernous sinus fistulas with detachable latex balloons (Serbinenko, 1971). However, until 1980s, the neurointerventional techniques were rudimentary and considered largely experimental, reserved for settings deemed surgically difficult e.g. treatment of giant or surgically inaccessible aneurysms (Liu, 2006).

Late 1980s and early 1990s witnessed a rapid growth in the discipline of INR, increasing the range of neurovascular disorders that fell within its realm, and for which it offered newer, safer, and less-invasive treatment alternatives. Its applications expanded from the treatment of surgically difficult aneurysms to now newer procedures for arteriovenous malformations, traumatic vascular injuries, and highly vascular tumours of head, neck, and spine (Renowden, 2005). Developments that led to

this evolution were multifactorial; however, improved imaging techniques and novel medical devices created the milieu which encouraged a rapid evolution of interventional techniques (Strother, 2000). In this regard, a need for better procedural guidance and control in the interventional suite lead to the introduction of new imaging techniques such as digital subtraction angiography (DSA), roadmap fluoroscopic guidance, and three-dimensional (3D) DSA; which improved both the quality and quantity of information available to the neurointerventionsit to adequately plan, control, and optimize the sophisticated endovascular procedures. In parallel, novel devices such as microcathetrs, electrolytically detachable coils, vascular reconstruction prosthesis, and newer embolic agents enhanced the range of materials available for neurovascular treatments to ensure improved procedural outcomes (Liu, 2006; Strother, 2000). Together, these innovations helped redefine and enhance the neuroradiologist's role from a consultant providing diagnostic services to an interventionist providing minimally invasive neurosurgical interventions and assuming an active role in treatment.

Currently, neuroendovascular procedures exist for a large number of conditions including intracranial aneurysms, cerebral vasospasm, AVMs, dural arteriovenous fistulas, intra- and extra-cranial atherosclerosis, acute ischaemic stroke, and vascular head and neck tumours (Renowden, 2005). However, when considering the potential for growth, two entities with the largest impact on INR practice are the *intracranial aneurysm treatment* and the acute *stroke interventions* (Cloft et al., 2002). The intracranial aneurysms occur with an incidence of ≈9.0 aneurysms per 100,000 patient-

years, prevalence of 3.7 – 6.0% (angiographic studies), and have a 5-year cumulative rupture risk of ≈1.2% (Keedy, 2006; Menghini et al., 1998; Wermer et al., 2007). An estimated 30,000 patients in the United States experience aneurysmal subarachnoid haemorrhage (SAH) (Keedy, 2006). While a small proportion of aneurysms may not be amenable to endovascular treatment e.g. the small-unruptured aneurysms with favourable natural history, aneurysms with devastating neurological sequela of rupture, or the aneurysms for which endovascular treatment is deemed not suitable, nevertheless the intracranial aneurysm treatment continues to constitute a large proportion of the INR procedure volume (Cloft et al., 2002). Following the publication of International Subarachnoid Aneurysm Trial (ISAT) results, demonstrating the superiority of endovascular coil embolisation over neurosurgical clipping, the endosaccular coil embolisation (ECE) remained the primary endovascular means for aneurysm treatment (figure 1.1) (Molyneux, 2002). However, aneurysms with complex morphology such as large size, wide necks, and fusiform shape presented a technical challenge (Lubicz et al., 2010). In addition, the durability of coil embolisation was soon recognized as a major concern with reported high recurrence rates (20.8%, 95% CI 19.8 – 21.9%) (Ferns et al., 2009). To address the shortcomings of ECE, parent vessel reconstruction with flow diverter (FD) devices have recently emerged as an alternative treatment strategy (figure 1.2) (Lubicz et al., 2010). The work in chapters 09 – 11 of this thesis concerns the initial clinical experience with this new treatment approach, and based on the initial experience, a new grading system is proposed to monitor the angiographic outcomes for FDs. This work (chapters 10 and 11) was published soon

after its completion to inform the neurointerventional community on the safety and efficacy of FDs. Since then growing evidence has accumulated on the use of FDs, and several institutions now attempt flow diversion as first line of treatment for unruptured intracranial aneurysms (Arrese et al., 2013; Brinjikji et al., 2013; Chalouhi et al., 2014; Zanaty et al., 2014).

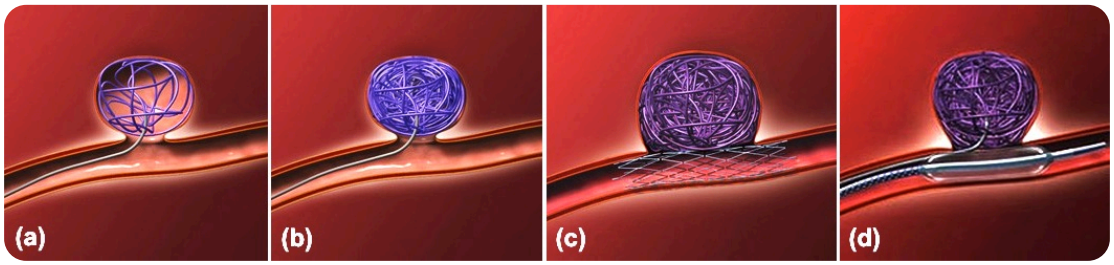


Figure 1.1: Coil embolisation treatment for intracranial aneurysms. Schematic representation of various coil-embolisation techniques for intracranial aneurysms: (a and b) endosaccular coil embolisation (ECE), (c) stent-assisted ECE, and (d) balloon assisted ECE.

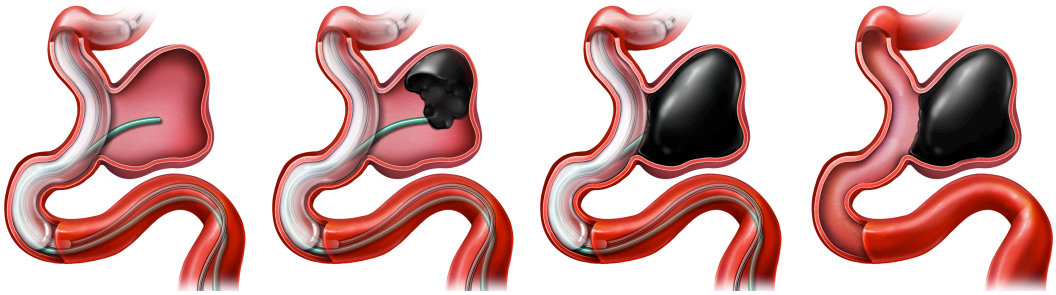


Figure 1.2: Flow diversion principle for treatment of intracranial aneurysms. A flow diverter device deployment in the parent vessel across the aneurysm neck creates a barrier at the 'parent vessel – aneurysm' interface with subsequent intrasaccular thrombosis and aneurysm occlusion.

For acute ischaemic stroke, endovascular management is emerging as an attractive treatment alternative with extensive ongoing research in this area (Meyers et al., 2011). Stroke is the third leading cause of death and the leading cause of long-term disability in industrialized nations. Annually, approximately 795,000 people suffer a new (approx. 610,000) or recurrent (approx. 185,000) stroke in the US with significant economic impact (73 billion US healthcare dollar bills per annum) (Go et al., 2014). The traditional treatment of acute ischaemic stroke with systemic thrombolysis remains the standard of care, however, newer endovascular treatment alternatives have emerged which include intra-arterial thrombolysis, mechanical thromboembolectomy, suction thrombectomy, angioplasty, and the most promising stent retriever thrombectomy (Khalessi et al., 2011; Meyers et al., 2011; Ruff and Froehler, 2013). Compared with intravenous thrombolysis, endovascular treatment achieves higher recanalisation rates and better clinical outcomes (Berkhemer et al., 2015). However, the results of prior randomised controlled trials (SYNTHESIS Expansion, MR RESCUE, and IMS-III trials) highlighted that with a longer delay in initiating the endovascular therapy, the higher recanalisation rates fail to translate into better clinical outcomes (Broderick et al., 2013; Ciccone et al., 2013; Kidwell et al., 2013). An endovascular acute stroke intervention can only be effective if salvageable brain tissue exists; for irreversibly damaged tissue, not only the endovascular treatment is ineffective but can be potentially harmful (Meyers et al., 2011). A strict time-criterion cannot reliably predict when the transition from ischaemia to infarction occurs for a particular patient and is therefore inadequate to select patients for endovascular treatment. With a limited time-window for

revascularisation, an expedited imaging evaluation to characterise brain tissue viability is thus invaluable, which in most instances is performed using computer tomography (CT) or magnetic resonance imaging (MRI), both of which provide anatomical and physiological data (Meyers et al., 2011). In an emergent setting, however, transferring a patient first to the CT or MR scanner for diagnosis and then to interventional suite can significantly delay the revascularisation treatment. In this regard, availability of diagnostic imaging capabilities in the interventional room to provide the anatomical and physiological information essential to patient selection can shorten the interval between the patient's arrival to a stroke treatment facility and the onset of a revascularisation procedure, with expected improvements in angiographic and clinical outcomes. An ambitious concept of 'one-stop-shop' has thus been advanced for the neurointerventional suite of the future where a single room capable of providing the facilities to perform endovascular intervention would also have the diagnostic imaging capabilities to obtain the anatomical and physiological data, traditionally obtained from CT or MR imaging (figure 1.3) (Strother, 2012). Such setup using the advanced flat detector equipped C-arm systems in combination with the novel devices, would conceivably be beneficial in achieving improved procedural and clinical outcomes by: (a) allowing in-room selection of patients for revascularisation treatment thereby reducing the time from patient's arrival at a dedicated stroke treatment centre to the onset of revascularisation procedure and (2) enhancing the interventional environment to achieve improved procedural guidance through provision of both anatomical and physiological data (Strother, 2012). The work in chapters 02 – 08 explores the

diagnostic imaging potential of the C-arm systems used in the neurointerventional suite, particularly for extracting the physiological information on cerebral perfusion using an optimised parenchymal blood volume (PBV) imaging protocol in a cohort of aneurysmal SAH patients with delayed cerebral ischaemia (DCI).

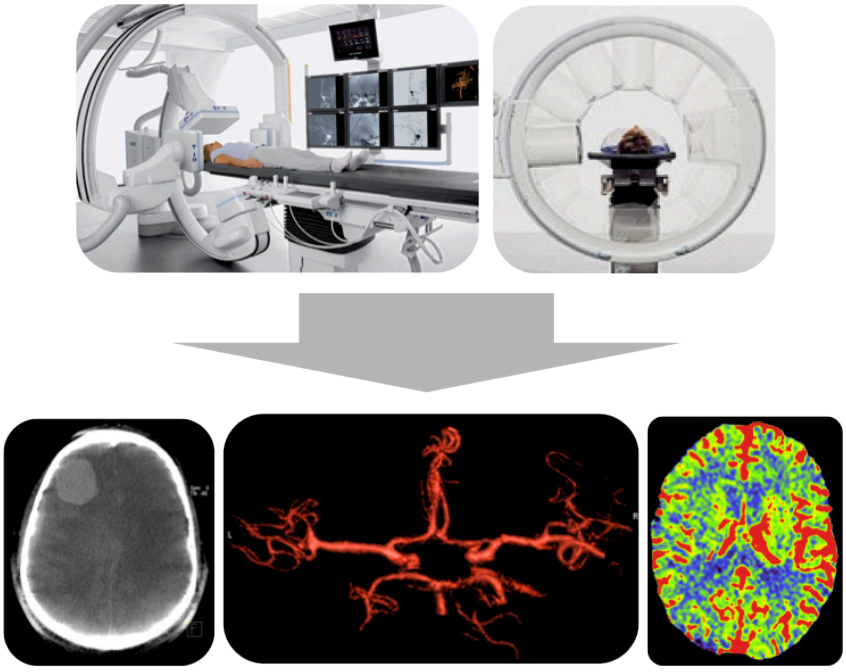


Figure 1.3: 'One-stop-shop' neurointerventional suite with diagnostic and interventional capabilities. The same C-arm imaging apparatus used for procedural guidance can generate images of brain parenchyma and vessels, and has potential for perfusion imaging.

In summary, keeping in view the current trends and the historical development of INR into a separate discipline, it will not be wrong to believe that the future of this highly technology driven specialty would remain dependent on the advancements in medical devices and the imaging systems used in the interventional suite. The work under consideration thus addresses the two themes central to INR practice i.e. the

imaging and the devices used for neuroendovascular procedures. In the first part (chapters 2-8) of this work, cross-sectional imaging potential of *C-arm imaging systems* to evaluate the brain structure and function is explored through its application in the particular clinical setting of delayed cerebral ischaemia (DCI) following aneurysmal SAH. The second part (chapters 9-11) of thesis concerns the study of a new *flow diverter device* for treatment of intracranial aneurysms.

1.2 Thesis Structure and Organization

As described above, the work under consideration is organized into two parts: (a) chapters 02 – 08 focus on the cross-sectional imaging potential of C-arm systems, specifically the PBV protocol imaging in the interventional suite, and (b) chapters 09 – 11 describe the early experience with a new FD device and propose a novel grading schema for evaluating the angiographic outcomes after flow diversion treatment. The individual chapters (02 – 08 and 09 – 11) are connected under these two themes. Each chapter is loosely structured along the lines of a research paper with the aim that in addition to being part of the whole, it may also function as a standalone piece of work for the convenience of reader. This approach was chosen to allow the reader a flexibility of choosing any chapter and be able to understand its core concepts without the necessity of having gone through the antecedent sections. Figure 1.4 provides an overview of the thesis.

The first part of thesis concerning C-arm flat detector computed tomography (C-arm FDCT or C-arm CT) imaging begins with an introduction to the C-arm FDCT

technique, which includes an overview of the underlying physics and the applications of C-arm FDCT cross-sectional imaging in neurointerventional suite from the standpoint of project's commencement (chapter 2). This is followed by an introductory discussion of the perfusion imaging, the potential role of perfusion imaging in neurointerventional suite, and the theoretical background of C-arm CT PBV imaging (chapter 3).

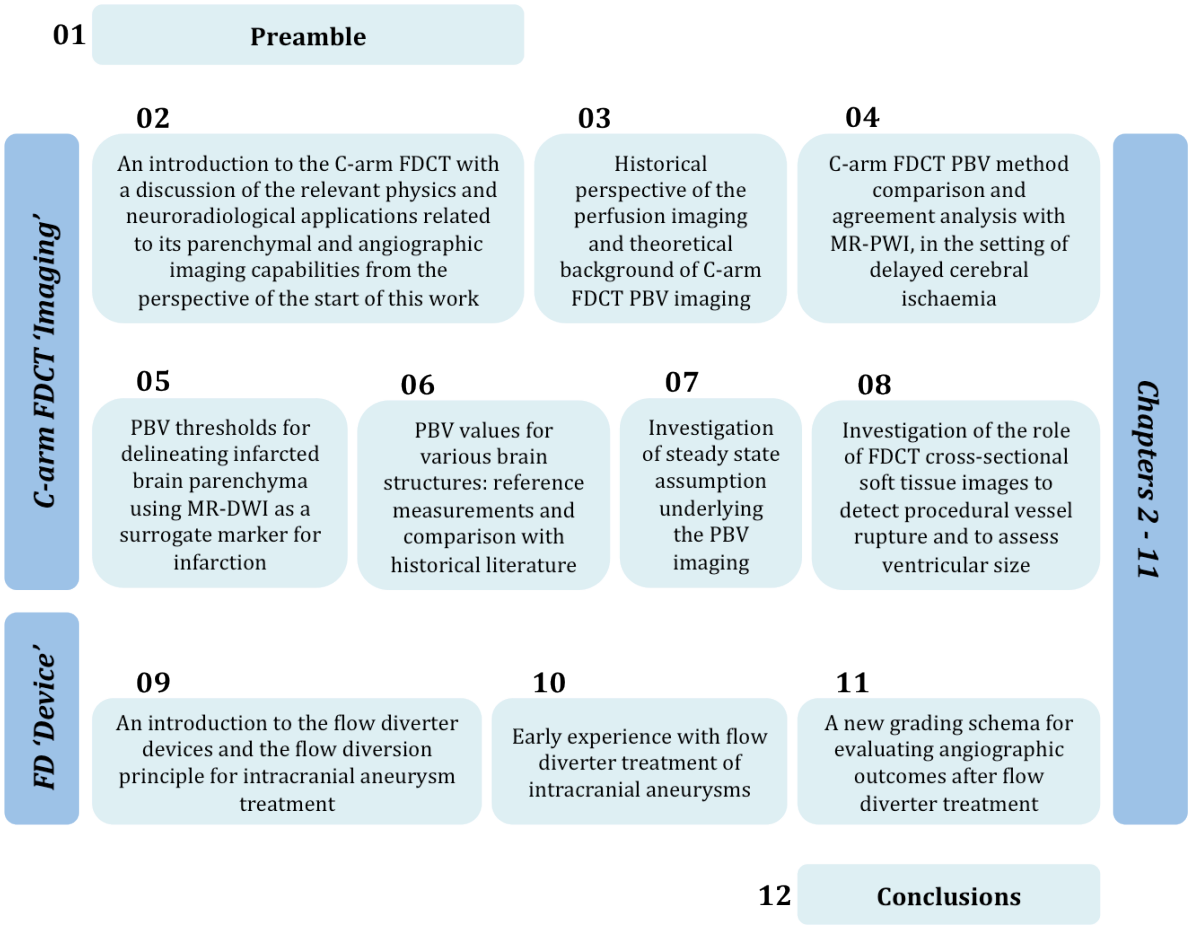


Figure 1.4: An illustrative overview of the thesis chapters and their central themes.

Chapter 4 explores the relationship of C-arm CT PBV parameter to MR perfusion parameters and concludes that PBV is a composite parameter distinct from CBV with

weightings of both CBF and CBV. In the subsequent chapter, absolute and relative PBV thresholds for demarcation of infarcted brain parenchyma are estimated (chapter 5). Chapter 6 provides a catalogue of reference PBV values for various regions of the brain. To what extent the steady-state assumption underlying PBV calculations is met in a clinical setting, is investigated in the next chapter (chapter 7). The work in chapter 8 was conducted before the start of patient recruitment for the C-arm CT PBV project and investigates the utility of C-arm FDCT cross-sectional soft tissue images in detecting the procedural vessel rupture and evaluating the ventricular size.

The second part of thesis concerning early clinical experience with the flow diversion treatment of intracranial aneurysms begins with an introduction to the flow diversion principle (chapter 9). In the next chapter, early clinical experience with an FD device is discussed – at the time of its publication, this work represented the largest multicentre experience with an FD device and informed the neurointerventional community on the safety and efficacy of flow diversion treatment – the discussion for this chapter is kept relevant to the time it appeared in public domain, however, a more updated discussion on the current status of the FDs used for intracranial aneurysm treatment is included in chapter 09 (chapter 10). A novel grading schema to monitor the angiographic outcomes of flow diversion treatment is discussed in chapter 11 – this grading schema was published in 2011 and in the subsequent years has found application in both research and clinical practice. The final chapter provides a brief summary of conclusions of this work (chapter 12).

2

C-arm FDCT: The Technique and its Applications in Interventional Neuroradiology

2.1 Abstract

Background and purpose: C-arm flat detector computed tomography (C-arm FDCT or FDCT) is an imaging tool available in the interventional suite that provides three-dimensional (3-D) volumetric imaging data through application of CT-like reconstruction algorithms to a series of two-dimensional (2D) projections obtained during C-arm rotation. The technique is relatively new and at its current level of performance, lags behind conventional CT in terms of image quality. However, the advantage of its availability in the interventional room has prompted neuroradiologists to identify clinical settings where its role is uniquely beneficial. This chapter briefly reviews the physics and the applications of C-arm FDCT soft tissue and angiographic imaging (from the standpoint of commencement of the work discussed in subsequent chapters 03 – 08).

Conclusions: FDCT images allow detection of procedural complications, evaluation of low radiopacity stents, and assessment of endosaccular coil packing in intracranial aneurysms. Additional roles are 3D angiography that provides an accurate depiction of vessel morphology with intravenous administration of low-concentration radiographic contrast media and a potential for perfusion imaging due to its dynamic scanning capability. A single scan combining soft tissue and angiographic examinations reduces the radiation dose and examination time. Ongoing developments in flat detector technology and reconstruction algorithms are expected to further enhance its performance and increase the range of its applications. If current research confirms its potential for assessing cerebral haemodynamics by perfusion scanning, the

combination would redefine it as an invaluable tool for interventional neuroradiology procedures. The perfusion imaging and its existing capabilities of parenchymal and angiographic imaging would also extend its use to the triage of acute stroke patients.

2.2 Introduction

Interventional neuroradiology and endovascular minimally invasive treatments have shown growth in the last decade owing, in part, to the improvements in therapeutic devices (Strother, 2000). This increase in the number and range of conditions amenable to neuro-endovascular treatments stimulated parallel developments in radiographic imaging. The ability of two-dimensional imaging (i.e. digital subtraction angiography (DSA) and standard fluoroscopy) to characterize three-dimensional anatomy is inherently inadequate and there had been a need to develop robust systems capable of three-dimensional vascular and soft tissue imaging in the interventional suite. The introduction of three-dimensional DSA partly addressed the problem but the low-contrast resolution of most angiographic systems remained inadequate for soft tissue imaging. One proposed solution was to integrate a CT or MR scanner in the treatment room but this idea had limited applicability due to high cost of such composite systems and space constraints (Orth et al., 2008).

Development of hybrid C-arm systems capable of cross-sectional soft tissue imaging started with the application of CT-like reconstruction algorithms to conventional angiographic data (Grass et al., 1999). Initial results, obtained using image intensifier based angiographic systems, demonstrated the feasibility of this principle (Linsenmaier et al., 2002). However, performance parameters of these systems were inadequate to resolve soft tissue details until the introduction of digital flat panel detectors. The flat detectors (FD) overcame most limitations of data collection with conventional image intensifiers and, together with refinements of cone-beam

reconstruction algorithms, have proved pivotal in bringing soft tissue imaging into the neurointerventional suite (Kalender and Kyriakou, 2007; Neitzel, 2005).

C-arm angiographic systems equipped with flat panel detectors and capable of volumetric imaging – referred herein as C-arm flat detector computed tomography (C-arm FDCT) – were introduced for clinical use in 2004 and have found applications across specialities for both vascular and non-vascular interventions (Wallace et al., 2008). Reports on the clinical use of C-arm FDCT first appeared in the interventional neuroradiology literature, which were thence followed by reports of its use in general radiology. This chapter aims to discuss the basic physical principles of C-arm FDCT technique and reviews the literature in regard to its use in interventional neuroradiology.

2.3 Physics of C-arm FDCT

C-arm FDCT and cone-beam CT employ different gantries but share a similar imaging principle and, therefore, the two terms have often been used interchangeably in the literature. In C-arm FDCT, the area of interest is scanned over an angular range of *180° plus the fan-angle*. A series of two-dimensional projection images are obtained over this semi-circular scan trajectory followed by application of CT-like reconstruction algorithms (modified Feldkamp algorithm) to generate three-dimensional volumetric reconstructions which can be viewed in orthogonal planes (Kalender and Kyriakou, 2007). The technique uses the C-arm mechanical set-up equipped with FDs and relies on the same x-ray source used for C-arm fluoroscopy and digital angiography. However, the x-ray tube operation more closely resembles conventional CT (cCT) in that the

automatic exposure control (AEC) maintains a fixed tube voltage over the scan range, modulating the tube current only. An unaltered tube voltage is meant to avoid any fluctuations in the beam energy that may result in inconsistent attenuation measurements and image artefacts. Cone beam x-ray geometry and the two-dimensional nature of the detectors allow volumetric imaging in a single rotation of the source and detector, a key feature distinguishing FDCT from cCT (Kalender and Kyriakou, 2007).

The idea of applying CT-like algorithms to angiographic acquisitions was first explored in C-arm systems equipped with image intensifiers (Fahrig et al., 1997; Linsenmaier et al., 2002). However, the limited dynamic range and low-contrast detectability of image intensifiers restricted their use for high-contrast vessel imaging only (Akpek et al., 2005b; Kalender and Kyriakou, 2007). Development of flat panel detectors with improved performance parameters and their incorporation in angiographic systems renewed interest in low-contrast (soft tissue) imaging. Compared with the image intensifiers, FDs offer better image quality with significantly improved detective-quantum-efficiency (DQE), modulation-transfer-function (MTF), dynamic range, and dose efficiency (Cowen et al., 2008).

The FDs integrated in currently available angiographic systems consist of two independent layers in optical contact: (a) a fluorescence scintillator screen (needle shaped crystals of Caesium Iodide (CsI)) which absorbs and converts the impinging x-rays into light photons and (b) a layer of photodiodes (hydrogenated amorphous Silicon, aSi-H) which functions to convert light photons into a digital image signal (figure 2.1) (Neitzel, 2005). The detectors have been designed to convert the incident

photons into a geometry conserving electrical signal as efficiently as possible.

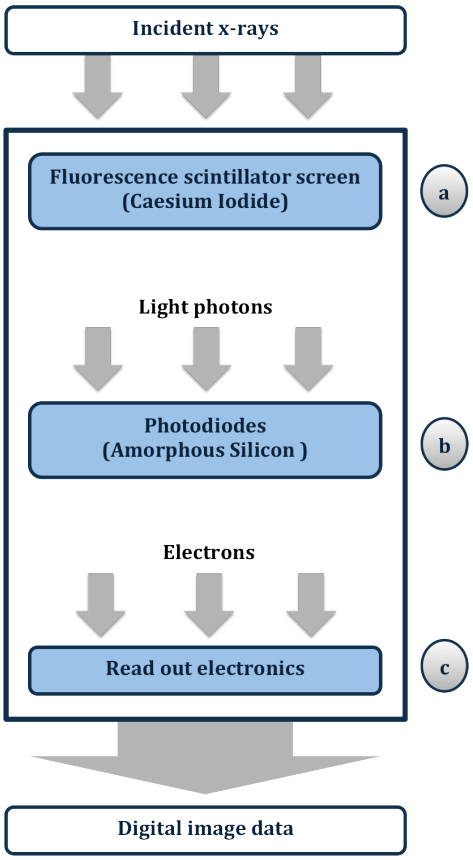


Figure 2.1: Schematic illustration of a flat panel detector used in currently available biplane C-arm angiographic systems. Incident x-ray beam is absorbed and converted into light photons by the fluorescence scintillator screen (a); a layer of photodiodes absorbs the light photons with subsequent generation of electron-hole pairs which are stored as geometry conserving charge (b); the read out electronics are responsible for converting the geometry conserving electrical signal into digital data which can be reconstructed into an image (c).

The indirect nature of this conversion process (i.e. through an intervening step of luminescent light generation) has important implications to the choice of screen thickness. While a greater screen thickness increases absorption efficiency and consequently the DQE, it adversely affects the MTF due to light photon scatter and leads to a loss of spatial resolution. For currently used FDs, a 500 µm (approx.) thick layer of

needle shaped CsI crystals allows an optimum trade-off between DQE and MTF (Neitzel, 2005). The choice of CsI as the scintillator substance imposes a limit on the read-out speed of flat panel detectors. Due to the slow scintillation response of CsI, FDs suffer from the *after-glow phenomenon* at high image acquisition rates, in which each projection carries a ghost of the prior image. With correction, currently available systems can achieve frame rates of 15 to 30 per second without causing image degradation. Corresponding scan times for a single sweep of *180° plus the fan-angle* typically fall in the range of 6 to 20 seconds and are considerably longer than those for cCT (Gupta et al., 2006; Orth et al., 2008).

Large area FDs can be constructed from plasma deposition of aSi-H. With an area of 30×40 cm^2, currently available FDs offer a field-of-view (FOV) approaching 18 cm in the z-direction (Gupta et al., 2006). While a craniocaudal coverage of this order is an advantage for imaging a large anatomical region such as the head in a single scan (thereby obviating any need for patient translation or repeat scanning), there is a marked increase in the scattered radiation (Gupta et al., 2006; Orth et al., 2008). The ratio of scattered radiation to primary radiation at detector surface may exceed 3.0 for FDCT (cone beam geometry) compared with ~0.2 for cCT (fan-beam geometry), and accounts for much of the image quality differences observed between the two techniques (Kyriakou and Kalender, 2007). Numerous strategies have been devised to reduce the amount of scatter (e.g. bow-tie filters and anti-scatter grids) or to correct for the scatter-induced degradation of image quality. Currently available C-arm FDCT systems employing these strategies offer a contrast resolution that is comparable to cCT and is sufficient to resolve details to an attenuation difference of 5-10 Hounsfield Units.

Although spatial resolution of FDCT is influenced by multiple factors, the size of individual detector elements remains its primary determinant. Each FD element consists of a sensitive area and a portion covered by detector electronics; the ratio of these two parameters defining the *'fill factor'*. Decreasing detector element size below a certain limit reduces the fill factor to the point at which DQE losses become prominent. As a result, there is a limit to the smallest optimum detector element size and thus to spatial resolution (Neitzel, 2005). For currently available FDCT systems, an isotropic spatial resolution potentially approaching 150×150×150 μm^3 is theoretically achievable (Gupta et al., 2006). Compared with cCT, this resolution is superior in terms of both voxel size and their isotropic nature, with the latter allowing manipulation of reconstructed images and interactive viewing of FDCT volumes in a more flexible and efficient manner (Akpek et al., 2005b).

A comparison of FDCT to cCT is desirable. However, from a neurointerventional perspective, such a comparison should be mindful of the primary advantage of FDCT technique i.e. its availability in the catheter laboratories. Image quality, though relevant, should not be the sole criterion for evaluating its value as a clinical imaging tool. The potential applications of FDCT are many and their realisation depends on the provision of images with sufficient quality to answer queries arising in association with treatment procedures in the angiography room. The ubiquitous role of cCT as primary diagnostic tool remains unchallenged.

2.4 Applications of FDCT in the Angiography Suite

2.4.1 Evaluation of Intracranial Stents Used in the Treatment of Stenotic Arterial Disease

2.4.1.1 Procedural Evaluation

Angioplasty and deployment of endovascular stents are treatments for symptomatic intracranial atherosclerotic disease in patients with vessel stenosis refractory to medical treatment (Buhk et al., 2008; Gröschel et al., 2009; Suh et al., 2008). Adjunctive use of stents in coil embolisation treatment of cerebral aneurysms particularly those with fusiform, wide neck, or complex morphology is known (Akpek et al., 2005a; Wakhloo et al., 2008), in addition to their use for vessel salvage (Yoo et al., 2009), and for the treatment of acute vessel thrombosis (Levy et al., 2007). A new generation of stents with tighter mesh architecture, designed to promote thrombosis of intracranial aneurysms through flow diversion, have recently become available and are in use for treatment of aneurysms with complex morphology (Sadasivan et al., 2009).

Stenting, however, is not without its limitations. Peri-procedural complications, notably acute and subacute in-stent thrombosis occur in approx. 10% of cases while long-term restenosis rates have been reported in a range of 8-30% (Fiorella et al., 2007; Riedel et al., 2009; Zaidat et al., 2008). Evidence from the cardiology literature highlights many predisposing variables for these adverse events (Honda and Fitzgerald, 2003). Among them, procedure related factors (e.g. stent under-expansion, incomplete vessel wall apposition) are considered the most important and their prevention and management depends on a detailed knowledge of the position of a deployed stent and

its conformity to the vessel wall. Availability of this information to the operator can help optimize stent use to reduce the complication rate and improve the treatment safety and efficacy (Honda and Fitzgerald, 2003). Stents designed for intracranial use incorporate features such as low profile outline, flexible structure, adequate radial strength, and trackability. These design features, imposed by the anatomy of cerebral vasculature, frequently result in low radiopacity and consequent poor radiographic visibility of intracranial stents (Benndorf et al., 2005). Small stent size and superimposed bony structures further compromise their visibility on conventional digital radiography (DR) and fluoroscopy (Ebrahimi et al., 2007). CT angiography and MR angiography suffer from considerable stent associated artefacts and have insufficient spatial resolution to adequately visualise current neurovascular stents (Buhk et al., 2008; Ebrahimi et al., 2007).

In contrast, FDCT has emerged as a technique with performance characteristics suitable for imaging such small, high-contrast structures. A sub-millimeter isotropic spatial resolution allows visualization of stent struts as small as 50-70 μm (Figure 2.2). Three-dimensional volumes acquired with FDCT can be rotated and reformatted to yield images in any plane, allowing stent visibility unmatched by any other current clinical imaging modality. Ebrahimi and colleagues used FDCT, DR, and fluoroscopy to evaluate deployment properties of four different types of intracranial stents in an in-vitro, curved vessel model (Ebrahimi et al., 2007). They found that FDCT showed the stent structure in considerably more detail compared to DR and fluoroscopy. Projections reconstructed for different desired orientations, including but not limited to the orthogonal and enface views, allowed details of the deployed stent architecture to

be studied in multiple planes. FDCT was able to show complications such as kinking, simulated prolapse of the stent struts at the aneurysm neck, and any tendency to flatten during bending. On DR and fluoroscopy, only the terminal markers of the stents were consistently visualised, allowing merely an indirect assessment of deployment.

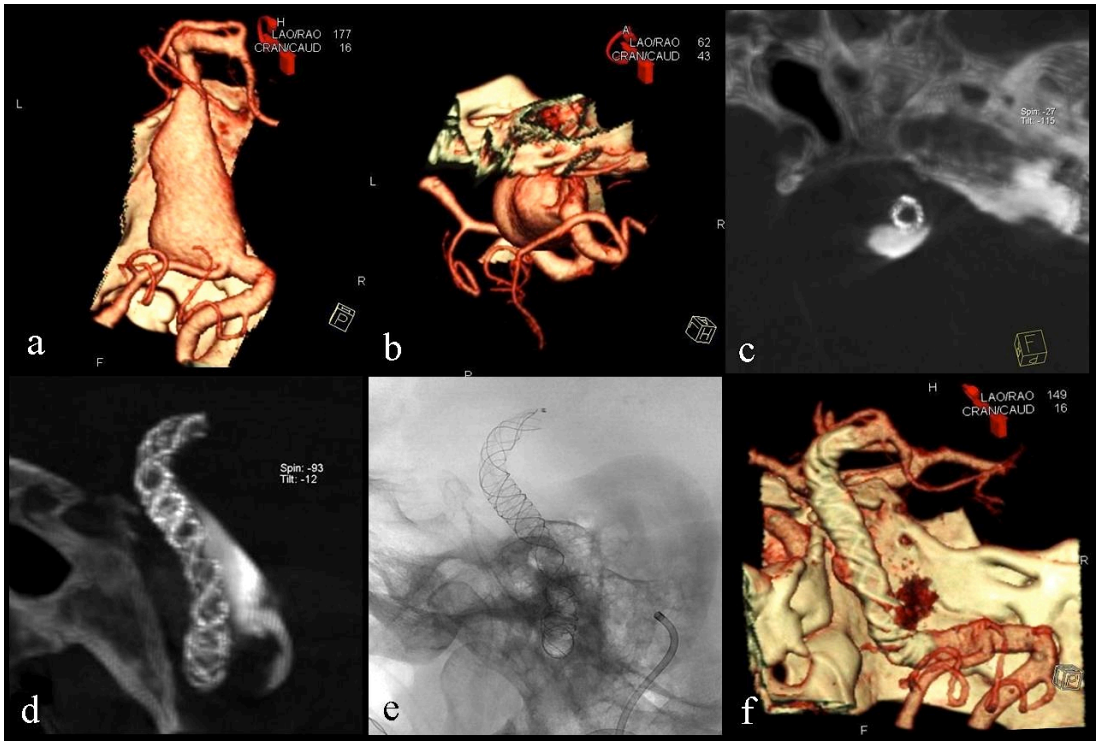


Figure 2.2: C-arm FDCT evaluation of intracranial stents. A giant fusiform basilar artery aneurysm treated with a combination of LEO and SILK stents (BALT International): (a, b) pre-stent CTA; (c, d) axial and sagittal FDCT MIP images showing the stent architectures; (e) post-stent lateral radiograph; (f) post-stent CTA image.

Benndorf et al. reported their experience with FDCT imaging performed immediately following stent placement in three patients for vessel stenosis (two intracranial and one extracranial) (Benndorf et al., 2005). FDCT images allowed a detailed assessment of stent position, deployment characteristics, and adaptation to the

vessel wall. For one patient with atherosclerotic stenosis of the internal carotid artery, the images showed asymmetric deployment of the stent with a narrowed lumen. Soft tissue images from the same volume revealed a calcified plaque preventing expansion of the stent. Compared with FDCT, both visualization of the stent and assessment of plaque morphology were inadequate with subtracted as well as non-subtracted DR images. Although, a post-procedural CTA examination can help to assess vascular patency in such a setting, it requires patient transfer to the CT room and assessment of the stent lumen may be inaccurate because of a tendency for CTA to overestimate the degree of in-stent stenosis (Trossbach et al., 2004). FDCT on the other hand allows an immediate, accurate procedural assessment of the deployed stent while the patient is still on the angiography table.

2.4.1.2 Follow-up Imaging

The follow-up examination to detect in-stent stenosis, generally requires intra-arterial DSA. However, DSA is invasive and carries a 1.3% risk of procedure-related neurological complications (Willinsky et al., 2003). CT angiography, an alternative, has problems of overestimating in-stent stenosis, while the value of MRA in assessing the stent lumen is compromised by metal-related susceptibility artefact and signal loss (Ebrahimi et al., 2007; Trossbach et al., 2004). To investigate the value of FDCT for stent follow-up, Buhk and colleagues obtained FDCT studies with intravenous administration of contrast material in patients after intracranial stenting, and found the reconstructed images to allow a reliable assessment of the stent lumen that correlated with flow measurements made using transcranial Doppler sonography (Buhk et al., 2008). Intravenous FDCT may thus represent a safe, less invasive, and cost effective alternative

to DSA for stent follow-up, which could be performed on an outpatient basis. Simultaneous visualization of all intracranial vessels and CT-like images of brain parenchyma reconstructed from the same volume provide additional useful information, reducing the overall radiation and contrast doses for the patient.

2.4.2 Evaluation of Stents Used in the Treatment of Intracranial Aneurysms

2.4.2.1 Procedural Evaluation

Stent-assisted coil embolisation is a well established treatment option for the management of wide neck and fusiform aneurysms (Akpek et al., 2005a; Wakhloo et al., 2008). The deployed stent serves as a scaffold helping to contain endosaccular coils. To ensure safe and effective stent placement there is a need to: (a) evaluate the position and deployment of stent at the desired place and (b) detect any coil prolapse into the parent artery or herniation of stent struts into the aneurysm sac. The nitinol wires of the stent struts have poor radiopacity and DR images can only reliably detect the platinum markers placed at intervals (usually just at the ends) on the currently available stents (Ebrahimi et al., 2007). Thus only a gross estimate of the stent position is possible without a reliable assessment on whether the stent was adequately deployed in the vessel lumen. With DR images alone, the position of the stent and its relationship with coils may remain unclear and incomplete deployment or vessel wall apposition may go unnoticed.

FDCT examination offers a solution to this imaging problem within the interventional suite. Richter et al. studied 11 patients with FDCT technique who had

undergone stent-assisted coil embolisation procedures (Richter et al., 2007). The images were compared with DSA to determine their efficacy in evaluating deployment characteristics of the stent and position of the coils within aneurysms. For aneurysms smaller than 10 mm in diameter, favourable assessments were possible, with a stent visibility sufficient to exclude any coil prolapse through the stent struts or herniation of the struts into the aneurysm. For aneurysms greater than 10 mm, beam-hardening artefacts from the larger endoaneurysmal coil-mass impaired stent visibility in some cases, particularly at the aneurysm neck. In a subset of patients (n = 3), an additional FDCT scan was carried out after stent deployment but before placement of coils. These images allowed excellent visualisation of the stent network throughout its length. The same volume data, reformatted to generate soft tissue images of the brain parenchyma, allowed assessment of the size of the cerebral ventricles and helped to exclude any procedural haemorrhagic complication.

2.4.2.2 Follow-up Evaluation

Aneurysms treated by coil embolisation recur in 20% to 30% of cases, warranting routine follow-up examination (Li et al., 2006; Piotin et al., 2007). For detection of recanalization, the imaging follow-up is obtained at three to six months after treatment by either using catheter angiography, an invasive technique, or the time-of-flight MR angiography (TOF-MRA) with which the evaluation may be limited secondary to metallic coil-mass related susceptibility artefact. Does FDCT have any diagnostic value for follow-up after coil embolisation of intracranial aneurysms?

This question was systematically explored by Buhk et al. in twenty-two patients

undergoing routine six-month follow-up examination after coil embolisation (Buhk et al., 2009). An FDCT scan was performed in addition to the standard follow-up regimen i.e. catheter angiography and TOF-MRA. Catheter angiography, the gold standard, was consistently rated superior to the other two modalities. Artefacts appeared to impair the image quality of FDCT and MRA. For FDCT, aneurysm size (and therefore the number of coils used to pack the sac) or the presence of an implanted stent were major factors determining the artefact load, which significantly degraded the image quality for aneurysms exceeding 10 mm in diameter. For MRA, artefacts were most prominent in patients with implanted stents. However, all three techniques were comparable in terms of evaluating the degree of aneurysm occlusion and detecting any residual neck or residual sac. Their findings highlight potential utility of FDCT for the follow-up of coiled aneurysms especially in the presence of stents when susceptibility artefacts degrade image quality of TOF-MRA. Conversely, with increasing size of the aneurysm, beam-hardening artefacts caused by embolisation coils limit FDCT assessment.

2.4.3 Angio-room Availability of CT-like Soft Tissue Images

Availability of CT-like images of brain parenchyma obtained using the same apparatus as employed for guiding the interventional treatment, could be of particular value during endovascular procedures, and may have a potential role in the management of acute stroke patients. The neuro-endovascular procedures, despite advancements in interventional techniques, are associated with risks and complications (van Rooij et al., 2006). One such complication is perforation of the aneurysm sac or a vessel during coil embolisation, an infrequent but a potentially fatal event, early detection and vigilant management of which can improve patient outcomes (Cloft and Kallmes, 2002; Gallas et

al., 2008). Procedural rupture can be inferred from findings such as extravasation of contrast medium and extrusion of coils, or from secondary signs e.g. unexpected shift of vascular structures due to acutely developing haematoma, deterioration of neurological status, or an abrupt alteration of heart rate and blood pressure (Ming-Hua Li et al., 2006). However, a reliance on the secondary signs can potentially overlook minor perforations that may cause a late deterioration of patient's neurological status after an apparently uneventful embolisation procedure. In such situations, a conventional CT may provide parenchymal information that can assist not only in the detection of procedural rupture but also help in the assessment of distribution and extent of extravasation. Therefore, when a procedural perforation is suspected, transfer of the patient for a conventional CT scan is generally considered (Engelhorn et al., 2008; Heran et al., 2006). This strategy, however, delays decision-making in an emergent procedural setting, disrupts the workflow, and potentially compromises patient monitoring during transfer (Heran et al., 2006).

Availability of CT-like images of brain parenchyma (Figure 2.3) in the interventional suite, capable of reliable detection or exclusion of a suspected procedural complication, can reasonably be expected to overcome these logistic problems and can potentially improve patient outcomes. Reports on early clinical experience with FDCT in this context have been promising. In one of the early reports, Heran et al. commented on the utility of intracranial soft tissue information conveyed by FDCT for the management of suspected complications and its influence on the subsequent treatment decisions (Heran et al., 2006). FDCT images were found to be of sufficient quality for detection of haemorrhagic complications and for the assessment of internal CSF spaces.

A comparison of FDCT images with pre-procedural imaging for one patient revealed an increase in the extent of SAH, ventricular enlargement, and presence of new intraventricular blood (which prompted a decision to place an external ventricular drain (EVD). Successful placement of EVD was confirmed by FDCT and the patient was found to be neurologically intact upon recovery from anaesthesia. In two other patients, FDCT images helped to exclude suspected procedural complications, thereby avoiding any unnecessary surgical intervention and increasing the confidence in subsequent management. Following this report, others systematically explored whether FDCT images are of adequate quality for assessment of CSF spaces and for reliable detection/exclusion of intracranial haemorrhage.

2.4.3.1 Detection of Intracerebral Haemorrhage

Struffert et al. evaluated the image quality and the value of FDCT for detection of intracerebral haemorrhage (ICH) by comparison with cCT in a series of 60 patients (44 ICH-positive; 16 ICH-negative, serving as controls) (Struffert et al., 2009). In their experience, image artefacts (motion, beam-hardening, and ring artefacts) affected FDCT more frequently than cCT. This artefact load combined with relatively poor soft tissue resolution, contributed towards overall degradation of FDCT image quality, which was consistently rated inferior to cCT. Soderman and colleagues also reported similar findings and described FDCT as suffering from image artefacts more frequently and to a greater extent than cCT (Söderman et al., 2008). Nonetheless, both groups considered the image quality to be suitable for diagnostic assessment and for reliable detection and delineation of ICH in most cases. The technique was poor at detecting small haematomas (especially those located close to skull base) in the presence of motion

artefacts. This tendency for FDCT to underestimate the size of small haemorrhagic lesions may translate into a low sensitivity of the technique for detecting small procedural perforations; a notion to which further support comes from the observations of Soderman et al. who described the haemorrhagic lesions and oedema to be less distinct on FDCT images. It follows from the relatively poor contrast resolution of FDCT that the technique may also not be able to reliably depict the extent of hypoattenuating lesions such as oedema of the brain tissue following an ischaemic insult. The images should, therefore be interpreted with caution so as not to underestimate the severity of ischaemic brain injury.

The ability of FDCT to detect acute intracranial haemorrhage was evaluated by Arakawa et al. who studied the minimal size of haematomas detectable using an animal model, created by injecting blood or a mixture of blood and radiographic contrast media into the swine brain (Arakawa et al., 2008). All experimental haematomas mimicking procedural haemorrhages were detectable with FDCT; the smallest being 0.14 cm^2. Experimental lesions representing non-procedural haemorrhages were also detectable when the haematocrit of injected blood was in the range of 29 – 37%; the smallest detected lesion in this category being 0.17 cm^2. The sizes of lesions measured on FDCT were 1-35 % smaller than at necropsy and this discrepancy was more prominent for small sized lesions. The difference was attributed to the relatively poor low-contrast resolution of FDCT. A subgroup of animals was also imaged by cCT and comparison of the two imaging techniques found that lesions were more distinct and better delineated on cCT. FDCT image quality was considered suitable for haematoma detection and delineation but it lacked the exquisite contrast resolution of cCT.

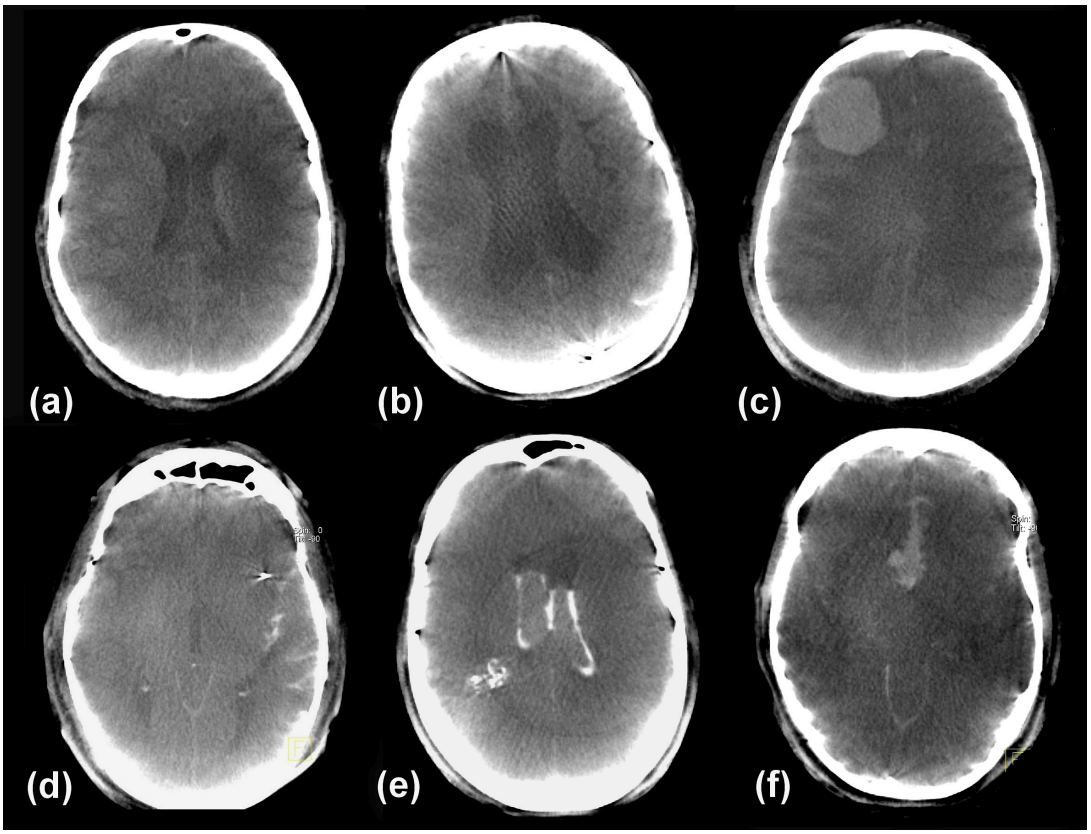


Figure 2.3: Evaluation of brain parenchyma with C-arm FDCT. FDCT images in different patients showing: (a) normal sized ventricles; (b) enlarged ventricles; (c) frontal haematoma; (d) procedural rupture during coil embolisation with extravasation of radiographic contrast media in the Sylvan fissure and sulci over the left temporal lobe; (e) intraventricular contrast and haemorrhage; and (f) anterior interhemispheric hematoma.

2.4.3.2 Detection of Subarachnoid Haemorrhage and Assessment of Ventricles

In a similar comparative study, Doelkin and colleagues explored the ability of FDCT to visualise subarachnoid haemorrhage (SAH) and to assess the internal CSF spaces (n = 32: 22 SAH-positive; 10 SAH-negative controls) (Doelken et al., 2008). In patients presenting with acute SAH, two radiologists evaluated the extent and dissemination of haemorrhage on FDCT and compared it with findings on cCT. Both evaluators correctly identified SAH-negative patients, with only one false negative reading. However, in line

with the findings reported for ICH, there was a tendency to underestimate the extent of SAH on FDCT images. In the FDCT readings, the Fisher scores were lower and haemorrhage was identified on a fewer number of slices compared with cCT. Complete agreement between the two techniques was observed for Evans index (a ratio of ventricular size to cerebral size), used as a maker for assessment of internal CSF spaces.

2.4.3.3 Role of FDCT in Determining the Immediate Post-procedural Management of Patients

The impact of FDCT on the management of patients undergoing neuroendovascular procedures, was addressed in a prospective audit study (n = 44) (White et al., 2008). White et al. used a five-point ordinal scale to assess how FDCT influenced the management of patients. The scale was designed to identify various situations ranging from those where FDCT resulted in the wrong management decision to instances where FDCT was the major factor contributing towards subsequent management. In addition, FDCT images were rated for image definition and for the presence of artefacts. The technique helped to identify procedural rupture, mass effect associated with haematomas, rebleeding, ischaemia, and hydrocephalus. In 18 of 44 patients, FDCT was considered a prime or substantive factor in planning subsequent management of the patients while in no case did its interpretation result in a wrong treatment decision. Image quality, despite the presence of artefacts, was reported as conveying sufficient diagnostic information to make a decision regarding the presence or absence of complications, and no patient required an additional CT examination to answer this clinical question.

2.4.4 FDCT Angiography

FDCT can delineate contrast-enhanced vessels; and due to its better contrast resolution compared with 3D-DSA, offers angiography with lower concentrations of radiographic contrast media. A closer match between the densities of blood and radiographic contrast material allows the contrast to fill vessels more uniformly and to give a better depiction of vascular morphology. This is especially relevant when angiography is performed to study intracranial aneurysms. Non-uniform distribution of contrast in aneurysms with certain orientations is known to influence their appearance on 3D-DSA (Ernemann et al., 2003). Jou and colleagues reported significant differences between the appearances of two basilar artery aneurysms on 3D-DSA and FDCT. FDCT, using a more diluted contrast material, revealed anterior portions of the aneurysms, which were consistently underestimated by 3D-DSA. Though unexplored systematically, such discrepancies in estimation of aneurysm morphology may be more common and FDCT angiography may be less prone to artefacts and give a better depiction of vascular morphology (Jou et al., 2007).

An intravenous protocol for contrast media administration, apart from being less invasive, offers the advantages of simultaneous visualization of all intracranial vessels with a single injection (Figure 2.4). Assessment of all intracranial vessels with a single contrast injection is of particular benefit in patients with multiple intracranial vascular lesions, study of which would otherwise require multiple intra-arterial injections for DSA examination. The intravenous protocol may thus reduce the contrast and the radiation dose compared with 3D-DSA. In addition, appropriate projection angles can

be worked out from the same acquisition, which may subsequently be useful in planning an interventional procedure.

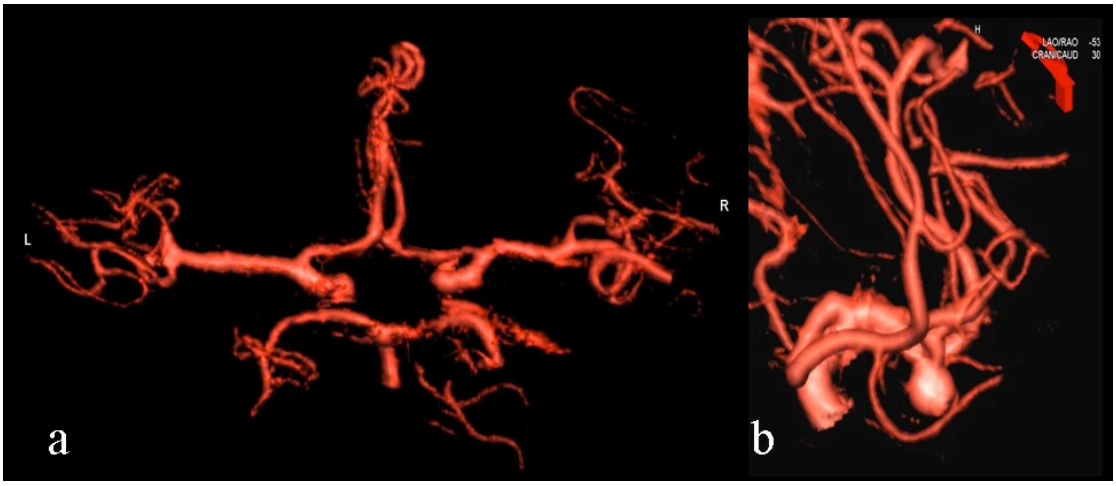


Figure 2.4: Evaluation of intracranial vessels with C-arm FDCT. Volume-rendered FDCT images showing: (a) the circle of Willis following an intravenous administration of 100 ml of 50% Niopam 300 (Bracco spa, Milan, Italy) infused at 5 ml/second and (b) middle cerebral artery bifurcation artery aneurysm after an intra-arterial injection of 33 ml of 15% Niopam 300.

2.4.5 FDCT Perfusion

Exploiting the temporal dimension for C-arm FDCT with sequential acquisition of images i.e. perfusion scanning, is of potential interest (Gupta et al., 2006). However, the flat panel detectors currently used in angiography systems are limited by the scintillation speed of CsI and thus the number of projections that can be acquired per second (Kalender and Kyriakou, 2007; Orth et al., 2008). This eventually translates into longer scan duration, typically in the range of 5-20 seconds for the currently available C-arm angiographic systems. With a temporal resolution of this order, dynamic perfusion imaging is not possible with C-arm systems. However, newer direct type flat detectors and faster reconstruction algorithms are being researched which might

overcome this limitation. With dynamic perfusion imaging added to its existing capability of soft tissue imaging and angiographic imaging, C-arm FDCT has the potential to become an omni-scanning technique available in the neurointerventional suite. Such systems would extend the role of FDCT imaging to the triage of acute stroke patients as well as improve the management of patients undergoing all types of endovascular treatment.

2.5 Conclusion

C-arm FDCT is a promising imaging tool for neurointerventional applications. At the current level of performance, it lags behind conventional CT in terms of image quality. However, the advantage of it being available in the interventional suite outweighs its image quality related disadvantages in specific clinical settings. The utility of FDCT for detection of procedural complications, evaluation of low radiopacity stents, and assessment of coil packing in small-sized aneurysms has been reviewed. Further developments in detector technology and reconstruction algorithms are expected to enhance the performance of C-arm FDCT and would increase the range of its applications. Perfusion imaging with C-arm angiographic systems is an exciting new area under research, which would redefine C-arm FDCT as an invaluable tool for the rapid assessment of cerebral haemodynamics in addition to characterizing vessel morphology and providing CT-like parenchymal images.

3

C-arm FDCT Parenchymal Blood Volume Imaging: Historical Perspective and Introduction to the Technique

3.1 Historical Background

Soon after the discovery of x-rays, their potential role in producing images of internal anatomy was conceived; radiography has since played a pivotal role in medical diagnosis. Historically, the radiologists were more interested in employing imaging as a tool to depict morphology, which therefore constituted the primary criterion for evaluating new medical imaging techniques. An interest in extracting functional information from the medical images emerged with the introduction of radiographic contrast media, which prompted qualitative judgements of organ function during radiographic examinations (Blomley et al., 1997). Egas-Moniz, the Portuguese neurologist and pioneer of cerebral angiography, was aware that the radiographic images not only contained anatomical details but also embedded functional information. In his seminal work, he commented on the physiology of cerebral circulation using the serially obtained angiographic images (Taveras, 1990).

Demands for the functional imaging in the early years of radiology were largely met by nuclear-medicine techniques, while the role of x-ray based imaging remained limited to the characterisation of morphology. This division persisted for a considerable period of time despite poor spatial resolution of nuclear-medicine imaging techniques (Wintermark et al., 2005). With the introduction of computed tomography (CT), an interest in x-ray based quantitative functional imaging emerged, and in 1980, Axel proposed that brain perfusion could be estimated by monitoring the temporal changes in CT number of the cerebral tissue following administration of radiographic contrast material (Axel, 1980). Technical limitations prevented clinical application of this

concept for a decade before advancements in CT technology and enhanced computational resources could allow cerebral perfusion measurements (Axel, 2004; Gobbel et al., 1991).

Cerebral perfusion imaging plays an important role in a diverse group of disorders including acute ischaemic stroke, vasospasm following subarachnoid haemorrhage (SAH), head trauma, brain neoplasms, and chronic cerebrovascular disorders (Sa de Camargo and Koroshetz, 2005). Among these, acute ischaemic stroke is the major application due to its high prevalence and impact on health care costs (Hoeffner et al., 2004). In ischaemic stroke, perfusion imaging helps to classify hypoperfused brain tissue into ischaemic penumbra (salvageable tissue at risk of infarction in the absence of recanalization) and infarct core (irreversibly damaged tissue). This information improves patient selection for potentially harmful thrombolytic therapy (Meyers et al., 2011; Schaefer et al., 2008). Keeping in view the spectrum of clinical applications for perfusion imaging of brain, parameters such as widespread availability, accessibility in emergency setting, quantitative accuracy, rapidity of measurements, and cost-effectiveness are considered to evaluate the application potential of a modality (Wintermark et al., 2005). Among the currently available perfusion imaging techniques, CT perfusion (CTP) and magnetic resonance perfusion-weighted imaging (MR-PWI) best qualify these criteria and are in routine clinical use. A comparative overview of the CTP and MR-PWI is provided in table 3.1 while a summary of perfusion parameters commonly used in clinical practice is given in table 3.2 (Fieselmann et al., 2011; Khandelwal, 2008; Konstas et al., 2009).

Table 3.1 A comparison of CT and MR perfusion imaging techniques

	CT Perfusion	MR Perfusion
1. Tracer	Iodinated contrast	a. Gadolinium for DSC# and DCE± b. Magnetized protons for ASL$
2. Tracer and image signal	Linear relationship of image signal to contrast concentration	Non-linear relationship of image signal to contrast concentration
3. Underlying principle	Indication dilution and central volume principles	Indication dilution and central volume principles
4. Mathematical models	1. Doconvolution based 2. Non-doconvolution based (maximum slope model and Fick principle of conservation of mass)	1. Doconvolution based 2. Non-doconvolution based (maximum slope model and Fick principle of conservation of mass)
5. Parameters	CBV, CBF, MTT	CBV, CMF, MTT
6. Absolute quantification	Yes (absolute values may however be vendor software dependent)	No (except ASL)
7. Principal advantages	Widespread availability, cost-effective, time-efficient, accessible in emergent setting, absolute quantification, non-magnetic environment, higher spatial resolution	Extended coverage, no radiation exposure, higher SNR, greater sensitivity and specificity, additional valuable sequences in the same session including DWI and T2*-weighted (can detect microbleeds)
8. Principal disadvantages	Limited craniocaudal coverage, radiation and iodinated contrast exposure, absolute values may be vendor software dependent	Magnetic environment and associated logistical challenges for ICU patients, semi-quantitative nature of parameter values
9. Strength of recommendation in acute cerebral ischaemic (Latchaw et al., 2009, 2003)	"Quantitative CTP may probably be useful to differentiate between reversible and irreversible ischaemic tissue in acute stroke patients" (AHA strength of recommendation: **grade c**)	"MRI perfusion and diffusion techniques are probably useful in differentiating between reversible and irreversible ischaemic tissue in acute stroke patients" (AHA strength of recommendation: **grade b**)

DSC, dynamic susceptibility contrast; ± DCE, dynamic contrast enhanced; $ ASL, arterial spin labelling

Table 3.2 Perfusion parameters used in routine clinical practice

Perfusion parameter	Definition and units of measurement	Interpretation in acute ischaemia
Cerebral blood volume (CBV)	Volume of flowing blood in a given brain region Units: ml /100 grams	CBV lesion volume defines infarct core
Cerebral blood volume (CBF)	Volume of blood flowing through a given brain region per unit time Units: ml / 100 grams / minute	CBF or MTT lesion volume defines penumbra. Core penumbra mismatch is defined as the difference between CBF or MTT lesion volume and the CBV lesion volume
Mean transit time (MTT)	Average transit time of blood through a given region of brain Units: seconds	

3.1.1 Relevance of Parenchymal and Perfusion Imaging in Neuro-interventional Suite

Interventional neuroradiology (INR) is the branch of medicine that offers minimally invasive treatment for vascular disorders of head and neck. This relatively young specialty underwent major developments over the last two decades due to advancements in imaging, procedural techniques, and therapeutic devices concurrent with an ever-increasing interest in finding less invasive treatment alternatives (Strother, 2000). A large number of cerebrovascular disorders, previously treated by open neurosurgical techniques, are now amenable to minimally invasive treatment in

interventional catheter laboratories (Qureshi, 2004). Conventionally, the interventional suite relies on high-contrast vessel imaging i.e. two-dimensional (2D) digital subtraction angiography (DSA) and fluoroscopy for procedural guidance and control (Orth et al., 2008). Low-contrast cross-sectional parenchymal imaging (morphological and functional) was until recently not available in the interventional suite. When confronted with the need to obtain information on the intracranial soft tissue morphology or the perfusion status of brain, the operators therefore relied on conventional CT or MR imaging (Engelhorn et al., 2008). This approach has minimal utility in a procedural setting as it entails patient transport from the interventional suite to the diagnostic CT or MR scanner, and involves interruption or termination of ongoing interventional procedure, movement of patient away from the sterile environment of angiography suite, loss of precious time in emergent setting, and a disruption to the workflow of both diagnostic and interventional imaging facilities (White et al., 2008).

In the last decade, advancements in the detector technology and the mechanical properties of C-arm systems, used in the interventional suite for fluoroscopy, created the possibility of rotational scanning at high frame rates (figure 3.1) (Gupta et al., 2006). New detector systems, known as flat panel detectors (FDs), were introduced which were particularly suited for morphological (soft-tissue) imaging due to their higher x-ray absorption efficiency and improved contrast resolution (Wallace et al., 2009). The incorporation of FDs into the C-arm angiographic systems in routine clinical use, lead to an interest in developing protocols for morphological and functional imaging.

The imaging protocol for morphological imaging using the FD equipped C-arm systems is in current clinical use and is termed C-arm flat detector computed tomography (FDCT) (Gupta et al., 2008; Kalender and Kyriakou, 2007). Using this application, cross-sectional CT-like soft tissue images of an organ of interest are obtained while the patient is on angio-table and allow detection of intracranial haemorrhage, evaluation of ventricular size, guidance of drainage procedures, and immediate assessment of intracranial coil/stent placement (Doelken et al., 2008). Availability of this tool has the potential to optimise the interventional suite for patient management through timely detection of events such as procedural complications, which had hitherto required transporting patients to a diagnostic CT scanner (White et al., 2008).

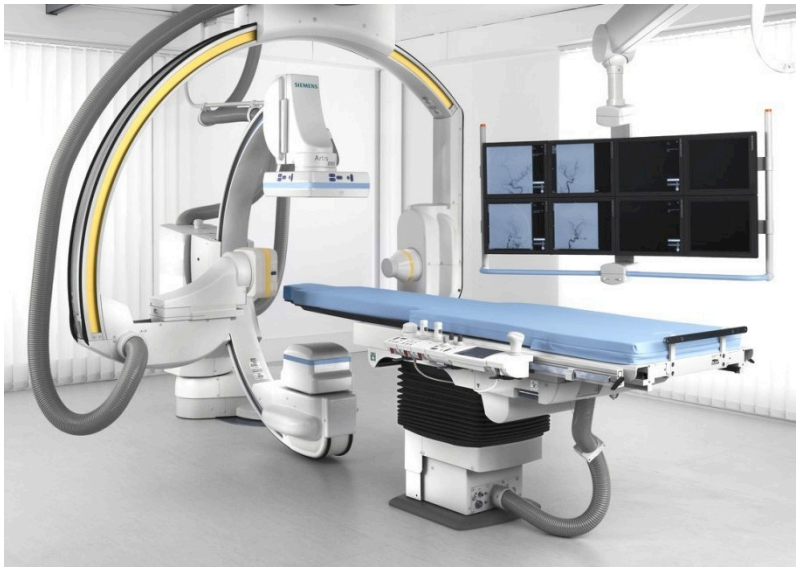


Figure 3.1: A flat detector equipped biplane C-arm angiography system used in the neurointerventional suite.

To enhance the neurointerventional environment and to realise the full imaging potential of C-arm systems, the next stage involves developing perfusion-imaging protocols. Existing perfusion imaging techniques i.e. CTP and MR-PWI, lack an environment conducive to therapeutic interventions, and are of little benefit for detecting altered cerebrovascular physiology during interventions and in the event of procedural complications. However, unlike CTP and MR-PWI, the temporal resolution of the current C-arm systems is inadequate to monitor the passage of radiographic contrast media through the cerebral circulation. This limitation is related to the nature of detectors and constraints of the mechanical apparatus, which restrict the duration for a single C-arm rotational acquisition to a minimum of 5-seconds (Gupta et al., 2006; Orth et al., 2008). Considering the brain transit time for radiographic contrast media (range 8sec-13sec), temporal sampling rates of this order are too slow to obtain enough data points to construct a time-attenuation-curve from the projection series, hence preventing measurement of dynamic perfusion parameters (i.e. cerebral blood flow and mean transit time). However, using an optimized contrast injection and scan protocol, it is possible to estimate parenchymal blood volume (PBV), another haemodynamic parameter which is thought to be equivalent to cerebral blood volume (CBV) (Zellerhoff et al., 2009). The ability to measure PBV in interventional room has implications for the management of brain ischaemia. For CTP and MR-PWI, CBV is known to be of prognostic significance in patients with acute brain ischaemic where a reduced CBV serves as a surrogate marker for the infarct core; an equivalence between the PBV and the CBV may thus portend a similar role for PBV (Wintermark et al., 2008, 2002).

Furthermore, monitoring the interventional procedures using a parameter of physiological significance, parenchymal morphological images, and angiographic information - all extracted from a single C-arm CT scan data without additional contrast or radiation dose - could optimise the interventional suite to realise the full potential of C-arm imaging and improve the efficacy of neurointerventional procedures.

3.2 Theoretical Background

Based on the principles of indicator dilution theory, Leon Axel, in 1980 first proposed the methods for measuring cerebral perfusion using rapid sequence CT scanning and a non-diffusible tracer (Axel, 1980). It was only a decade later that ultrafast CT scanners became available with temporal sampling rates sufficient to estimate the time-attenuation-curves from a scanned region of interest to allow application of Axel's methods (Gobbel et al., 1991). Dynamic CT imaging using the cine-mode is now in routine clinical use for perfusion imaging of brain.

Cross-sectional C-arm FDCT imaging used in the interventional room and the conventional CT employ a similar principle. For image reconstruction, both techniques implement the filtered back projection algorithm to a series of 2D projections acquired over a semi-circular scan trajectory (C-arm system) or a circular scan trajectory (CT). However, detector properties and mechanical limitations of the C-arm gantry restrict the duration of a single rotational volume scan to a minimum 5-seconds for the currently available C-arm systems; the sampling interval prolonged further by the inability of C-arm to rotate continuously in the same direction (Gupta et al., 2006). Considering the transit time for radiographic contrast media through the cerebral

vasculature (range 8-14 seconds), temporal sampling rates of this order are inadequate to monitor its passage through cerebral circulation and reconstruct the time-concentration-curve. Technical limitations of the C-arm systems, therefore, prevent estimation of dynamic perfusion parameters (cerebral blood flow and mean transit time) - a problem similar in nature to the dilemma CTP imaging faced in 1980s. Nevertheless, current C-arm systems could be used to measure PBV using an optimized contrast injection and scan protocol (Zellerhoff et al., 2009).

For a single compartment model using the dynamic perfusion imaging, the CBV can be calculated using equation 1 (Konstas et al., 2009; Zellerhoff et al., 2009):

$$CBV = \frac{CH}{\rho} \cdot \frac{\int_0^\infty C_{tissue}(t)\,dt}{\int_0^\infty C_{artery}(t)\,dt} = \frac{CH}{\rho} \cdot \frac{\int_0^\infty C_{tissue}(t)\,dt}{\int_0^\infty C_{vein}(t)\,dt} \qquad \textit{(Equation 1)}$$

(CH is the correction factor for difference between arterial and capillary haematocrit differences and $\boldsymbol{\rho}$ takes into account the density of brain tissue (Konstas et al., 2009).)

As discussed above, for rotational scans, the C-arm systems in current clinical use are incapable of monitoring the temporal changes in concentration of contrast media due to inadequate temporal resolution. To overcome this limitation, a contrast injection protocol could be designed that allows the contrast to reach a steady-state concentration in the entire volume of interest including cerebral arteries, veins, and the brain tissue (i.e. microvasculature). With an ideal steady-state contrast concentration achieved in cerebral vasculature ($C_{tissue} = C_{artery} = C_{vein}$) and no change in contrast

concentration over the scan duration), equation 1 can be replaced by equation 2 (Zellerhoff et al., 2009):

$$CBV = \frac{CH}{\rho} \bullet \frac{C_{tissue}}{C_{artery}} = \frac{CH}{\rho} \bullet \frac{C_{tissue}}{C_{vein}} \qquad \textit{(Equation 2)}$$

To satisfy the steady-state assumption, contrast injection parameters need a careful adjustment. Typically, following an instantaneous (or compact) intravenous injection of the radiographic contrast medium, the contrast concentration initially rises to a peak followed by exponential drop related to the clearance of contrast from the organ of interest i.e. the brain (figure 3.2).

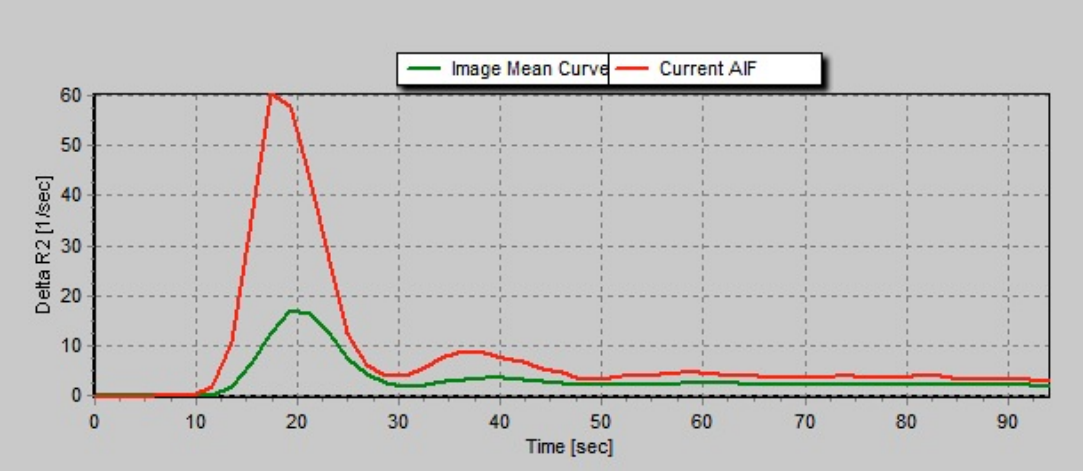


Figure 3.2: Tracer kinetics in the cerebral vasculature following intravenous administration. A compact bolus of contrast material (paramagnetic agent in this image) is administered through the right antecubital vein, 2 seconds following the initiation of scan (t = 0); the contrast appears in the cerebral circulation after 8-10 seconds (arm-to-head transit time). The steep upslope of the time-concentration-curve indicates rising contrast concentration in cerebral vasculature, followed by gradual decline in its concentration indicating clearance of the injected contrast material. Following the first-pass, the secondary peaks are related to the recirculation of contrast material.

Dispersion effects in the systemic circulation alter the profile of a contrast bolus administered intravenously. Primary determinant for the dispersion effects is the cardiovascular status of the subject, and these dispersion effects are aggravated in the presence of ischaemic stroke, vasospasm, and other cerebrovascular disorders that may induce a delay in circulation times through the scanned volume (Bae, 2010; Bae and Heiken, 2005; Fleischmann, 2005). To overcome these effects and to ensure that the cerebral vasculature is scanned when the administered contrast medium is in a steady-state or near steady-state distribution, two parameters are of paramount importance: (a) injection duration and (b) x-ray delay (describes the duration between the contrast injection and the start of C-arm scan). Injection duration considerably longer than the scan time ensures that the segment of time-concentration-curve with steady contrast concentration is long enough to accommodate the scan (Zellerhoff et al., 2009).

Following the administration of radiographic contrast media in the ante-cubital vein, 'arm-to-head transit time' determines its arrival in the cerebral vasculature. The parameter has considerable inter-subject variation due to differences in cardiovascular circulation times, affected in turn by the body weight, cardiovascular status, and other physiological parameters (Bae and Heiken, 2005). A fixed scan delay for all is therefore not desirable. To solve this problem and to ensure that the scanning takes place in the steady part of the time-concentration-curve for each patient, we decided to use 2D fluoroscopic images. These images allowed monitoring the passage of contrast medium through the cerebral circulation; using this information, the C-arm acquisition could then be triggered at a consistent time-point during the passage of contrast medium

through cerebral circulation for all scans. For this project, on the basis of preliminary work shared with our collaborators at other centres, we decided to use the maximal opacification of superior sagittal sinus (venous phase for the passage of contrast media) as the imaging marker designating the earliest time-point for the onset of steady-state or near steady-state contrast concentration in cerebral vasculature, and therefore to serve as an optimal trigger for the acquisition of contrast-enhanced C-arm CT scan.

3.2.1 Contrast Material Injection Protocol

In the exploratory phase, we studied various parameters for the contrast injection that could alter the bolus profile during its passage through the systemic circulation and affect the time-course of contrast enhancement in cerebral circulation. These parameters included iodine administration rate (iodine concentration of contrast medium and injection rate), volume of contrast material administered, injection duration, x-ray delay, injection pressure, and effect of saline chaser. An optimal injection protocol for the contrast-enhanced C-arm scan was reached at by studying the density changes on angiographic images obtained after modifying one or more of these parameters. The injection protocol that offered best trade-off between the amount of radiographic contrast administered and achieving a near steady-state was: intravenous administration of 80 ml Iopamidol bolus (370 mg Iodine per ml; Niopam 370, Bracco, Italy) through the right ante-cubital vein at an injection rate of 4 ml per second over a duration of 20 seconds, using a power injector at an injection pressure of 300 pounds per square inch (psi).

3.2.2 C arm CT PBV Scan Protocol

C-arm imaging was performed on a biplane flat-detector equipped angiography system (Axiom Artis dBA; Siemens Medical Solutions, Forchheim, Germany) in the neuro-interventional suite of Department of Neuroradiology, West Wing, John Radcliffe Hospital, Oxford, UK. The patients lied supine on the angiography table and were instructed to hold their head still and pause breathing when requested (if awake) at the beginning of the mask and contrast-enhanced (or fill) runs. A restraint device secured patients' head in place to further limit head movement and resulting motion-related artefacts. A trained anaesthetist continuously monitored the heart rate, oxygen saturation, and end tidal carbon dioxide during the scan (if general anaesthesia were used).

The imaging protocol included two rotational acquisitions: mask and contrast-enhanced runs (figure 3.3). Projection data for each run was acquired using the following parameters: 419 projection images, 0.5^0 frame angle, 210^0 angular scan range, 8-seconds acquisition time, 0.36 **μ**Gy radiation dose per frame. The contrast-enhanced dataset was acquired following manually triggered intravenous injection of radiographic contrast material Niopam 370 (Bracco spa, Milan, Italy) using a power injector (Medrad, Inc. Philadelphia). The injection parameters were: contrast concentration 370 mg Iodine/ml, volume 80ml, injection rate 4 ml/sec administered through the antecubital vein, injection pressure 300 psi, and injection duration 20 seconds. Passage of contrast material through the cerebral vasculature was monitored

on 2D fluoroscopic images (2 frames/sec) and the contrast-enhanced run was triggered when maximal opacification of the superior sagittal sinus was observed.

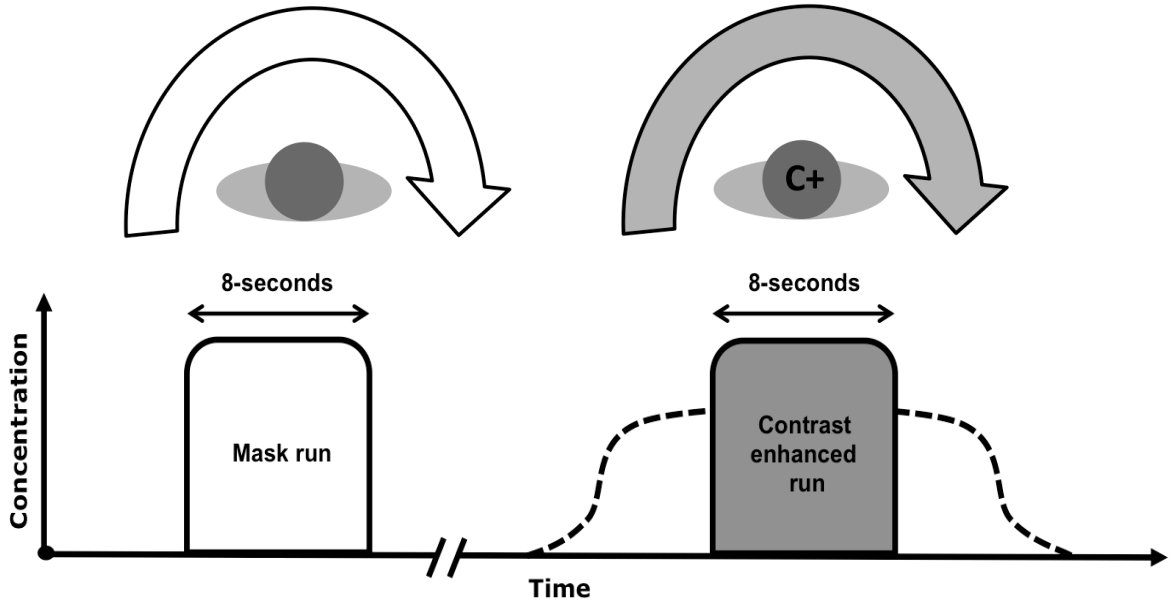


Figure 3.3: C-arm FDCT scan protocol for PBV measurement. The mask run is acquired before intravenous contrast injection and the contrast-enhanced run is acquired after administration of intravenous contrast material.

3.2.3 Post-processing of the C-arm Scan Projectional Data

Post-processing of the C-arm scan projectional data to generate color-coded PBV maps was performed using a prototype software on a dedicated research workstation (Leonardo, Siemens AG, Healthcare). The steps involved are described below and are illustrated in figure 3.4 (Zellerhoff et al., 2009).

1. Reconstruction of the 3D volumes from the mask and the contrast-enhanced runs projection data. The automated post-processing at this stage included corrections for radiation scatter, beam hardening, truncation, and ring artefacts.

2. Co-registration of the two volumes, the mask and the contrast-enhanced, using a rigid registration algorithm to compensate for head motion between the mask and the fill runs.

3. Subtraction of the mask volume from the contrast-enhanced volume to obtain a voxel-wise distribution of x-ray attenuation differences between the two volumes related to the presence of radiographic contrast which has a linear relationship to PBV.

4. Normalisation of the subtraction volume with an input function automatically estimated from the histogram analysis of subtraction volume (90% threshold value; used to compensate for image noise) as shown in figure 3.5.

5. Application of the hematocrit correction factor to account for differences in plasma fraction between the large and small calibre vessels.

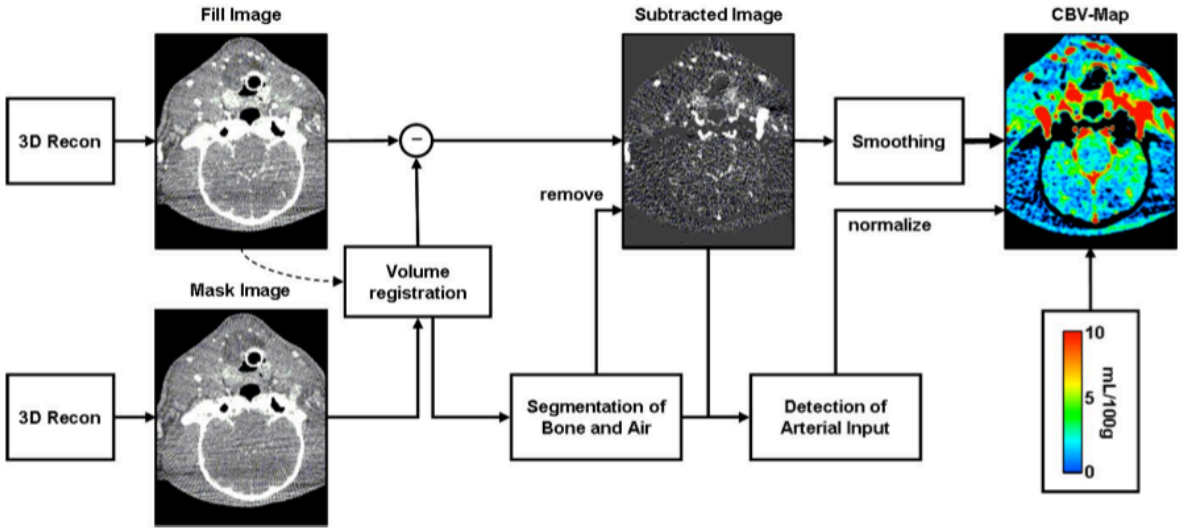


Figure 3.4: An overview of the post-processing steps for calculation of parametric PBV maps (Zellerhoff et al., 2009).

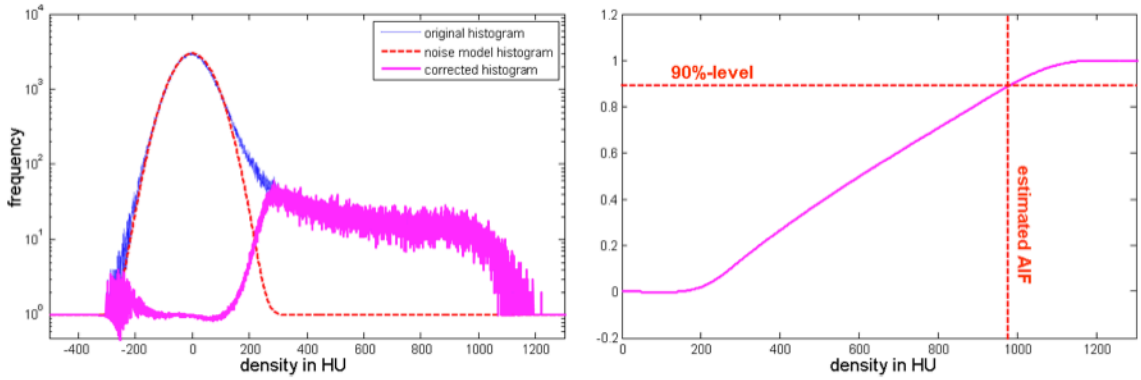


Figure 3.5: Estimation of input function from the histogram analysis of subtraction volume. The original subtraction volume based image-intensity histogram is corrected for image noise. A 90% threshold value of the maximum histogram-based image intensity is automatically calculated and used for normalisation to calculate PBV (Zellerhoff et al., 2009).

6. Color-coding with a standard color look-up table (LUT) to generate the color-coded PBV maps for visualization and interpretation (figure 3.6c). The final PBV values were expressed in units of ml/1000 ml of cerebral tissue. PBV values for any subsequent region-of-interest analysis were converted to more commonly used units of ml/100 g using a simple conversion factor that takes into account the cerebral tissue density (1.05 g/ml).

Additionally, the contrast-enhanced dataset was reconstructed separately on a commercially available dedicated workstation (Leonardo, Siemens AG, Healthcare) to obtain VRT (volumetric rendering technique) and MIP (maximum intensity projection) reconstructions for evaluation of the cerebral vasculature (figure 3.6a). CT-like soft tissue reconstructions were obtained from either the mask or contrast-enhanced dataset (figure 3.6b).

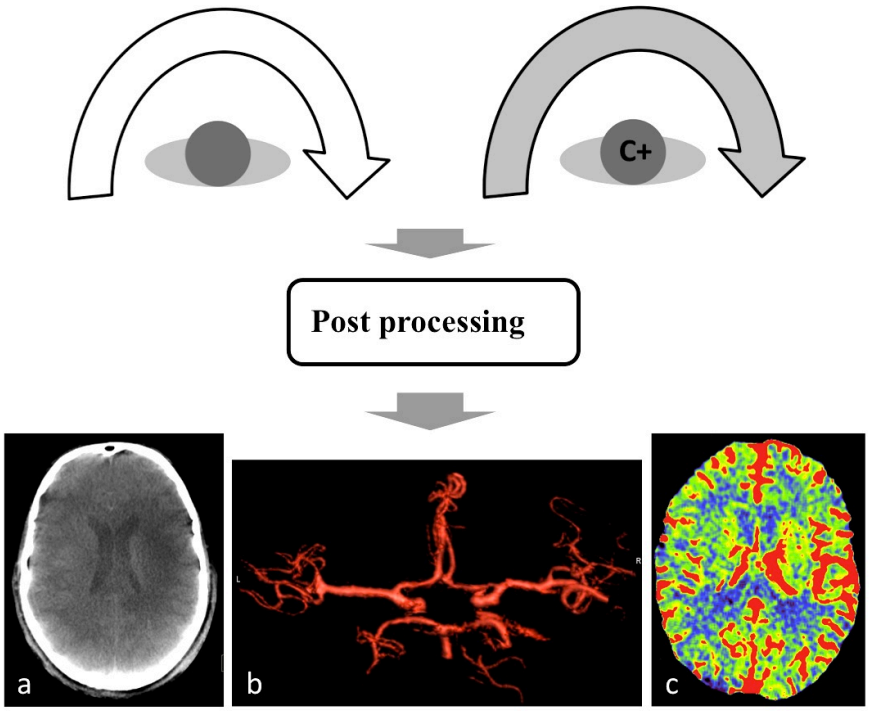


Figure 3.6: An overview of the C-arm FDCT PBV scan. Two rotational projection datasets are acquired, without and with intravenous administration of contrast material. Post-processing of the datasets acquired as part of a single scan generates (a) cross-sectional soft tissue images of brain parenchyma, (b) angiographic images, and (c) whole brain PBV maps.

The whole brain C-arm CT PBV maps thus generated were used in the subsequent analysis to:

(1) explore the agreement between the C-arm CT PBV and the MR-PWI derived CBV and CBF parameters (chapter 04);

(2) investigate if the C-arm CT PBV is blood-volume or blood-flow weighted (chapter 04);

(3) determine the optimal C-arm CT PBV thresholds for the demarcation of irreversibly infarcted brain parenchyma (chapter 05);

(4) create a catalogue of C-arm CT PBV values for various regions of the brain (chapter 06);

(5) investigate if the degree to which steady-state contrast concentration is achieved for a C-arm CT scan influences the agreement between the resulting PBV measurements and the MR-PWI derived CBV; the 2D projection data from the mask and contrast-enhanced runs of the C-arm CT PBV protocol scan was used to determine how well the steady-state assumption was met for the clinical scans (chapter 07).

4

C-arm FDCT PBV Imaging in Delayed Cerebral Ischaemia following Aneurysmal Subarachnoid Haemorrhage

4.1 Abstract

Background and purpose: C-arm FDCT PBV measurements allow assessment of cerebral haemodynamics in the neurointerventional suite. This chapter explores the feasibility of C-arm CT PBV imaging and the relationship between the C-arm CT PBV and the MR-PWI derived CBV and CBF parameters in aneurysmal-SAH patients developing delayed cerebral ischaemia (DCI).

Materials and methods: 26 patients with DCI following aneurysmal-SAH underwent a research C-arm CT PBV scan using a biplane-angiography system (Axiom-Artis dBA; Siemens Healthcare, Germany) and contemporaneous MR-PWI scan as part of a prospective study. Quantitative whole-brain atlas-based volume of interest (VOI) analysis in conjunction with Pearson correlation and Bland-Altman tests was performed to explore the agreement between C-arm CT PBV and MR-derived CBV and CBF measurements.

Results: All patients (n = 26) received medical management while 8 patients (31%) underwent selective intra-arterial chemical angioplasty. Colour-coded C-arm CT PBV maps were 91% sensitive and 100% specific in detecting the perfusion abnormalities noted on MR-PWI. C-arm CT rPBV demonstrated good agreement and strong correlation with both MR-rCBV and MR-rCBF measurements; with both agreement and correlation stronger for MR-rCBF relative to MR-rCBV. Measurement bias was minimal and limits of agreement included clinically significant C-arm CT rPBV discrepancies. Both agreement and correlation improved for C-arm CT PBV versus the geometric mean of MR-rCBV and MR-rCBF ($\sqrt{}$ MR-rCBV × MR-rCBF), compared with MR-rCBV or

MR-rCBF alone. Analysis of weighted means showed that the C-arm CT PBV has a preferential blood-flow weighting (≈60% blood-flow and ≈40% blood-volume weighting).

Conclusions: In this first report on the application of C-arm CT PBV imaging in patients with DCI and its comparison with MR-PWI, we demonstrate that C-arm CT PBV is a composite perfusion parameter incorporating both blood-flow and blood-volume weightings. That PBV has preferential (≈60%) blood-flow weighting is an important finding, which is of clinical significance when interpreting the C-arm CT PBV maps, particularly in the setting of acute brain ischaemia, where an assumed CBV equivalence can potentially overestimate the infarcted tissue and lead to under-selection of patients for endovascular treatment. In addition, feasibility of this non-invasive objective assessment tool for DCI patients is demonstrated. With its soft tissue, angiographic and perfusion imaging capabilities, C-arm CT imaging has potential for in-room selection of acute brain ischaemia patients for revascularisation procedures.

4.2 Introduction

Recent developments in flat detector equipped angiographic systems have made it possible to study cerebral haemodynamics in the neuro-interventional suite (Zellerhoff et al., 2009). C-arm rotational image datasets acquired with and without intravenous contrast administration are analysed using the principles of image-subtraction and indicator-dilution theory to generate quantitative voxel-wise maps of a parameter called parenchymal blood volume (PBV) (Zellerhoff et al., 2009). Initial studies have compared the C-arm flat detector computed tomography (C-arm FDCT or C-arm CT) PBV with only the CTP-derived cerebral blood volume (CBV) measurements (Ahmed et al., 2009; Bley et al., 2010; Struffert et al., 2012, 2011). The C-arm CT PBV calculations are performed in a manner similar to that proposed for multi-detector CTA by Hamburg et al. (Hamberg et al., 1996). For multi-detector CT, the CTA-source images (CTA-SI) can be used alone or be post-processed to generate colour-coded PBV maps (Kloska et al., 2007; Lu et al., 2011; Wittkamp et al., 2010). Sharma et al. showed that despite theoretical models suggesting these images (CTA-SI or colour-coded CT PBV maps) to be predominately blood-volume weighted, technique related factors impart a preferential blood-flow weighting to them (Sharma et al., 2011). However, whether the C-arm CT derived PBV images are preferentially blood-flow or blood volume weighted, has not been studied yet.

Availability of C-arm CT PBV technique in the neurointerventional suite is of particular interest in patients with aneurysmal subarachnoid haemorrhage (SAH). Cerebral perfusion abnormalities have been shown to serve as an early diagnostic

marker for delayed cerebral ischaemia (DCI), the leading cause of morbidity and mortality in patients surviving the initial ictus of SAH (Dankbaar et al., 2010, 2009; Diringer et al., 2011; Sanelli et al., 2011). For these patients, availability of C-arm CT PBV maps in the interventional suite could potentially be useful as a baseline assessment and in allowing early identification of cerebral perfusion abnormalities in the interventional suite, which if present could assist in planning an intervention without the need for patient transfer between the diagnostic and interventional suites.

This chapter aimed to: (1) investigate the relationship between C-arm CT PBV and the MR-PWI derived CBV and cerebral blood flow (CBF) parameters, and (2) explore the feasibility of C-arm CT PBV protocol scanning in patients with aneurysmal SAH who developed delayed clinical deterioration.

4.3 Materials and Methods

With local research ethics committee approval, a series of patients (n = 26) with aneurysmal SAH meeting the inclusion and exclusion criteria were enrolled in this prospective study.

Inclusion criteria were: patients aged over 18 years with documented aneurysmal SAH who subsequently developed symptoms and signs suggesting DCI and requiring confirmatory imaging - a situation necessitating admission and management in neuro-intensive care unit (neuro-ICU). At our institution, SAH is diagnosed using non-contrast CT (NCCT) head or with cerebrospinal fluid (CSF) sampling by lumbar puncture when initial NCCT head is negative but clinical suspicion of SAH remains high, and is graded as described by Fisher et al. (Fisher et al., 1980). The diagnosis of DCI was

based on clinical assessment by the multidisciplinary neuro-ICU team and was defined as clinical deterioration (focal neurological deficits or reduced level of consciousness) lasting 2 hours or longer with no evidence of rebleed or hydrocephalus on NCCT head, and no other medical causes such as infections or metabolic disturbances to explain the neurological deterioration.

Exclusion criteria were: a history of allergy to iodinated contrast medium, renal impairment, pregnancy, or contraindications to MR examination. All recruited patients had undergone aneurysm repair by endovascular coil embolisation. Written informed consents were obtained from patients or, if they were unable to complete the consent process, from a family member or a designated surrogate as defined by the research ethics committee approval for the study. Clinical records for all patients were collected and reviewed. The patients underwent a clinically indicated MRI examination using a protocol that included perfusion-weighted sequences concurrent with the research C-arm CT scan using PBV protocol. The imaging protocols and post-processing steps for the two imaging studies are described in the following sections. Additional subsequent imaging was performed as clinically indicated. Clinical and imaging data with patient-identifying information was anonymised and coded. Anonymised data was stored in a research database while the identifying variables were stored in a separate identification database; the two databases were linked through codes, which were accessible to the members of Oxford Neurovascular and Neuroradiology Research Unit (ONNRU) involved in this particular study, in accordance with the research ethics committee guidelines.

4.3.1 C-arm Flat Detector Computed Tomography (FDCT) Imaging

C-arm FDCT scans were performed on a flat detector equipped biplane angiography system (Axiom Artis dBA; Siemens Healthcare, Germany) in the neuro-interventional suite of Department of Neuroradiology, West Wing, John Radcliffe Hospital, Oxford, UK. As described in chapter 03, the imaging protocol included two rotational acquisitions: the mask and the contrast-enhanced (or fill) runs. Projection data for each run was acquired using the following parameters: 419 projection images, 0.5^0 frame angle, 210^0 angular scan range, 8 seconds acquisition time, 0.36 **μ**Gy radiation dose per frame. The contrast-enhanced dataset was acquired following manually triggered intravenous injection of radiographic contrast material Niopam 370 (Bracco spa, Milan, Italy) using a power injector (Medrad, Inc. Philadelphia). The injection parameters were: contrast concentration, 370 mg Iodine/ml; volume, 80ml; injection rate, 4 ml/sec administered through the antecubital vein; injection pressure, 300 pounds per square inch (psi); and injection duration, 20 seconds. Passage of contrast material through the cerebral vasculature was monitored on two-dimensional (2D) fluoroscopic images (2 frames/sec) and the contrast-enhanced run was triggered when maximal opacification of the superior sagittal sinus was observed.

Post-processing of the data to generate colour-coded PBV maps was performed on a dedicated research workstation (Leonardo, Siemens AG, Healthcare) using a prototype software. Briefly, the steps involved were: (1) co-registration of the two volumes, the mask and the contrast-enhanced, (2) subtraction of the mask volume from the contrast-enhanced volume, (3) normalisation of the subtracted data with an input

function automatically estimated from the histogram analysis of vascular tree, (4) colour-coding with a standard colour look-up table to generate the PBV colour-coded maps for visualization and interpretation (a detailed discussion of these post-processing steps is included in chapter 03). The final PBV values were expressed in units of ml/1000 ml of cerebral tissue. PBV values for the volume-of-interest (VOI) analysis were converted to more commonly used units of ml/100 g using a simple conversion factor that takes into account the cerebral tissue density (1.05 g/ml). For visualization of the vessels, the contrast-enhanced dataset was reconstructed separately on a commercially available dedicated workstation (Leonardo, Siemens AG, Healthcare). VRT (volumetric rendering technique) and MIP (maximum intensity projection) reconstructions were used to evaluate the cerebral vasculature. CT-like soft tissue reconstructions were obtained in all cases.

4.3.2 Magnetic Resonance (MR) Imaging

A standard MR scan protocol comprising axial and sagittal T1-weighted, axial T2-weighted, diffusion-weighted, perfusion-weighted, and time-of-flight (TOF) angiography sequences was performed on Philips Achieva 1.5 Tesla MRI unit. The sequence details and the parameters used for each sequence are discussed below.

1. Sagittal T1-weighted: Repetition time (TR) 700ms, time-to-echo (TE) 16ms, field-of-view (FOV) 149×252 mm, reconstruction matrix 480×480, slices 25, slice thickness 5mm, voxel size 0.53×0.53×5mm, sequence duration 2min 32sec.

2. Axial T1-weigted post-Gadolinium: TR 704ms, TE 16ms, FOV176×250, reconstruction matrix 512×512, slices 25, slice thickness 5mm, voxel size 0.49×0.49×5mm, sequence

duration 2min 22.2sec

3. Axial T2-weighted: TR 5061ms, TE100ms, FOV 174×250mm, reconstruction matrix 512×512, slices 25, slice thickness 5mm, voxel size 0.65×0.65×5mm, sequence duration 2min 36sec.

4. Diffusion-weighted: TR 2897ms, TE 73ms, FOV 174×249mm, reconstruction matrix 144×144, slices 25, slice thickness 5mm, voxel size 1.74×1.73×5mm, b-values 0 and 1000, EPI factor 51, sequence duration 34sec.

5. TOF angiography: TR 26ms, TE 6.9ms, FOV 200×200mm, reconstruction matrix 512×512, slices 140, slice thickness 0.5mm, voxel size 0.39×0.39×0.5mm, sequence duration 6min 14.4sec.

6. Perfusion-weighted: Perfusion data was acquired using the dynamic susceptibility contrast (DSC) technique with the following parameters: T2*-weighted gradient-echo echoplanar sequence, TR 2000ms, TE 44ms, FOV 248×248 mm, reconstruction matrix 256×256, voxel size 0.98×0.98×4mm, SENSE factor 2.1, bandwidth 806 Hz/pixel, sequence duration 1min 46sec. Paramagnetic contrast material was administered intravenously with an MR-compatible power injector (Medrad Inc.) at 5 ml/sec followed by 10ml saline flush. Fifteen slices covering the whole brain were acquired at 50 time points following the injection of 0.2 mmol/kg of Gadopentate (Prohance, Bracco Diagnostics Inc., Italy)

Post-processing of the perfusion data was performed using a commercially available software (nordicICE perfusion package, NordicNeuroLab, Bergen, Norway), both CE

marked and FDA approved. After motion correction of the raw data, perfusion maps were created using the standard singular value deconvolution (SVD) technique. Arterial input function (AIF) to deconvolve the dynamic tissue response curve was automatically determined and SVD regularization was achieved with the truncated SVD approach (cut-off fraction 0.20) and iterative thresholding (target oscillation index 0.10). Semi-quantitative, leakage-corrected output perfusion maps for clinical interpretation included: cerebral blood flow (CBF), cerebral blood volume (CBV), mean transit time (MTT), and time to peak (TTP).

4.3.3 Further Post-processing and Quantitative VOI Analysis

Quantitative/semi-quantitative parametric perfusion maps for the two techniques were further post-processed using the FMRIB software library (FSL) tools (Jenkinson et al., 2012). Brain extraction tool (BET) was used to delete the non-brain tissues from the images of interest (Smith, 2002). Linear registration of the C-arm PBV maps and the MR perfusion parametric maps (CBF, CBV, and MTT) for each patient was performed to the T1-weighted average structural template brain volume in the MNI152 space with FMRIB linear image registration tool (FLIRT) (Jenkinson et al., 2002). Binarized predefined cortical and subcortical volumes of interest (VOIs), as defined in the Harvard-Oxford structural brain atlas, were applied to the co-registered parametric maps. The 56 VOIs used for each hemisphere are summarized in table 4.1 and are depicted in figure 4.1. Mean, median, and standard deviation values of each parameter were extracted for all VOIs encompassing both hemispheres. Given the semi-quantitative nature of MR perfusion parameters, inter-hemispheric ratios of each

parameter were calculated (e.g. right PBV / left PBV = relative PBV or rPBV) and subsequently used for statistical analysis (section 3.3.4). Figures 4.2-4.11 provide an overview of these image post-processing steps. For qualitative image analysis, two readers (an experienced neuroradiologist and a trained researcher) interpreted the parametric colour-coded perfusion maps for MR-PWI and C-arm CT PBV in a blinded fashion. A consensus interpretation of the colour-coded maps was used to define the perfusion abnormalities.

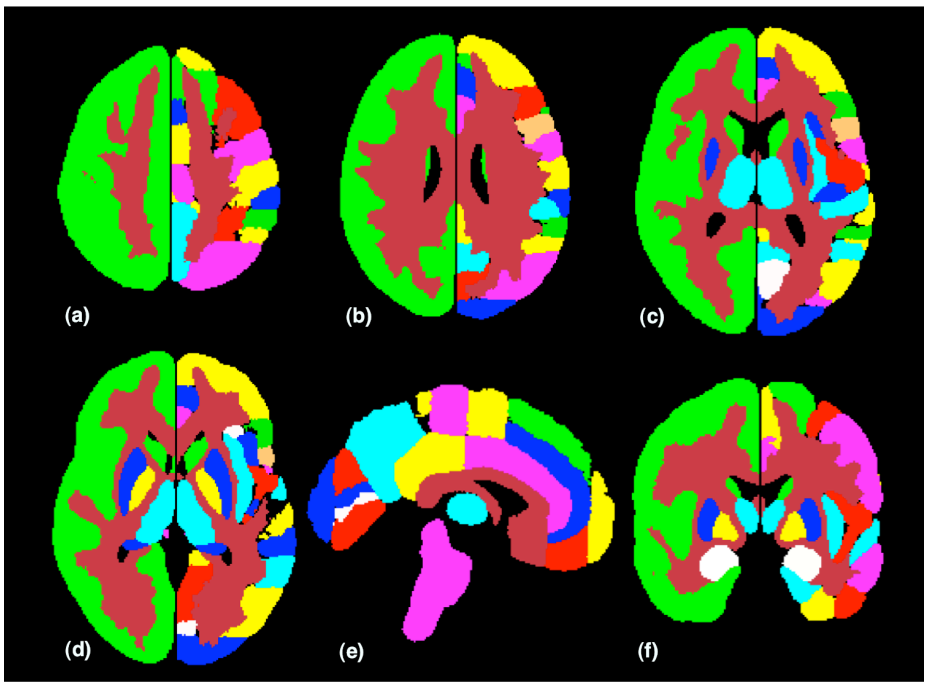


Figure 4.1: Harvard-Oxford structural brain atlas-based VOIs. Colour-coded illustration depicting the Harvard-Oxford structural brain atlas-based 3D VOIs of cortical and subcortical structures encompassing the whole brain, which were used for image analysis. Binarised masks of the 3D VOIs in orthogonal planes are shown. These binarised masks were used for extracting perfusion parameter values for various brain structures, which were subsequently used in the statistical analysis.

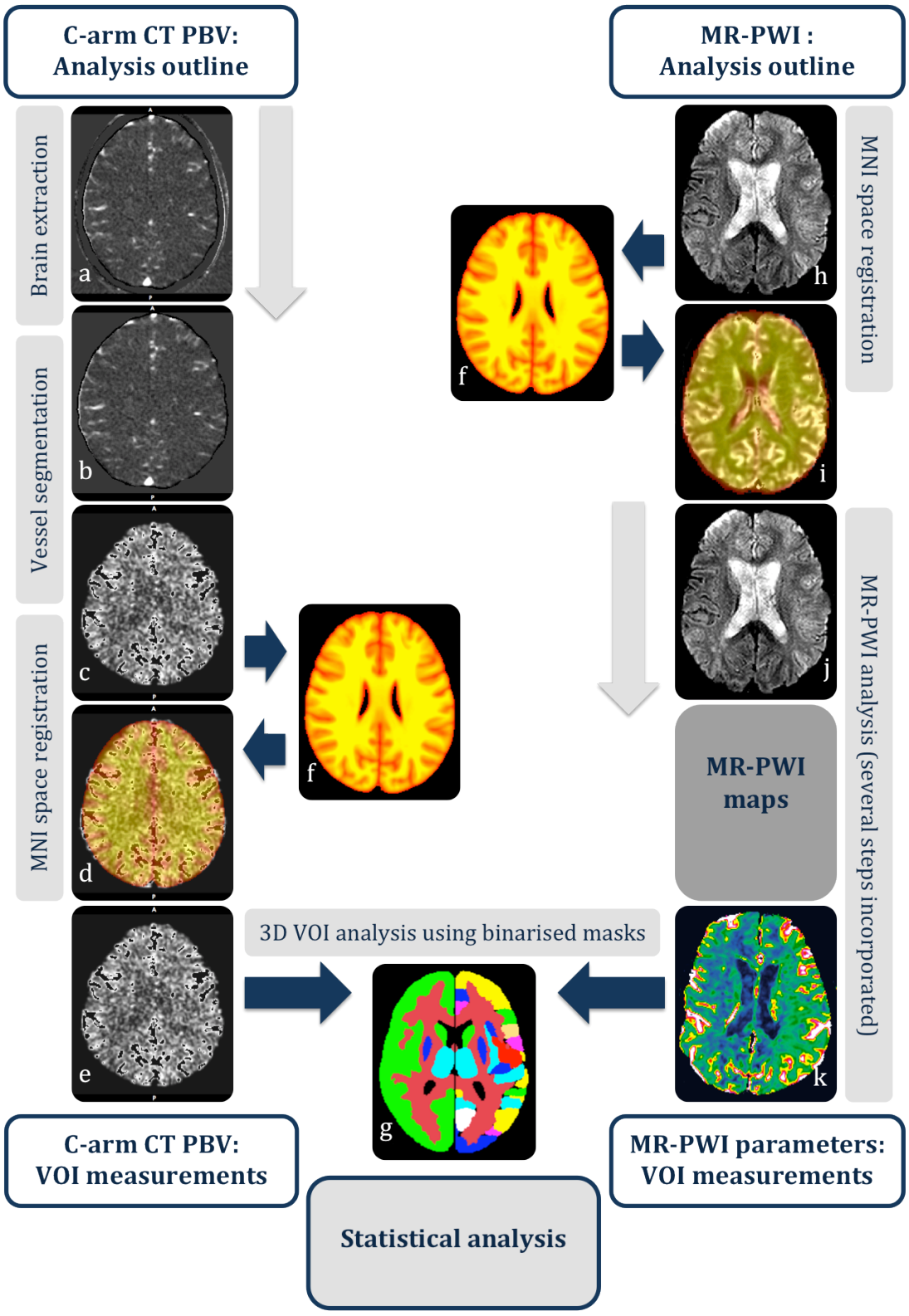


Figure 4.2: A schematic overview of the image post-processing (continued on next page):

(a) a C-arm CT PBV dataset before brain extraction; (b) PBV dataset following brain-extraction using FSL BET utility; (c) PBV dataset following threshold-based segmentation of the vascular structures; (d) registration of the PBV volume to the T1-weighted average structural template brain volume in MNI152 space; (e) brain-extracted, co-registered, vessel-segmented PBV volume in MNI152 space; (f) T1-weighted average structural template brain volume in MNI152 space to which the C-arm CT PBV maps and the MR-PWI data were coregistered; (g) binarised 3D-VOIs of cortical and subcortical structures encompassing the whole brain; (h) dynamic T2* weighted MR-PWI dataset; (i) registration of the MR-PWI to T1-weighted average structural template brain volume in MNI152 space; (j) registered MR-PWI dataset which was subsequently post-processed to extract perfusion parametric maps preserving the spatial coordinates in MNI152 space; (h) motion-corrected, vessel-segmented, brain-extracted, leakage-corrected, registered MR-PWI maps. Subsequently, using the binarised 3D-VOIs, the perfusion parametric values were obtained for the cortical and subcortical structures, which were then used in the statistical analysis described in section 3.2.4.

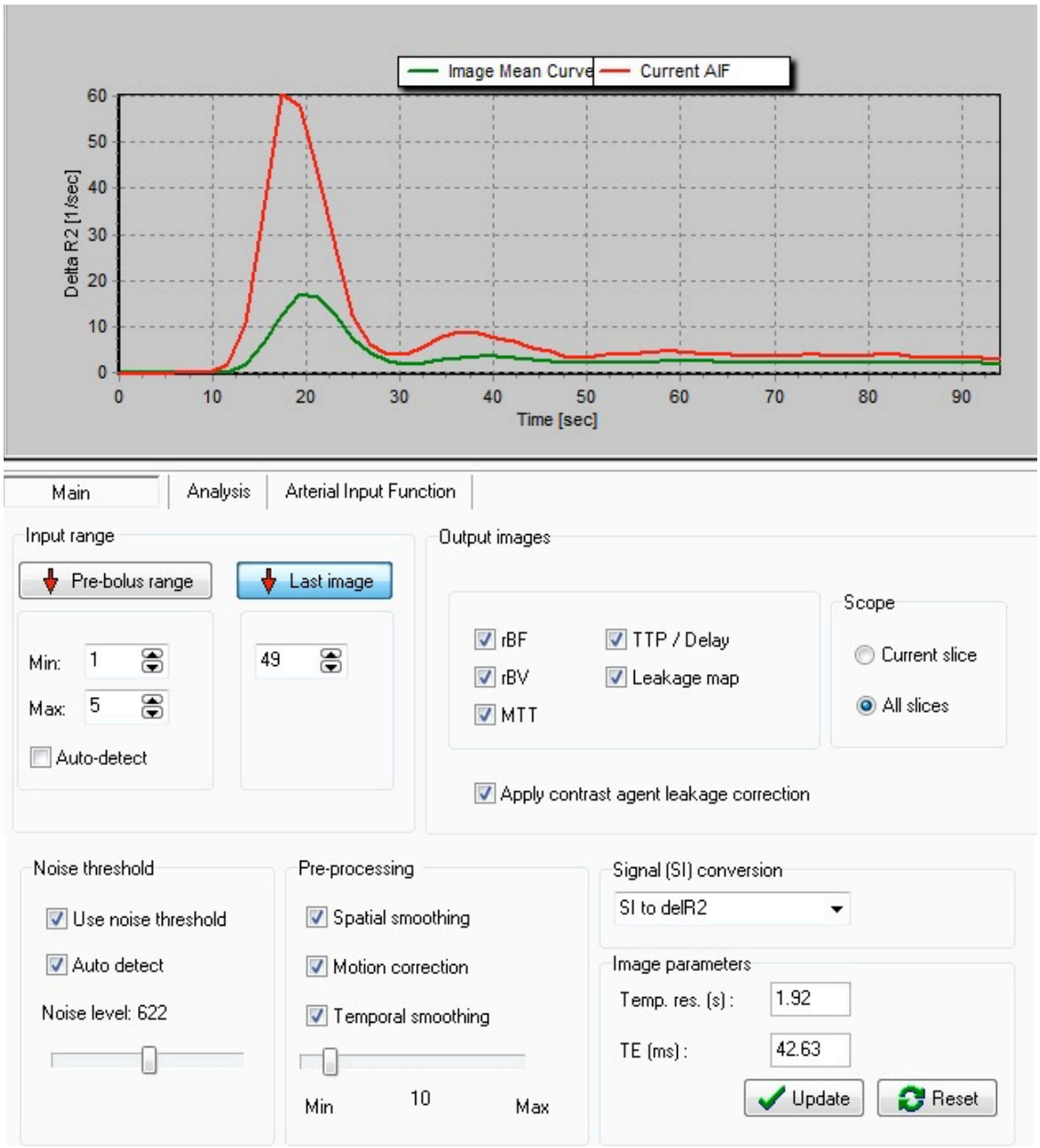


Figure 4.3: MR-PWI analysis overview. The image mean and the AIF delta-R2* curves are depicted for an MR-PWI dataset. Perfusion analysis included: corrections for noise and motion, spatial and temporal smoothing of the time series data, and the contrast leakage correction.

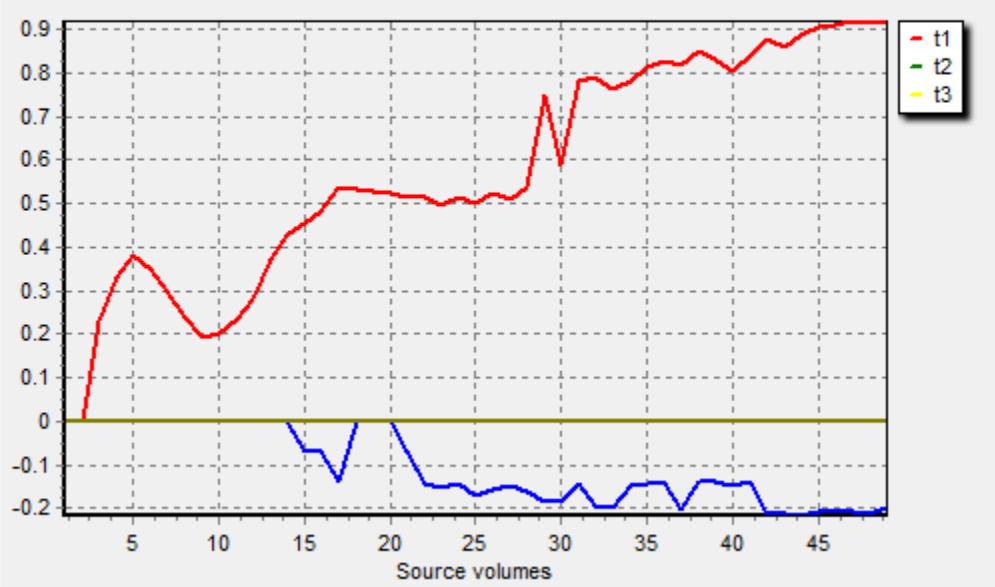


Figure 4.4a: Head motion (translation in mm) over time for an MR-PWI dataset. The MR perfusion analysis was designed to correct for any head motion.

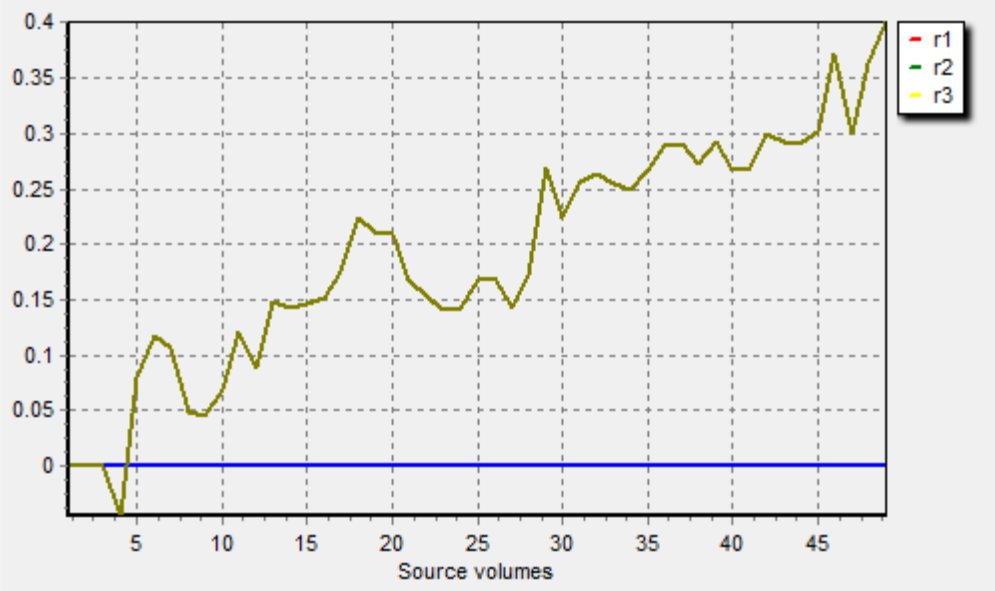


Figure 4.4b: Head motion (rotation in degrees) over time for an MR-PWI dataset. The MR perfusion analysis was designed to correct for any head motion.

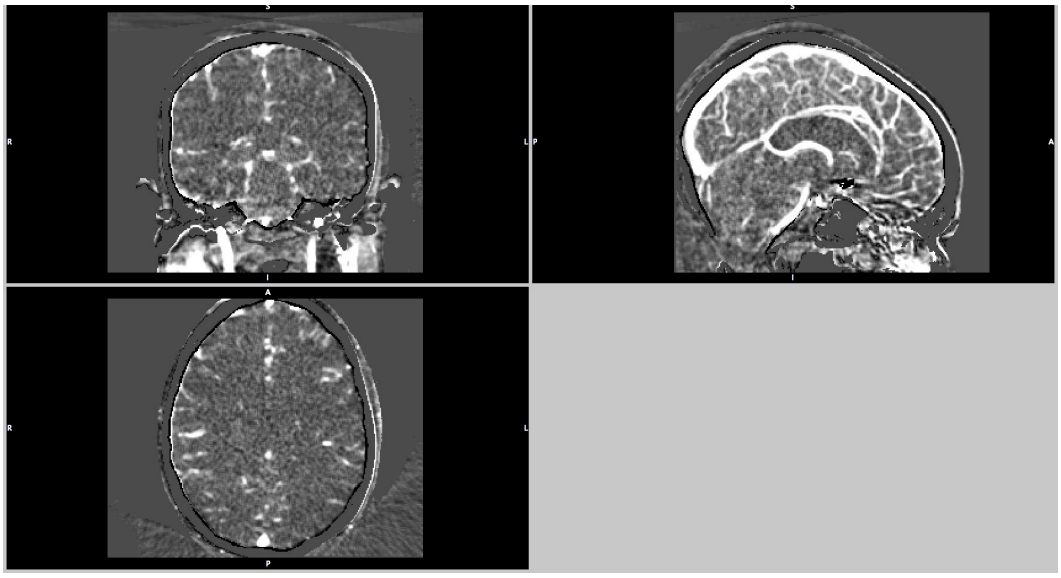


Figure 4.5: C-arm CT PBV dataset prior to post-processing.
Orthogonal reconstructions of an illustrative C-arm CT PBV dataset prior to post-processing for VOI analysis show head and neck soft tissues in addition to brain parenchyma, both of which are included in the C-arm CT scan field-of-view.

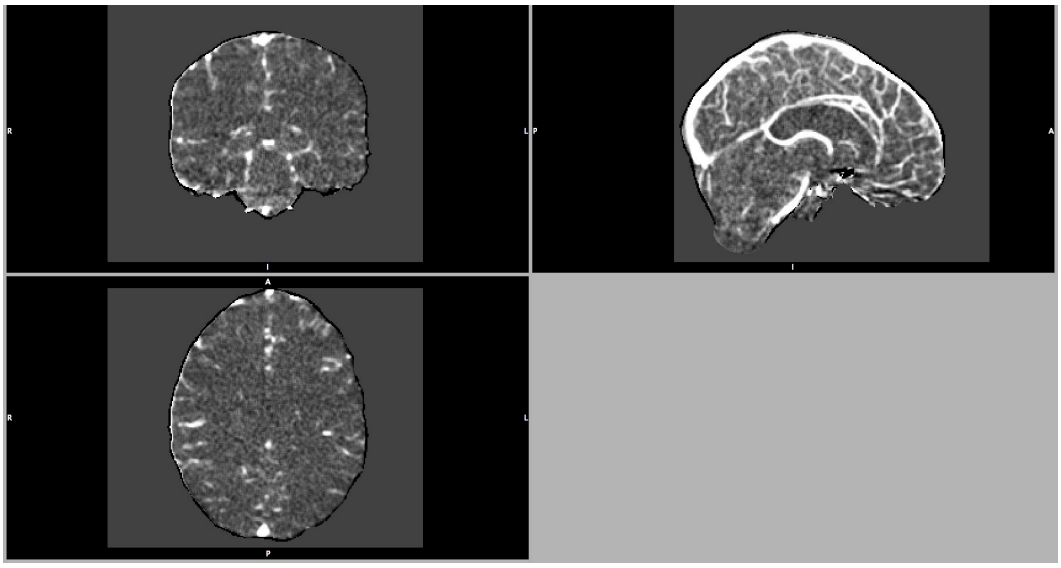


Figure 4.6: C-arm CT PBV dataset subsequent to brain extraction.
An illustrative reconstructed C-arm CT PBV dataset subsequent to semi-automated segmentation of brain using FSL brain extraction tool.

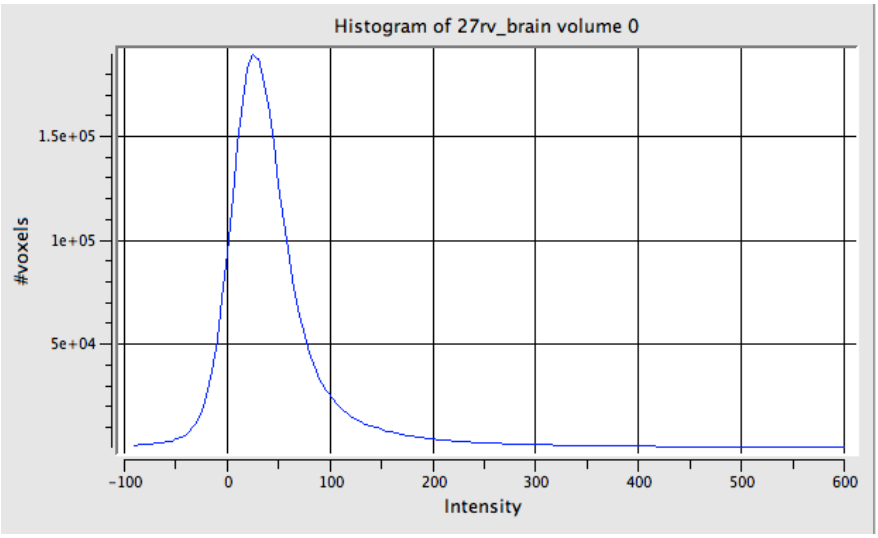


Figure 4.7: Image histogram for a C-arm CT PBV dataset.
Image histogram for an illustrative reconstructed C-arm CT PBV dataset subsequent to brain extraction.

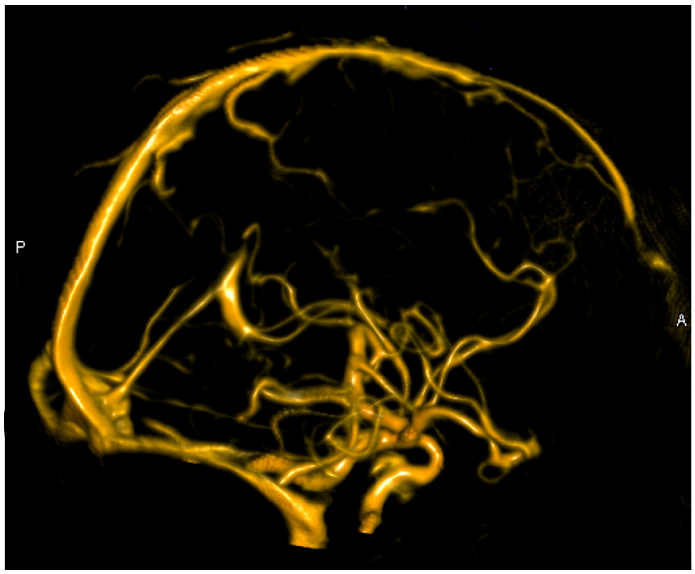


Figure 4.8: Opacification of the major intracranial vascular structures in a C-arm CT PBV protocol scan. VRT reconstruction of an illustrative reconstructed C-arm CT PBV dataset demonstrates opacification of the major intracranial vascular structures. These vascular structures were subsequently segmented using a threshold-based approach based on the review of histogram data to avoid overestimation of PBV values.

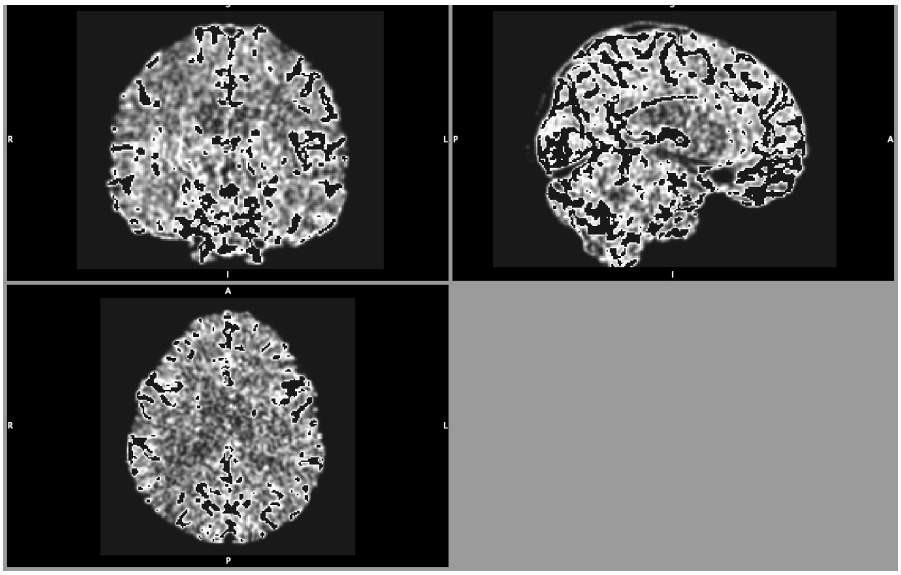


Figure 4.9: C-arm CT PBV dataset subsequent to vascular segmentation. Illustrative reconstructed C-arm CT PBV dataset subsequent to threshold-based segmentation of major vascular structures using FSL maths utility.

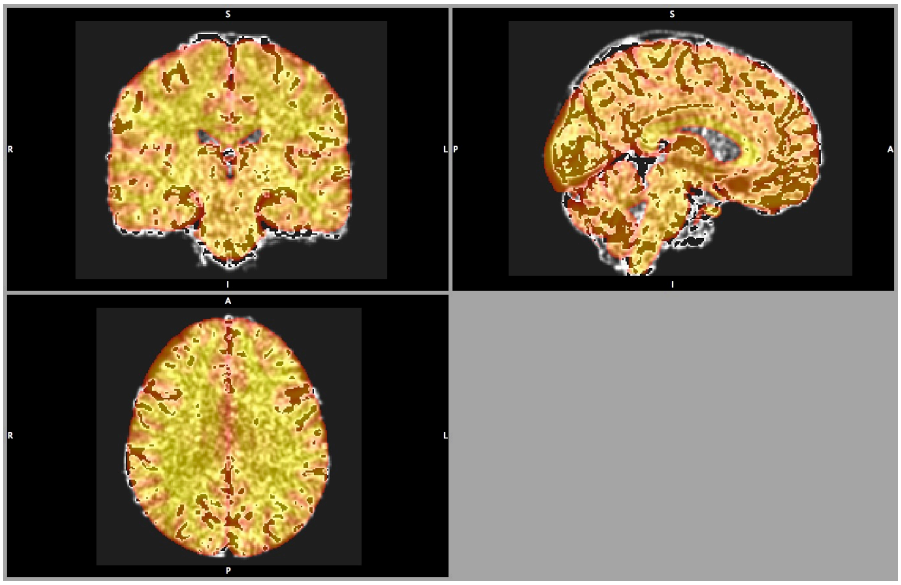


Figure 4.10: C-arm CT PBV dataset subsequent to coregisteration. Illustrative reconstructed C-arm CT PBV dataset in orthogonal planes subsequent to registration with a T1-weighted average structural template brain volume in MNI152 space depicted as yellow image overlay.

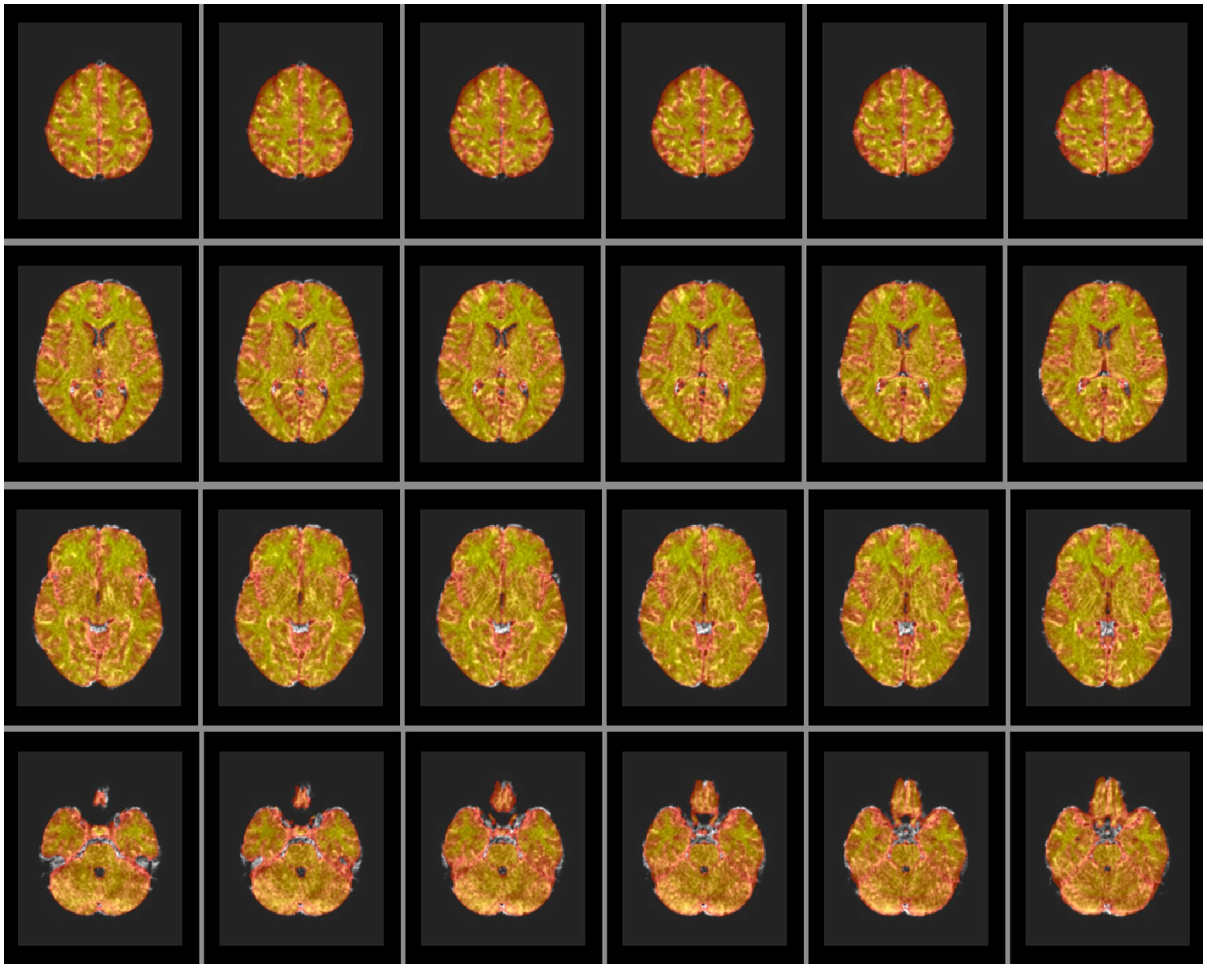


Figure 4.11: C-arm CT PBV dataset subsequent to coregisteration (axial reconstructions). Illustrative reconstructed C-arm CT PBV dataset subsequent to registration with a T1-weighted average structural template brain volume in MNI152 space depicted as yellow image overlay. Multiple axial slices at various levels with complete overlap of the two volumes confirmed adequate co-registration. A similar review was performed for sagittal and coronal plane reconstructions to establish anatomical correspondence between the coregistered volumes.

4.3.4 Statistical Analysis

Statistical analysis to explore the correlation and agreement between C-arm CT rPBV and MR derived rCBF and rCBV parameters was performed. Pearson correlation coefficient (r) was calculated for: (a) C-arm CT rPBV and MR-rCBV, (b) C-arm CT rPBV and MR-rCBF, and (c) C-arm CT PBV and the geometric mean of MR-rCBV and MR-rCBF ($\sqrt{}$ MR-rCBV × MR-rCBF); separately for cortical and subcortical VOIs. To assess the agreement between the two techniques, Bland-Altman analysis was employed (Martin Bland and Altman, 1986). The level of agreement was explored by plotting the difference (C-arm rPBV versus MR-rCBV; C-arm rPBV versus MR-rCBF; C-arm CT PBV versus the geometric mean of MR-rCBV and MR-rCBF ($\sqrt{}$ MR-rCBV × MR-rCBF)) against the respective mean of the two measurements being studied; separately for both cortical and subcortical VOIs. Bias (mean difference) and 95% limits of agreement (mean difference ± 1.96 × standard deviation) were calculated to assess the systematic difference and the degree of agreement, respectively.

In the next step, to explore the blood-flow and blood-volume weightings for C-arm CT rPBV, weighted means of MR-rCBV and MR-rCBF were calculated by assigning relative weights of 0.2, 0.4, 0.5, 0.6, and 0.8 to each parameter in a converse fashion. Bland-Altman and Pearson correlation analysis were performed for C-arm CT rPBV versus each of the calculated weighted means of MR-rCBF and MR-rCBV (rCBF 0.8 + rCBV 0.2; rCBF 0.6 + rCBV 0.4; rCBF 0.5 + rCBV 0.5; rCBF 0.4 + rCBV 0.6; rCBF 0.2 + rCBV 0.8). All statistical analysis was performed using GraphPad Prism Software, San Diego California, USA.

4.4 Results

4.4.1 Study Population Characteristics

A total of 26 patients (mean age 55 years; men 9, women 17) entered the study. SAH on admission NCCT were graded: Grade-4 in 16 (61%), Grade 3 in 9 (35%), while one patient's NCCT head did not show evidence of SAH which was proven after lumbar puncture (4%). The ruptured aneurysms treated by coil embolisation were: <5mm in 5 (20%), 5-10mm in 17 (65%), and 10-15mm in 4 (15%). Aneurysm locations were: anterior cerebral artery, 4 (15%); peri-callosal artery, 1 (4%); anterior communicating artery, 7 (27%); middle cerebral artery, 2 (8%); posterior communicating artery, 10 (38%); basilar artery, 1 (4%); and internal carotid artery, 1 (4%). Patients' WFNS (world federation of neurosurgical societies) grades at the time of admission to hospital were: Grade-1 in 16 (61%), Grade-2 in 7 (27%), Grade-3 in 2 (8%), and Grade-4 in 1 patient (4%). The onset of clinical deterioration after SAH varied from day-2 post-SAH to day-12 post-SAH (median, day-7 post-SAH).

After the diagnosis of DCI, all patients received standard medical management by the multidisciplinary neuro-ICU team according to the institutional protocol, with no change in treatment between the two study scans (MR-PWI and C-arm CT PBV). Physiological parameters were recorded for each patient and stability between the scans was ensured. Mean duration between the C-arm FDCT PBV scan and the MR imaging was 124 minutes. Using the colour-coded parametric maps, MR perfusion abnormalities (focal perfusion deficits or asymmetric hemispheric perfusion) were diagnosed in 23 patients (88%) as evidenced by decreased CBF, decreased CBV, or

prolonged MTT. C-arm CT correctly identified 21 of the 23 patients with MR perfusion abnormalities (sensitivity relative to MR-PWI, 0.91). The 3 patients with normal MR perfusion distribution were correctly interpreted to have normal C-arm PBV maps (specificity relative to MR-PWI, 1.0). Of the 26 patients, 8 (31%) underwent chemical angioplasty with selective intra-arterial Nimodipine administration, of whom 2 (8%) received chemical angioplasty treatment twice. Catheter angiogram findings in conjunction with the clinical/neurological status of patients were used as the primary criteria by the treating interventional neuroradiologist to determine if chemical angioplasty would be beneficial to the patient. The patient characteristics are summarized in table 4.2.

4.4.2 Quantitative Image Analysis

(a) The Bland-Altman analysis demonstrated good agreement between the C-arm CT rPBV and the MR-rCBV and rCBF measurements, both for cortical and subcortical VOIs. In its comparison against MR-rCBV and rCBF, there was minimal bias in the C-arm CT rPBV measurements (C-arm CT rPBV vs MR-rCBF, 0.022 ± 0.17 and 0.062 ± 0.17; C-arm CT rPBV vs MR-rCBV, 0.036 ± 0.20 and 0.032 ± 0.24, for cortical and subcortical VOIs respectively). The width of interval between the 95% limits of agreement was relatively narrower for C-arm CT rPBV vs MR-rCBF (−0.31 to 0.35 and −0.32 to 0.44, for cortical and subcortical VOIs respectively) compared with C-arm CT rPBV vs MR-rCBV (−0.39 to 0.46 and −0.47 to 0.53, for cortical and subcortical VOIs respectively), indicating better agreement for C-arm CT rPBV vs MR-rCBF. The C-arm CT rPBV measurements showed good correlation with both MR-rCBV and MR-rCBF, which were

statistically significant ($p < 0.001$). The correlation was slightly stronger for C-arm CT rPBV vs MR-rCBF ($r = 0.85$ and 0.78) compared with C-arm CT rPBV vs MR-rCBV ($r = 0.72$ and 0.69). Overall the techniques correlated better for cortical VOIs compared with the subcortical VOIs.

(b) Given the slightly better correlation and stronger agreement of C-arm CT rPBV with MR-rCBF compared with MR-rCBV, which suggested that C-arm CT rPBV may have weightings of both rCBV and rCBF, the geometric mean of MR-rCBV and MR-rCBF ($\sqrt{}$ MR-rCBV × MR-rCBF) was calculated; the correlation and agreement analysis were then performed for C-arm CT PBV versus the geometric mean of MR-rCBV and MR-rCBF. There was improved agreement and better correlation of C-arm CBT PBV with the geometric mean of MR-rCBV and MR-rCBF ($\sqrt{}$ MR-rCBV × MR-rCBF), compared with MR-rCBV or MR-rCBF alone (calculated in the first step). For C-arm CT rPBV vs $\sqrt{}$ MR-rCBV × MR-rCBF, results of agreement and correlation analysis were: bias 0.018 ± 0.13 and 0.042 ± 0.13; 95% limits of agreement −0.25 to 0.29 and −0.28 to 0.36; and Pearson correlation coefficient (r) 0.89 (95% CI: 0.86 to 0.91) and 0.86 (95% CI 0.83 to 0.89), for cortical and subcortical VOIs respectively.

(c) To explore the relative weightings of MR-rCBV and rCBF for C-arm CT rPBV, weighted means of MR-rCBV and rCBF were calculated by assigning relative weights of 0.2, 0.4, 0.5, 0.6, and 0.8 to MR-rCBV and rCBF in a converse fashion; the agreement and correlation analyses ware then performed for each of the calculated weighted means. MR-rCBF 0.6 + MR-rCBV 0.4 (60% rCBF and 40% rCBV) showed best agreement and correlation with C-arm CT PBV (Bland-Altman analysis: bias 0.015 ± 0.119 and 0.043 ±

0.118; 95% limits of agreement −0.21 to 0.24 and −0.23 to 0.31; and Pearson correlation coefficient (r): 0.91 (95% CI: 0.89 to 0.93) and 0.88 (95% CI 0.85 to 0.90), for cortical and subcortical VOIs respectively). The results of Bland-Altman analysis and the Pearson correlation analysis are summarized in tables 4.3 - 4.4 and are depicted in figure 4.12 – 4.14. Illustrative case examples are presented in figure 4.15 and 4.16.

Table 4.1 **Harvard-Oxford structural brain atlas based volumes of interest (VOIs) used for the analysis of C-arm CT PBV and MR perfusion maps**

Number	Volume of Interest	Number	Volume of Interest
1	Frontal Pole	**29**	Temporal Fusiform Cortex, posterior division
2	Insular Cortex	**30**	Temporal Occipital Fusiform Cortex
3	Superior Frontal Gyrus	**31**	Planum Polare
4	Middle Frontal Gyrus	**32**	Heschl's Gyrus (includes H1 and H2)
5	Inferior Frontal Gyrus, pars triangularis	**33**	Planum Temporale
6	Inferior Frontal Gyrus, pars opercularis	**34**	Postcentral Gyrus
7	Precentral Gyrus	**35**	Superior Parietal Lobule
8	Frontal Medial Cortex	**36**	Supramarginal Gyrus, anterior division
9	Lobule Cortex (formerly Supplementary Motor Cortex)	**37**	Supramarginal Gyrus, posterior division
10	Subcallosal Cortex	**38**	Angular Gyrus
11	Paracingulate Gyrus	**39**	Precuneous Cortex
12	Cingulate Gyrus, anterior division	**40**	Parietal Operculum Cortex
13	Cingulate Gyrus, posterior division	**41**	Lateral Occipital Cortex, superior division
14	Frontal Orbital Cortex	**42**	Lateral Occipital Cortex, inferior division
15	Frontal Operculum Cortex	**43**	Intracalcarine Cortex
16	Central Opercular Cortex	**44**	Cuneal Cortex
17	Temporal Pole	**45**	Lingual Gyrus
18	Superior Temporal Gyrus, anterior division	**46**	Occipital Fusiform Gyrus
19	Superior Temporal Gyrus, posterior division	**47**	Supracalcarine Cortex
20	Middle Temporal Gyrus, anterior division	**48**	Occipital Pole
21	Middle Temporal Gyrus, posterior division	**49**	Caudate
22	Middle Temporal Gyrus, temporooccipital part	**50**	Putamen
23	Inferior Temporal Gyrus, anterior division	**51**	Pallidum
24	Inferior Temporal Gyrus, posterior division	**52**	Thalamus
25	Inferior Temporal Gyrus, temporooccipital part	**53**	Hippocampus
26	Parahippocampal Gyrus, anterior division	**54**	Amygdala
27	Parahippocampal Gyrus, posterior division	**55**	Accumbens
28	Temporal Fusiform Cortex, anterior division	**56**	Brain-Stem

Table 4.2 Demographics, clinical characteristics, and imaging and treatment details for the recruited patients

Patient number	Age (years)	Gender (M/F)	Aneurysm location	Aneurysm size (mm)	WFNS grade	Fischer grade	DCI onset (day) *	MR-PWI deficits	PBV deficits	Medical management	Angioplasty
1	47	M	Anterior communicating artery	6 × 4	1	3	6	+	+	+	+
2	55	F	Left anterior cerebral artery	12 × 10	3	4	10	+	+	+	–
3	61	F	Right posterior communicating artery	8 × 5	2	3	9	+	+	+	–
4	49	F	Anterior communicating artery	10 × 7	1	3	4	+	+	+	–
5	68	F	Right posterior communicating artery	10 × 6	2	4	8	+	+	+	–
6	71	F	Anterior communicating artery	6 × 5	1	4	4	+	+	+	+
7	46	M	Right middle cerebral artery	4 × 3	3	3	6	+	+	+	++
8	77	F	Left anterior cerebral artery	6 × 4	1	4	4	+	+	+	–
9	46	M	Right posterior communicating artery	4 × 4	1	4	9	+	+	+	–
10	50	F	Right internal carotid artery	3 × 3	1	3	2	+	+	+	–
11	53	F	Basilar artery tip	7 × 6	2	3	5	+	+	+	+
12	55	M	Right posterior communicating artery	5 × 3	2	4	12	+	+	+	–
13	55	F	Left posterior communicating artery	4 × 4	2	4	7	+	+	+	–
14	69	F	Left anterior cerebral artery	11 × 7	1	4	2	+	+	+	+
15	66	M	Anterior communicating artery	7 × 5	1	0**	10	+	+	+	–
16	45	M	Anterior communicating artery	15 × 8	2	4	8	+	+	+	+
17	66	M	Right middle cerebral artery	8 × 3	4	4	7	+	+	+	+
18	30	M	Anterior communicating artery	7 × 4	1	3	9	+	+	+	–
19	39	F	Right posterior communicating artery	5 × 3.5	1	4	11	+	+	+	++
20	50	F	Anterior communicating artery	4 × 3.5	1	4	5	+	+	+	–
21	69	M	Right posterior communicating artery	7 × 4	1	4	6	–	–	+	–
22	39	F	Right posterior communicating artery	10 × 9	1	4	5	–	–	+	–
23	52	F	Right posterior communicating artery	5 × 5	1	4	7	+	+	+	–
24	54	F	Left posterior communicating artery	8 × 5	1	3	8	+	+	+	–
25	58	F	Right anterior cerebral artery	5 × 4	1	3	5	–	–	+	–
26	60	F	Left peri-callosal artery	12 × 8	2	4	5	+	+	+	–

* DCI onset - clinical deterioration occurring on ‘n’th day after aneurysmal SAH

** NCCT head was negative for SAH, which was later confirmed on lumbar puncture

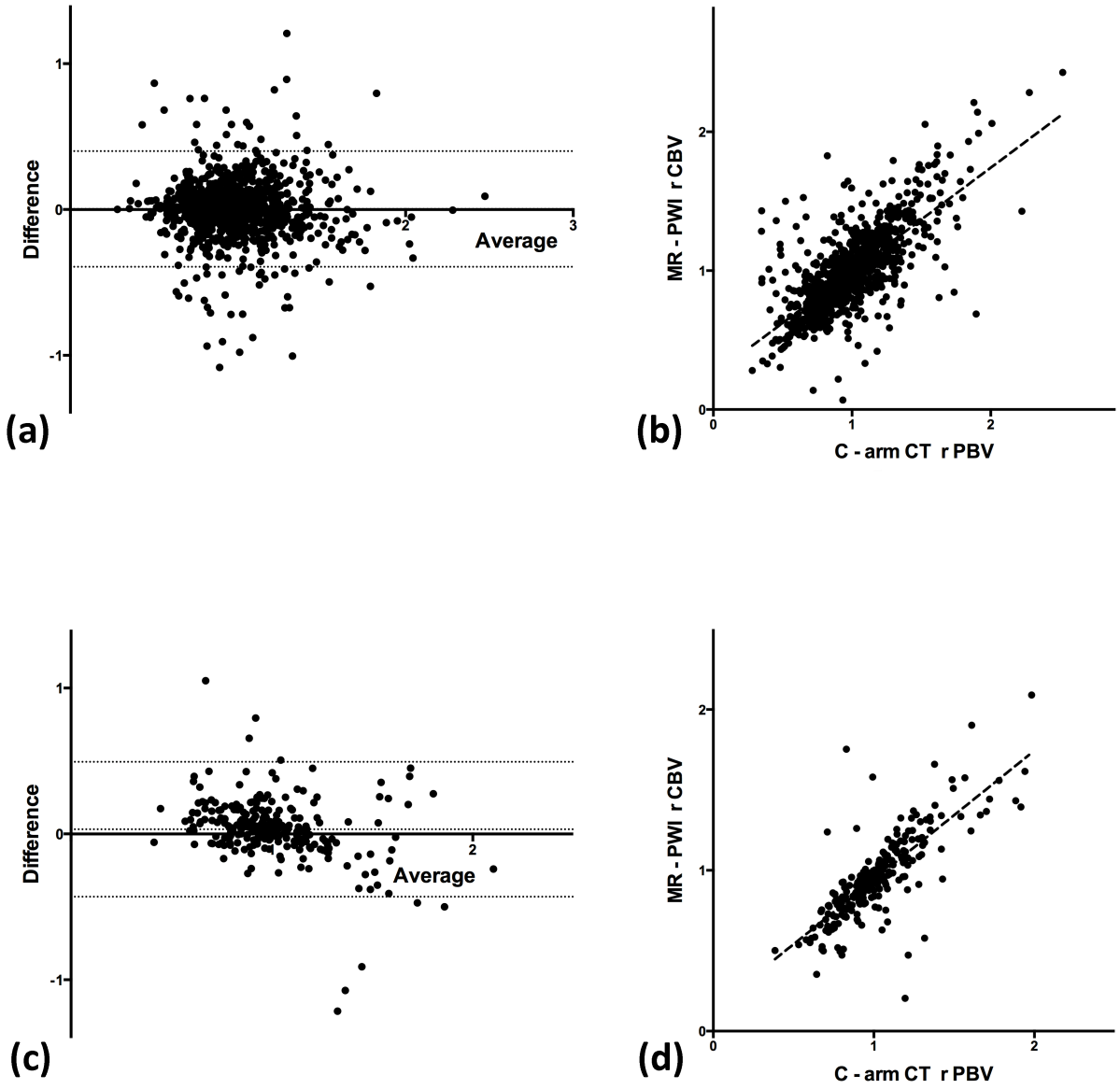


Figure 4.12: Agreement and correlation analysis plots for C-arm CT rPBV versus MR-PWI rCBV. Bland-Altman plots of agreement (a and c) and Pearson correlation plots (b and d) of C-arm CT rPBV versus MR-PWI rCBV for cortical (a and b) and subcortical (b and d) VOIs respectively.

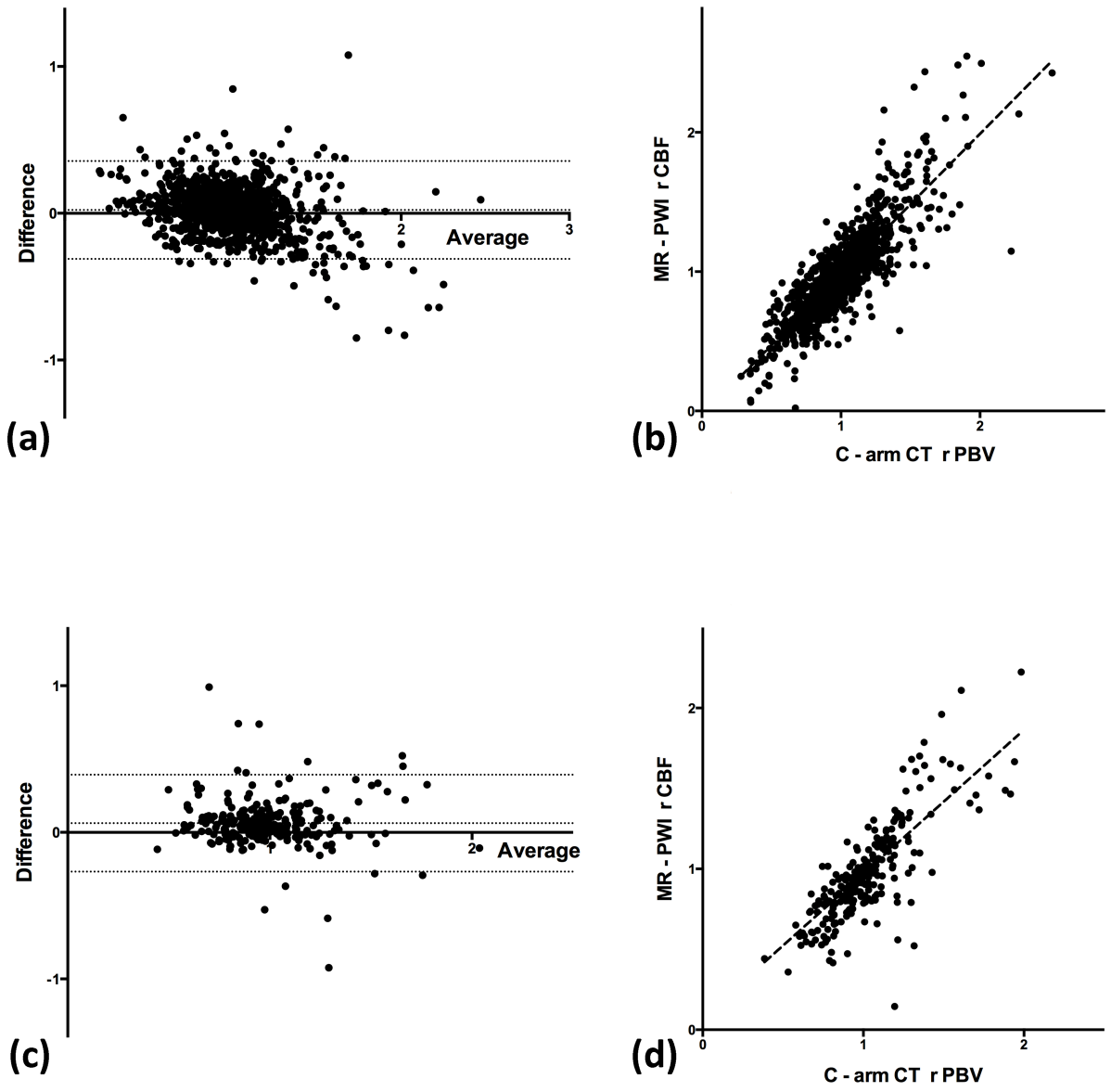


Figure 4.13: Agreement and correlation analysis plots for C-arm CT rPBV versus MR-PWI rCBF. Bland-Altman plots of agreement (a and c) and Pearson correlation plots (b and d) for C-arm CT PBV versus MR-PWI rCBF for cortical (a and b) and subcortical (c and d) VOIs respectively.

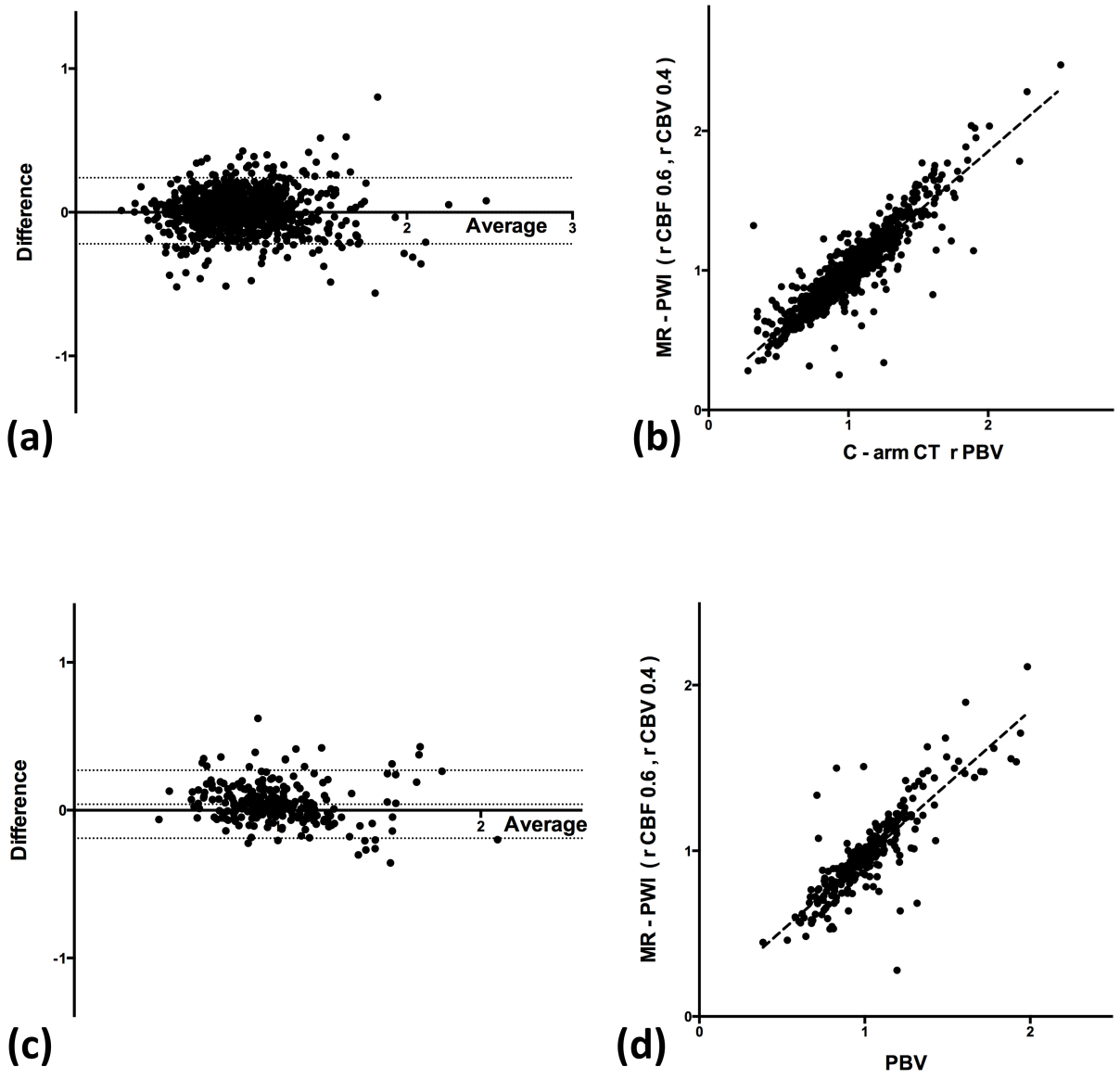


Figure 4.14: Agreement and correlation analysis plots for C-arm CT rPBV versus weighted mean of MR-PWI rCBV and rCBF. Bland-Altman plots of agreement (a and c) and Pearson correlation plots (b and d) for C-arm CT PBV versus weighted mean of MR-PWI rCBV and rCBF (rCBF 0.6, rCBF 0.4) for cortical (a and b) and subcortical (c and d) VOIs respectively.

Table 4.3 Results of Bland Altman analysis of agreement and Pearson correlation analysis

	Bland Altman analysis			Pearson correlation analysis			
	Bias	**SD of bias**	**95% limits of agreement**	**r**	**95% CI**	**R-square**	**p-value**
Cortical VOIs:							
C-arm CT rPBV vs MR-rCBF	0.022	0.17	−0.31 to 0.35	0.85	0.83 to 0.86	0.71	< 0.001
C-arm CT rPBV vs MR-rCBV	0.036	0.20	−0.39 to 0.46	0.72	0.69 to 0.75	0.52	< 0.001
C-arm CT rPBV vs √(MR-rCBV × MR-rCBF)	0.018	0.13	−0.25 to 0.29	0.89	0.86 to 0.91	0.75	< 0.001
Subcortical VOIs							
C-arm CT rPBV vs MR-rCBF	0.062	0.17	−0.32 to 0.44	0.78	0.73 to 0.82	0.61	< 0.001
C-arm CT rPBV vs MR-rCBV	0.032	0.24	−0.47 to 0.53	0.69	0.62 to 0.75	0.47	< 0.001
C-arm CT rPBV vs √(MR-rCBV × MR-rCBF)	0.042	0.13	−0.28 to 0.36	0.86	0.83 to 0.89	0.69	<0.001

Table 4.4 Results of Bland Altman agreement and Pearson correlation analyses for weighted MR-rCBF and rCBV

	Bland Altman analysis			Pearson correlation analysis			
C-arm CT rPBV vs	**Bias**	**SD of bias**	**95% limits of agreement**	**r**	**95% CI**	**R-square**	**p-value**
Cortical VOIs							
MR-rCBF 0.8 + MR-rCBV 0.2	0.019	0.148	−0.26 to 0.30	0.88	0.85 to 0.90	0.76	<0.001
MR-rCBF 0.6 + MR-rCBV 0.4	0.015	0.119	−0.21 to 0.24	0.91	0.89 to 0.93	0.81	<0.001
MR-rCBF 0.5 + MR-rCBV 0.5	0.018	0.127	−0.24 to 0.28	0.84	0.81 to 0.88	0.76	<0.001
MR-rCBF 0.4 + MR-rCBV 0.6	0.023	0.133	−0.27 to 0.31	0.80	0.77 to 0.84	0.71	<0.001
MR-rCBF 0.2 + MR-rCBV 0.8	0.031	0.163	−0.33 to 0.39	0.77	0.73 to 0.81	0.62	<0.001
√(MR-rCBF × MR-rCBV)	0.018	0.132	−0.25 to 0.29	0.89	0.86 to 0.91	0.77	<0.001
Subcortical VOIs							
MR-rCBF 0.8 + MR-rCBV 0.2	0.052	0.127	−0.27 to 0.37	0.83	0.79 to 0.86	0.68	<0.001
MR-rCBF 0.6 + MR-rCBV 0.4	0.043	0.118	−0.23 to 0.31	0.88	0.85 to 0.90	0.75	<0.001
MR-rCBF 0.5 + MR-rCBV 0.5	0.041	0.139	−0.26 to 0.34	0.84	0.81 to 0.87	0.70	<0.001
MR-rCBF 0.4 + MR-rCBV 0.6	0.037	0.171	−0.30 to 0.37	0.79	0.76 to 0.83	0.64	<0.001
MR-rCBF 0.2 + MR-rCBV 0.8	0.034	0.219	−0.39 to 0.45	0.76	0.71 to 0.80	0.56	<0.001
√(MR-rCBF × MR-rCBV)	0.042	0.129	−0.28 to 0.36	0.86	0.83 to 0.89	0.69	<0.001

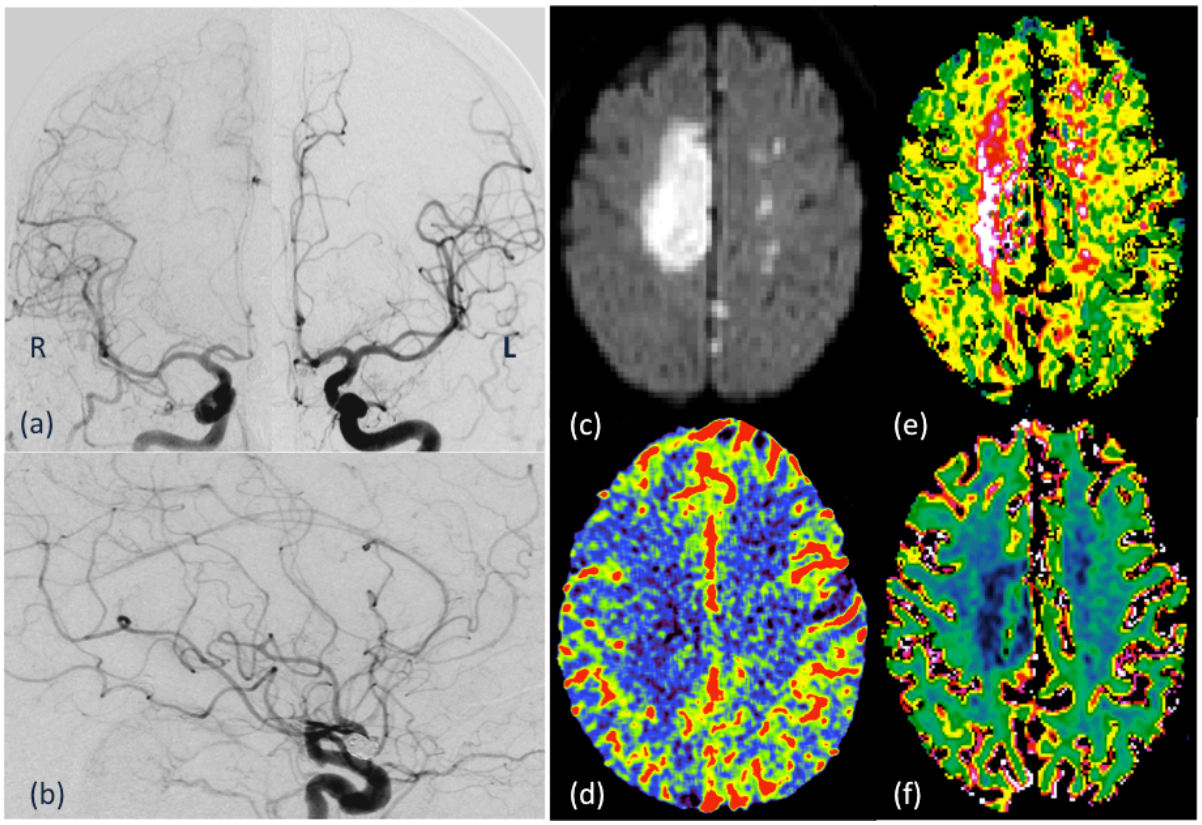


Figure 4.15: Illustrative case example 1. A 50 year-old-woman with ruptured anterior communicating artery aneurysm developing left hemiparesis on day 6 post-SAH: Catheter angiogram images (a & b) show intense vasospasm affecting both ACAs (right > left) with corresponding abnormality (restricted diffusion) on MR-DWI image indicating established infarcts in the same territory (c). C-arm CT PBV (d), MR-PWI rMTT (e), and MR PWI rCBV (f) images show asymmetric parametric deficits in the same distribution.

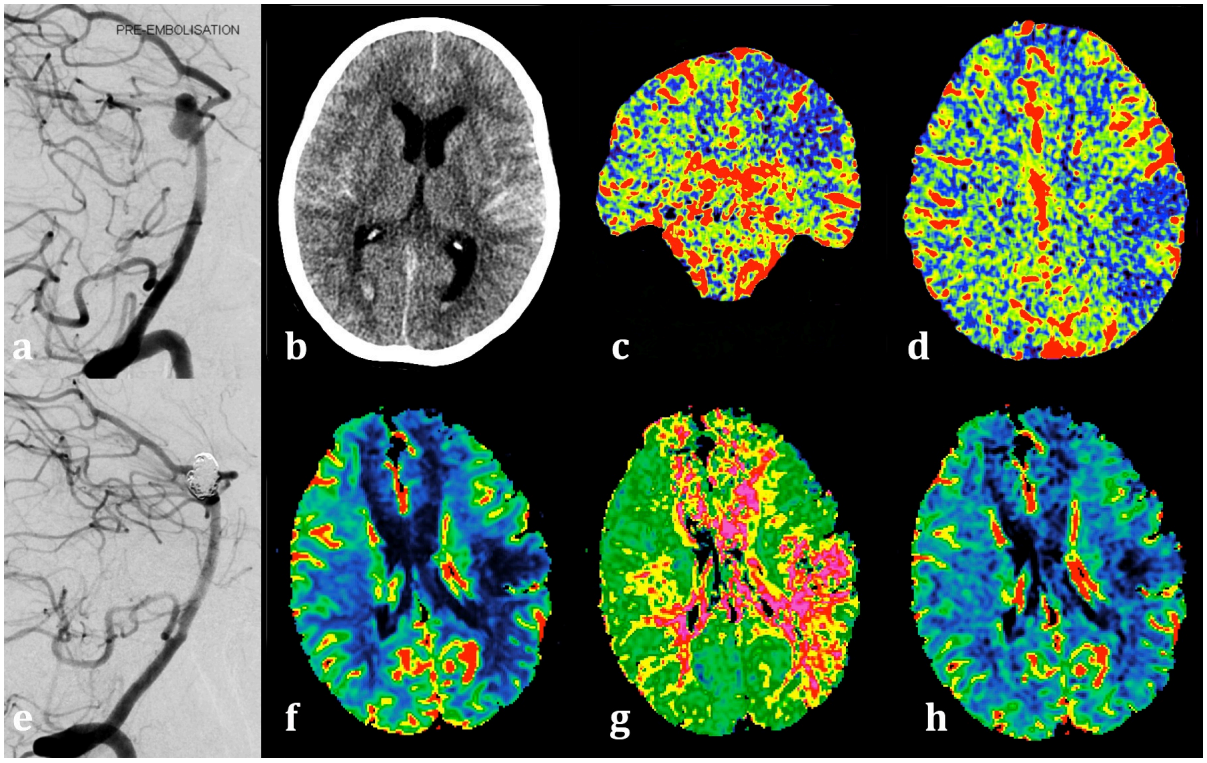


Figure 4.16: Illustrative case example 2. A 52 year-old-woman with ruptured basilar artery termination aneurysm (a) pre-treatment and (e) post-treatment catheter angiogram images show coil embolisation and complete angiographic occlusion of the basilar artery termination aneurysm; (b) NCCT performed after the development of neurological deficits (Day 4) excludes rebleed, hydrocephalus, or infarction; (c and d) coronal and axial sections of C-arm FDCT PBV maps (Day 6) show reduced PBV in both frontal lobes and in the left parietal lobe; and (f, g, and h) MR-PWI CBF, MTT, and CBV maps (Day 6) confirming a similar distribution of reduced perfusion in both frontal lobes and in the left parietal lobe.

4.5 Discussion

This chapter demonstrates the feasibility and potential value of intravenous PBV protocol C-arm FDCT imaging in patients with aneurysmal SAH who develop delayed clinical deterioration. We observed good correlation and agreement between the C-arm CT rPBV and MR-PWI derived rCBV and rCBF, with minimal bias and the 95% limits of

agreement that included clinically significant rPBV discrepancies. Our results demonstrate that the C-arm CT PBV is a composite parameter with both blood-flow and blood-volume weightings (better correlation and agreement of C-arm CT rPBV with the geometric mean of MR-rCBV and MR-rCBF ($\sqrt{}$ MR-rCBV × MR-rCBF) compared with MR-rCBV or MR-rCBF alone). Furthermore, the C-arm CT PBV has a preferential blood-flow weighting (≈ 60% blood-flow and ≈ 40% blood-volume weighting) as shown by the results of analysis performed using the weighted means of MR-rCBF and rCBV (table 4.3 and 4.4).

In comparing the C-arm CT PBV with the MR-PWI derived parameters, we focused on a quantitative analysis approach using predefined atlas-based cortical and subcortical VOIs encompassing the whole brain. The comprehensive set of VOIs (56 VOIs for each hemisphere) that we used, included all cortical and subcortical structures listed in table 4.1. Robust registration between the two datasets for each patient was performed to ensure that the VOIs being compared corresponded to the same anatomical locations in the brain. This approach makes our comparison objective and minimizes any observer bias that may be introduced if manually drawn 2D regions of interest (ROIs) were used. With limited number of 2D ROIs, used in the initial studies comparing C-arm CT PBV with CTP CBV where a limited brain volume coverage was available for CTP, there remains a possibility that certain locations of brain with perfusion deficits may be partially or completely excluded (Dankbaar et al., 2010, 2009; Rijsdijk et al., 2008). In addition, with limited brain coverage for CTP, its co-registration with another study is invariably inadequate and any differences in slice orientation can

lead to anatomical non-correspondence between the images being compared. With both C-arm CT imaging and MR-PWI, there is extended craniocaudal (z-axis) coverage; therefore co-registration of the two studies to achieve anatomical correspondence is convenient, and in conjunction with the VOIs including all brain regions, this approach ensures that no parts of the brain are excluded from the analysis and that the VOIs being compared represent the same regions of brain for the two imaging studies. We acknowledge that the perfusion deficits in DCI may not follow the exact anatomical boundaries of atlas-based VOIs; but using a combination of robust registration and whole brain VOIs makes the comparisons valid by virtue of anatomical correspondence and whole brain inclusion, irrespective of the distribution of perfusion abnormalities.

Previous reports documenting the accuracy of C-arm CT PBV technique in both animal and human subjects used CTP as a comparison standard and restricted their analysis to comparison of PBV with CBV measurements only (Ahmed et al., 2009; Bley et al., 2010; Struffert et al., 2012, 2011, 2010). A comparison of C-arm CT PBV against CTP-CBV alone makes an a-priori assumption regarding equivalence of C-arm CT PBV and CTP-CBV, which is not completely unjustified based on the theoretical understanding (chapter 03). Our observations support the findings of previous reports in confirming the agreement between CBV and C-arm CT PBV by using a different perfusion imaging modality i.e. MR-PWI. However, exploratory nature of analysis in this chapter comparing C-arm CT rPBV against both MR-PWI rCBV and rCBF, with no a-priori assumption regarding equivalence of PBV and CBV provides additional insight into the composite nature of C-arm CT PBV parameter. We noticed a slightly higher

correlation and better agreement of C-arm CT rPBV with MR-rCBF in comparison with MR-rCBV. Subsequent analysis using the geometric mean of MR-rCBV and MR-rCBF *($\sqrt{MR\text{-}rCBV \times MR\text{-}rCBF}$),* which showed better correlation and agreement with C-arm CT PBV, compared with MR-rCBV or MR-rCBF alone, provided support to the proposition that C-arm CT PBV is a composite perfusion parameter, distinct from CBV, and likely has both CBV and CBF weightings. With further analysis using weighted means of MR-rCBF and rCBV we were able to demonstrate that C-arm CT PBV has approximately 60% blood-flow and 40% blood-volume weighting. These objective findings also corresponded with our subjective observations in the clinical setting where the deficits on colour-coded PBV maps were noted to visually correlate better with the pattern of abnormality on MR-CBF maps than with the pattern of abnormality on MR-CBV maps. None of the prior studies have explored this subject for C-arm CT PBV. However, our results are supported by similar findings for multi-detector CT (MDCT). The image data acquired by C-arm CT PBV protocol is post-processed using the principles of image subtraction and indicator dilution in a manner similar to that proposed initially for multi-detector CT/CTA PBV imaging (Hamberg et al., 1996). For MDCT, the CTA source images (SI) could be used alone or could be post-processed to generate colour-coded MDCT PBV maps (Kloska et al., 2007; Lu et al., 2011; Wittkamp et al., 2010). Sharma et al., using a CTA protocol with a scan duration (1 sec/rotation and table speed 15-30 mm/sec) and contrast injection parameters comparable to our C-arm CT PBV examination, showed that despite theoretical models suggesting MDCT PBV images to be predominately blood-volume weighted, with more rapid modern CTA protocols used

in clinical practice, these images were in fact blood-flow weighted (Sharma et al., 2011). In this setting, blood-volume weighting is facilitated by (a) longer delay and lower contrast injection rates to change the temporal shape of the time-concentration curve or (b) by longer scanning times to acquire data over a larger segment of the time-concentration-curve, while the converse factors favour blood-flow weighting (Konstas et al., 2009). Furthermore, keeping in view the altered cerebrovascular haemodynamics in the setting of DCI (our study population), with vessel narrowing and subsequent increased intracranial vascular resistance, the passage of intravenously administered contrast medium through the cerebral vasculature could have been delayed resulting in the C-arm FDCT projections being acquired while the contrast concentration in the cerebral microvasculature may still have been rising, thus providing another contributory factor to preferential blood-flow weighting of the resulting C-arm CT PBV measurements.

We did not use 'presence of infarcts on the follow-up imaging', as a criteria to define DCI. The absence of infarcts on follow-up imaging does not completely exclude prior DCI, since the cerebral ischaemia could have been transient and the infarction prevented by spontaneous resolution or by successful treatment (all patients enrolled in our study received medical management while some underwent chemical angioplasty) (Dankbaar et al., 2010). Thus using a follow-up imaging criterion to retrospectively define DCI can potentially underestimate the occurrence of DCI. Instead, the patients recruited for this research were initially labelled to have DCI on the basis of clinical criteria (as used by the neuro-ICU team at our institution which included clinical

deterioration e.g. new focal deficit or decrease in consciousness, lasting 2 hours or longer with no evidence for rebleed, hydrocephalus on NCCT, or other medical cause), imaging confirmation of which was subsequently performed. The confirmation of the clinically labelled DCI using MR imaging imposed logistical constraints for neuro-ICU patients particularly related to the *continuous monitoring equipment* that these very sick patients required. These constraints were less challenging for C-arm FDCT scanning due to a more open and non-magnetic environment.

The C-arm CT PBV technique is new and there are no established guidelines regarding its incorporation in the workflow for management of DCI patients. Our study demonstrates that the whole brain PBV measurements correspond with MR-PWI and this evaluation provides an insight into cerebral haemodynamics in an interventional setting. We anticipate that this information can be of potential benefit in a subset of aneurysmal SAH patients, for example: (a) a C-arm CT PBV scan at the time of initial embolisation treatment may serve as a baseline for critically ill patients with large volume SAH (high Fischer grade) considered at high risk for developing DCI, and (b) in aneurysmal SAH patients developing DCI with no improvement in their neurological status despite aggressive medical management, who undergo catheter angiogram to evaluate the degree of angiographic vasospasm, a C-arm CT PBV study may either provide useful supplemental information on the haemodynamic significance of angiographic large-vessel vasospasm or help to identify the microvascular dysfunction which may not be detectable on the 2D-DSA. For these patients, PBV abnormalities, if present may have a predictive value for DCI similar to CTP parameters and help plan a

rescue intervention without the need for patient transfer between the diagnostic and interventional suites. In this chapter, the feasibility of C-arm CT PBV imaging in the setting of DCI following aneurysmal SAH and its agreement with MR-PWI is demonstrated, however, future studies investigating the correlation of C-arm CT PBV deficits to the development of infarction on follow-up imaging and larger studies specifically exploring its utility in the diagnosis and management of DCI would be needed to elucidate its true clinical value.

Apart from the major advantage of its availability in the interventional suite, C-arm CT PBV protocol imaging offers additional features including: (a) an extended craniocaudal coverage that allows whole brain evaluation in a single sweep, (b) isotropic spatial resolution that makes omniplane reconstructions of the C-arm CT PBV maps possible (both a and b may not synchronously be available for CTP and MR-PWI), (c) large vessel angiographic reconstructions from the data collected during contrast-enhanced run of the C-arm CT PBV protocol scan, and (d) cross-sectional CT-like soft tissue reconstructions of the brain parenchyma from the data collected during the mask run. The large vessel reconstructions can reliably evaluate the patency and calibre of large intracranial arteries for the presence of an occlusion or vasospasm; while the soft tissue reconstructions, despite their inferior low-contrast resolution compared with conventional CT, are of adequate quality to allow assessment of ventricular size, intracranial haemorrhage (cerebral oedema, hydrocephalus, and rebleeding are possible causes of delayed clinical deterioration that may mimic DCI), and procedural vessel rupture (discussed in detail in chapter 8) (Kamran et al., 2010). Thus, a single

intravenous PBV protocol C-arm CT examination provides soft tissue, angiographic, and haemodynamic information, obtaining which may otherwise require multiple imaging studies. Diagnostic information thus obtained may assist the clinical decisions, while avoiding repeat examinations and reducing the overall radiographic contrast and radiation doses. The ability to extract diagnostic anatomical and physiological data in an interventional environment has potential implications for management of patients with ischaemic cerebrovascular disease. In the setting of acute stroke, for example, a single C-arm CT study can help exclude intracranial haemorrhage, assess large vessel patency, and estimate tissue viability; thereby assisting in patient selection for endovascular revascularisation treatment without the need to transfer patients to a CT or MR scanner. A reduction in the duration between the patients' arrival at a stroke treatment facility and start of revascularisation procedure thus achieved would increase the likelihood of improved procedural and clinical outcomes. Additionally, by virtue of its availability in the interventional suite, it can help optimise and assess the success of revascularisation procedures in restoring perfusion while the patient is still on angio-table.

We used MR-PWI as a reference standard while the previous studies have used CTP as the comparison standard for C-arm CT PBV evaluation (Ahmed et al., 2009; Bley et al., 2010; Mordasini et al., 2012; Struffert et al., 2012, 2011, 2010). CTP offers obvious advantages including widespread availability, easier logistics, absolute quantification of perfusion parameters, and relatively few contraindications. However, its limited craniocaudal coverage may be restrictive in the setting of DCI, where the ischaemic

changes could be multifocal or global in nature (Dankbaar et al., 2010, 2009; Mir et al., 2013; Sanelli et al., 2011). Our choice of MR-PWI as a reference standard was thus driven partly by its extended craniocaudal coverage but largely by the lack of radiation exposure with MR imaging; with an aim to limit radiation dose for the critically ill study subjects undergoing a research scan that involved radiation exposure and who typically underwent multiple x-ray based diagnostic imaging studies. Another advantage of choosing MR imaging was the availability of diffusion-weighted images from the scanning session, which are sensitive to detect early cytotoxic oedema and infarction (88-100% sensitivity to detect early infarcts) (Mills et al., 2013). However, both MR-PWI and CTP are well established and validated perfusion imaging techniques, routinely used in clinical practice. A disadvantage of MR-PWI derived perfusion parameters is their semi-quantitative nature due to the lack of a direct linear relationship between the MR signal intensity and the paramagnetic contrast medium concentration (Essig et al., 2013). In contrast, absolute quantification of the perfusion parameters is possible with CTP due to a linear relationship between the iodinated contrast medium concentration and the CT number (Hounsfield Units), which is of particular advantage when serial perfusion measurements are made (Konstas et al., 2009). Recent literature however suggests that the absolute perfusion parameter values estimated with CTP may vary considerably for various vendor software applications (Kudo et al., 2009; Zussman et al., 2011). We recognized these limitations and in our analysis we used the inter-hemispheric ratios of the perfusion parameters for both the MR-PWI and C-arm CT techniques. While its theoretically possible that in

multifocal or diffuse ischaemia where symmetric perfusion deficits exist, the interhemipheric ratios for MR-PWI may be misleading. This limitation of using interhemipheric ratios in a clinical setting would apply to the C-arm CT PBV as much as it applies to MR-PWI, if the clinician were to rely solely on the interhemispheric ratios. However, an advantage of C-arm CT PBV imaging is that absolute PBV measurements (given the use of iodinated contrast and x-rays) are also provided, and in the setting of multifocal or diffuse ischaemia these absolute measurements provide information that may be overlooked if only the interhemispheric ratios were used.

Although measurement of a physiological parameter (PBV) of potential prognostic significance is an important step towards functional imaging in the neurointerventional suite, mechanical constraints prevent dynamic perfusion imaging with the C-arm systems (Struffert et al., 2012). Temporal resolution of the C-arm systems in current clinical use (gantry rotation time 6 – 8 seconds) is inadequate to accurately define the time-concentration-curve for cerebral vasculature during the passage of radiographic contrast, unlike CTP or MR-PWI where the sampling times are much shorter (~1-2 seconds). As a result, parameters such as MTT, reported to be most specific for microvascular and macrovascular ischaemia cannot be estimated with C-arm CT imaging (Etminan et al., 2013). At the current level of performance, thus C-arm CT PBV imaging remains inferior to the conventional dynamic perfusion imaging modalities and should not be considered to replace CTP or MR-PWI; rather it serves as an additional tool in the neurointerventionist's armamentarium. In evaluating its value as a clinical imaging tool, therefore the application-related advantages given its

availability in interventional setting should be weighed against the image performance related disadvantages. New generation multi-axis C-arm angiographic systems based on robotic technology allow shorter rotation times and hold the potential for dynamic perfusion imaging. Preliminary work in canines based on interleaved scanning to augment the temporal resolution for C-arm systems has shown promising results in allowing estimation of CBF and MTT (Fieselmann et al., 2012; Royalty et al., 2013). Further advancements such as improved flat detector contrast detectability and read-out speed, improvements in C-arm system design, and newer software algorithms are expected to support this development, which would allow a detailed 'one-stop' assessment of patients with cerebral ischaemia in the neurointerventional suite.

4.6 Conclusion

In conclusion, the work in this chapter provides insight into the nature of C-arm CT PBV parameter and demonstrates the feasibility of C-arm CT PBV imaging in the setting of DCI following aneurysmal-SAH. In this first report on the application of C-arm CT PBV imaging in patients with DCI and its comparison with MR-PWI, we demonstrate that C-arm CT PBV is a composite perfusion parameter incorporating both blood-flow and blood-volume weightings. That PBV has preferential (60%) blood-flow weighting, is an important finding with potential clinical significance, particularly when interpreting the C-arm CT PBV maps in the setting of acute brain ischaemia, where an assumed CBV equivalence can potentially overestimate the infarcted tissue and lead to selection of fewer patients for endovascular treatment. In this regard, for the purpose of clarity, we recommend that the term parenchymal blood volume (PBV) should be preferred and

the term cerebral blood volume (CBV) be avoided when referring to this haemodynamic parameter measured using C-arm CT imaging. As a non-invasive objective assessment tool, the ability of a single C-arm CT study to provide both anatomical (soft tissue and angiographic) and physiological information in the interventional suite improves the workflow, can avoid repeat examinations, serve as a diagnostic marker for DCI, potentially allow in-room selection of patients for intra-arterial angiography and angioplasty, and has implications for management of patients with acute stroke.

5

C-arm FDCT PBV Thresholds for Identification of Infarcted Parenchyma

5.1 Abstract

Background and purpose: C-arm FDCT parenchymal blood volume (PBV) imaging allows functional assessment of brain parenchyma in the neurointerventional suite. This chapter aims to determine the optimal C-arm FDCT PBV thresholds for demarcating irreversibly infarcted brain parenchyma using areas of restricted diffusion on MR imaging as a surrogate marker for infarction.

Materials and Methods: Twenty-six patients with delayed cerebral ischaemia (DCI) following aneurysmal subarachnoid haemorrhage (SAH) underwent a research C-arm CT PBV scan using a biplane angiography system and contemporaneous MR imaging. Infarct and peri-infarct tissue volumes of interest (VOIs) and their homologues VOIs in the contralateral uninvolved hemisphere were delineated based on the review of diffusion-weighted, perfusion-weighted, and apparent diffusion coefficient MR images. Voxel-based receiver-operating-characteristic (ROC) curve analysis was performed to estimate the optimal absolute and normalised PBV values for demarcating the infarct voxels.

Results: For twelve patients with areas of restricted diffusion, the mean infarct volume was 6.38 ml (SD 7.09ml) and mean peri-infarct tissue volume was 22.89ml (SD 21.76ml). Based on the voxel-based ROC curve analysis, optimal absolute and normalised PBV thresholds for infarcted parenchyma were 2.49 ml/100gm (AUC 0.76, sensitivity 0.69, specificity 0.71) and 0.67 (AUC 0.77, sensitivity 0.69, specificity 0.72) respectively; (p-value for both <0.01). For the moderate-to-severely ischaemic peri-infarct zone, the mean PBV values of the involved hemisphere VOIs were lower

compared with the uninvolved hemisphere VOIs (p-value < 0.01). However, for the mild-to-moderately ischaemic peri-infarct zone, there was no statistically significant difference between the mean PBV values of the involved and uninvolved hemisphere VOIs (p-value > 0.05).

Conclusion: The results of this chapter demonstrate that C-arm FDCT PBV maps in conjunction with optimal thresholds can be sensitive and specific for irreversibly infarcted parenchyma. PBV maps allow reliable detection of moderate-to-severe ischaemia; however, can potentially underestimate mild-to-moderate ischaemia. C-arm CT PBV thresholds for infarction have not been studied previously and are of value in providing an accurate assessment of the brain viability and identification of irreversibly infarcted parenchyma in the interventional suite, with implications for guiding the revascularisation procedures in acute brain ischaemia.

5.2 Introduction

Flat detector equipped C-arm angiographic systems used in the neurointerventional suite are now capable of measuring parenchymal blood volume (PBV) using a specially designed scan protocol (Zellerhoff et al., 2009). The imaging data acquired following intravenous radiographic contrast administration is processed to generate whole brain PBV maps, available for review while the patient is on angio-table. Initial reports documented agreement between the C-arm flat detector computed tomography (C-arm FDCT or C-arm CT) PBV and the CT perfusion (CTP) derived cerebral blood volume (CBV) (Ahmed et al., 2009; Bley et al., 2010; Struffert et al., 2012, 2011). In the previous chapter, we observed that C-arm CT PBV is not identical to CBV and it has both blood-volume and blood-flow weightings (60% CBF and 40% CBV); a finding which explains the agreement between C-arm CT PBV and CTP-CBV noted in the previous reports, while providing further insight into the composite nature of C-arm CT PBV parameter.

Availability of PBV maps in the interventional suite is an important development with potential implications for the management of patients with ischaemic cerebrovascular disease and their selection for revascularisation procedures (Struffert et al., 2012). In the setting of acute brain ischaemia, the primary role of perfusion imaging is to discriminate between the ischaemic (salvageable) and the infarcted (non-salvageable) tissues (Wintermark et al., 2013). Thresholds for various dynamic perfusion-imaging (CTP or MR-PWI) parameters are used in this regard to identify and estimate the amount of ischaemic and infarcted tissues. Given the reported agreement between C-arm CT PBV and other perfusion imaging techniques, and an observation by Struffert et

al. that the areas of reduced PBV on initial PBV maps correlate with the infarct volume on follow-up imaging in patients with acute middle cerebral artery (MCA) occlusion, a potential application of PBV imaging in the interventional suite could be to demarcate the ischaemic or infarcted tissues in a manner similar to dynamic perfusion imaging modalities (Struffert et al., 2012). For CTP, though debate exists as to which perfusion parameter best defines ischaemic or infarcted tissues, thresholds for various parameters have been reported (Campbell et al., 2011; Christensen et al., 2009; Kamalian et al., 2011, 2012; Murphy et al., 2006). However, given the composite nature of PBV with combined blood-flow and blood-volume weightings, neither the CBV nor the CBF thresholds typically reported for CTP may be applicable to C-arm CT PBV measurements. Optimal thresholds specific to PBV measurements do not exist and need to be investigated.

The aims of this chapter were: (1) to determine the optimal C-arm CT PBV thresholds for irreversibly infarcted parenchyma using contemporaneous MR-DWI in the patients with delayed cerebral ischaemia (DCI) following aneurysmal subarachnoid haemorrhage (SAH) and (2) to investigate if the C-arm CT PBV values in the peri-infarct ischaemic zone allow reliable demarcation of the ischaemic tissue.

5.3 Materials and Methods

With local research ethics committee approval, a series of patients (n = 26) with aneurysmal SAH meeting the inclusion and exclusion criteria were enrolled in this prospective study. Inclusion criteria were patients aged over 18 years with documented aneurysmal SAH who subsequently developed symptoms and signs suggesting DCI and

requiring confirmatory imaging. At our institution, SAH is diagnosed using non-contrast CT (NCCT) head or cerebrospinal fluid (CSF) sampling by lumbar puncture when initial NCCT head is negative but clinical suspicion of SAH remains high. The extent of SAH on NCCT was graded as described by Fisher et al. (Fisher et al., 1980). The diagnosis of DCI was based on clinical assessment by the multidisciplinary neuro-intensive care unit (neuro-ICU) team and was defined as clinical deterioration (focal neurological deficits or reduced level of consciousness) lasting 2 hours or longer with no evidence of rebleed or hydrocephalus on NCCT head, and no other medical causes such as infections or metabolic disturbances. Exclusion criteria were: a history of allergy to iodinated contrast medium, renal impairment, pregnancy, or contraindications to MR examination. All recruited patients had undergone aneurysm repair by endovascular coil embolisation. Written informed consents were obtained from patients or if they were unable to complete the consent process, from a family member or a designated surrogate as defined by the research ethics committee approval for the study. All recruited patients underwent an MRI examination using a protocol that included diffusion- and perfusion-weighted sequences, concurrent with the research PBV protocol C-arm CT scan. The imaging protocols and post-processing steps for the two imaging studies are described in the following sections.

5.3.1 C-arm FDCT Imaging

C-arm FDCT scans were performed on a flat detector equipped biplane angiography system (Axiom Artis dBA; Siemens Healthcare, Germany) in the neuro-interventional suite of Department of Neuroradiology, West Wing, John Radcliffe Hospital, Oxford. The

imaging protocol included two rotational acquisitions: mask and contrast-enhanced (or fill) runs. Projection data for each run was acquired using the following parameters: 419 projection images, 0.5^0 frame angle, 210^0 angular scan range, 8 seconds acquisition time, 0.36 **μ**Gy radiation dose per frame. The contrast-enhanced dataset was acquired following a manually triggered intravenous injection of radiographic contrast material Niopam 370 (Bracco spa, Milan, Italy) using a power injector (Medrad, Inc. Philadelphia). The injection parameters were: contrast concentration, 370 mg Iodine/ml; volume, 80ml; injection rate, 4 ml/sec administered through the antecubital vein; injection pressure, 300 psi; and injection duration, 20 seconds. Passage of contrast material through the cerebral vasculature was monitored on two-dimensional (2D) fluoroscopic images (2 frames/sec) and the contrast-enhanced run was triggered when maximal opacification of the superior sagittal sinus was observed.

Post-processing of the data to generate color-coded PBV maps was performed on a dedicated research workstation (Leonardo, Siemens AG, Healthcare) using prototype software. The steps involved were: (1) co-registration of the two volumes, the mask and the contrast-enhanced, (2) subtraction of the mask volume from the contrast-enhanced volume, (3) normalization of the subtracted data with an input function automatically estimated from the histogram analysis of vascular tree, (4) color-coding with a standard colour look-up table to generate the color-coded PBV maps for visualization and interpretation (a detailed discussion of these post-processing steps in included in chapter 03). The final PBV values are expressed in units of ml/1000 ml of cerebral tissue. PBV values for volume-of-interest (VOI) analysis were converted to more

commonly used units of ml/100 g by using a simple conversion factor that takes into account the cerebral tissue density (1.05 g/ml). For visualization of the vessels, the contrast-enhanced dataset was reconstructed separately on a commercially available dedicated workstation (Leonardo, Siemens AG, Healthcare). VRT (volumetric rendering technique) and MIP (maximum intensity projection) reconstructions were used to evaluate the cerebral vasculature. CT-like soft tissue reconstructions were obtained in all cases.

5.3.2 MR Imaging

A standard MR scan protocol comprising sagittal T1-weighted, axial T1-weighted, axial T2-weighted, diffusion-weighted, perfusion-weighted, and time-of-flight (TOF) MR angiography sequences was performed on Philips Achieva 1.5 Tesla MRI unit. Details for the diffusion and perfusion weighted sequences are discussed below.

1. Diffusion weighted: Repetition time (TR) 2897ms, time-to-echo (TE) 73ms, field-of-view (FOV) 174×249mm, reconstruction matrix 144×144, slices 25, slice thickness 5mm, voxel size 1.74×1.73×5mm, b-values 0 and 1000, EPI factor 51, sequence duration 34sec.

2. Perfusion-weighted: Perfusion data was acquired using the dynamic susceptibility contrast (DSC) technique with the following parameters: T2* weighted gradient echo echoplanar sequence, TR 2000ms, TE 44ms, FOV 248×248 mm, reconstruction matrix 256×256, voxel size 0.98×0.98×4mm, SENSE factor 2.1, bandwidth 806 Hz/pixel, sequence duration 1min 46sec. Paramagnetic contrast material was administered intravenously with an MR-compatible power injector (Medrad Inc.) at 5 ml/sec

followed by 10ml saline flush. Fifteen slices covering the whole brain were acquired at 50 time points during the injection of 0.2 mmol/kg of gadopentate (Prohance, Bracco Diagnostics Inc.)

Post-processing of the perfusion data was performed using commercially available software (nordicICE perfusion package, NordicNeuroLab, Bergen, Norway). After motion correction of the raw data, perfusion maps were created using the standard singular value doconvolution (SVD) technique. Arterial input function (AIF) to deconvolve the dynamic tissue response curve was automatically determined and SVD regularization was achieved with the truncated SVD approach (cut-off fraction 0.20) and iterative thresholding (target oscillation index 0.10). Semi-quantitative, leakage-corrected output perfusion maps for clinical interpretation included: cerebral blood flow (CBF), cerebral blood volume (CBV), mean transit time (MTT), and time to peak (TTP).

5.3.3 Further Post-processing and Quantitative VOI Analysis

C-arm CT PBV, MR-PWI, MR apparent diffusion coefficient (ADC), and MR-DWI images were further processed using the FMRIB's software library (FSL) tools (Jenkinson et al., 2012). Brain extraction tool (BET) was used to delete the non-brain tissues from the images of interest followed by linear registration of the C-arm PBV maps and the MR-PWI, -PWI, and -ADC images for each patient to the T1-weighted average structural template brain volume in MNI152 space with FMRIB linear image registration tool (FLIRT) (Jenkinson et al., 2002; Smith, 2002). Alignment of all coregistrations was visually confirmed in three orthogonal planes. Areas of infarction were identified based

on the review of MR-DWI images and ADC maps. Three-dimensional (3D) VOIs corresponding to the infarct core were defined on the DWI images with a semiautomated approach using MRIcro software (Rorden and Brett, 2000). In the next step, the infarct core VOIs were grown to include the peri-infarct ischaemic parenchyma identified as the region of asymmetrically reduced CBF (<95% relative to the mean contralateral hemisphere CBF) surrounding the infarct core defined on the DWI images. From the grown VOIs that included both the infarct core and the peri-infarct ischaemic tissue, the infarct core VOIs were subtracted thus creating the subtraction VOIs defining only the peri-infarct ischaemic tissue. In the contralateral normal hemisphere, mirrored homologues tissue VOIs were then created corresponding to the affected hemisphere infarct core and peri-infarct ischaemic tissue VOIs. All VOIs were subsequently transposed onto co-registered C-arm CT PBV maps. Figure 5.1 and 5.3 (page 114) illustrate the VOI masks used for analysis. Mean, median and standard deviation of the absolute PBV values in all VOIs were measured using FSL maths and FSL stats utilities. Normalised PBV values were calculated by dividing absolute PBV value for each VOI with the mean contralateral hemisphere PBV value obtained using separate hemispheric masks. Figure 5.2 provides a schematic overview of the image post-processing and analysis steps.

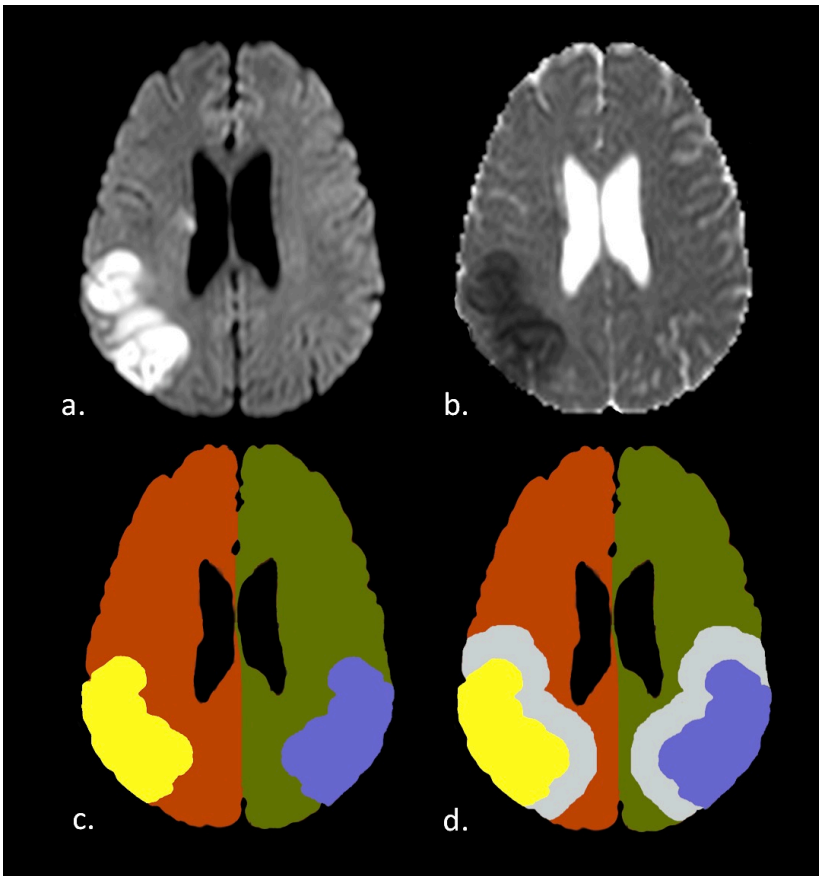


Figure 5.1: Binary masks used for VOI analysis. An area of restricted diffusion was identified on the MR-DWI images and ADC maps (a and b). Corresponding to the area of restricted diffusion (surrogate for infarcted tissue), a VOI mask (yellow) was created by a semiautomatic approach, along with a mirrored VOI mask (blue) in the contralateral normal hemisphere. Surrounding the VOI mask corresponding to the area of restricted diffusion, a peri-infarct tissue VOI mask (grey) was created based on the review of MR-PWI rCBF maps. Mirrored VOI mask for the peri-infarct tissue in the contralateral normal hemisphere was constructed by transposing the peri-infarct tissue VOI mask. Hemispheric masks for the ipsilateral (orange) and contralateral hemisphere (green) were constructed for calculation of normalised PBV values.

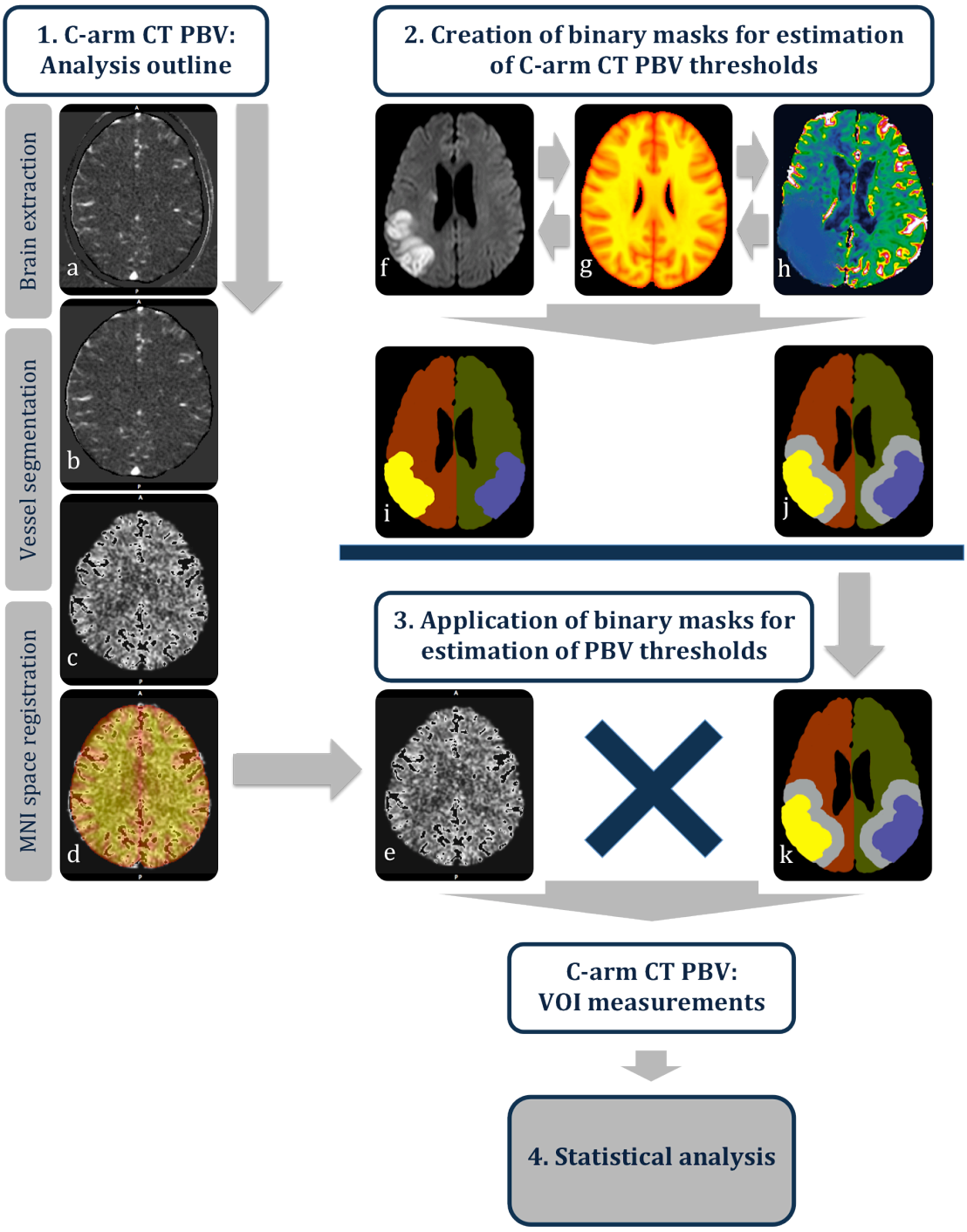


Figure 5.2: A schematic overview of the image post-processing and analysis .

1. A C-arm CT PBV dataset before brain extraction (a); PBV dataset following brain-extraction using FSL BET utility (b); PBV dataset following threshold-based segmentation of the vascular structures (c); registration of the PBV volume to the T1-weighted average structural template

brain volume in MNI152 space (d); brain-extracted, co-registered, vessel-segmented PBV volume in MNI152 space (e).

2. DWI/ADC maps (f) and MR-PWI maps (h), registered to the standard average T1-weighted brain volume in standard MNI152 space (g) were used to define areas of infarction and ischaemia; binarised masks of 3D-VOIs corresponding to areas of infarction/ischaemia and other masks described in figure 5.1 were then created (i and j).

3. The binarised masks (k) were subsequently applied to the post-processed C-arm CT PBV maps (e) to obtain PBV measurements for the 3D-VOIs, which were then used in the statistical analysis described in section 5.2.4.

5.3.4 Statistical Analysis

(a) Paired t-test was performed to investigate if: (a) mean PBV in the infarct tissue VOIs and the mean PBV in contralateral uninvolved homologues tissue VOIs were statistically different, and (b) mean PBV in peri-infarct ischaemic parenchyma VOIs and the mean PBV in contralateral uninvolved homologues tissue VOIs were statistically different.

(b) To test the predictive performance of C-arm CT PBV maps across various thresholds for demarcating infarcted tissue, voxel-based receiver-operating-characteristic (ROC) curve analysis was performed. Sensitivity and specificity of PBV maps for demarcating the infarct voxels (DWI/ADC abnormality) from the non-infarct voxels across patients as a function of increasing PBV thresholds were computed. Accuracy of PBV maps in demarcating the infarct voxels (DWI/ADC abnormality) from the non-infarct voxels was determined from the area under curve (AUC) statistic that ranges from 0.5 (no predictive value) to 1 (absolute predictive value). The ROC curve

analysis was performed separately for the absolute and the normalised PBV values. The final absolute and normalised PBV thresholds for demarcating infarcted tissue were calculated as the optimal ROC curve points with equally attributed weights to sensitivity and specificity. Statistical analysis was performed using GraphPad Prism Software, San Diego California, USA.

5.4 Results

5.4.1 Study Population Characteristics

A total of 26 patients (mean age 55 years; men 9, women 17) entered the study. Patients' WFNS (world federation of neurosurgical societies) grades at the time of admission to hospital were: Grade-1 in 16 (61%), Grade-2 in 7 (27%), Grade-3 in 2 (8%), and Grade-4 in 1 patient (4%). The extent of SAH on admission NCCT was graded: Grade-4 in 16 (61%), Grade-3 in 9 (35%), while one patient's NCCT head did not show evidence of SAH which was proven after lumbar puncture (4%). The onset of DCI after SAH varied from day-2 post-SAH to day-12 post-SAH (median, day-7 post-SAH). All patients received medical management following the diagnosis of DCI by the multidisciplinary neuro-ICU team. Of the 26 patients, 8 (31%) underwent chemical angioplasty with selective intra-arterial Nimodipine administration, 2 (8%) of whom received chemical angioplasty treatment twice. Mean duration between the C-arm FDCT PBV scan and the MR examination was 124 minutes. Of the 26 patients, 12 patients had areas of restricted diffusion (MR-DWI and ADC images). On the MR-DWI images for these 12 patients, 22 VOIs each for infarcted parenchyma, peri-infarct ischaemic tissue, and their contralateral homologues tissue were defined (total 22 × 4 VOIs). Table 5.1

describes the demographic, aneurysm, and clinical characteristics of the recruited patients and the details of DWI lesions.

5.4.2 Quantitative Image Analysis

For the patients with areas of restricted diffusion on DWI images, mean DWI lesion volume (infarcted parenchyma) was 6.38 ml (SD, 7.09ml; range 0.91ml to 26.5ml) and the mean peri-infarct ischaemic tissue volume was 22.89 ml (SD, 21.76ml; range 4.18 ml to 85.61ml).

Mean PBV values in the infarct VOIs were significantly lower compared to the mean PBV values in the mirrored contralateral uninvolved homologues tissue VOIs (paired t-test p-value <0.01), as illustrated in the box-whisker plot (figure 5.4). Voxel-based ROC curve analysis was performed for both absolute and normalised C-arm CT PBV volumetric parametric maps, and the resulting ROC curves are shown in figures 5.7a and 5.7b. Optimal absolute C-arm CT PBV threshold identifying the infarcted parenchyma using DWI abnormality as a marker was 2.49 mL/100gm. Corresponding AUC, sensitivity, and specificity were 76.4% (95% CI, 76.1-76.7), 69.35% (95% CI, 68.91-69.78), 70.65% (95% CI, 70.24-71.06) (p value < 0.01), respectively. Optimal normalised C-arm CT PBV threshold was 0.67. Corresponding AUC, sensitivity, and specificity were 76.9 (95% CI, 76.6-77.1), 69.37 (95% CI, 69.0-69.72), and 72.17 (95% CI, 71.83-72.51) (p value < 0.01), respectively.

A paired-samples t-test conducted to compare the mean PBV values for peri-infarct ischaemic tissue VOIs and the mean PBV values for corresponding mirrored VOIs in the contralateral uninvolved hemisphere showed no significant difference

between the mean PBV values for two groups of VOIs (p-value > 0.05). Given this finding, the analysis was extended by dividing each of the peri-infarct VOIs into two segments based on the review of MR-rCBF maps: (a) moderate-to-severely ischaemic peri-infarct zone with MR-CBF < 75% relative to the mean contralateral hemisphere CBF, and (b) mild-to-moderately ischaemic peri-infarct zone with MR-rCBF 75 – 95% relative to the mean contralateral hemisphere CBF (figure 5.3). VOIs and binary masks for the two zones were created for both the involved and the uninvolved hemisphere by following the same approach as used earlier in the analysis (described in section 5.2.3), followed by the application of the binary masks to the C-am CT PBV maps. Means PBV values for the two sets of VOIs corresponding to the mild-to-moderate and the moderate-to-severely ischaemic peri-infarct zones were then compared with their contralateral homologues tissue VOIs using the paired-samples t-test. For the moderate-to-severely ischaemic peri-infarct zone, the mean PBV values of the involved hemisphere VOIs were statistically significantly lower compared with the uninvolved hemisphere VOIs (figure 5.5 (p-value < 0.01)). However, for the mild-to-moderately ischaemic peri-infarct zone, there was no statistically significant difference between the mean PBV values of the involved and uninvolved hemisphere VOIs (figure 5.6 (p-value > 0.05)).

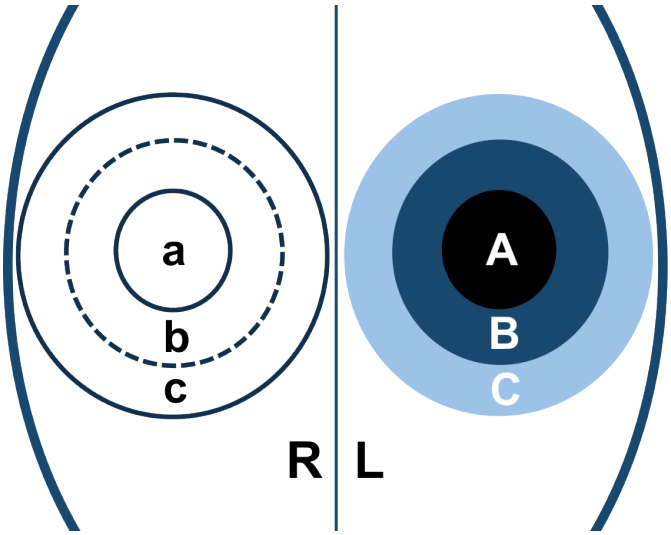


Figure 5.3: Schematic illustration of the infarct and peri-infarct VOIs. In the involved hemisphere (L), the infarct VOI (A) corresponds to the area of restricted diffusion (surrogate for infarction) on DWI and ADC images. Surrounding the infarct VOI, the peri-infarct zone (B+C) corresponds to the region of asymmetrically reduced MR-PWI CBF (CBF < 95% relative to the mean contralateral hemisphere CBF). The peri-infarct zone (B+C) was further subdivided into a mild-to-moderately ischaemic zone (B (CBF 75-95%, relative to mean contralateral hemisphere CBF)) and a moderate-to-severely ischaemic zone (C (CBF < 75-95%, relative to mean contralateral hemisphere CBF). Contralateral homologues tissue VOIs in the uninvolved hemisphere (R) corresponding to infarct (a) and peri-infarct zones (b+c) were created by transposing the involved hemisphere VOIs across midline.

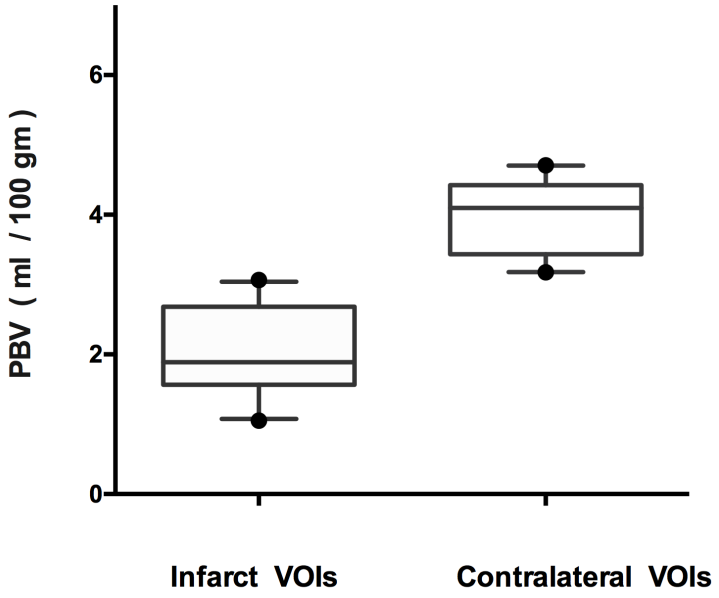


Figure 5.4: Plot of mean PBV values for the infarct VOIs.
Box-whisker plot showing PBV (mean and SD) in the infarct VOIs (areas of restricted diffusion) and in the mirrored contralateral homologues tissue VOIs.

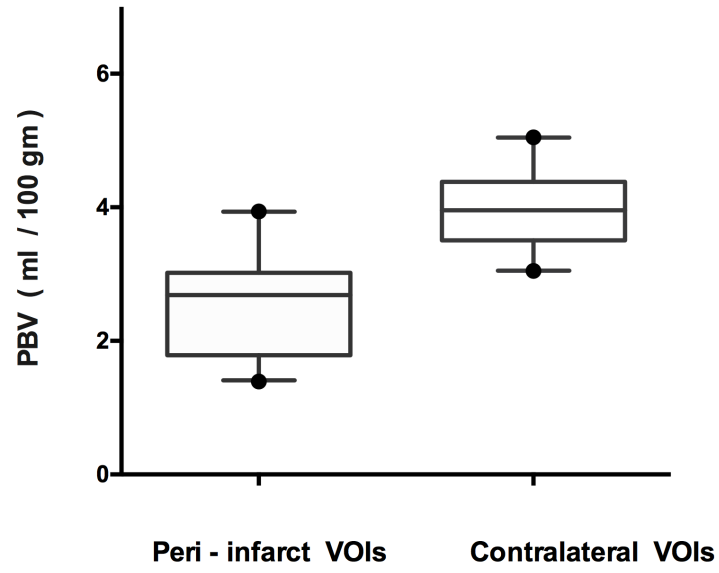


Figure 5.5: Plot of mean PBV values for the moderate to severely ischaemic, peri-infarct VOIs.
Box-whisker plot showing PBV (mean and SD) in the moderate to severely ischaemic, peri-infarct VOIs (rCBF < 75%) and in the mirrored contralateral homologues tissue VOIs

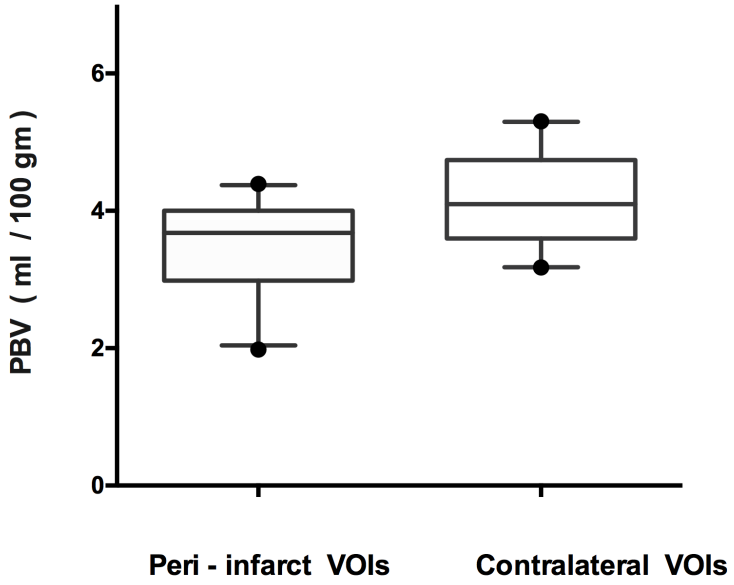


Figure 5.6: Plot of mean PBV values for the mild to moderately ischaemic, peri-infarct VOIs. Box-whisker plot showing PBV (mean and SD) in the mild to moderately ischaemic, peri-infarct VOIs (rCBF 75 – 95%) and in the mirrored contralateral homologues tissue VOIs

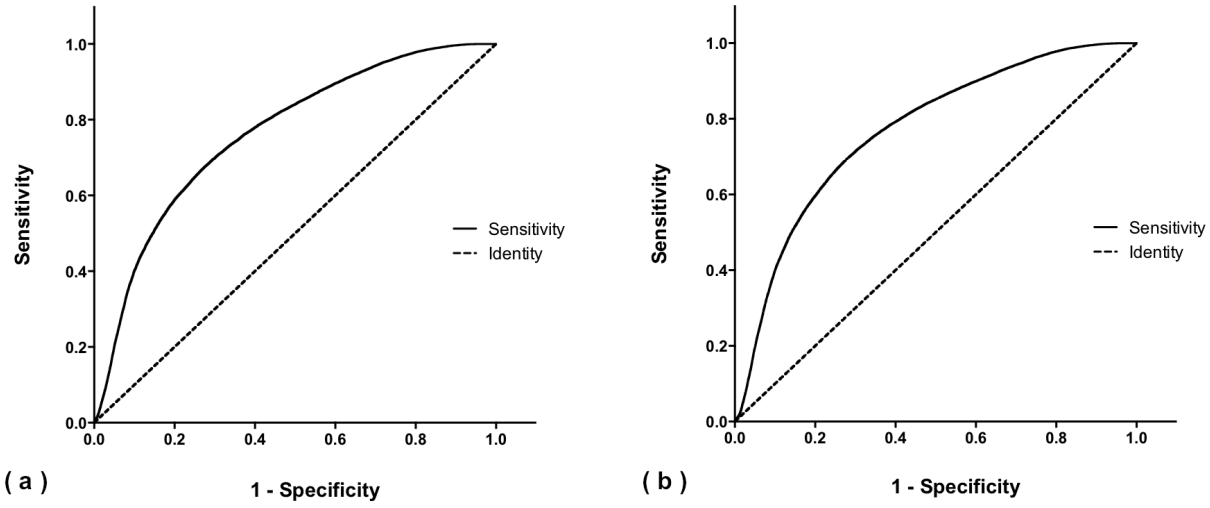


Figure 5.7: ROC curves for absolute and normalised PBV. Voxel-based ROC curves for absolute PBV (a) and normalised PBV (b), with near identical configuration. Absolute and normalised PBV thresholds for demarcating the areas of restricted diffusion were chosen by defining the optimal point on ROC curve with equally attributed weights to sensitivity and specificity.

Table 5.1 Demographic, aneurysm, and clinical characteristics of the patients and the location of DWI lesions

Patient number	Age (years)	Gender (M/F)	Aneurysm location	Aneurysm size (mm)	WFNS grade	Fischer grade	DWI deficits	DWI deficits distribution
1	47	M	Anterior communicating artery	6 × 4	1	3	+	Right frontal operculum; right centrum semiovale
2	55	F	Left anterior cerebral artery	12 × 10	3	4	–	_
3	61	F	Right posterior communicating artery	8 × 5	2	3	–	_
4	49	F	Anterior communicating artery	10 × 7	1	3	–	_
5	68	F	Right posterior communicating artery	10 × 6	2	4	–	_
6	71	F	Anterior communicating artery	6 × 5	1	4	+	Right frontal and left posterior frontal lobes
7	46	M	Right middle cerebral artery	4 × 3	3	3	+	Bi-frontal and posterior left parietal lobes
8	77	F	Left anterior cerebral artery	6 × 4	1	4	–	_
9	46	M	Right posterior communicating artery	4 × 4	1	4	–	_
10	50	F	Right internal carotid artery	3 × 3	1	3	+	Right frontal lobe
11	53	F	Basilar artery tip	7 × 6	2	3	+	Left frontal lobe
12	55	M	Right posterior communicating artery	5 × 3	2	4	–	_
13	55	F	Left posterior communicating artery	4 × 4	2	4	–	_
14	69	F	Left anterior cerebral artery	11 × 7	1	4	+	Bi-frontal lobes
15	66	M	Anterior communicating artery	7 × 5	1	0*	–	_
16	45	M	Anterior communicating artery	15 × 8	2	4	+	Right parietal lobe and corpus striatum
17	66	M	Right middle cerebral artery	8 × 3	4	4	+	Right parietal lobe and sylvian fissure
18	30	M	Anterior communicating artery	7 × 4	1	3	+	Left frontal lobe
19	39	F	Right posterior communicating artery	5 × 3.5	1	4	+	Right parietal lobe
20	50	F	Anterior communicating artery	4 × 3.5	1	4	–	_
21	69	M	Right posterior communicating artery	7 × 4	1	4	–	_
22	39	F	Right posterior communicating artery	10 × 9	1	4	+	Right frontal lobe
23	52	F	Right posterior communicating artery	5 × 5	1	4	+	_
24	54	F	Left posterior communicating artery	8 × 5	1	3	+	_
25	58	F	Right anterior cerebral artery	5 × 4	1	3	+	Right frontal lobe
26	60	F	Left peri-callosal artery	12 × 8	2	4	–	_

* NCCT head was negative for SAH, which was later confirmed on lumbar puncture

5.5 Discussion

This chapter reports optimal absolute and normalised C-arm CT PBV threshold values for demarcating the irreversibly infarcted brain parenchyma in the neurointerventional suite.

In determining the PBV threshold for infarcted brain parenchyma, areas of restricted diffusion identified on the review of DWI images and ADC maps were used as a marker for irreversibly infarcted tissue. Although DWI abnormality is not perfectly specific for infarct core, it is highly accurate and is an accepted standard both for clinical care and research analysis (Schellinger et al., 2010; Wintermark et al., 2013, 2008). In our analysis, we used 3D VOIs, defined semi-automatically for the DWI abnormality (infarcted parenchyma), which along with mirrored contralateral homologues tissue VOIs were transposed onto the co-registered C-arm CT PBV maps before performing the ROC curve analysis. This objective approach towards image analysis reduces any bias that may be introduced due to subjective differences in image display such as colour look up tables (LUT) for PBV maps, window settings, and pixel conspicuity which can be sources of error for manual segmentation (Kamalian et al., 2011).

That any perfusion study represents a 'snapshot' in time and the cerebral haemodynamics as well as thresholds for ischaemic damage may vary over time, are well-recognised issues from CTP imaging of acute brain ischaemia. For acute stroke imaging, this limitation may be addressed through stratifying data by duration post-ictus (Kamalian et al., 2011). However, unlike acute ischaemic stroke, complex

pathophysiology of cerebral vasospasm and resulting haemodynamic alterations make it difficult to define a specific time-of-onset for DCI secondary to vasospasm. Moreover, limited number of patients in our study precluded any such analysis, which could theoretically be performed using an arbitrary time-point such as development of neurological deficits in post-SAH patients.

An important factor that may introduce variability in C-arm CT PBV measurements and consequently shift the optimal PBV thresholds for infarction is how well the steady-state assumption is met. For calculation of C-arm CT PBV, the intravenously administered iodinated contrast material is assumed to have reached a *steady-state concentration* in the cerebral vasculature (contrast concentration in arteries = contrast concentration in tissues = contrast concentration in veins), maintained for the duration of scan (Zellerhoff et al., 2009). If this assumption is fully met, the C-arm CT PBV would be equivalent to the CBV derived from dynamic perfusion imaging modalities. However, an ideal steady-state may not be achieved in practice for the clinical scans and the contrast profile in the cerebral vasculature may show significant inter-subject differences due to various factors such as recirculation of contrast, haemodynamic perturbation effect, and slow bolus transit in the setting of low cardiac output and multifocal vasospasm (Bae, 2010). Preferential contrast wash-in or wash-out during the acquisition of fill run data for C-arm CT PBV study (8-seconds) may result in variable blood-flow weighting to the calculated PBV. In the previous chapter we found that for clinical examinations, the C-arm CT PBV has ≈ 60% CBF and 40% CBV weighting with similar supporting observations for multi-detector CT (Konstas et al., 2009; Sharma et al., 2011). Thus

differences in contrast dynamics can result in differences in blood-flow and blood-volume weighting to PBV, which can translate into differences in final PBV measurements. Assuming identical contrast dynamics or an ideal steady-state in all patients despite the differences in their haemodynamic physiology may overlook the blood-flow weighting to C-arm CT PBV particularly in cases where the TDCs depart significantly from the steady-state, thus potentially resulting in overestimation (or underestimation) of irreversibly infarcted parenchyma when using a specific threshold. This limitation can be overcome by a simple ROI-based time-density-curve (TDC) analysis of the raw C-arm CT projection data for clinical PBV scan that can provide an estimate of how adequately the steady-state contrast concentration was achieved during a particular study (discussed in more detail in chapter 7).

Our results indicate that the measured PBV values in the peri-infarct ischaemic tissue may or may not show reduction depending upon the severity of ischaemic insult. We found that in moderate-to-severely ischaemic peri-infarct tissue (criteria: MR-rCBF < 75%, relative to mean contralateral uninvolved hemisphere CBF), the PBV measurements showed statistically significant reduction compared with the contralateral uninvolved homologues tissue. However, PBV values in the mild-to-moderately ischaemic peri-infarct parenchyma (rCBF 75–95%) were not significantly reduced relative to the contralateral uninvolved homologues tissue. The peri-infarct ischaemic zone we identified for analysis is conceptually similar to the penumbra region seen in the setting of acute ischaemic stroke. These findings are interesting and can be explained by the combined blood-volume and blood-flow

weighting to C-arm CT PBV (discussed in chapter 4), whereby overall PBV values may be maintained in mild-to-moderate ischaemia. CT perfusion literature informs that in the setting of acute ischaemic stroke, the infarcted tissue shows matched decrease in CBV and CBF (Murphy et al., 2006; Powers et al., 1984). However, the ischaemic tissue surrounding the infarct core has only reduced CBF while the CBV may be maintained or elevated secondary to autoregulatory haemodynamics whereby pre-capillary vessels dilate in response to decreased cerebral perfusion pressure (Powers et al., 1984). In the setting of severe or prolonged ischaemia, the autoregulatory mechanisms fail, leading to eventual reduction in CBV. The degree to which the CBF is reduced and whether the CBV is elevated, maintained, or reduced are thus functions of the severity of ischaemic insult. Findings in the previous chapter showed that with combined blood-volume and blood-flow weighting (discussed in chapter 04), C-arm CT PBV behaves as a composite parameter, similar to the interaction term CBV×CBF used by Murphy et al. for CTP (which was shown to be a better predictor for differentiation of infarcted tissue from non-infarcted tissue compared with using CBV or CBF alone) (Murphy et al., 2006). Thus in the irreversibly infarcted tissue, due to an underlying matched decrease in CBV and CBF, we see a definitive reduction in PBV (figure 5.8). In the peri-infarct ischaemic region of reduced CBF, PBV would be maintained when the ischaemic insult is less severe and the autoregulatory mechanisms are intact and thus effective in increasing the regional CBV (figure 5.8a). On the contrary, PBV measurements would be reduced if the ischaemia prolongs or worsens in severity with consequent impaired autoregulation, ineffective in increasing or maintaining the CBV (figure

5.8c). Therefore, C-arm CT PBV measurements would reliably detect moderate to severe ischaemia but can potentially underestimate mild to moderate ischaemia.

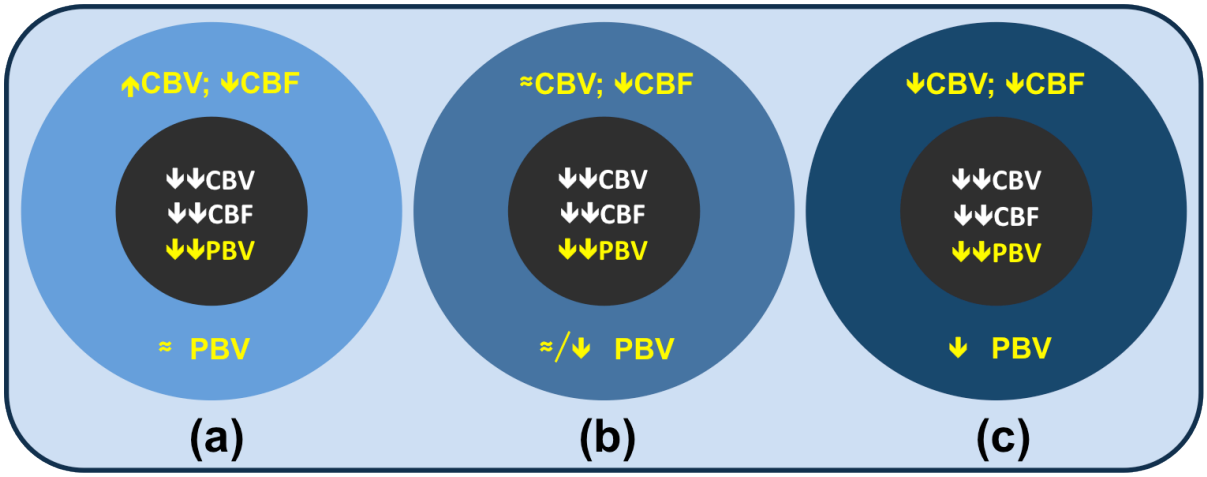


Figure 5.8: A theoretical understanding of C-arm CT PBV at various degrees of ischaemia. In the infarcted tissue (black central zone in a, b, and c), matched decrease in CBV and CBF with consequent reduced PBV is observed given its combined blood-flow and blood-volume weightings. In mild ischaemia (a), CBF is reduced while there is compensatory autoregulatory increase in CBV, consequently PBV values may be maintained. In moderate ischaemia (b), the CBF reduces further and despite autoregulation CBV may not increase, consequently PBV values may be in the lower part of normal range or begin to show mild reduction. In severe ischaemia bordering infarction (c), both CBV and CBF would be decreased with consequent reduction in PBV.

We recognize that C-arm CT PBV imaging cannot replace MR-DWI, which is highly accurate in demarcation of irreversibly infarcted brain parenchyma. However, its availability in the neurointerventional suite is a unique advantage with implications for management of acute cerebrovascular ischaemia. Struffert et al. proposed that the PBV maps may potentially be used to guide the revascularisation procedures through their ability to monitor the brain viability (Struffert et al., 2012). In this regard, a single C-arm CT study can provide both the anatomical and

physiological data for acute stroke patients in the interventional suite without the need to transfer patients to CT or MR facilities. For example, the C-arm CT soft tissue images can reliably exclude intracranial haemorrhage, the angiographic reconstructions can help evaluate proximal vessel occlusion, and the PBV maps provide patient-specific physiological data that can potentially be used, instead of the more generalized and non-specific time-criteria, in selecting appropriate patients for acute stroke interventions particularly when a significant delay exists between initial imaging and patient arrival in angiography suite (Maulaz et al., 2005; Struffert et al., 2012). Similarly, in the aneurysmal SAH patient who develop delayed clinical deterioration, the PBV maps can be used to determine the haemodynamic significance of vessel narrowing detected on catheter angiogram and to identify any ongoing ischaemia or established infarcts thus guiding the angioplasty procedures. For these applications, extended craniocaudal coverage allowing whole-brain PBV measurements would be particularly beneficial e.g. the changes related to vasospasm may be multifocal or global in nature and the acute ischaemic stroke may be in a distribution located outside the traditional supratentorial coverage of CTP, and may thus be better evaluated with extended craniocaudal coverage of C-arm CT PBV.

For CTP and MR-PWI, thresholds of various perfusion parameters have been studied to demarcate the irreversibly infarcted parenchyma and it is widely recognized that the generalizability of any specific threshold may be limited secondary to marked differences across different algorithms and post-processing softwares (Konstas et al., 2009; Kudo et al., 2009). For C-arm CT PBV measurement,

currently only one commercially available application (Syngo Neuro PBV IR; Siemens, Erlangen, Germany) exists. It is conceivable that in future similar other post-processing platforms would become available, in which case the validation of thresholds reported in this study across different platforms would be imperative.

Optimal PBV thresholds reported in this chapter were assessed for whole brain tissue VOIs. However, differences between the grey and white matter exist regarding cellular composition, metabolism, the normal perfusion parameter values, and their neurochemical response to ischaemia (Dohmen et al., 2001; Helenius et al., 2003; Stys et al., 1990). Tissue-specific infarction thresholds may thus be more informative in predicting the tissue outcomes in the setting of cerebrovascular ischaemia (Arakawa et al., 2006). In our cohort, the limited number of patients and DWI lesions precluded such tissue-specific analysis to explore the differential variability of grey and white matter to ischaemia. Future studies including larger number of patients with cerebral ischaemia may help in addressing this issue.

5.6 Conclusion

In conclusion, this chapter reports: (a) the optimal absolute and normalised C-arm CT PBV threshold values for demarcation of the irreversibly infarcted parenchyma in the neurointerventional suite, and (b) the C-arm CT PBV maps reliably detect moderate-to-severe ischaemia but can potentially underestimate mild-to-moderate ischaemia with intact autoregulatory mechanisms, likely related to its combined blood-flow and blood-volume weighting. Optimal C-arm CT PBV thresholds for infarction have not been studied previously and are of value in providing an

objective criterion for demarcation of irreversibly infarcted parenchyma. An accurate assessment of the brain viability thus obtained has implications for management of acute brain ischaemia.

6

Whole Brain C-arm FDCT PBV: Reference Measurements

6.1 Abstract

Background and purpose: Parenchymal blood volume imaging using C-arm FDCT in the neurointerventional suite is a new technique, reference measurements for which have not been reported previously. The purpose of this chapter was to create a catalogue of reference PBV measurements for various anatomical regions encompassing the whole brain, using a three-dimensional (3D) volume of interest (VOI) analysis.

Materials and methods: Thirty C-arm FDCT datasets of 26 patients with aneurysmal SAH, acquired using a biplane angiography system (Axiom-Artis dBA; Siemens Healthcare, Germany) as part of a prospective study comparing C-arm CT PBV with MR-PWI, were analysed. PBV values for various brain regions were calculated with an automated analysis using 58 pre-defined atlas-based 3D-VOIs encompassing the whole brain. VOIs partially or completely overlapping regions of DWI abnormality or MR-CBF asymmetry were excluded from the analysis.

Results: Of the 30 C-arm CT PBV datasets, 14 (54%; 12 patients) had areas of restricted diffusion, majority of which were focal. PBV values for cerebral cortex and cerebral white matter were 4.01 ± 0.47 (mean ± standard deviation) and 3.01 ± 0.39 ml/100ml. Lobar PBV values were: frontal lobe 4.2 ± 0.8, temporal lobe 4.2 ± 0.9, parietal lobe 3.9 ± 0.7, and occipital lobe 4.3 ± 0.8 ml/100ml. Basal ganglia and brainstem PBV values were 3.4 ± 0.7 and 4.6 ± 0.6 ml/100ml respectively.

Conclusion: Compared with the typical reference CBV values reported in literature for Positron Emission Tomography, the gold standard for perfusion imaging, the PBV values were relatively high for the white matter and relatively low for the cortical grey matter. These differences could be secondary to the composite nature of PBV or alternatively be related to the method of differentiation between the grey matter and the white matter. The reported catalogue of PBV values for various brain regions would be useful to inform the future studies and could be used in clinical practice when interpreting PBV maps.

6.2 Introduction

Developments in flat detector technology and new reconstruction algorithms allow the currently used C-arm systems to generate CT-like soft tissue images of brain parenchyma in the neurointerventional suite (Kalender and Kyriakou, 2007; Struffert et al., 2009). Additionally, using intravenous iodinated contrast and a specially designed C-arm flat detector computed tomography (C-arm FDCT or C-arm CT) protocol, it is possible to estimate parenchymal blood volume (PBV), a perfusion parameter of haemodynamic significance (Zellerhoff et al., 2009). With its availability to provide reliable anatomical and physiological information in the interventional suite, the technique has potential role in the management of patients with ischaemic cerebrovascular disease (Mordasini et al., 2012; Struffert et al., 2012).

The C-arm CT PBV imaging is relatively new and no reference PBV measurements for various brain regions are available. Initial reports compared C-arm CT PBV with CTP-derived measurements of cerebral blood volume (CBV), in both canines and humans (Ahmed et al., 2009; Bley et al., 2010; Struffert et al., 2012, 2011). The principle for measurement of CBV with a dynamic perfusion imaging modality such as CTP and the principle for measurement of PBV with C-arm CT are not identical. For dynamic perfusion imaging, area under the time-density-curve (AUC) provides a measure of CBV; whereas for C-arm FDCT a subtraction-normalisation analysis is performed to calculate PBV (Konstas et al., 2009; Zellerhoff et al., 2009). In this regard, the assumption that intravenously administered contrast material reaches a steady-state concentration in cerebral vasculature ($C_{arteries} = C_{tissue} = C_{veins}$) is used to infer an

equivalence of C-arm CT PBV to the CBV derived from a dynamic perfusion imaging modality. In our experience, the ideal steady-state assumption is rarely met (discussed in more detail in chapter 7) and the C-arm CT PBV has both blood-flow and blood-volume weightings (discussed in chapter 4) – supporting observations exist for multi-detector CT where the CTA source images (CTA-SI) could be used to calculate MDCT PBV (Sharma et al., 2011). Keeping in view the composite nature of C-arm CT PBV parameter with combined blood-flow and blood-volume weighting, the typical reference measurements for CBV reported for dynamic perfusion imaging modalities cannot be used. Reference measurements specific to C-arm CT PBV have not been studied previously. The limited number of initial studies on C-arm CT PBV compared it with CTP CBV only, using a relatively few two-dimensional (2D) regions of interest (ROIs) (Ahmed et al., 2009; Bley et al., 2010; Struffert et al., 2011). These ROIs were manually drawn, fewer in number, and were placed on a limited number of slices corresponding to CT perfusion (CTP) images. One of the major advantage of C-arm CT PBV, however, is its extended craniocaudal coverage with a field of view (FOV) encompassing the whole brain in a single sweep, which along with isotropic voxels allows omniplane reconstructions of whole brain PBV volumes, thereby maximizing the utility of whole brain PBV data (Kamran et al., 2010). Hence, estimating PBV values of various brain regions, most of which are located outside the traditional CTP slices, would be useful to inform the future studies and these values could also be used as a reference when interpreting PBV maps in a clinical setting.

This chapter aimed to create a catalogue of reference PBV measurements for various anatomical regions encompassing the whole brain, using a three-dimensional volume of interest (3D VOI) analysis.

6.3 Materials and Methods

Thirty C-arm FDCT scans of 26 patients were retrospectively analysed. The clinical and imaging data was acquired as part of a prospective study comparing C-arm CT PBV with MR-PWI, approved by local research ethics committee. The study included adult patients aged over 18 years with documented aneurysmal subarachnoid haemorrhage (SAH) who subsequently developed symptoms and signs suggesting delayed cerebral ischaemia (DCI), requiring confirmatory imaging. At our institution, SAH is diagnosed using non-contrast CT (NCCT) head or cerebrospinal fluid (CSF) sampling by lumbar puncture when initial NCCT head is negative but clinical suspicion of SAH remains high, and is graded as described by Fisher et al. (Fisher et al., 1980). The diagnosis of DCI was based on clinical assessment by the multidisciplinary neuro-intensive care unit (neuro-ICU) team and was defined as clinical deterioration (focal neurological deficits or reduced level of consciousness) lasting 2 hours or longer with no evidence of rebleed or hydrocephalus on NCCT head, and no other medical causes such as infections or metabolic disturbances.

Exclusion criteria were: a history of allergy to iodinated contrast material, renal impairment, pregnancy, or contraindications to MR examination. All recruited patients had undergone aneurysm repair by endovascular coil embolisation. Written informed consents were obtained from patients or, if they were unable to complete the consent

process, from a family member or a designated surrogate as defined by the research ethics committee approval for the study. All recruited patients underwent an MRI examination using a protocol that included standard sequences (including perfusion- and diffusion-weighted sequences) concurrent with the research C-arm CT scan using PBV protocol. We recorded the patients' age and gender, clinical status on admission (world federation of neurosurgical societies (WFNS) score), amount of blood on the admission scan (Fisher grade), location of the aneurysm, and the treatment details. The imaging protocols and post-processing steps for the two imaging studies are described in the following sections. Additional subsequent imaging was performed as clinically indicated.

6.3.1 C-arm FDCT Imaging

C-arm FDCT scans were performed on a flat detector equipped biplane angiography system (Axiom Artis dBA; Siemens Healthcare, Germany) in the neuro-interventional suite. The imaging protocol included two rotational acquisitions: mask and contrast-enhanced runs. Projection data for each run was acquired using the following parameters: 419 projection images, 0.5^0 frame angle, 210^0 angular scan range, 8 seconds acquisition time, 0.36 μGy radiation dose per frame. The contrast-enhanced dataset was acquired following a manually triggered intravenous injection of radiographic contrast material, Niopam 370 (Bracco spa, Milan, Italy), using a power injector (Medrad, Inc. Philadelphia). The injection parameters were: contrast concentration 370 mg, Iodine/ml; volume, 80ml; injection rate, 4 ml/sec administered through the antecubital vein; injection pressure, 300 pounds per square inch (psi); and

injection duration, 20 seconds. Passage of contrast material through the cerebral vasculature was monitored on 2D fluoroscopic images (2 frames/sec) and the contrast-enhanced run was triggered when maximal opacification of the superior sagittal sinus was observed.

Post-processing of the data to generate color-coded PBV maps was performed on a dedicated research workstation (Leonardo, Siemens AG, Healthcare) using prototype software. The steps involved were: (1) co-registration of the two volumes, the mask and the contrast-enhanced, (2) subtraction of the mask volume from the contrast-enhanced volume, (3) normalisation of the subtracted data with an input function automatically estimated from the histogram analysis of vascular tree, (4) color-coding with a standard colour look-up table to generate the PBV colour-coded maps for visualization and interpretation (a detailed discussion of these post-processing steps is included in chapter 03). In the clinical setting, the final PBV values are expressed in units of ml/1000 ml of cerebral tissue. PBV values for VOI analysis were converted to units of ml/100 ml to facilitate comparison with historical Positron Emission Tomography (PET) derived CBV values. For visualization of the vessels, the contrast-enhanced dataset was reconstructed separately on a commercially available dedicated workstation (Leonardo, Siemens AG, Healthcare). VRT (volumetric rendering technique) and MIP (maximum intensity projection) reconstructions were used to evaluate the cerebral vasculature. CT-like soft tissue reconstructions were obtained in all cases.

6.3.2 MR Imaging

A standard MR scan protocol comprising sagittal T1-weighted, axial T1-weighted, axial T2-weighted, diffusion-weighted, perfusion-weighted, and time-of-flight (TOF) angiography sequences was performed on Philips Achieva 1.5 Tesla MRI unit. The parameters used for perfusion- and diffusion-weighted sequences are described below (complete sequence details and the parameters used for each sequence have been discussed in chapter 04).

1. Diffusion-weighted: Repetition time (TR) 2897ms, time-to-echo (TE) 73ms, FOV 174×249mm, reconstruction matrix 144×144, slices 25, slice thickness 5mm, voxel size 1.74×1.73×5mm, b-values 0 and 1000, EPI factor 51, sequence duration 34sec.

2. Perfusion weighted: Perfusion data was acquired using the dynamic susceptibility contrast (DSC) technique with the following parameters: T2*-weighted gradient echo echoplanar sequence, TR 2000ms, TE 44ms, FOV 248×248 mm, reconstruction matrix 256×256, voxel size 0.98×0.98×4mm, SENSE factor 2.1, bandwidth 806 Hz/pixel, scan duration 1min 46sec. Paramagnetic contrast material was administered intravenously with an MR-compatible power injector (Medrad Inc.) at 5 ml/sec followed by 10ml saline flush. Fifteen slices covering the whole brain were acquired at 50 time points following the injection of 0.2 mmol/kg of Gadopentate (Prohance, Bracco Diagnostics Inc., Italy)

Post-processing of the perfusion data was performed using commercially available software (nordicICE perfusion package, NordicNeuroLab, Bergen, Norway). After motion correction of the raw data, perfusion maps were created using the

standard singular value doconvolution (SVD) technique. Arterial input function (AIF) to deconvolve the dynamic tissue response curve was automatically determined and SVD regularization was achieved with the truncated SVD approach (cut-off fraction 0.20) and iterative thresholding (target oscillation index 0.10). Semi-quantitative leakage-corrected output perfusion maps for clinical interpretation included: cerebral blood flow (CBF), cerebral blood volume (CBV), mean transit time (MTT), and time to peak (TTP).

6.3.3 Further Post-processing and Quantitative VOI Analysis

Quantitative analysis of the volumetric C-arm CT PBV data was performed using the FMRIB's software library (FSL) tools (Jenkinson et al., 2012). The PBV volumes for each subject were registered to the average standard template T1-weighted brain volume aligned in the MNI152 space using FMRIB linear image registration tool (FLIRT) (Jenkinson et al., 2002). Brain extraction tool (BET) utility was then used to delete the non-brain tissue from the images of interest (Smith, 2002). Histogram analysis of the PBV volumes was performed for each dataset and based on this analysis, the voxels representing large vascular structures were segmented out (figure 6.1). Binarized predefined cortical and subcortical 3D-VOIs encompassing the whole brain, as defined in the Harvard-Oxford structural brain atlas, were applied to the C-arm CT PBV maps for each patient using the FSL-maths utility. The 56 VOIs for each hemisphere, which were used in the analysis, are depicted in figure 6.2 and 6.3. MR-DWI and apparent diffusion coefficient (ADC) maps were used to identify any areas of signal abnormality, which could represent infarcted tissue (figure 6.4). In addition, based on the review of

MR-PWI maps, areas of asymmetric CBF (>10% asymmetry) were delineated. VOIs that partially or completely overlapped regions of DWI or CBF abnormality were excluded from the analysis along with the corresponding VOIs in the contralateral hemisphere. Mean, median, and standard deviation (SD) values of PBV were extracted for all VOIs (excluding the ones overlapping with areas of MR-DWI and CBF abnormality) encompassing both hemispheres using the FSL-stats software. PBV measurements for each anatomical region (VOI) in two hemispheres were averaged. The same analysis steps were repeated for all C-arm CT PBV datasets (n = 30). Across-subjects PBV mean and SD values were then calculated. A schematic overview of the image post-processing and analysis is presented in figure 6.1.

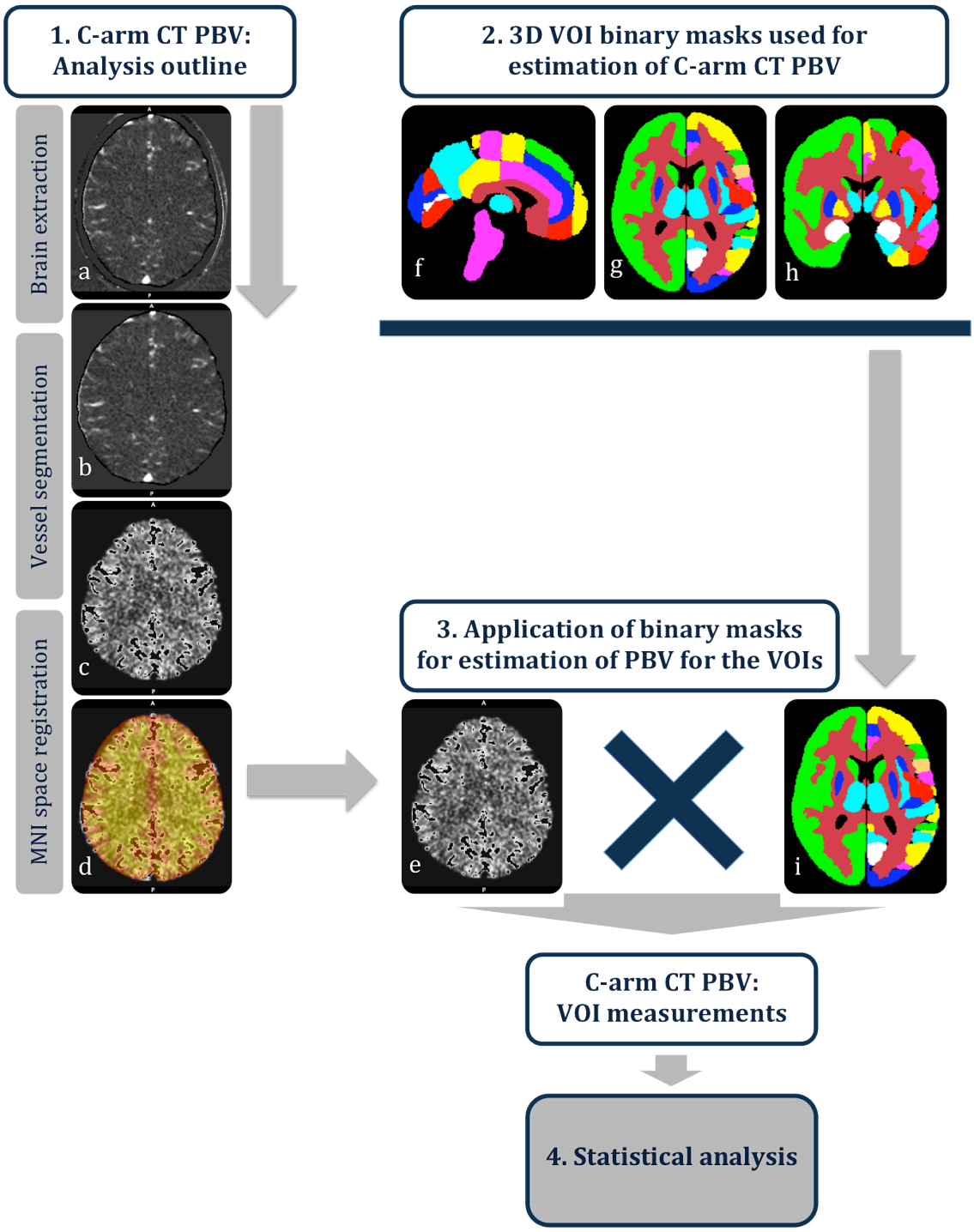


Figure 6.1: A schematic overview of the image post-processing and analysis.

1. A C-arm CT PBV dataset before brain extraction (a); PBV dataset following brain-extraction using FSL BET utility (b); PBV dataset following threshold-based segmentation of the vascular

structures (c); registration of the PBV volume to the average standard template T1-weighted brain volume in MNI152 space (d); brain-extracted, co-registered, vessel-segmented PBV volume in MNI152 space (e).

2. Binarised masks of the 3D-VOIs corresponding to the cortical and subcortical structures encompassing the whole brain (f, g, and h).

3. The binarised VOI masks (i) were subsequently applied to the post-processed C-arm CT PBV maps (e) to obtain PBV measurements for the 3D-VOIs, which were then used in the statistical analysis described in section 6.2.4.

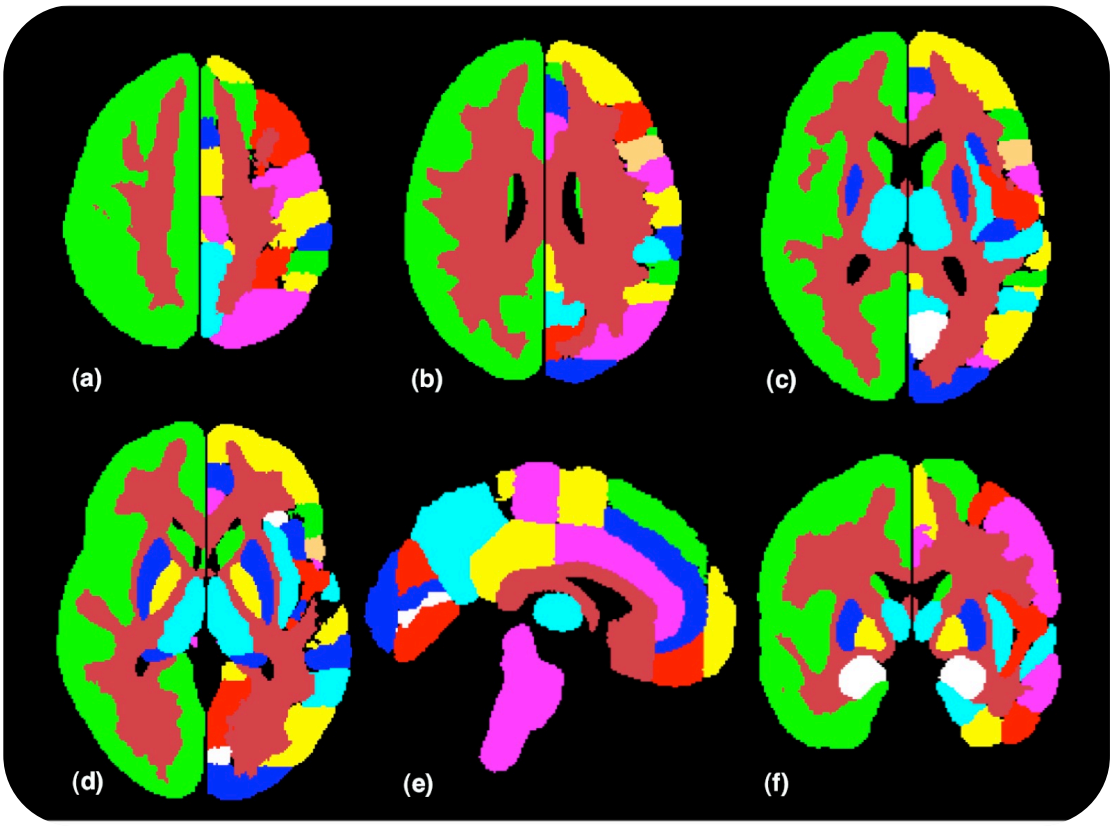


Figure 6.2: Harvard-Oxford brain atlas-based volumes of interest (VOIs).

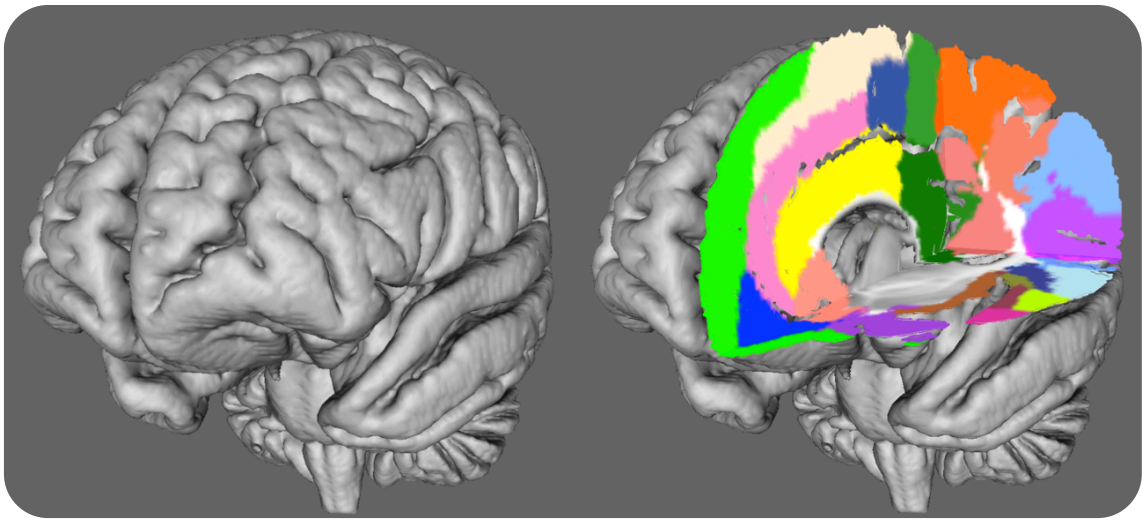


Figure 6.3: A volume rendered three-dimensional depiction of VOIs on surface shaded brain volume.

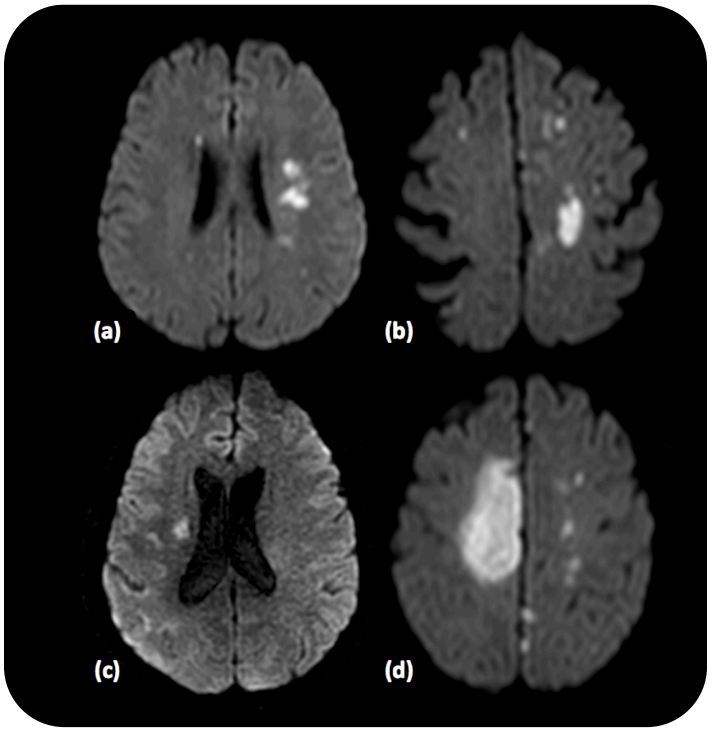


Figure 6.4: Representative DWI images of patients showing areas of restricted diffusion. VOIs that overlapped such areas of signal abnormality on either the DWI or ADC images were excluded from analysis.

6.4 Results

A total of 30 C-arm CT PBV datasets for 26 patients (mean age 55 years; men 9, women 17) enrolled in the study were reviewed. The patients' SAH on admission NCCT were graded: Grade-4 in 16 (61%), Grade-3 in 9 (35%), while one patient's NCCT head did not show evidence of SAH which was proven after lumbar puncture (4%). The ruptured aneurysms treated by coil embolisation were: <5mm in 5 (20%), 5-10mm in 17 (65%), and 10-15mm in 4 (15%). Locations were: anterior cerebral artery, 4 (15%); peri-callosal artery, 1 (4%); anterior communicating artery, 7 (27%); middle cerebral artery, 2 (8%); posterior communicating artery, 10 (38%); basilar artery, 1 (4%); and internal carotid artery, 1 (4%). Patients' WFNS grades at the time of admission to hospital were: Grade-1 in 16 (61%), Grade-2 in 7 (27%), Grade-3 in 2 (8%), and Grade-4 in 1 patient (4%).

The patient characteristics are summarized in table 6.1. Of the 26 patients, 14 patients had areas of restricted-diffusion, majority of which were focal and cortical; the details of the DWI lesions are described in table 6.1. Figure 6.4 shows example DWI lesions in representative cases. During the VOI analysis, the atlas-based predefined VOIs that overlapped with the areas of restricted diffusion or areas of asymmetric MR-CBF (>10% asymmetry) were eliminated from the analysis.

The results of VOI analysis are summarized in tables 6.2a and 6.2b and figures 6.5a and 6.5b. Mean PBV for cerebral cortex was 4.01 ± 0.47 ml/100ml (mean ± standard deviation) and cerebral white matter 3.01 ± 0.39 ml/100ml. Mean lobar PBV values were: frontal lobe, 4.2 ± 0.8 ml/100ml; temporal lobe, 4.2 ± 0.9 ml/100ml;

parietal lobe, 3.9 ± 0.7 ml/100ml; and occipital lobe, 4.3 ± 0.8 ml/100ml. Basal ganglia and brainstem mean PBV values were 3.4 ± 0.7 ml/100ml and 4.6 ± 0.6 ml/100ml respectively.

Table 6.1 Demographic, aneurysm, and clinical characteristics of the patients and the details of DWI lesions

Patient number	Age (years)	Gender (M/F)	Aneurysm location	Aneurysm size (mm)	WFNS grade	Fischer grade	DWI deficits	DWI deficits distribution	VOIs excluded
1	47	M	Anterior communicating artery	6 × 4	1	3	+	Right frontal operculum; right centrum semiovale	+
2	55	F	Left anterior cerebral artery	12 × 10	3	4	−	–	–
3	61	F	Right posterior communicating artery	8 × 5	2	3	−	–	–
4	49	F	Anterior communicating artery	10 × 7	1	3	−	–	–
5	68	F	Right posterior communicating artery	10 × 6	2	4	−	–	–
6	71	F	Anterior communicating artery	6 × 5	1	4	+	Right frontal and left posterior frontal lobes	+
7	46	M	Right middle cerebral artery	4 × 3	3	3	+	Bi-frontal and posterior left parietal lobes	+
8	77	F	Left anterior cerebral artery	6 × 4	1	4	−	–	–
9	46	M	Right posterior communicating artery	4 × 4	1	4	−	–	–
10	50	F	Right internal carotid artery	3 × 3	1	3	+	Right frontal lobe	+
11	53	F	Basilar artery tip	7 × 6	2	3	+	Left frontal lobe	+
12	55	M	Right posterior communicating artery	5 × 3	2	4	−	–	+
13	55	F	Left posterior communicating artery	4 × 4	2	4	−	–	–
14	69	F	Left anterior cerebral artery	11 × 7	1	4	+	Bi-frontal lobes	+
15	66	M	Anterior communicating artery	7 × 5	1	0*	−	–	–
16	45	M	Anterior communicating artery	15 × 8	2	4	+	Right parietal lobe and corpus striatum	+
17	66	M	Right middle cerebral artery	8 × 3	4	4	+	Right parietal lobe and sylvian fissure	+
18	30	M	Anterior communicating artery	7 × 4	1	3	+	Left frontal lobe	+
19	39	F	Right posterior communicating artery	5 × 3.5	1	4	+	Right parietal lobe	+
20	50	F	Anterior communicating artery	4 × 3.5	1	4	−	–	–
21	69	M	Right posterior communicating artery	7 × 4	1	4	−	–	–
22	39	F	Right posterior communicating artery	10 × 9	1	4	+	Right frontal lobe	–
23	52	F	Right posterior communicating artery	5 × 5	1	4	+	–	–
24	54	F	Left posterior communicating artery	8 × 5	1	3	+	Anterior sylvian fissure	+
25	58	F	Right anterior cerebral artery	5 × 4	1	3	+	Right frontal lobe	+
26	60	F	Left peri-callosal artery	12 × 8	2	4	−	–	–

* NCCT head was negative for SAH, which was later confirmed on lumbar puncture

6.2a C-arm CT PBV measurements (ml/100ml) for the atlas-based predefined VOIs (1-35)

Number	Volume of Interest	Mean	SD	Median	SEM	25th Percentile	75th Percentile
1	*Cerebral White matter*	3.01	0.39	3.08	0.05	2.84	3.25
2	*Cerebral Cortex*	4.01	0.47	4.04	0.06	3.71	4.35
3	Frontal Pole	3.51	0.55	3.46	0.07	3.03	3.95
4	Insular Cortex	4.34	0.77	4.28	0.10	3.83	4.76
5	Superior Frontal Gyrus	3.92	0.60	3.92	0.08	3.46	4.36
6	Middle Frontal Gyrus	3.45	0.73	3.55	0.09	2.77	3.96
7	Inferior Frontal Gyrus, pars triangularis	3.92	0.99	3.68	0.13	3.21	4.39
8	Inferior Frontal Gyrus, pars opercularis	4.21	0.85	4.13	0.11	3.69	4.87
9	Precentral Gyrus	3.81	0.54	3.81	0.07	3.46	4.20
10	Frontal Medial Cortex	4.50	1.08	4.54	0.14	3.72	5.35
11	Supplementary Motor Cortex	4.44	0.84	4.63	0.11	3.63	5.10
12	Subcallosal Cortex	4.31	0.99	4.33	0.13	3.74	5.18
13	Paracingulate Gyrus	4.49	0.81	4.43	0.10	4.12	5.09
14	Cingulate Gyrus, anterior division	4.42	0.88	4.40	0.11	3.96	4.92
15	Cingulate Gyrus, posterior division	4.56	0.69	4.58	0.09	4.15	5.00
16	Frontal Orbital Cortex	4.44	0.76	4.51	0.10	4.01	5.01
17	Frontal Operculum Cortex	4.55	0.87	4.57	0.11	3.93	5.16
18	Central Opercular Cortex	4.58	0.80	4.64	0.10	3.89	5.17
19	Temporal Pole	4.22	0.70	4.11	0.09	3.70	4.80
20	Superior Temporal Gyrus, anterior division	3.95	0.85	3.69	0.11	3.39	4.52
21	Superior Temporal Gyrus, posterior division	3.77	0.82	3.68	0.10	3.23	4.16
22	Middle Temporal Gyrus, anterior division	3.86	0.75	3.98	0.10	3.42	4.39
23	Middle Temporal Gyrus, posterior division	3.83	0.75	3.95	0.10	3.25	4.33
24	Middle Temporal Gyrus, temporooccipital part	3.62	0.69	3.66	0.09	3.25	4.03
25	Inferior Temporal Gyrus, anterior division	3.19	1.20	3.20	0.15	2.45	4.16
26	Inferior Temporal Gyrus, posterior division	3.65	0.71	3.66	0.09	3.15	4.29
27	Inferior Temporal Gyrus, temporooccipital part	3.88	0.71	3.87	0.09	3.53	4.38
28	Parahippocampal Gyrus, anterior division	4.55	0.95	4.54	0.12	3.92	5.11
29	Parahippocampal Gyrus, posterior division	4.98	0.85	5.08	0.11	4.51	5.53
30	Temporal Fusiform Cortex, anterior division	3.34	1.34	3.34	0.17	2.87	4.31
31	Temporal Fusiform Cortex, posterior division	4.14	0.76	4.19	0.10	3.56	4.68
32	Temporal Occipital Fusiform Cortex	4.80	0.82	4.87	0.11	4.40	5.39
33	Planum Polare	5.23	1.07	5.32	0.14	4.63	5.88
34	Heschl's Gyrus (includes H1 and H2)	5.30	0.98	5.28	0.12	4.77	6.05
35	Planum Temporale	4.41	0.92	4.41	0.12	3.73	5.08

Table 6.2b C-arm CT PBV measurements (ml/100ml) for the atlas-based predefined VOIs (36-58)

Number	Volume of Interest	Mean	SD	Median	SEM	25th Percentile	75th Percentile
36	Postcentral Gyrus	3.78	0.68	3.82	0.09	3.19	4.31
37	Superior Parietal Lobule	3.88	0.79	3.85	0.10	3.31	4.47
38	Supramarginal Gyrus, anterior division	3.68	0.83	3.58	0.11	3.16	4.18
39	Supramarginal Gyrus, posterior division	3.65	0.58	3.75	0.07	3.26	4.01
40	Angular Gyrus	3.61	0.65	3.62	0.08	3.16	3.98
41	Precuneous Cortex	4.50	0.68	4.56	0.09	4.18	4.96
42	Parietal Operculum Cortex	4.24	0.70	4.17	0.09	3.86	4.72
43	Lateral Occipital Cortex, superior division	3.51	0.67	3.49	0.09	3.08	3.95
44	Lateral Occipital Cortex, inferior division	3.53	0.68	3.54	0.09	3.12	3.89
45	Intracalcarine Cortex	4.69	0.79	4.76	0.10	4.18	5.20
46	Cuneal Cortex	4.51	0.79	4.59	0.10	3.84	5.12
47	Lingual Gyrus	5.11	0.74	5.19	0.09	4.44	5.61
48	Occipital Fusiform Gyrus	5.05	1.03	5.10	0.13	4.28	5.66
49	Supracalcarine Cortex	4.56	1.01	4.62	0.13	3.87	5.28
50	Occipital Pole	3.44	0.62	3.38	0.08	3.01	3.85
51	Caudate	3.14	0.90	3.33	0.11	2.54	3.87
52	Putamen	3.90	0.63	4.04	0.08	3.54	4.37
53	Pallidum	3.30	0.64	3.38	0.08	2.97	3.56
54	Thalamus	4.53	0.61	4.62	0.08	4.20	4.96
55	Hippocampus	4.96	0.82	5.16	0.10	4.46	5.58
56	Amygdala	4.56	0.84	4.68	0.11	3.99	5.01
57	Accumbens	3.56	0.85	3.62	0.11	3.08	4.20
58	Brain-Stem	4.64	0.59	4.61	0.08	4.30	4.97

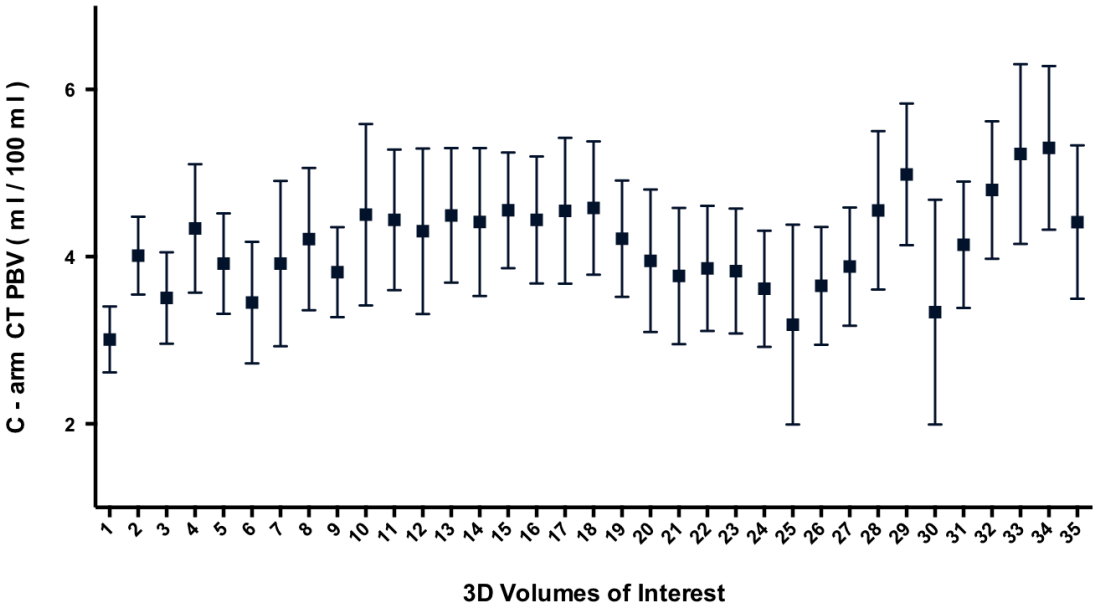


Figure 6.5a: C-arm CT PBV values (mean and standard deviation) for the VOIs 1-35

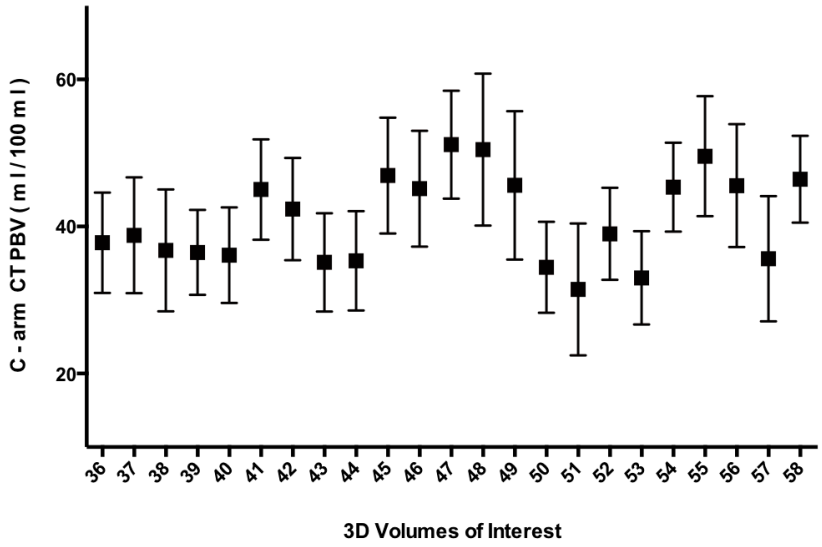


Figure 6.5b: C-arm CT PBV values (mean and standard deviation) for the VOIs 36-58

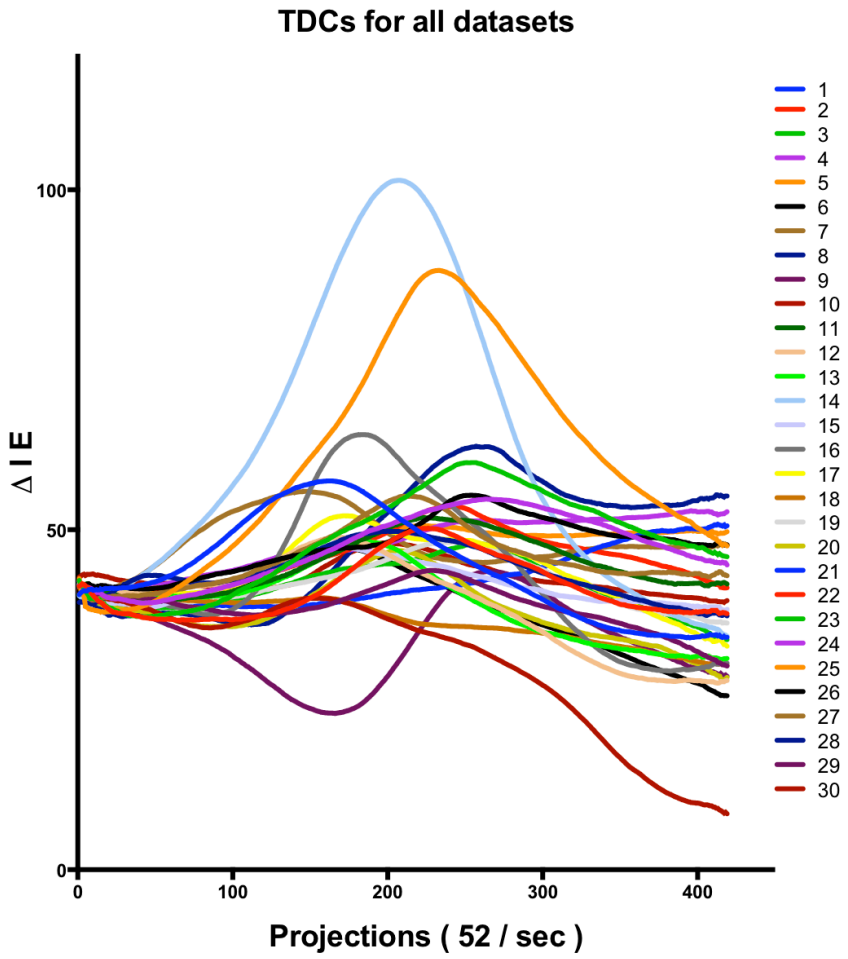


Figure 6.6: TDCs for C-arm FDCT datasets. Locally weighted scatterplot smoothed (LOWESS) time-density-curves (TDCs) for the C-arm FDCT datasets (n = 30) extracted from the C-arm FDCT rotational projection data demonstrating the differences in contrast kinetics in the cerebral vasculature of different patients.

6.5 Discussion

This chapter provides a catalogue of reference C-arm CT PBV measurements for various brain regions using atlas-based anatomical 3D-VOIs encompassing the whole brain. No such measurements have previously been reported for C-arm CT PBV.

To our knowledge, all studies investigating the accuracy of C-arm CT PBV have used CTP CBV as a reference standard for comparison (Ahmed et al., 2009; Bley et al., 2010; Struffert et al., 2012, 2011). The principle for measurement of CBV with a dynamic perfusion imaging modality such as CTP and the principle for measurement of PBV with C-arm FDCT are not identical. With dynamic perfusion imaging, area under the time-density-curve (TDC) provides a measure of CBV whereas with C-arm CT a steady-state contrast concentration in cerebral vasculature following a prolonged intravenous contrast injection along with a subtraction-normalisation analysis is used to calculate PBV (Konstas et al., 2009; Zellerhoff et al., 2009). In this regard, the assumption that intravenously administered contrast material reaches a steady-state concentration in cerebral vasculature ($C_{arteries} = C_{tissue} = C_{veins}$) is used to infer an equivalence of C-arm CT PBV to the CBV derived from dynamic perfusion imaging. In our experience, the ideal steady-state assumption is not fully met (chapter 07) and the C-arm CT PBV has both blood-flow and blood-volume weighting (chapter 04). This is illustrated in figure 6.6 by the smoothed TDCs derived from the rotational 2D projections acquired as part of C-arm FDCT protocol, and is discussed in more detail in the following chapter. Consequently, strictly speaking, the CBV derived from dynamic perfusion imaging and the C-arm CT PBV parameters are not identical. Hence, the

typical reference measurements of CBV reported for dynamic perfusion imaging modalities cannot be used for C-arm CT PBV. Moreover, given the recent introduction of C-arm CT PBV imaging for clinical use, the PBV measurements for various brain regions have not been systematically studied so far. A comprehensive set of PBV values for various brain regions were thus determined using a robust quantitative analysis approach. These values are expected to inform the future studies and could serve as a reference when interpreting PBV maps in clinical practice.

In order to minimise the effect of large cerebral vessels on PBV calculation, we excluded all vascular pixels by defining a certain threshold. It was difficult to determine a consistent threshold value that would hold true across all datasets due to inter-subject differences in cerebrovascular contrast dynamics. Therefore, for each dataset, the extent of vascular area was visually assessed at varying levels of threshold along with histogram analysis to choose the best value. This approach reduces the likelihood of under or over-segmentation of vascular structures, which could result in over- or under-estimation of the PBV, respectively. In reporting the whole brain C-arm CT PBV measurements, we adopted an automated quantitative analysis approach using predefined atlas-based cortical and subcortical 3D-VOIs encompassing the whole brain. This is in contrast to the few previous comparison studies on C-arm CT PBV all of which used a limited number of manually drawn 2D-ROIs on fewer slices. The comprehensive set of VOIs (56 VOIs for each hemisphere) we used included all cortical and subcortical structures as listed in table 6.1. This approach makes our measurements objective and minimises any observer bias that may be introduced if manually drawn (operator

dependent) ROIs were used.

In comparison with the CBV values reported for Positron Emission Tomography (PET), the gold standard for perfusion imaging, our C-arm CT PBV measurements were relatively high for the white matter and relatively low for the cortical grey matter. For example, PET-based mean cortical CBV was 4.8 ml/100ml in the study by Hatazawa et al., 4.3 ml/100ml in the study by Yamaguchi et al., and 4.7 ml/100ml in the study by Leenders et al.; whereas the mean C-arm CT PBV in this study was 4.0 ml/100ml (SD 0.47 ml/100ml) (Hatazawa et al., 1995; Leenders et al., 1990; Yamaguchi et al., 1986). PET-based white matter CBV have been reported 2.4 ml/100ml by Hatazawa et al. and 2.7 ml/100ml by Leenders et al. whereas the mean C-arm CT PBV in our study was 3 ml/100ml (SD 0.39 ml/100ml) (Hatazawa et al., 1995; Leenders et al., 1990). These differences, although not large as indicated by the overlap of 2SD (standard deviation) intervals, are likely related to the fact that PBV and CBV are different parameters, which are calculated using different principles as described above. While PBV may have a preferential blood-volume weighting, it is not identical to CBV, therefore a perfect correspondence between C-arm CT PBV and the PET-based CBV values was not expected. Relatively high white matter and relatively low cortical PBV measurements could partly be attributed to the method of differentiation between grey and white matter. The C-arm CT datasets were registered to the T1-weighted average structural template brain volume in standard MNI152 space before application of pre-defined atlas based 3D-VOIs. During the registration, certain parts of cortical grey matter could be misregistered as white matter and this may result in relatively higher white matter

PBV values. The underestimation of grey matter PBV may similarly occur if pixels of higher PBV values than the average grey matter PBV are misregistered as the white matter (particularly at the grey-white matter junction) and consequently excluded from the calculation of grey matter PBV. Precise differentiation of grey matter from the white matter using the C-arm FDCT images alone is difficult due to relatively poor low-contrast resolution of the technique (~10 Hounsfield units).

Limited number of subjects is a major drawback for the analysis discussed in this chapter, which aimed to establish the reference PBV measurements that ought to be generalizable. The study population did not include healthy normal subjects – instead the recruited individuals were patients with aneurysmal-SAH, many of whom had areas of asymmetric perfusion and some had areas of restricted diffusion on DWI images representing infarcts. We tried to overcome this limitation by excluding any VOIs corresponding to the regions of asymmetric perfusion or DWI abnormality from both hemispheres. Only the PBV values for the remainder of VOIs were used in the analysis. Additionally the PBV measurements were averaged across subjects for each VOI, an approach that can minimise the effect of outlier values. While the reported measurements may not be truly representative of PBV values in a normal population, they are the best approximation given the ethical and logistical constraints in performing such measurements on healthy normal individuals using a technique that involves exposure to both ionising radiation and iodinated contrast material.

6.6 Conclusion

In conclusion, this chapter reports the reference measurements of C-arm CT PBV, a composite perfusion parameter, for various brain regions encompassing the whole brain using a robust quantitative volumetric analysis. Areas with restricted diffusion or asymmetric perfusion were excluded from the analysis. While the PBV values reported in this chapter may not be truly representative of PBV values in a normal population, they represent the best approximation given the ethical and logistical constraints to performing such measurements in healthy normal individuals due to the contrast and radiation exposures involved. No such reference values for the C-arm CT PBV have been reported previously; the catalogue of reference PBV values we present is expected to inform the future studies and would be of value in clinical practice when interpreting PBV maps.

7

Time Density Curve Analysis of C-arm FDCT PBV Imaging

7.1 Abstract

Background and purpose: Estimation of parenchymal blood volume (PBV) using C-arm flat detector computed tomography (C-arm FDCT or C-arm CT) in the neurointerventional suite assumes a steady-state contrast concentration in cerebral vasculature for the scan duration. Using time-density-curve (TDC) analysis, we explored if the steady-state assumption is met for C-arm CT PBV scans, and how consistent are the contrast material dynamics in cerebral vasculature across patients.

Materials and methods: Thirty C-arm FDCT datasets of 26 patients with aneurysmal SAH, acquired using a biplane angiography system (Axiom-Artis dBA; Siemens Healthcare, Germany) as part of a prospective study comparing C-arm CT PBV with MR-PWI, were analysed. TDCs were extracted from the two-dimensional rotational projections. Nonlinear regression analysis was performed to estimate the *goodness-of-fit* of TDCs to a steady-state horizontal-line-model. Statistical similarity among the individual TDCs was tested using non-parametric Kruskal-Wallis test and Dunn's multiple comparisons test; p-values adjusted for multiple comparisons were computed. A subgroup analysis was subsequently performed to investigate the influence of differences in TDC characteristics on the resulting PBV measurements and their agreement with MR-CBV.

Results: Despite identical scan parameters and contrast injection protocol, the individual TDCs were statistically non-identical ($p < 0.0001$). Using Dunn's multiple comparisons test, of the total 435 individual comparisons among the 30 TDCs, 330 comparisons (62%) reached statistical significance for difference (adjusted p-value

<0.0001). All TDCs deviated significantly (p<0.0001) from the steady state horizontal line model. PBV values of those datasets for which the TDCs showed largest deviations from the steady–state model demonstrated poor agreement and correlation with MR-CBV, compared with the PBV values of those datasets for which the TDCs were closer to steady–state.

Conclusion: How well the steady state assumption is met during a C-arm CT PBV scan determines preferential blood-volume or blood-flow weighting to PBV; at respective extremes these weightings represent different perfusion parameters, abnormal measurements of which denote different types of underlying tissue injury with unique prognostic significance. While interpreting the C-arm FDCT PBV maps, this distinction has important implications for patient management.

7.2 Introduction

C-arm imaging systems have traditionally been used for high-contrast vessel imaging in the interventional suite (Kamran et al., 2010). However, with the introduction of flat detector technology, novel reconstruction algorithms, and implementation of specially designed protocols, these systems are now capable of generating whole brain parenchymal blood volume (PBV) maps in addition to providing cross-sectional soft tissues images of brain parenchyma (Zellerhoff et al., 2009). Initial reports have compared C-arm flat detector computed tomography (C-arm FDCT or C-arm CT) PBV measurements with CT perfusion (CTP) derived cerebral blood volume (CBV) in both canines and humans (Ahmed et al., 2009; Bley et al., 2010; Struffert et al., 2011, 2010).

For the calculation of C-arm CT PBV, the intravenously administered iodinated contrast material is assumed to have reached a *steady-state concentration* in the cerebral vasculature (contrast concentration in arteries = contrast concentration in veins), which is maintained for the duration of scan (Zellerhoff et al., 2009). Based on this assumption, the C-arm CT PBV is inferred to be equivalent to the CBV derived from dynamic perfusion imaging modalities such as CTP or MR perfusion-weighted imaging (MR-PWI). However, to what extent the *steady-state assumption* is met for the clinical C-arm CT PBV scans has not been studied. The limited number of published reports on C-arm CT PBV have used CTP-derived CBV as a reference standard for quantitative comparisons; and none of these studies explored the relationship of C-arm CT PBV to cerebral blood flow (CBF), a dynamic perfusion parameter (Ahmed et al., 2009; Bley et al., 2010; Struffert et al., 2012, 2011, 2010). In our prior work (chapter 4), we explored

the relationship of whole brain C-arm CT PBV to MR derived CBV and CBF, and reported that C-arm CT PBV is a composite parameter with both blood-flow and blood-volume weightings, with our results supporting a preferential blood-flow weighting (≈60%) to C-arm CT PBV (chapter 4). Observations similar to ours exist for multi-detector CT (MDCT) where the CTA-source images (CTA-SI) could be used alone or be post-processed to generate whole brain color-coded MDCT PBV maps (Kloska et al., 2007; Wittkamp et al., 2010). In this regard, Sharma et al. showed that despite theoretical models suggesting the CTA-SIs (and MDCT PBV maps) to be predominately blood-volume weighted, when used in a clinical setting these images are preferentially blood-flow weighted (Sharma et al., 2011). For MD-CTA, injection rate of ~5ml/sec and scan delay time of 15-20 seconds are thought to alter the temporal characteristics of time-density-curve (TDC), which along with faster MDCT acquisition times eliminate the *steady-state contrast concentration assumption* thus imparting a preferential blood-flow weighting to the resulting images (Konstas et al., 2009). However, for C-arm CT PBV scans, the injection protocol and scan times for which are slightly different from those typically used for MD-CTA, the contrast material dynamics in the cerebral vasculature have not been studied.

The aims of this chapter were: (a) to test the assumption that iodinated contrast material administered using a standard injection protocol as part of C-arm CT PBV scan reaches a steady-state concentration in cerebral vasculature for the duration of scan, (b) to explore how consistent are the dynamics of contrast material in cerebral vasculature across patients by using TDC analysis of the raw C-arm FDCT projection

data, and (c) to investigate the influence of differences in TDC characteristics of the clinical C-arm CT PBV scans on the resulting PBV measurements and their agreement with MR-CBV.

7.3 Materials and Methods

Thirty C-arm FDCT PBV protocol scans of 26 patients were analysed. The clinical and imaging data were acquired as part of a prospective study, approved by local research ethics committee, comparing C-arm CT PBV with MR-PWI. The study included adult patients aged over 18 years with documented aneurysmal subarachnoid haemorrhage (SAH) who subsequently developed symptoms and signs suggesting delayed cerebral ischaemia (DCI) and requiring confirmatory imaging - a situation necessitating admission and management in neuro-intensive care unit (neuro-ICU). At our institution, the SAH is diagnosed using non-contrast CT (NCCT) head or cerebrospinal fluid (CSF) sampling by lumbar puncture when initial NCCT head is negative but clinical suspicion for SAH remains high, and is graded as described by Fisher et al. (Fisher et al., 1980). The diagnosis of DCI was based on clinical assessment by the multidisciplinary neuro-ICU team and was defined as clinical deterioration (focal neurological deficits or reduced level of consciousness) lasting 2 hours or longer with no evidence of rebleed or hydrocephalus on NCCT head, and no other medical causes such as infections or metabolic disturbances to explain the clinical/neurological deterioration.

Exclusion criteria were: a history of allergy to iodinated contrast medium, renal impairment, pregnancy, or contraindications to MR examination. All recruited patients had undergone aneurysm repair by endovascular coil embolization. Written informed

consents were obtained from patients or if they were unable to complete the consent process, from a family member or a designated surrogate as defined by the research ethics committee approval for the study. All recruited patients underwent an MRI examination using a standard protocol that included diffusion- and perfusion-weighted sequences concurrent with a research C-arm CT scan using a PBV protocol. For all recruited individuals, we recorded age, gender, clinical status on admission (world federation of neurological societies (WFNS) grade), amount of blood on the admission scan (Fischer grade), aneurysm location and treatment. For the purpose of current study, we focused our analysis on the C-arm FDCT imaging, the imaging protocol and post-processing steps for which are described in the following section.

7.3.1 C-arm FDCT Imaging

C-arm FDCT scan was performed on a flat detector equipped biplane angiography system (Axiom Artis dBA; Siemens Healthcare, Germany) in the neuro-interventional suite. The imaging protocol included two rotational acquisitions: mask and contrast-enhanced (or fill) runs. Projection data for each run was acquired using the following parameters: 419 projection images, 0.5^0 frame angle, 210^0 angular scan range, 8 seconds acquisition time, 0.36 **μ**Gy radiation dose per frame. The contrast-enhanced dataset was acquired following a manually triggered intravenous injection of radiographic contrast material, Niopam 370 (Bracco spa, Milan, Italy), using a power injector (Medrad, Inc. Philadelphia). The injection parameters were: contrast concentration, 370 mg Iodine/ml; volume, 80ml; injection rate, 4 ml/sec through the antecubital vein; injection pressure, 300 pounds per square inch (psi); and injection

duration, 20 seconds. Passage of contrast material through the cerebral vasculature was monitored on two-dimensional (2D) fluoroscopic images (2 frames/sec) and the contrast-enhanced run was triggered when maximal opacification of the superior sagittal sinus was observed.

In the clinical setting, post-processing of the data to generate color-coded PBV maps was performed on a dedicated research workstation (Leonardo, Siemens AG, Healthcare) using prototype software. The post-processing steps include: (1) co-registration of the mask and the contrast-enhanced volumes, (2) subtraction of the mask volume from the contrast enhanced volume, (3) normalisation of the subtracted data with an input function automatically estimated from the histogram analysis of vascular tree, (4) color-coding with a standard colour look-up table to generate the PBV color-coded maps for visualization and interpretation. The final PBV values were expressed in units of ml/100gm of cerebral tissue. For visualization of the vessels, the contrast-enhanced dataset was reconstructed separately on a commercially available dedicated workstation (Leonardo, Siemens AG, Healthcare). VRT (volumetric rendering technique) and MIP (maximum intensity projection) reconstructions were used to evaluate the cerebral vasculature. CT-like soft tissue reconstructions were obtained in all cases.

7.3.2 Time Density Curve (TDC) Analysis

Thirty C-arm FDCT datasets, each comprising of a mask and a contrast-enhanced (fill) run were included in the analysis. The mask and the fill runs, each consisted of 419 two-dimensional (2D) rotational projections, acquired over an angular scan range of 210^0

and a time period of 8 seconds (2 projections/degree; 52 projections/sec). Rectangular regions of interest (ROIs) were applied to the 2D projections of mask and fill runs as depicted in figure 7.1. To illustrate, on the mask run, a rectangular ROI was drawn on the first of 419 projections above the level of orbital roof and propagated to the remaining projections such that the ROI spanned the anterioposterior dimension of head on the lateral projections and the lateral (coronal) dimension of head on the frontal projections. Mean image intensity (IE) in the ROI for each projection of the mask run was measured (419 measurements). The same ROIs used for the mask run were subsequently applied to the co-registered projections of contrast-enhanced (fill) run and mean IEs in the ROIs of the fill run were measured (419 measurements). Mean IEs of the ROIs for the mask run projections were then subtracted from the mean IEs of the corresponding ROIs for the fill run projections. IE differences between the mask and the fill runs represented differences in the degree of x-ray attenuation between the two runs. The IE differences thus calculated for the rotational projections were corrected for sequential percentage differences in the head diameter over the semi-circular scan trajectory as illustrated in figure 7.2. The corrected image differences were related to the presence of iodinated contrast in cerebral vasculature administered intravenously as part of C-arm CT PBV protocol. These corrected IE differences between the mask and the fill runs for each patient were plotted against the number of projections (or time; frame rate 52 projections/sec) to generate time-density-curves. The image analysis was performed using Image J software (Image J, U. S. National Institutes of Health, Bethesda, Maryland, USA).

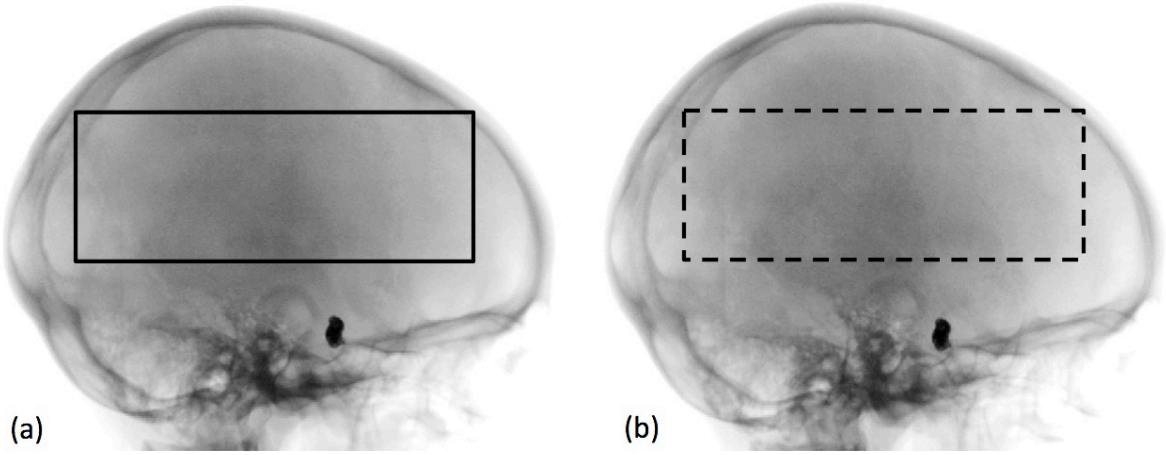


Figure 7.1: Illustration of ROI placement on the 2D C-arm FDCT rotational projections. The rectangular ROIs were placed on the 2D projections of the mask run (a) and were subsequently transposed onto the respective projections of contrast-enhanced run (b). The IEs for rotational projections were corrected for sequential percentage differences in the head diameter between the frontal and lateral projections.

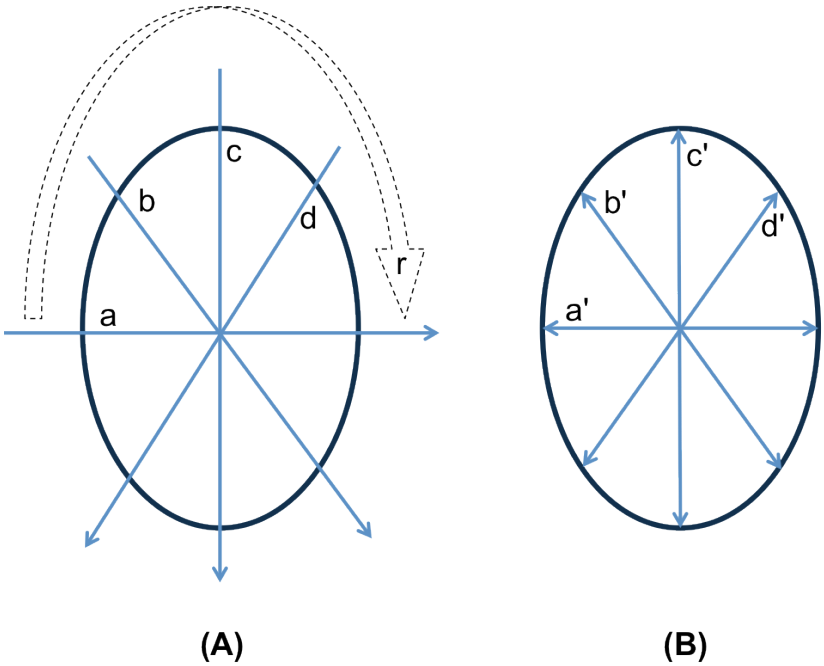


Figure 7.2: Correction of IE differences for the differences in head diameter (tissue thickness) (continued on next page).

The x-ray beam travelling anteroposterior (c; frontal projection) traverses a larger thickness of imaged volume (c') compared with an x-ray beam travelling right-to-left (a; lateral projection) that traverses a smaller thickness of imaged volume (a'). Also the beams are acquired at different time points during the C-arm rotation (r), during which the contrast concentration in the cerebral vasculature is changing. As a result differences in attenuation measured between the two beams are related to both i.e. the difference in tissue thickness that the beams have to traverse and the differences in contrast concentration between the two time points at which they are acquired.

The attenuation measurements therefore need correction for differences in the head diameter (tissue thickness). Following correction, the differences in attenuation measurements (i.e. image intensity differences) would truly be related to the differences in contrast concentration over time.

The percentage changes in head diameter were measured for the rotational projections acquired over a semi-circular scan trajectory. Similarly, for the IE differences between the mask and contrast-enhanced runs, the percentage changes were calculated from projection 1 to 419.

The percentage changes in head diameter over scan trajectory were subtracted from the corresponding percentage changes in the IE differences. The residuals represented percentage values, which were truly related to differences in contrast concentration amongst the rotational projections. These were converted back to the absolute attenuation values for subsequent analysis.

7.3.3 Statistical Analysis

Gross patterns of the TDCs were initially explored using a model-free curve-fitting methodology. Locally-weighted-scatterplot-smoothing (LOWESS) was applied to the scatterplots of IE differences versus time to generate smooth TDCs (model-free curve-fitting approach that uses local weights for TDC smoothing was chosen to preserve the measured characteristics of the curves). D'Agostino-Pearson normality test was performed to evaluate if the data followed a Gaussian distribution. IE differences were noted to deviate significantly from the normal distribution prompting non-parametric statistical analysis.

To explore if the TDCs for individual datasets met the steady-state assumption, a *horizontal line model* computed for each dataset using least-squares method was employed which represented the ideal steady-state contrast material concentration in the cerebral vasculature. Nonlinear regression analysis was used to fit the *steady-state horizontal line model* to each TDC dataset. Parameters for goodness-of-fit to the steady-state model were calculated and Runs test was performed to evaluate if there was significant deviation of the data points on the measured TDCs from the steady-state model.

To test the statistical similarity among the TDCs for individual C-arm CT datasets, we employed non-parametric Kruskal-Wallis test. Dunn's multiple comparisons test was subsequently performed to compare each dataset's TDC to every other dataset's TDC and the p-values adjusted for multiple comparisons were computed.

In the next step, to test if the differences in temporal characteristics of the TDCs contribute towards differences in final PBV measurements and their agreement with MR-CBV, the C-arm CT PBV datasets were segregated into two groups. Group A included 10 datasets for which the TDCs showed largest deviations from the horizontal line steady-state model (figure 7.3b; datasets 21-30) while group B included 20 datasets for which the TDCs were closer to steady state (figure 7.3b; datasets 1-20). For the two groups, Pearson correlation and Bland-Altman analysis were performed to explore the correlation and agreement of the C-arm CT rPBV values with the MR-rCBV, in a manner previously discussed in chapter 04. All statistical analysis was performed using Graphpad Prism version 6.0a (GraphPad Software, San Diego California USA).

7.4 Results

7.4.1 Patient Characteristics

Thirty C-arm FDCT datasets of 26 patients (mean age 55 years; men 9, women 17) acquired using PBV protocol were reviewed. All patients had aneurysmal SAH on admission and underwent coil embolisation. On the admission NCCT head, the SAH Fischer grades were: Grade-4 in 16 (61%), Grade-3 in 9 (35%), while one patient's initial NCCT head did not show evidence of SAH which was proven on lumbar puncture (4%). The aneurysms were: <5mm in 5 (20%), 5-10mm in 17 (65%), and 10-15mm in 4 (15%). Locations of ruptured aneurysms were: anterior cerebral artery, 4 (15%); peri-callosal artery, 1 (4%); anterior communicating artery, 7 (27%); middle cerebral artery, 2 (8%); posterior communicating artery, 10 (38%); basilar artery, 1 (4%); and internal carotid artery 1 (4%). WFNS grades at the time of initial presentation were: Grade-1 in

16 (61%), Grade-2 in 7 (27%), Grade-3 in 2 (8%); and Grade-4 in 1 patient (4%). The patient characteristics are summarized in table 7.1.

7.4.2 Statistical Analysis

The locally-weighted-scatterplot-smoothed TDCs for each dataset illustrating the gross patterns of contrast material dynamics are depicted in figures 7.3a and 7.3b. A visual comparison of smoothed TDCs shows that while temporal characteristics of some TDCs depart markedly from the steady-state (figure 7.3b; datasets 21-30); a greater proportion of TDCs remain fairly closer to the expected steady-state with minimal slow upslope or downslope during the scan interval (figure 7.3b; datasets 1-20). Descriptive statistics for the differences in image intensity between the mask and the contrast-enhanced runs' projections measured over time are summarized in table 7.2.

The initial results of Kruskal-Wallis test demonstrated that despite the identical scan parameters and contrast material injection protocols, the 30 TDCs are statistically non-identical (Kruskal-Wallis statistic 3722; $p < 0.0001$). Subsequent Dunn's multiple comparisons test showed that of the total 435 individual comparisons among the 30 TDCs, 330 comparisons (62%) reached statistical significance for difference (adjusted p-value <0.0001) while the remaining 105 comparisons (38%) did not reach statistical significance for difference.

Horizontal line steady-state model fit to each dataset was performed as depicted in figure 7.4. The runs test showed that all the TDCs deviated significantly ($p<0.0001$) from the *ideal steady-state horizontal line model* constructed individually for each dataset.

The results of subgroup agreement and correlation analysis of C-arm CT rPBV vs MR-rCBV were: (a) *Group A:* bias 0.052 ± 0.31 and 0.065 ± 0.29; 95% limits of agreement −0.65 to 0.75 and −0.62 to 0.74; and Pearson correlation coefficient (r), 0.60 (95% CI: 0.55 to 0.64) and 0.58 (95% CI 0.54 to 0.63), for cortical and subcortical VOIs respectively; and (b) *Group B:* bias 0.026 ± 0.18 and 0.030 ± 0.18; 95% limits of agreement −0.24 to 0.29 and −0.27 to 0.33; and Pearson correlation coefficient (r), 0.84 (95% CI: 0.81 to 0.87) and 0.81 (95% CI 0.77 to 0.84), for cortical and subcortical VOIs respectively. Thus the PBV values for the datasets with largest deviations of TDCs from the horizontal line steady-state model had both poor agreement and worse correlation with MR CBV, compared with the PBV values for those datasets with TDCs closer to the steady state.

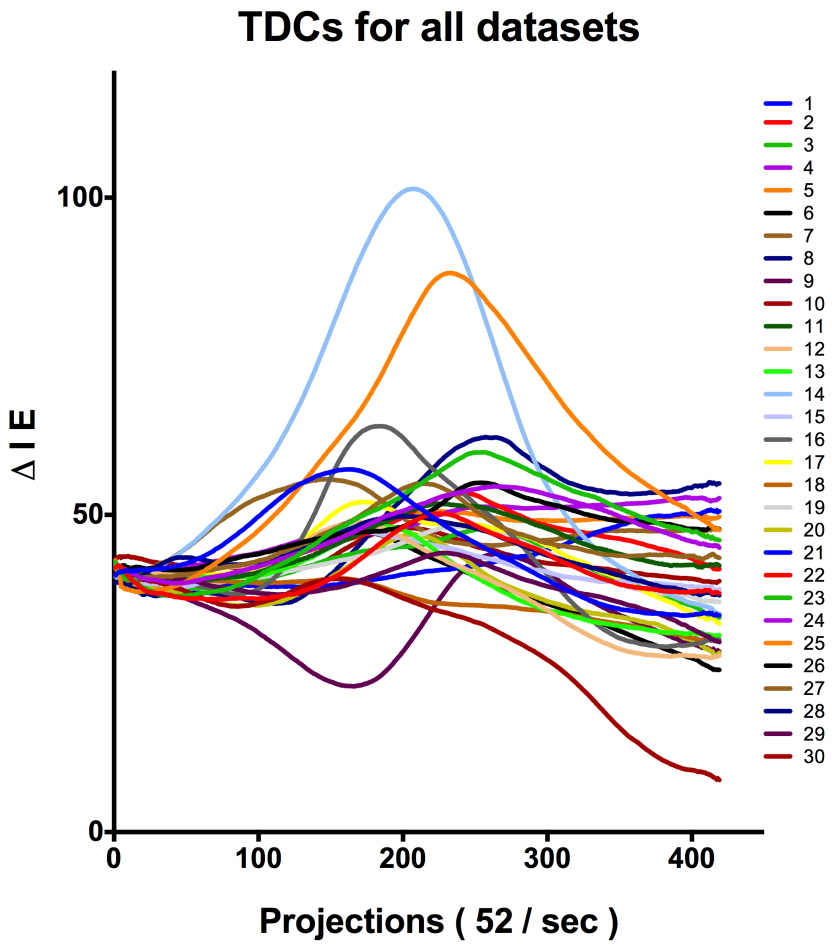


Figure 7.3a: Locally-weighted-scatterplot-smoothed (LOWESS) TDCs (aggregated). The measured TDCs for C-arm FDCT datasets (n=30) show that while majority of the TDCs remain close to steady-state (a steady-state TDC is expected to be a horizontal line with no upslope or downslope), some TDCs deviate markedly from the expected steady-state.

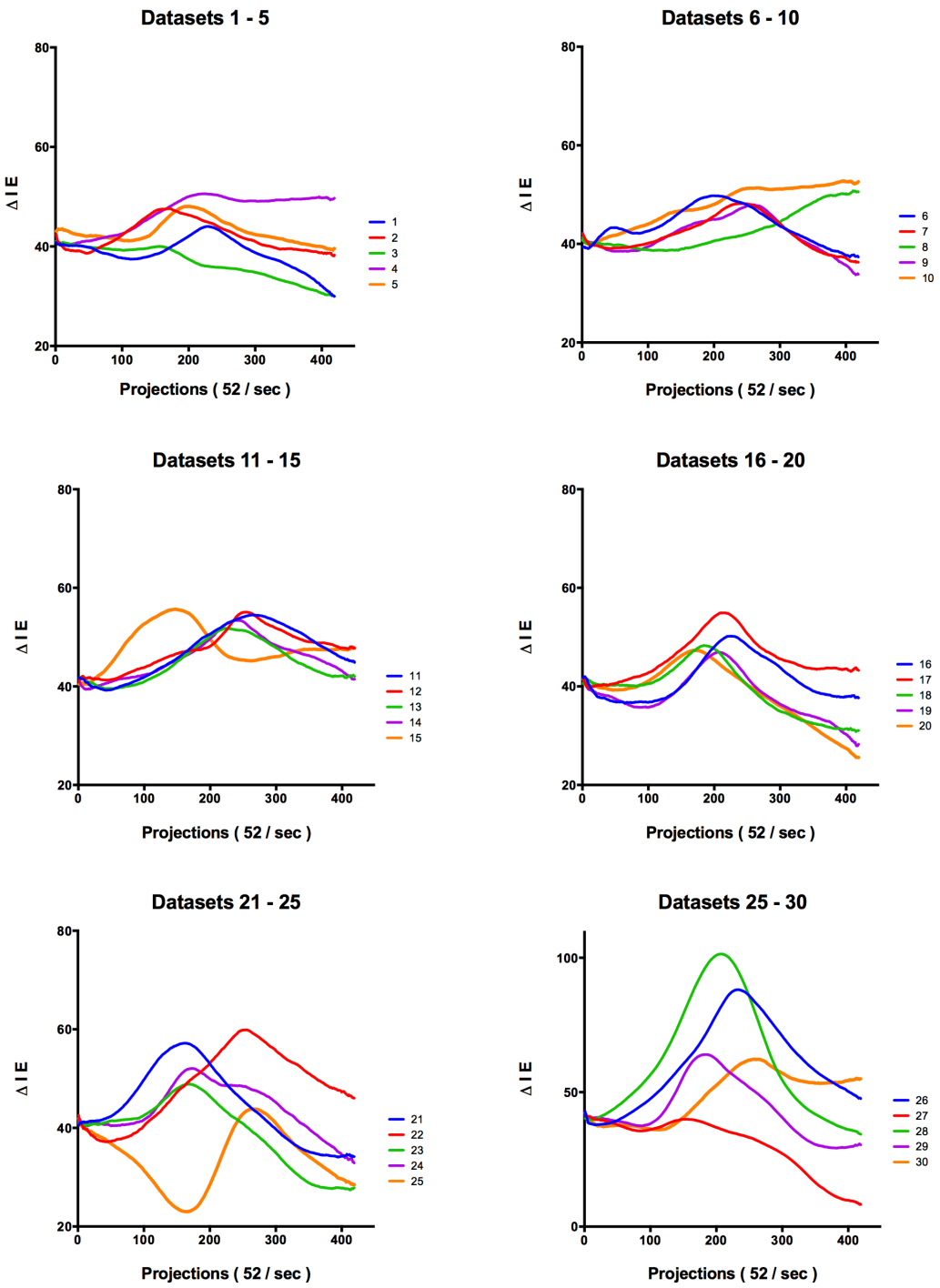


Figure 7.3b: Locally-weighted-scatterplot-smoothed (LOWESS) TDCs in subgroups. TDCs for the datasets grouped according the degree of approximation to steady-state e.g. TDCs of datasets 1-5 show close approximation to ideal steady-state while TDCs for datasets 25-30 show marked deviation from steady state.

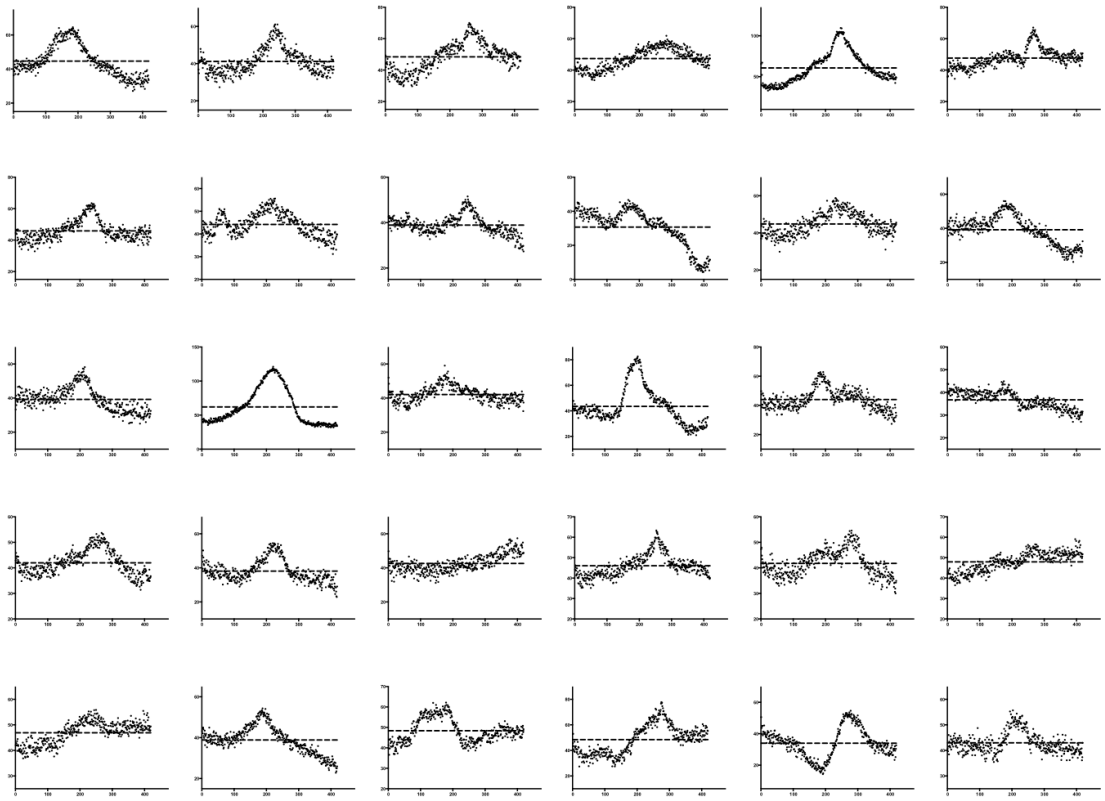


Figure 7.4: Steady-state model fitting for the TDCs.
Plots of horizontal line steady-state model fit for TDCs (n=30)
using nonlinear regression analysis

Table 7.1 Demographic, aneurysm, and clinical characteristics of the study population

Patient number	Age (years)	Gender (M/F)	Aneurysm location	Aneurysm size (mm)	WFNS grade	Fischer grade
1	47	M	Anterior communicating artery	6 × 4	1	3
2	55	F	Left anterior cerebral artery	12 × 10	3	4
3	61	F	Right posterior communicating artery	8 × 5	2	3
4	49	F	Anterior communicating artery	10 × 7	1	3
5	68	F	Right posterior communicating artery	10 × 6	2	4
6	71	F	Anterior communicating artery	6 × 5	1	4
7	46	M	Right middle cerebral artery	4 × 3	3	3
8	77	F	Left anterior cerebral artery	6 × 4	1	4
9	46	M	Right posterior communicating artery	4 × 4	1	4
10	50	F	Right internal carotid artery	3 × 3	1	3
11	53	F	Basilar artery tip	7 × 6	2	3
12	55	M	Right posterior communicating artery	5 × 3	2	4
13	55	F	Left posterior communicating artery	4 × 4	2	4
14	69	F	Left anterior cerebral artery	11 × 7	1	4
15	66	M	Anterior communicating artery	7 × 5	1	0*
16	45	M	Anterior communicating artery	15 × 8	2	4
17	66	M	Right middle cerebral artery	8 × 3	4	4
18	30	M	Anterior communicating artery	7 × 4	1	3
19	39	F	Right posterior communicating artery	5 × 3.5	1	4
20	50	F	Anterior communicating artery	4 × 3.5	1	4
21	69	M	Right posterior communicating artery	7 × 4	1	4
22	39	F	Right posterior communicating artery	10 × 9	1	4
23	52	F	Right posterior communicating artery	5 × 5	1	4
24	54	F	Left posterior communicating artery	8 × 5	1	3
25	58	F	Right anterior cerebral artery	5 × 4	1	3
26	60	F	Left peri-callosal artery	12 × 8	2	4

* NCCT head was negative for SAH, which was later confirmed on lumbar puncture

Table 7.2 TDC descriptive statistics for the differences in image intensity between the mask and the contrast-enhanced runs' projections measured over time

Dataset	Projections	Mean	SD	SEM	IQR	Minimum	Maximum	Skewness	Kurtosis
1	419	44.64	9.28	0.45	13.13	27.14	64.55	0.48	-0.75
2	419	41.19	6.70	0.33	8.46	27.31	61.09	0.84	0.23
3	419	48.43	9.27	0.45	13.62	29.69	69.97	0.05	-0.65
4	419	47.31	6.39	0.31	11.07	33.58	61.82	-0.07	-1.04
5	419	60.75	19.18	0.94	25.32	32.95	109.5	0.71	-0.34
6	419	47.64	5.90	0.29	6.85	34.49	67.04	0.79	0.85
7	419	45.86	6.43	0.31	7.23	32.87	63.46	0.87	0.28
8	419	44.19	4.97	0.24	7.99	31.17	55.6	0.13	-0.69
9	419	38.90	4.14	0.20	5.05	27.31	51.54	0.30	0.50
10	419	30.71	10.87	0.53	12.34	4.369	46.65	-1.00	-0.02
11	419	44.83	5.84	0.29	9.03	29.89	58.73	0.29	-0.71
12	419	39.16	8.17	0.40	10.80	20.27	55.98	-0.21	-0.69
13	419	39.24	6.91	0.34	9.55	25.01	58.19	0.38	-0.41
14	419	61.98	27.12	1.33	43.48	32.08	121	0.78	-0.83
15	419	42.09	4.65	0.23	6.05	32.35	59.07	0.45	0.01
16	419	43.50	14.66	0.72	14.88	20.96	82.58	0.99	0.31
17	419	44.00	6.97	0.34	8.91	27.35	62.83	0.52	0.04
18	419	36.71	3.72	0.18	6.41	27.05	44.92	-0.26	-0.79
19	419	41.98	4.77	0.23	6.57	31.42	53.69	0.40	-0.56
20	419	38.11	6.43	0.31	8.00	22.92	54.5	0.71	0.00
21	419	42.59	5.09	0.25	6.91	31.2	57.4	0.54	-0.05
22	419	46.05	5.34	0.26	6.24	35.16	63.29	0.81	0.58
23	419	41.76	5.06	0.25	7.65	30.01	54.57	0.29	-0.56
24	419	47.94	4.69	0.23	7.04	36.49	59.03	-0.28	-0.71
25	419	46.91	4.41	0.22	6.83	36.9	55.85	-0.37	-0.85
26	419	38.86	6.69	0.33	8.35	22.83	54.32	-0.02	-0.40
27	419	48.39	5.93	0.29	9.16	36.61	62.17	0.41	-0.85
28	419	48.45	11.49	0.56	18.23	27.42	77.75	0.24	-0.86
29	419	33.98	9.36	0.46	12.00	14.32	54.61	0.15	-0.56
30	419	42.97	4.06	0.20	4.80	35.47	55.69	0.88	0.33

7.5 Discussion

Our results demonstrate that despite the same scan parameters and identical contrast injection protocols, the measured TDCs vary significantly among patients undergoing C-arm CT PBV examination. Furthermore, the administered contrast material does not reach the assumed 'ideal steady-state' in the cerebral vasculature for the duration of scan. However, the TDC temporal characteristics of most datasets remain close to the steady-state while TDCs of some datasets deviate markedly from the steady-state. The degree to which the measured TDCs approximate the steady-state influences the agreement of resulting PBV values with MR-CBV. This is illustrated by our findings that the rPBV values of those datasets for which the TDCs showed largest deviations from the steady-state model demonstrated poor agreement and correlation with MR-rCBV, compared with the rPBV values of those datasets for which the TDCs were closer to the steady-state.

Multiple factors may explain as to: (a) why a steady-state contrast concentration is not achieved in the cerebral vasculature despite a prolonged slow contrast injection (duration 20 seconds, rate 4ml/sec; the current standard for C-arm CT PBV imaging), and (b) why differences in temporal characteristics of TDCs exist among subjects despite identical contrast injection protocol and scan parameters. Given the identical injection and scan parameters, only patient factors can explain the observed differences. Regarding *'(a)'*, from a physiological standpoint, following a peripheral intravenous contrast injection, bolus dispersion occurs that is governed by factors such as regional blood flow and tissue perfusion. For prolonged injections, recirculation of

the contrast becomes an important factor. Normal recirculation times may range 15-40 seconds. Given the 20 seconds long injection that is used for C-arm CT PBV protocol, some recirculation of contrast would thus begin during the contrast material administration. The recirculated contrast-enhanced blood would reach the cerebral circulation in a non-simultaneous fashion due to multiple circulatory pathways in the body. Consequently, the new contrast medium and the recirculated contrast medium may mix and lead to gradual increase in the concentration of contrast material in cerebral circulation. In addition, a power injected large contrast volume accelerates the slow peripheral venous blood flow and may perturb the haemodynamic physiology of cardiovascular system to a variable extent. This *haemodynamic perturbation effect* is more significant for a larger contrast volume, administered at higher injection rate. As a result of recirculation and haemodynamic perturbation effect, the steady state is not sustained and the TDC may show an upslope or downslope. In regards to *'(b)'*, *the between-subject differences in the TDCs* may also be explained by multiple patient-related factors of which the most important are differences in body size i.e. height and weight, cardiovascular recirculation time (determined by cardiac output), age and gender (Bae, 2010). Additionally, the cerebrovascular physiology may be altered to a variable extent in various patients following aneurysmal SAH due to factors such as vessel narrowing and microvascular dysfunction. Lastly, permeabilities at the microvasculature-cellular interface in the cerebral tissue become important if there has been breakdown of the blood-brain barrier (BBB), and can differ among patients, thereby contributing to the between-subjects differences.

Understanding the contrast material dynamics in cerebral vasculature is important when calculating and interpreting a perfusion parameter. The C-arm systems in current clinical use are limited in their temporal resolution due to slow rotational speed (minimum 5seconds); the temporal resolution is further degraded by their inability to rotate continuously in the same direction (Fieselmann et al., 2012). Gantry rotation time for C-arm CT PBV scanning is typically 8-10 seconds, which is too long to adequately resolve voxel-wise TDCs and thus to apply the standard CTP algorithms (Zellerhoff et al., 2009). As a result, only PBV measurements can be performed with the current C-arm systems using a specially designed prolonged injection protocol that aims to achieve steady-state contrast concentration in entire cerebral vasculature. For single compartment model using the dynamic perfusion imaging, the CBV can be calculated using equation 1:

$$CBV = \frac{\int_0^\infty C_{tissue}(t)\ dt}{\int_0^\infty C_{artery}(t)\ dt} = \frac{\int_0^\infty C_{tissue}(t)\ dt}{\int_0^\infty C_{vein}(t)\ dt} \qquad \textit{(Equation 1)}$$

With an ideal steady state contrast concentration achieved in cerebral vasculature ($C_{tissue} = C_{artery} = C_{vein}$), and no change in contrast concentration over the scan duration), equation 1 can be replaced by equation 2:

$$CBV = \frac{C_{tissue}}{C_{artery}} = \frac{C_{tissue}}{C_{vein}} \qquad \textit{(Equation 2)}$$

The C-arm CT PBV measurements performed using the steady-state imaging would thus be equivalent to the CBV derived from dynamic perfusion imaging (Hamberg et al., 1996; Zellerhoff et al., 2009). However, if the steady-state were not achieved, as is shown by the temporal shape of the TDCs in figure 7.3a and 7.3b, the resulting PBV measurements would not be equivalent to CBV and could only have a certain blood-volume weighting. Given the iodinated contrast material used for x-ray imaging consists of relatively small molecules that are highly diffusible, delivery of contrast material through the circulation to a tissue of interest is primarily flow-limited (Bae, 2010). Thus an upslope or downslope of the TDC would indicate preferential contrast wash-in or wash-out into the tissue of interest and would impart a blood-flow weighting to the PBV measurements (as shown by the results discussed in chapter 04). The greater the TDC deviates from the ideal steady-state, the lesser would be equivalence of C-arm CT PBV to CBV. The above discussion explains the results of subgroup analysis where the PBV values of those datasets for which the TDCs showed largest deviations from the steady-state model, also demonstrated poor agreement and correlation with MR-CBV, compared with the PBV values of those datasets for which the TDCs were closer to the steady–state. These issues have previously not been explored for C-arm CT PBV imaging. However, our results are supported by observations for MD-CTA where: (a) a slow contrast injection, long injection-to-scan delay, and longer scanning facilitate blood-volume weighting (Hunter et al., 1998); (b) higher contrast injection rates (5-7 ml/sec), shorter injection-to-scan delay, and faster scanning alter the temporal shape of TDC and eliminate the near steady-state during acquisition of CTA images.

Consequently the resulting CTA source images (and MDCT PBV images) are less blood-volume weighted and more blood-flow weighted, similar to our findings for C-arm CT PBV (Konstas et al., 2009; Sharma et al., 2011).

Abnormalities identified on the CBV and CBF maps (from dynamic perfusion imaging modalities) are known to represent different underlying tissue injury and each has a unique prognostic significance. Therefore, in a clinical setting, it is important to know as to how well the steady-state assumption was met for a particular PBV study and if the measured C-arm CT PBV is predominately blood-volume or blood-flow weighted. Diminished CBF with relatively preserved CBV indicates ischaemia i.e. salvageable tissue (ischaemic penumbra in stroke patients); whereas decreased CBV (and therefore decreased CBF) indicates infarction i.e. non-salvageable tissue (infarct core in the stroke patients) (Allmendinger et al., 2012). In a neuro-interventional setting, the distinction between the two has important implications for patient management. To illustrate this, consider a procedural setting where an ischaemic stroke patient is undergoing revascularisation treatment, and the operator performs a C-arm CT PBV scan to assess the brain viability and to guide the treatment planning. In this situation if there is significant enlargement of the pre-treatment PBV abnormality or development of new large PBV abnormality: an equivalence of PBV to CBV (steady-state achieved) would indicate tissue infarction favouring treatment termination; on the contrary, a significant blood-flow weighting to PBV (steady-state not achieved) may only indicate ongoing tissue ischaemia and thus further revascularisation attempts may be beneficial. Similarly, the distinction is important when C-arm CT PBV may be used

for selecting stroke patients for revascularisation treatment.

We propose that a simple ROI-based TDC analysis of the raw C-arm CT projection data be implemented in the workflow of PBV scanning. It would provide an estimate of how adequately the steady-state contrast concentration was achieved during a particular C-arm CT PBV scan, which would inform the clinician interpreting the PBV maps on how closely an abnormality detected on PBV maps might correlate to a CBV (surrogate for infarction) or a CBF (surrogate for ischaemia) abnormality. Assuming a steady-state in all patients may overlook the blood-flow weighting to C-arm CT PBV in cases where the TDCs depart significantly from the steady-state, thus potentially resulting in under-estimation of salvageable brain tissue.

Although the current C-arm angiographic systems are limited in their temporal resolution (as discussed above), new generation multi-axis angiographic systems based on robotic technology allow shorter rotation times and hold the potential for dynamic perfusion imaging in the neurointerventional suite. Fieselmann et al. proposed a new strategy that employs interleaved scanning to augment the temporal resolution for C-arm systems (Fieselmann et al., 2012, 2010). Preliminary work in canines using this technique has shown promising results allowing estimation of CBF (Royalty et al., 2013). Further advancements such as improved FD contrast detectability and read out speed, improvements in C-arm system design and software algorithms are expected to support this development and allow dynamic perfusion imaging in the interventional suite for detailed one-stop assessment of patients with cerebral ischaemia.

7.6 Conclusion

This chapter demonstrates that for clinical C-arm CT PBV examinations, the administered contrast material does not reach the assumed 'ideal steady-state' for the duration of scan, and the temporal characteristics of TDCs vary significantly among patients despite the same scan parameters and identical contrast material injection protocol. However, using a consistent prolonged injection protocol, TDCs for most datasets approximate the assumed steady-state. The degree to which this approximation is achieved influences the blood-volume weighting and the agreement of resulting PBV measurements with CBV. These factors have not been studied previously for the clinical C-arm CT PBV scans and are of clinical significance e.g. a knowledge of how adequately the steady-state was achieved during a PBV scan can inform the clinician interpreting the PBV maps on how closely the abnormality detected on PBV maps might correlate to a CBV or a CBF abnormality, each of which represent different underlying tissue injury and have unique prognostic significance. Assuming a steady-state in all patients may over-estimate blood-volume weighting to C-arm CT PBV in cases where the TDCs depart significantly from the steady-state, thus potentially resulting in under-estimation of salvageable brain tissue.

8

Utility of Parenchymal C-arm FDCT Imaging in the Neurointerventional Suite

8.1 Abstract

Background and purpose: C-arm systems used in the neurointerventional suite can generate cross-sectional CT-like soft tissue images of brain parenchyma, which may allow a timely detection of complications during the endovascular treatments. The purpose of this chapter was to investigate if the parenchymal soft tissue information provided by C-arm flat detector computed tomography (FDCT) was adequate for identification of procedural rupture and assessment of ventricular size.

Materials and methods: All C-arm FDCT images of the patients who underwent an embolisation treatment in a 12-month period and for whom a C-arm FDCT examination was performed were retrospectively analysed. The images were independently evaluated by two neuroradiologists for the presence of procedural vessel rupture and hydrocephalus in three steps: first, FDCT images alone; then, FDCT images with procedural details and, finally FDCT images with concurrent conventional CT imaging. Sensitivity, specificity, predictive values, and accuracy of C-arm FDCT images for the detection of procedural vessel rupture and hydrocephalus were calculated. Fishers exact test was performed to evaluate the independence of evaluators' assessments. Interobserver agreement was measured by Cohen's kappa-coefficient.

Results: FDCT images correctly identified or excluded hydrocephalus in all 31 patients with excellent interobserver agreement (kappa 1.0). For procedural rupture, detection and interobserver agreement were moderate with FDCT images alone (kappa 0.52). Additional clinical information improved both (kappa 0.82), with no additional benefit from perioperative imaging.

Conclusion: FDCT images of brain parenchyma are of adequate quality to identify procedural vessel rupture and for evaluation of the ventricular size.

8.2 Introduction

C-arm angiographic systems used in the neurointerventional suite collect projection data using a technique which is similar to the cone-beam volume CT and involves rotational volume scanning with a cone-shaped x-ray beam and two-dimensional (2D) x-ray detectors (Smyth et al., 2006). A similar scanning principle prompted the application of CT-like reconstruction algorithms to the projection data acquired with the C-arm systems, thus combining the benefits of greater flexibility and mobility of C-arm systems with advantages of CT, and raising the possibility of obtaining CT-like soft tissue reconstructions of brain parenchyma in the interventional suite (Linsenmaier et al., 2002). The idea was first applied to C-arm systems equipped with image intensifiers. However, performance parameters of image intensifiers were limited in terms of low dynamic range, poor low-contrast-resolution, and image distortions resulting from the effects of changing magnetic interferences during rotational movement of C-arm. As a result, cross-sectional soft tissue imaging was not possible with image intensifiers and the use of C-arm systems remained restricted to high-contrast vessel imaging only. Advanced sensor systems, known as flat panel detectors, were developed to overcome the insufficiencies of image intensifiers. Flat detectors, with their higher absorption efficiency, wider dynamic range, fast digital read-out, and dynamic acquisition of data at higher frame rates were particularly suited to the role of obtaining cross-sectional CT like soft-tissue images in the interventional suite (Gupta et al., 2006). The imaging protocol used to generate cross-sectional CT-like soft tissue images using the C-arm systems is termed C-arm flat detector computed tomography (C-arm FDCT or FDCT).

Contrast resolution of FDCT is approximately 10 Hounsfield Units (HU), which despite being inferior to the excellent contrast detectability of conventional CT (1 HU), is within acceptable range for specific applications in the neurointerventional suite, most important among which is detection of procedure-related complications (Kalender and Kyriakou, 2007).

Procedure-related vessel perforation is an important complication for neuroendovascular treatment technique (Doerfler et al., 2001; Li et al., 2006). The event, although relatively infrequent (range 2 to 7.6 % for various centres), is potentially fatal; timely detection and vigilant management of which can significantly improve the clinical outcomes (Cloft and Kallmes, 2002; Levy et al., 2001; Tummala et al., 2001). Major procedural vessel rupture can be obvious and is easily recognised when there is marked extravasation of contrast medium, unexpected shift of vascular structures due to acutely developing haematoma, or sudden deterioration of neurological status of the patient (Li et al., 2006). Minor perforations, on the other hand, can easily be overlooked and cause late deterioration of patient's neurological status after an apparently uneventful embolisation procedure. Decision-making in this setting rests upon the availability of appropriate imaging that can provide information on the status of intracranial soft tissues. Therefore, when a procedural vessel rupture is suspected, the usual practice is to transport the patient for a conventional CT scan; a strategy that has its own drawbacks including disruption of workflow, loss of precious time during transportation, and movement of patient away from the sterile environment of neuroradiology suite (Gupta et al., 2008). Availability of cross-sectional

soft tissue images that may allow a reliable assessment of ventricular system, brain parenchyma and, subarachnoid space in the interventional suite could help avoid the need to transfer patient from the sterile interventional environment to the diagnostic CT suite, thereby facilitating workflow, saving time in emergent situations, and improving the clinical outcomes for patients experiencing this potentially devastating procedural complication. C-arm FDCT application provides CT-like cross-sectional soft tissue images of brain parenchyma while the patient is on angio-table. Initial reports document adequate quality of FDCT images for visualizing the ventricular system and for detection of intracranial haemorrhage (Doelken et al., 2008; Heran et al., 2006).

This chapter aims to investigate if the soft tissue information provided by C-arm FDCT cross-sectional images is adequate for identification of procedural rupture and assessment of ventricular size.

8.3 Materials and Methods

A retrospective review of the clinical and imaging data was performed for 31 consecutive patients (21 women, 10 men; mean age 48.5 years, range 13-79 years) who underwent C-arm FDCT examination following endovascular treatment in the neuroradiology department of John Radcliffe Hospital, between March 2007 and November 2008. The FDCT scan for each patient was performed either to investigate procedure-related complications or to assess the ventricular system. Clinical records, hospital picture archiving and communication system (PACS), radiology information system (RIS) and log of FDCT examinations were reviewed to collect procedure details, indication for FDCT examination, peri-operative imaging, and clinical outcomes for the

participants.

8.3.1 FDCT Data Acquisition and Post-processing

FDCT examinations were performed on a biplane C-arm angiography system equipped with flat panel detectors (Axiom Artis dBA; Siemens Healthcare, Forchheim, Germany). Rotational datasets were acquired using the following parameters: 543 projection images, 220˚ angular scan range, 20-seconds acquisition time, 0.36 μGy radiation dose per frame, flat panel detector area 30cm × 40cm. Rotational projection data was post-processed on a commercially available workstation (Leonardo; Siemens Medical Solutions), equipped with reconstruction software package (DynaCT 3D application) using a standard reconstruction algorithm (modified Feldkamp) similar to conventional CT. The post-processing included corrections for radiation scatter, beam hardening, truncation, and ring artefacts. The resulting volumetric datasets were reformatted to generate two sets of cross-sectional images with similar angulation and slice thicknesses of 3mm and 5mm in a 512×512 matrix.

8.3.2 FDCT Image Evaluation

Anonymised cross-sectional FDCT images were presented to two interventional neuroradiologists in three steps, as follows:

1. FDCT images only
2. FDCT images in conjunction with procedural details
3. FDCT images in conjunction with procedural details and concurrent perioperative CT imaging performed within twenty-four hours of procedure

At each stage of the three-step assessment, the evaluators (A and B) were asked to assess the images for:

(a) Presence or absence of hydrocephalus

(b) Presence or absence of procedural rupture

To avoid the recall bias in assessments, each evaluator was presented with anonymised data for each step in separate sessions and in a random order. Following the independent assessments, both evaluators reviewed FDCT studies for all patients together and in conjunction with procedural details, perioperative imaging studies and relevant clinical information. A consensus evaluation for each case was thus reached at regarding the presence or absence of procedural rupture and hydrocephalus. Using consensus evaluation as the reference standard, sensitivity, specificity, positive predictive value (PPV), negative predictive value (NPV), and accuracy of FDCT cross-sectional images to identify hydrocephalus and procedural rupture were calculated for the independent evaluations.

Fishers exact test was performed to evaluate the independence of evaluators' assessments for the presence or absence of procedure rupture (null hypothesis: probability of getting a positive read for the procedure rupture on the FDCT images is the same whether the procedure rupture is present or not present) (Fisher, 1922). Inter-observer agreement for independent evaluations at each of the three steps was measured using Cohen's kappa-coefficient (Cohen, 1960); a robust measure to assess the level of concordance between two sets of dichotomous ratings which takes into account the amount of agreement that could be expected to have occurred by chance.

The kappa-coefficient was interpreted according to the criteria in table 8.1 (Landis and Koch, 1977). Statistical analysis was performed using GraphPad Prism Software, San Diego California,USA.

Table 8.1 Landis and Koch criteria for the interpretation of Cohen's kappa statistic

Kappa (k)	Strength of agreement
< 0.20	Poor
0.21 – 0.40	Fair
0.41 – 0.60	Moderate
0.61 – 0.80	Good
0.81 – 1.00	Very good

8.4 Results

Clinical and imaging data for 31 consecutive patients undergoing C-arm FDCT examination following endovascular treatment was reviewed. Of these 31 patients, 23 (16 women, 7 men; mean age 50.6 years, age range 18-79 years) had intracranial aneurysms and were treated by embolisation with detachable platinum coils whereas 8 patients (women 5, men 3; mean age 42.5 years, age range 13-61 years) with arteriovenous malformations (AVMs) underwent embolisation with Onyx liquid embolic system (Micro Therapeutics, Inc., Irvine, CA) or Glubran 2 (GEM s. r. l., Viareggio, Italy). Radiation dose for a single 20-seconds rotational acquisition was

22mGy (weighted CT dose index).

8.4.1 Procedural Rupture

Based on the consensus evaluation, procedural rupture with extravasation of contrast or hyperattenuating blood was identified in 9 of the 31 studies. The results for three-step evaluation are described below and are presented in table 8.2.

8.4.1.1 FDCT Images Only

(a) Evaluator A: Four of nine cases with procedural rupture and 20 of 22 cases without procedural rupture correctly identified (sensitivity 0.44, specificity 0.91, PPV 0.67, NPV 0.80, accuracy 0.77).

(b) Evaluator B: Four of nine cases with procedural rupture and all cases without procedural rupture (n = 22) correctly identified (sensitivity 0.44, specificity 1, PPV 1, NPV 0.81, accuracy 0.84).

(c) Inter-observer agreement: Moderate (kappa coefficient 0.52).

(d) Fishers exact test yielded p-values of 0.043 and 0.004 for evaluators A and B (α 0.05) indicating diagnostic role of FDCT images.

8.4.1.2 FDCT Images in Conjunction with Procedural Details

Supplementation of FDCT images with relevant procedural details improved detection of procedural rupture for both observers.

(a) Evaluator A: Six of nine cases with procedural rupture and all cases without procedural rupture correctly identified (sensitivity 0.67, specificity 1, PPV 1, NPV 0.88,

accuracy 0.90).

(b) Evaluator B: Eight of nine cases with procedural rupture and all cases without procedural rupture correctly identified (sensitivity 0.89, specificity 1, PPV 1, NPV 0.96, accuracy 0.97).

(c) Inter-observer agreement: Very good (kappa coefficient 0.82).

(d) Fishers exact test yielded p-values of <0.001 for both evaluators A and B (α 0.05), indicating strong diagnostic role of FDCT images.

8.4.1.3 FDCT Images in Conjunction with Procedural Details and Concurrent Perioperative CT Imaging Performed within Twenty-four Hours of Procedure

Addition of perioperative CT imaging in the final stage of three-step evaluation did not improve the detection or exclusion of procedural rupture achieved on the basis of FDCT images and procedural details in the second step. Accordingly, the inter-observer agreement and results of Fishers exact test remained the same.

8.4.2 Hydrocephalus

Based on the consensus evaluations, hydrocephalus was present in 8 of the 31 studies. Both evaluators, at each stage of the three-step evaluation of FDCT images, correctly labelled the presence or absence of hydrocephalus in all patients with excellent inter-observer agreement for each step (kappa coefficient 1). Sensitivity, specificity, PPV, NPV, and accuracy of FDCT images for hydrocephalus detection were therefore 1 for both evaluators for each evaluation-step.

Table 8.2 Results of Fisher's exact test and contingency analysis for the evaluators A and B for the three-step FDCT images evaluation

	FDCT images only		FDCT images and procedure details		FDCT images, procedure details, and perioperative imaging	
	Evaluator A	**Evaluator B**	**Evaluator A**	**Evaluator B**	**Evaluator A**	**Evaluator B**
Fisher's exact test						
P value	0.0434	0.004	< 0.0001	< 0.0001	< 0.0001	< 0.0001
One- or two-tailed	Two-tailed	Two-tailed	Two-tailed	Two-tailed	Two-tailed	Two-tailed
Statistically significant ? (alpha<0.05)	Yes	Yes	Yes	Yes	Yes	Yes
Sensitivity	0.44	0.44	0.67	0.89	0.67	0.89
95% confidence interval	0.14 to 0.79	0.14 to 0.79	0.30 to 0.93	0.52 to 1.0	0.30 to 0.93	0.52 to 1.0
Specificity	0.91	1	1	1	1	1
95% confidence interval	0.71 to 0.99	0.85 to 1.0	0.85 to 1.0	0.85 to 1.0	0.85 to 1.0	0.85 to 1.0
Positive Predictive Value	0.67	1	1	1	1	1
95% confidence interval	0.22 to 0.96	0.40 to 1.0	0.54 to 1.0	0.63 to 1.0	0.54 to 1.0	0.63 to 1.0
Negative Predictive Value	0.8	0.81	0.88	0.96	0.88	0.96
95% confidence interval	0.59 to 0.93	0.62 to 0.94	0.69 to 0.97	0.78 to 1.0	0.69 to 0.97	0.78 to 1.0

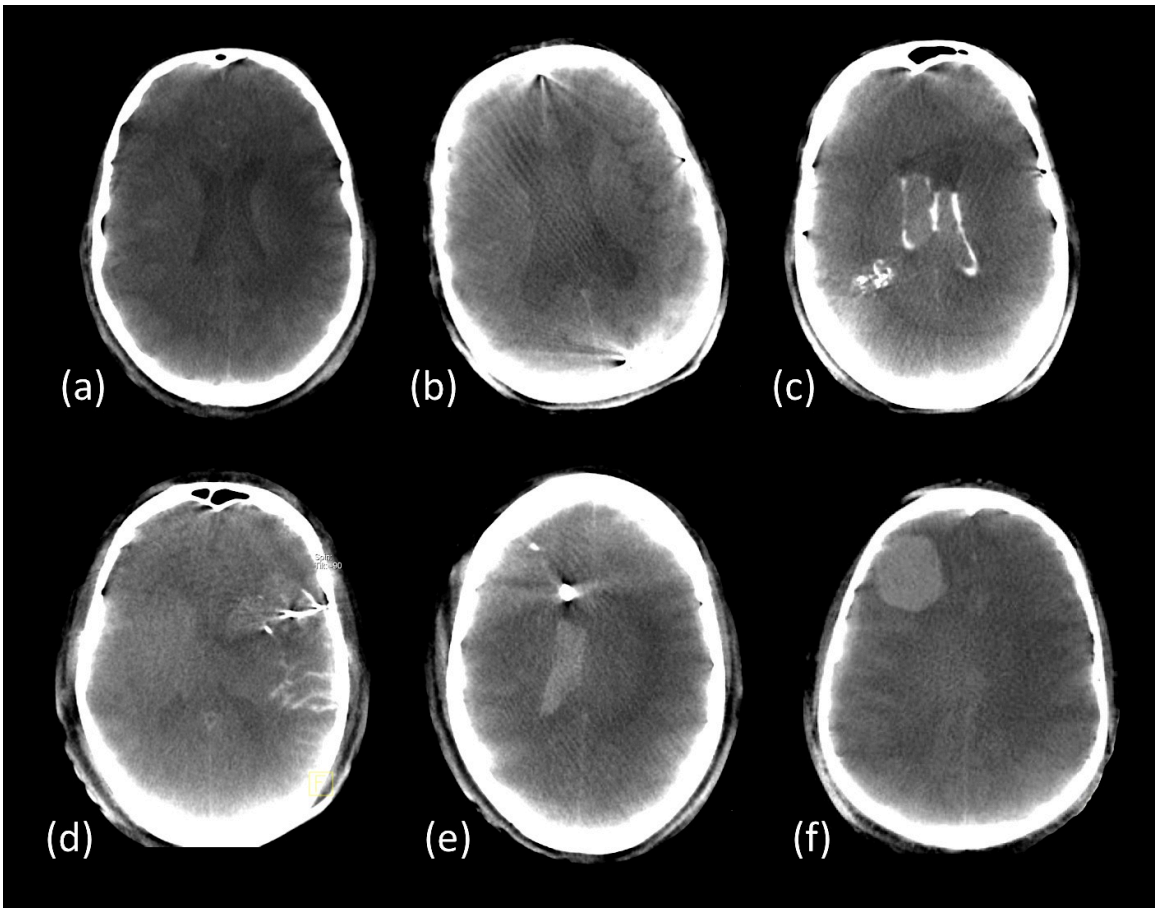


Figure 8.1: Illustrative cross-sectional C-arm FDCT images. FDCT images of different patients showing (a) normal size and configuration of ventricles, (b) enlarged ventricles (hydrocephalus), (c) intraventricular haemorrhage with layering of extravasated contrast material in a patient with procedural vessel rupture, (d) procedural vessel rupture with extravasation of hyperattenuating blood, (e) intraventricular haemorrhage in right lateral ventricle, and (e) right frontal hematoma.

8.4.3 Illustrative Cases

8.4.3.1 Illustrative Case 1

A 45-year-old woman presented with SAH (Fisher grade 4) and was found to have a right parietal AVM on CT angiography. Catheter angiogram redemonstrated the medium-size right parietal AVM with prominent feeding vessels off right middle cerebral artery (MCA) and showed a small right anterior choroidal artery aneurysm, the likely cause of subarachnoid and intraventricular haemorrhage. During the embolisation treatment, a microwire-induced perforation was suspected to have occured while attempting the catheterization of anterior choroidal artery beyond the cisternal segment. FDCT scan was performed immediately, which showed minimal interval ventriculomegaly, increase in the volume of intraventricular haemorrhage, and new layering contrast material in both lateral ventricles (figure 8.1c); thus providing confirmatory evidence of procedural rupture while the patient was on angio-table.

8.4.3.2 Illustrative Case 2

A 64-year-old man presented with acute onset headache. CT showed subarachnoid haemorrhage (SAH) centred in sylvian fissure, left frontal haematoma and a small subdural effusion. No aneurysm or vascular malformation was reported on CT angiography; however, a dissecting aneurysm of the prefrontal branch of left MCA was demonstrated on catheter angiogram. During embolisation treatment of the dissecting aneurysm, angiographic contrast extravasation was noted while trying to position the microcatheter close to the aneurysm. FDCT examination was performed which excluded expansion of the right frontal haematoma, extensive contrast extravasation, or interval

hydrocephalus (figure 8.1f). The procedure was successfully completed and the patient was extubated, without any deficits following recovery from anaesthesia.

8.4.3.3 Illustrative Case 3

A 52-year-old woman presented with headache for two weeks and new onset diplopia and ptosis of the left eye. Initial non-contrast CT examination was negative for SAH. CT angiography demonstrated a 7mm basilar artery aneurysm and a 5mm posterior communicating artery aneurysm. Lumber puncture produced uniformly blood-stained cerebrospinal fluid (CSF), providing confirmatory evidence for SAH. During the endovascular treatment, the posterior communicating artery aneurysm was successfully packed with six detachable platinum coils. However, a catheter-induced perforation occurred during the deployment of second coil into basilar artery aneurysm and a leakage of contrast was noticed from the dome of aneurysm. Heparin was reversed and the aneurysm was packed with four additional coils. Once the coils were in place, an FDCT examination was performed, which showed that there was no further contrast extravasation and ventricles were stable in size and configuration (figure 8.1a). The patient was extubated and recovered without any new neurological deficits or exacerbation of headache.

8.5 Discussion

The purpose of this chapter was to explore the utility of FDCT soft tissue images as a problem-solving tool in detecting common procedure-related complications encountered during the neuroendovascular treatments. Our results demonstrate that

the FDCT images can adequately assess the ventricular size and confirm the presence or absence of procedural vessel rupture.

Procedural vessel rupture is a potentially fatal complication for neuro-endovascular treatments. The design of our study with step-wise analyses of FDCT images, where each step added on to the information provided in the preceding setting, helped us to evaluate the contribution of FDCT images alone in detecting procedural rupture and to investigate how additional information (procedural details and concurrent perioperative imaging) available in the clinical setting affects the interpretation of FDCT images. With only FDCT images available, both evaluators detected approximately half the procedural perforations while they could reliably exclude it in nearly all cases without procedural rupture (sensitivity 0.44 and 0.44; specificity 0.91 and 1.0). Inferior soft tissue resolution of the technique (10 HU) compared with conventional CT (1 HU) explains the low sensitivity at this step and is in accordance with observations of Doelken et al. who found that FDCT underestimates the extent of SAH and is more likely to overlook subtle SAH (Doelken et al., 2008). Supplementation of FDCT images with procedural details increased the detection of procedural perforation for both readers while the complication was excluded in all cases without procedural rupture (sensitivity 0.67 and 0.89; specificity 1.0 and 1.0). With the availability of relevant procedural details, this setting more closely replicates the clinical situation where FDCT studies are usually performed. Considering the two settings together it can be inferred that although FDCT images alone may have a poor performance, the technique is of value in clinical context to reliably detect or exclude

procedural vessel rupture. It is known that procedural vessel perforations of clinical significance are usually associated with contrast extravasation. Due to poor low-contrast-detectability (LCD), in certain cases FDCT may not be able to resolve the difference between the extravasated blood in subarachnoid space and the CSF; thus a low sensitivity for detecting subtle extravasation of blood (Doelken et al., 2008). But any extravasated contrast, when present, is of sufficiently higher attenuation from the CSF to be readily detectible by FDCT (Figure 8.1). It further emphasizes the value of FDCT technique for detecting a clinically significant procedural rupture. This is supported by the observations of Heran et al. and White et al. who commented on the technique's utility in the neurointerventional setting for detection of complications including procedural rupture (Heran et al., 2006; White et al., 2008).

Our results on assessment of the ventricular system using FDCT are consistent with the other studies and can be explained by the performance parameters of this new imaging modality. In a study by White et al., FDCT images allowed adequate assessment of ventricles during the endovascular procedures and this information was a substantive factor in determining subsequent patient management (White et al., 2008). Doelkin et al. showed excellent concordance between FDCT and conventional CT images for assessment of ventricular size measured in terms of Evan Index (relationship between ventricular size and cerebral size) (Doelken et al., 2008). Ability of an imaging modality to differentiate between various low-contrast structures such as brain parenchyma and CSF spaces depends on its low-contrast detectability or soft tissue resolution. At the current level of performance, soft tissue resolution of FDCT is ≈10

Hounsfield Unit (HU) which, though inferior to conventional CT (low-contrast resolution 1HU), is adequate to distinguish CSF filled ventricles from surrounding brain parenchyma (CT number of CSF-filled ventricles ≈1HU, grey matter ≈40HU, white matter ≈30HU) (Kalender and Kyriakou, 2007). A reliable on-angio table assessment of the ventricles inside the interventional suite avoids the need to transfer patient for conventional CT. While identification of hydrocephalus can facilitate subsequent placement of emergent ventriculostomy catheter to decompress distended ventricles; excluding it in a setting of high suspicion can be reassuring and has the advantage of increasing confidence in the subsequent management.

At the current level of performance, FDCT image quality is inferior compared with the conventional CT. The technique should not be considered as a replacement for conventional CT; instead, its principle application lies in intraoperative imaging as a problem-solving tool. Availability of FDCT in the neurointerventional suite combined with its ability to reliably detect procedure-related complications obviates the need for patient transfer to conventional CT scanner when a procedural complication is suspected and cross-sectional imaging is indicated. Under these circumstances, application related advantages of FDCT clearly outweigh performance related disadvantages and define it as a valuable tool in the neuro-endovascular suite. A comparison with conventional CT should therefore only be made with reference to its intended use.

Since FDCT is a relatively new technique, issues such as optimum slice thickness and appropriate window-settings have not yet been standardized. In our study, where a

stack of 220 reformatted slices and reconstructions of 3mm and 5mm thickness were available on the workstation, the reporting radiologists showed a preference for the reconstructions with 5 mm slice thickness, which were thought to provide an optimum trade-off between the spatial and low-contrast resolutions. A window-level of 100HU and a window-width of 400HU were found appropriate during the review of FDCT images for procedural rupture and hydrocephalus. Other groups have reported preference for similar image window settings and slice thickness parameters (Doelken et al., 2008). Radiation dose during an FDCT examination is dependent upon multiple factors including x-ray tube voltage, tube current, and scan duration. In addition, due to volumetric nature of FDCT acquisitions, it takes into account the irradiated craniocaudal length. A single 20-seconds rotational acquisition involves a radiation exposure of 22mGy (weighted CT dose index), which is less compared to conventional non-contrast CT head (~50mGy, CT dose index). Shorter acquisitions (8 and 10 seconds) offer lower radiation exposure, but are associated with a compromise on image quality that may affect its performance in terms of detecting procedure-related complications (White et al., 2008).

We acknowledge several limitations for the work presented in this chapter. Utility of FDCT was assessed in a small number of patients, primarily due to two reasons: (a) it included patients undergoing endovascular treatment in a single centre and (b) procedural rupture is a rare complication of neuro-endovascular procedures. However the results are encouraging and there is a need to replicate the results in a multicentre study with a larger sample size. In addition, although both evaluators

reviewing the FDCT images were trained neuroradiologists, there was difference between their levels of experience, which might have influenced their assessments. Discordance (shown by a low kappa coefficient), particularly in the first step evaluation for procedural rupture, could partly be explained by the difference in their levels of experience. Lastly, for a small number of patients we could not recover either pre-operative or post-operative CT scans from the hospital database due to the patients either having been transferred from or to an outside hospital. We tried to overcome this limitation, by combining any perioperative imaging through a modification in the initial design of study, where the pre- and post-operative imaging were to be evaluated separately. A prospective audit study can avoid this issue.

8.6 Conclusion

C-arm FDCT cross-sectional soft tissue images are of adequate quality for reliable evaluation of the ventricular system and detection of procedural vessel rupture. Although, FDCT image quality is inferior to the conventional CT, application-related advantages of FDCT outweigh the performance related disadvantages and define it as a valuable tool in the neurointerventional suite.

9

Flow Diversion: A New Endovascular Treatment Technique for Intracranial Aneurysms

9.1 Intracranial Aneurysms and their Treatment

An aneurysm is focal dilatation of a blood vessel caused by complex interplay of factors, primarily the morphological characteristics of the vessel wall and the unfavourable local blood flow dynamics (Krings et al., 2011). Aneurysms of the intracranial vasculature are common, occurring in 0.5-6.0% of the general population (Menghini et al., 1998; Rinkel et al., 1998; Vlak et al., 2011). Most intracranial aneurysms either remain asymptomatic and undetected, or are discovered incidentally on neuroimaging studies; only a small proportion of aneurysms are brought to the medical attention as a result of aneurysm-related symptoms (Rinkel et al., 1998). The most devastating clinical presentation is spontaneous intracranial haemorrhage i.e. subarachnoid haemorrhage (SAH). Aneurysmal SAH carries a fatality rate of 32-67% and long term dependence rate of 10-20% (Cahill and Zhang, 2009; Johnston et al., 2002). Thus the aneurysm management goals are to prevent the first episode of aneurysmal bleed for unruptured aneurysms and, for ruptured aneurysms, secure the aneurysm against re-bleed (Johnston et al., 2002).

The treatment techniques for intracranial aneurysms have evolved since Walter Dandy's first successful surgical clipping of an intracranial aneurysm in 1937, however, the underlying principle remains valid i.e. to exclude the aneurysmal sac from circulation (Byrne and Szikora, 2012). Minimally invasive endovascular treatment using coil embolisation became popular following the introduction of electrolytically detachable platinum coils in 1990 (figure 9.1 a and b) (Guglielmi et al., 1991). Subsequent level-1 evidence on the safety, efficacy, and superiority of the coil

embolisation treatment technique over the neurosurgical clipping lead to its widespread acceptance as the first-line treatment for both ruptured and unruptured aneurysms (Cognard et al., 2011; Molyneux, 2002; Pierot et al., 2008; Spetzler et al., 2013). Endosaccular packing of aneurysm with metal coils and the consequent thrombosis completely obliterates the aneurysm in most cases. However, despite adequate aneurysm occlusion with metal coils, the structurally weak vascular segment that allowed de novo aneurysm formation remains exposed to the same unfavourable local haemodynamic forces. The durability of endosaccular coil embolisation (ECE) of aneurysms is thus a major concern and constitutes the primary weakness of ECE compared with neurosurgical clipping. In a systematic review of 8161 patients undergoing ECE, Ferns et al. reported adequate post-treatment aneurysmal occlusion in 91.2% cases. But on long-term follow up, one-fifth (20.8%) of the coiled aneurysms re-opened, requiring re-treatment in 10.3% (Ferns et al., 2009). Similar high re-treatment rates have been reported in other studies including for the patients randomized in International Subarachnoid Aneurysm Trial (ISAT) (Campi et al., 2007).

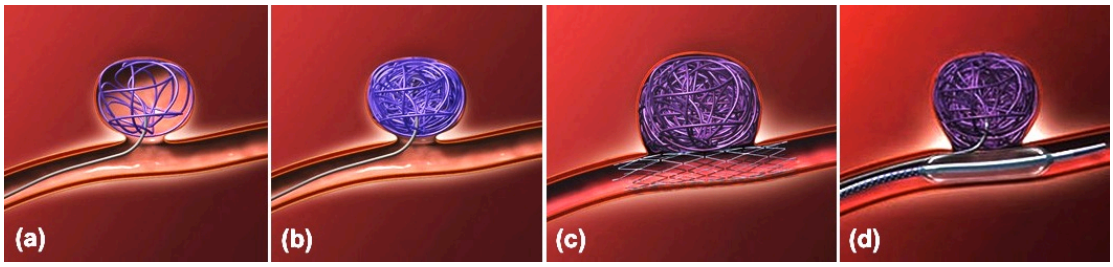


Figure 9.1: Coil embolisation treatment of intracranial aneurysms. Illustrative images demonstrating (a and b) endosaccular coil embolisation (ECE), (c) stent-assisted ECE, and (d) balloon assisted ECE.

From a theoretical standpoint, high recurrence rates observed after endosaccular coiling are related to its inability to effectively address the pathogenic factors underlying development of aneurysms i.e. the structural vessel wall weakness (segmental or circumferential) and unfavourable local haemodynamics. In addition, fusiform shape, complex morphology, large size, and wide neck aneurysms are difficult to treat by ECE alone, despite the use of modified techniques i.e. stent-assisted or balloon assisted coiling, and are reported to have higher recurrence rates (Byrne and Szikora, 2012; D'Urso et al., 2011) (figure 9.1 c and d).

9.1.1 Flow Diversion – a New Endovascular Treatment Approach

To address the shortcomings of ECE, endoluminal stents with low porosity were introduced as an alternative endovascular treatment (Kallmes et al., 2007; Lylyk et al., 2009). These vascular reconstruction devices, known as flow diverters (FDs) are deployed in the parent vessel across the neck of aneurysm with an aim to uncouple the blood flow between parent artery and the aneurysm sac. FD treatment goals are: (a) to reconstruct the parent vessel, repairing any segmental or circumferential vessel wall defects that lead to the origin and progression of the aneurysm and (b) to redirect blood flow along the long axis of parent vessel thereby modifying the haemodynamic forces acting on the aneurysm (D'Urso et al., 2011).

Once deployed, the FD device creates a physical barrier across the neck of aneurysm disrupting blood flow into and out of the aneurysm. The barrier introduced by the FD is augmented by the growth of endothelium and neointima on its inner surface, promoting stagnation and thrombosis of blood inside the sac (figure 9.2).

Ensuing endosaccular thrombosis may take several weeks to develop and can be followed on angiographic imaging. Endothelialisation of the FD, once achieved, marks complete reconstruction of the *parent vessel - aneurysm complex*, effectively excluding the aneurysm from the circulation and modifying the culprit pathogenic factors (Byrne and Szikora, 2012; D'Urso et al., 2011; Kamran et al., 2011).

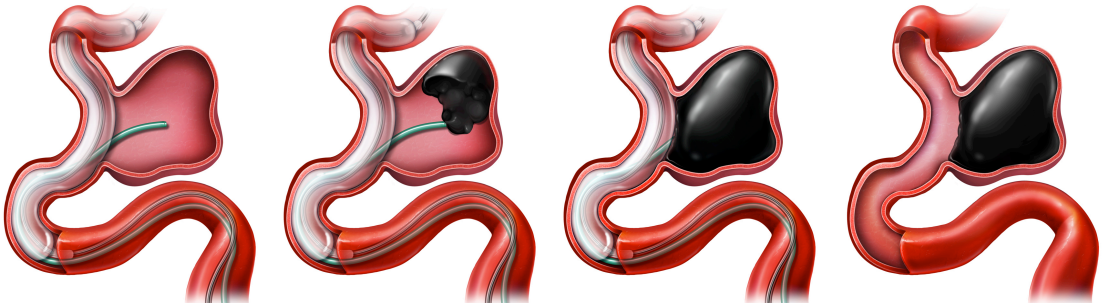


Figure 9.2: Flow diversion principle for treatment of intracranial aneurysms. A flow diverter device is deployed in the parent vessel across the aneurysm neck with disruption of the blood flow at 'parent vessel – aneurysm neck interface' and ensuing intrasaccular thrombosis.

9.1.1.1 Flow Diverters: Technical Specifications and Deployment Technique

The essential feature of a stent designed to induce aneurysm thrombosis by modifying blood inflow and outflow patterns is a lower effective porosity created by increased metal coverage. The major FD devices currently available for clinical use include: Silk FD (SILK; Balt Extrusion, Montmorency, France) which is CE (Conformité Européenne) marked since 2008; Pipeline Embolisation Device (PED; Covidien, Irvine, CA, USA), approved by the FDA (Food and Drug Administration, US) in 2011 and CE marked; Surpass FD (SURPASS; Stryker Neurovascular, Fremont, CA, USA) which is CE marked; and Flow Redirection Endoluminal Device system (FRED; MicroVention, Tustin, CA,

USA) which also is CE marked.

The Silk FD (SFD) is a flexible, self-expanding, braided mesh stent with flared ends and a pore size of 110 - 250 μm (figure 9.3a). Constructed from 48 braided nitinol (nickel-titanium alloy) and platinum microfilaments ~35 μm, SFD provides 35-55% metal coverage at its nominal diameter and a porosity of 45-60% (Kulcsár et al., 2010, p. 24; Tähtinen et al., 2012). Currently available SFDs cover a range of diameters (2-5 mm) and lengths (15-40 mm) and are equipped with four radiopaque markers to allow adequate visualisation under fluoroscopy (Murthy et al., 2014). The second generation Silk-plus FDs are now available with a tapered design allowing better conformity to the walls of vessels with variation between the proximal and distal diameters of the section to be stented. SFD deployment involves positioning a delivery microcatheter (Vasco 21, Balt, Montmorency, France) with its tip distal to the target aneurysm. This is followed by pushing the prosthesis, applied to a delivery microwire, to the tip of the delivery microcatheter. The system is then aligned with the aneurysm orifice under x-ray fluoroscopy and the SFD deployed by unsheathing it from the constraint of the microcatheter. This involves a combination of pushing the delivery wire and retrieving the microcatheter to allow the SFD to expand and to compensate for any resulting foreshortening. The SFD can be retrieved into the microcatheter and removed or repositioned even when up to 90% of its length has been extruded, a distinct advantage. No retrieval is possible thereafter. Endosaccular coils can be placed before the stent is deployed or afterwards via a second microcatheter positioned prior to SFD deployment, a technique often referred to as 'jailing' (Lubicz et al., 2010).

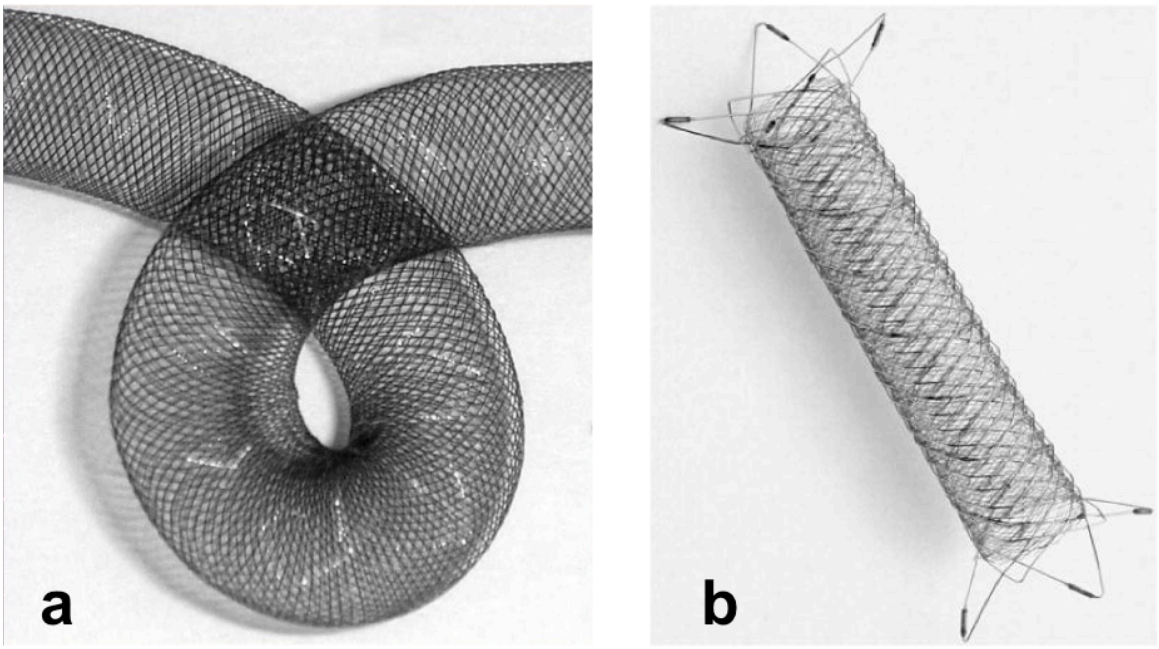


Figure 9.3: Silk and FRED FD devices: (a) the Silk flow diverter device (SFD; Balt Extrusion, Montmorency, France); (b) the flow redirection endoluminal device system (FRED; MicroVention, Tustin, CA, USA).

The PED is similar and is constructed from 48 microfilaments of 25% platinum and 75% nickel-cobalt-chromium alloy, with a metal coverage of 30-55% and porosity of 65 – 70%. It is available in sizes similar to SFD (diameters 2.5-5 mm, lengths 10-35 mm) (Szikora et al., 2010). Surpass FD is a low porosity (metal surface area coverage 30%), high pore density (21-31 pores / mm^2) cobalt-chromium construct with 12 platinum wires integrated and replacing an equal number of cobalt-chromium wires to increase the radiographic visibility. The device is preloaded on a delivery microcatheter (Vries et al., 2013). FRED FD is a braided, self-expandable nitinol construct with a stent-in-stent design that consists of an outer stent (16 struts) with high porosity and inner FD mesh (48 strands) with low porosity (figure 9.3b). These are available with a nominal

diameter of 3.5 – 5.5 mm and lengths varying according to the parent vessel diameter (range 7 – 55 mm). Four radiopaque markers at each end and two interwoven helical marker strands allow radiographic visibility. It allows resheathing after up to 50% of its deployment (Kocer et al., 2014).

9.1.2 Clinical Experience with Flow Diverter Devices

Following our initial experience with SFD (discussed in chapter 10; the largest multicenter series reporting FD outcomes at the time of its publication), a large number of reports have appeared in literature documenting the safety, angiographic and clinical outcomes, and complications associated with each of the commercially available FD devices (Arrese et al., 2013; Briganti et al., 2012; Brinjikji et al., 2013; Kallmes et al., 2014; Murthy et al., 2014; Saatci et al., 2012). With growing evidence on the safety and efficacy of FDs in achieving high complete aneurysm occlusion rates and acceptable procedure-related morbidity and mortality, several institutions now attempt flow diversion as first line of treatment for unruptured intracranial aneurysms (Zanaty et al., 2014). For ruptured aneurysms, however, the safety of FD treatment is yet to be established. With growing use of FDs, novel applications for this treatment option have been identified including treatment of dissecting intracranial aneurysms and arterial deconstruction to achieve gradual parent artery occlusion (Kuker et al., 2011; Wajnberg et al., 2014).

A meta-analysis of 1451 patients (1654 aneurysms) treated with FDs showed complete aneurysm occlusion rate of 76% (CI 70-81%); procedure-related morbidity 5% (4-7%) and mortality 4% (3-6%); post-operative subarachnoid haemorrhage rate

3% (2-4%); intraparenchymal haemorrhage rate 3% (2-4%); perforator infarction rate 3% (1-5%); ischemic stroke rate 6% (4-9%); with significantly lower odds of both perforator infarction and ischemic stroke among patients with anterior circulation aneurysms (Brinjikji et al., 2013). Another meta-analysis of 897 patients (1018 aneurysms) reported a similar complete aneurysm occlusion rate of 76% (CI 72-80%); early mortality rate 3% (2-4%); late mortality rate 1% (0.2-2%); early neurological morbidity 7% (6-9%); and delayed neurological morbidity 3% (1-4%) (Arrese et al., 2013). Similar findings were reported by the international retrospective study of the PED that reviewed 793 patients (906 aneurysms) treated at 17 centres worldwide. With PED, the neurological morbidity and mortality rate was 8%; spontaneous rupture rate 0.6%; intracranial haemorrhage rate 2%; ischemic stroke rate 5%; and neurological mortality rate 4%; with the neurological morbidity and mortality higher for the posterior circulation group (Kallmes et al., 2014). Table 9.1 provides a summary overview of the morbidity, mortality, and occlusion rates for FDs reported in major case series, systemic reviews, and meta-analysis. A brief discussion of the pertinent procedural and delayed complications associated with FD treatment is provided below.

9.1.2.1 Perforator and Side Branch Occlusion

Post-treatment patency of perforators and side branches arising from the vessel segment covered with high mesh density FD is a major concern with flow diversion treatment. The coverage of side branches or perforators is unavoidable in certain locations e.g. the anterior choroidal or ophthalmic arteries with internal carotid artery (ICA) implantation and the posterior cerebral or anterior inferior cerebellar artery with

basilar artery deployment. Initial evidence from animal models indicated that perforators remain patent following deployment of high mesh density implants as the neointimal endothelisation generally spares the perforator origins (Kallmes et al., 2007; Masuo et al., 2002). Clinical experience with FDs also suggests that in most instances the covered side branches either remain patent or asymptomatic e.g. in a series of 20 paraclinoid-ICA aneurysms, one-quarter of ophthalmic arteries underwent proximal thrombosis with none of the patients demonstrating visual changes or clinical symptoms (Puffer et al., 2012). In another series, 56 side branches were covered by Surpass FD in 30 patients; at 6 month follow-up, 6 branches lost antegrade flow with no clinical sequela, indicating the importance of collateral pathways that can maintain circulation in the event of perforator or side branch thrombosis (Vries et al., 2013). Following FD treatment, the perforator vessels in posterior circulation, however, are at greater risk of occlusion with higher likelihood of clinical sequela relative to the anterior circulation, which is thought to be related to the delicate perfusion and lack of collateral pathways to vital brainstem structures (Kulcsár et al., 2010; Phillips et al., 2012; Siddiqui et al., 2012). In the meta-analysis of 1654 FD treated aneurysms, Brinjikli et al. reported a 3% symptomatic perforator occlusion rate with significantly lower odds of perforator infarction (OR 0.10; CI 0.00 – 0.08) for patients with anterior circulation aneurysms compared with those with posterior circulation aneurysms. These findings support judicious use of FD in the vascular segments harbouring eloquent perforators or in the vascular segments with higher reported rates of perforator infarction, and if no better alternative treatment exists, avoiding the

overlapping of multiple FD devices which is known to further reduce the effective FD porosity (Alderazi et al., 2014; Brinjikji et al., 2013).

9.1.2.2 Delayed Haemorrhage

Delayed haemorrhage is the most dreaded complication after FD treatment and may represent either SAH or intraparenchymal haemorrhage (IPH).

SAH occurs in approximately 4% of patients, usually within the first postoperative month (2% occurrence rate after one month) with a higher risk among patients with large and giant aneurysms (Brinjikji et al., 2013). SAH in an acute (procedural) setting may be related to wire perforations; while enzymatic degradation of the aneurysmal wall during thrombosis has been hypothesized as the possible explanation for delayed SAH (Kulcsár et al., 2011; Turowski et al., 2011; Vries et al., 2013). Kulscar et al. collected 13 cases of post-procedural aneurysmal rupture from 12 centres worldwide (Kulcsár et al., 2011). In their review, patients experiencing this devastating complication shared some common characteristics: (a) 11 of 13 patients were symptomatic prior to treatment, (b) most patients were hypertensive, (c) all aneurysms were >15mm in size (mean 22±6mm), and (d) all saccular aneurysms had aspect ratio >1.6. All these factors are known to predispose aneurysms to a relatively high rupture risk. The procedures themselves were largely uneventful in that adequate FD deployment was achieved in majority (11 of 13) and post-deployment contrast material stagnation was observed for all treated aneurysms. However, an important observation was post-treatment persistence of the inflow jet in 11 of the 12 aneurysms for which an inflow jet had been identified prior to FD deployment. Insufficient flow

diversion in these cases indicated presence of inertia driven flow, and a potential change in the intra-saccular flow pattern could have exposed previously un-exposed areas to haemodynamic stress. The authors hypothesized this change is one contributory factor towards delayed aneurysmal rupture. At follow-up imaging, all aneurysms except one (for which thrombosis could not be evaluated) were occluded to a significant degree with thrombus (complete occlusion in 2, >90% occlusion in 5, and 50-90% occlusion in 5). Post-mortem histopathological examination in two patients showed intraluminal thrombi lacking significant organisation or cellular colonisation. From abdominal aortic aneurysms (AAA) literature, such thrombi are known to undergo continuous lysis and renewal, a process that may have been maintained by persistent low-grade intra-aneurysmal flow (as noted in the reported cases). These unstable thrombi contained within the aneurysm act as a source of secreted enzymes (proteases and elastases) leading to thinning and weakening of the aneurysmal wall. This is in contrast to thrombosis induced by ECE, where the thrombus is stable and leads to cicatrisation and reverse remodelling of the vessel wall. With appearance of reports of SAH for FD-treated aneurysms, adjunctive used of endosaccular coils was advised when treating larger aneurysms to improve the stability of induced thrombus, or to increase the flow diverting effect of FDs by layering the devices; manoeuvres which may have contributed to a decreased incidence of this complication (Brinjikji et al., 2013).

IPH has been reported to occur in 0 – 10 %, with a recent meta-analysis describing 3% rate for IPH among the FD-treated patients (Berge et al., 2012; Byrne et

al., 2010; Cruz et al., 2012; McAuliffe et al., 2012). The pathogenesis of IPH in this setting is not known, however, haemorrhagic transformation of ischemic stroke, antiplatelet therapy, and haemodynamic alterations consequent to FD placement have been proposed as possible mechanisms (Brinjikji et al., 2013; Cruz et al., 2012).

9.1.2.3 Perianeurysmal Oedema

There is a theoretical possibility that the unstable thrombus formed inside the aneurysmal sac after FD treatment may initiate an inflammatory reaction, which can potentially spread to the peri-aneurysmal brain parenchyma. Berge et al. hypothesised this process to be responsible for post-treatment exacerbation of symptoms (Berge et al., 2011). The authors followed 17 patients treated with FDs and correlated their clinical outcomes with MR imaging findings. Seven patients exhibited emergence of new neurological symptoms or worsening of previously present symptoms. MR imaging for this cohort (n = 7) showed signs suggestive of peri-aneurysmal inflammatory reaction, which were absent for the group with no clinical deterioration (n = 10). Furthermore, the clinical aggravation group had larger aneurysms embedded in brain parenchyma and had at least 50% sac thrombosis when the new or worsening symptoms occurred. These symptoms resolved within 30 days post-procedure in all but one patient and the inflammatory MR signs had disappeared on follow up imaging at 3 months. The authors therefore concluded that post-FD sac thrombosis initiates an inflammatory reaction that spreads transparietally to the adjacent parenchyma, an effect that is more pronounced in large or giant aneurysms due to a greater thrombus load, and explains the post-treatment clinical worsening. Considering the parallels with the post-

implantation syndrome observed after endovascular AAA repair, steroids are used to prevent or suppress this process when post-treatment exacerbation of symptoms occur which may be attributable to this inflammatory reaction; however, there is no proven role for steroid use in the setting of FD treatment.

9.1.2.4 Stenothrombotic Occlusion

Thrombus formation along the FD wall leading to FD occlusion, parent artery occlusion (PAO), or distal thromboembolic events may occur in the acute setting where it may be related to inadequate or resistance to the antiplatelet therapy (Becske et al., 2013; Brinjikji et al., 2013). Prompt injection of Abciximab thwarts acute thrombus formation in a procedural setting (Tähtinen et al., 2012). PAO secondary to late stenothrombotic events has also been reported in a small minority of patients resistant or non-compliant to antiplatelet therapy, with residual in-stent stenosis as another possible contributory factor; for various FD devices PAO occurred in 5 of 108 patients in PUFS trial (PED), 2 of 37 in PITA trial (PED); 7 of 70 in the registry by Byrne et al. (SFD); and 2 of 37 patients in the study by Vries et al. (Surpass FD) (Becske et al., 2013; Byrne et al., 2010; Nelson et al., 2011; Vries et al., 2013). Given the possibility of this complication, adequate dual antiplatelet therapy in both the pre-operative and post-operative (for several months) periods is now mandatory. Patients with residual in-stent stenosis are particularly at high risk for PAO and in such patients, a discontinuation of antiplatelet treatment can result in parent artery occlusion as late as 6 months post-treatment (Alderazi et al., 2014).

9.1.2.5 Distant Infarction

Distant infarctions are rare but have been reported and may remain clinically silent (Becske et al., 2013; Shankar et al., 2013). Excessive intravascular manipulation during FD deployment is thought to play a contributory role, however, with improved deployment techniques for available FDs this complication is less frequent.

9.2 Conclusion

Flow diversion has emerged as an attractive treatment alternative for patients with recurrent aneurysms after ECE or aneurysms with challenging morphology i.e. large or giant size, wide neck, or fusiform shape, which are difficult to treat by conventional coil embolisation and are known to have higher recurrence rates. Published data support the FD treatment to be technically feasible and to effectively achieve complete occlusion in a high proportion of treated aneurysms. Reported procedure related morbidity and mortality are not negligible, however, the complication rates are comparable to other endovascular treatment alternatives. Major areas of concerns are post-procedural aneurysmal rupture, thromboembolic complications, stent-induced parent vessel stenosis, and occlusion of FD-covered perforators with a risk of ischemic stroke.

Table 9.1 Morbidity, mortality, and occlusion rates for FDs in major case series, systemic reviews, and meta-analysis

Study (type)	Number of studies or centres	Patients (P); Aneurysms (A)	FD type	Morbidity rate (%)	Mortality rate (%)	Complete aneurysm occlusion at F up
1. Brinjikji et al. (meta-analysis)	29 studies	P 1451 A 1654	SFD, PED	5	4	76
2. Arrese et al. (meta-analysis)	15 studies	P 897 A 1018	SFD, PED	Early: 7.3 Late: 2.6	Early: 2.8 Late: 1.3	76.2
3. Leung et al. (systematic review)	10 studies	P 414 A 448	SFD, PED	Overall: 6.3 R*: 18.8 UR§: 6.1	Overall: 2.2 R: 12.5 UR: 0.8	82.8
4. Murthy et al. (systematic review)	8 studies	P 285 A 317	SFD	Early: 12.5 Late: 9.9	4.9	81.8
5. Kallmes et al. (multi-centre)	17 centres	P 793 A 906	PED	Early: 5.7 Late: 7.4	Early: 2.6 Late: 3.8	NA
6. Briganti et al. (multi-centre)	25 centres	P 273 A 295	SFD, PED	3.7	5.9	85
7. Saatci et al. (single centre)	Single centre	P 191 A 251	PED	1 Any event: 14.1	0.5	91.2

* R, ruptured aneurysm; § UR, unruptured aneurysm. Studies included in the table: 1 (Brinjikji et al., 2013) ; 2 (Arrese et al., 2013); 3 (Leung et al., 2012); 4 (Murthy et al., 2014); 5 (Kallmes et al., 2014); 6 (Briganti et al., 2012); and 7 (Saatci et al., 2012).

10

Early Experience in the Treatment of Intra-Cranial Aneurysms by Endovascular Flow Diversion: A Multi-centre Prospective Study

10.1 Abstract

Background and purpose: Flow diversion is a new approach to the endovascular treatment of intracranial aneurysms, which uses a high-density mesh stent to induce sac thrombosis. The flow diverter devices have been designed for the treatment of complex shaped and large size aneurysms. So far published safety and efficacy data (at the time of publication of the work discussed in this chapter) on this approach is sparse.

Materials and methods: Over 8 months, standardized clinical and angiographic data were collected on 70 patients treated with a flow diverter device (SILK flow diverter; SFD) in 18 centres worldwide. Treatment and early follow-up details were reviewed centrally. SFDs were deployed alone in 57 (81%) or with endosaccular coils in 10 (14%) aneurysms, which included: 44 (63%) saccular, 26 (37%) fusiform shapes and 18 (26%) small, 37 (53%) large, 15 (21%) giant sizes. Treatment outcome data up to 30 days were reported for all patients, with clinical (50 patients) and imaging (49 patients) follow-up (median 119 days) data available.

Results: Difficulties in SFD deployment were reported in 15 (21%) and parent artery thrombosis in 8 (11%) procedures. Procedural complications caused stroke in 1 and serious extracranial bleeding in 3 patients; 2 of whom developed fatal pneumonias. Delayed worsening of symptoms occurred in 5 patients (3 transient, 1 permanent neurological deficit, and 1 death) and fatal aneurysm bleeding in 1 patient. Overall permanent morbidity and mortality rates were 2 (4%) and 4 (8%), respectively. Statistical analysis revealed no significant association between complications and variables related to treated aneurysm morphology or rupture status.

Conclusion: This is the largest series, reporting outcome of the new FD treatment approach and provides data for future study design (at the time of publication of the work discussed in this chapter). Procedural difficulties in SFD deployment were frequent and anti-thrombotic prophylaxis appears to reduce the resulting clinical sequela, but at the cost of morbidity due to extracranial bleeding. Delayed morbidity appears to be a consequence of the new approach and warrants care in selecting patients for treatment and future larger studies.

10.2 Introduction

Coil embolisation has proved an effective treatment for most intracranial aneurysms but larger aneurysms, fusiform shaped aneurysms, and those with wide necks are technically challenging. Such aneurysms are also more liable to recurrence, which occurs in 20–30% (Thornton et al., 2002) and results in 10–12% of patients requiring retreatment (Campi et al., 2007; Ries et al., 2007). Adjuvant stenting was proposed in the mid-1990's, initially for fusiform aneurysms (Higashida et al., 1997) and more recently to support the neck region of intracranial saccular aneurysms to prevent recurrence (Lylyk et al., 2002). The principle that a stent placed in the parent artery can reduce blood flow in the sac of an aneurysm to the point of stagnation and thrombosis has been exploited for sometime in other anatomies and has now been extended to the intracranial vasculature in a new range of implants designed to be sufficiently flexible for intracranial navigation. These new devices, termed flow diverters (FDs), recently became available for clinical use. The SILK stent (Balt Extrusion, Montmorency, France) was approved in 2007. This self-expanding flexible stent is constructed of woven nitinol strands with low porosity, to retain blood flow in the parent artery and exclude the aneurysm sac. In order to assess the safety and efficacy of the SILK flow diverter (SFD), a multicentre registry was established. The intention of this chapter (the results of this work were published soon after its completion to inform the neurointerventional community on the safety and efficacy of the FD treatment) is to assess the device's performance in routine clinical practice by collecting data from as many users as possible.

10.3 Materials and Methods

10.3.1 Methods

10.3.1.1 Patient Recruitment

All centres using the SFD during 8 months (March to November, 2008) were invited to send anonymised and coded data to the Oxford Neurovascular and Neuroradiology Research Unit (ONNRU). Thirty centres world-wide used the device during this period. Eighteen centres participated and returned reports of consecutive treatments using a standard case report form (CRF). The study protocol defining data to be collected was established prior to recruitment and prior to most invitations.

Patients were selected for treatment locally at the treating centre on the basis that the target aneurysm was unsuitable for conventional endovascular or neurosurgical treatments (figure 10.1). The following exclusion criteria were set by the study steering committee: any contraindication to antiplatelet drugs, pregnancy, breast feeding, and aneurysms considered treatable with coils alone. The study protocol was defined as clinical audit using the UK National Research Ethics Service guidance (Defining Research 2007) and did not require research ethics committee approval. Each centre was responsible for obtaining appropriate permissions for data sharing.

10.3.1.2 Data Collection

Prior to treatment, modified Rankin scores (mRS) and Glasgow Coma Scores (GCS) were recorded. Therapists were asked to record any untoward procedural events (UPE) during procedures, any acute clinical complication and a GCS score after treatment. The CRF described UPEs as: catheterization failure, poor SFD positioning, SFD migration,

poor SFD opening on deployment, haemorrhage during or after the procedure, complications related to other devices, and partial or complete thrombosis of the parent artery.

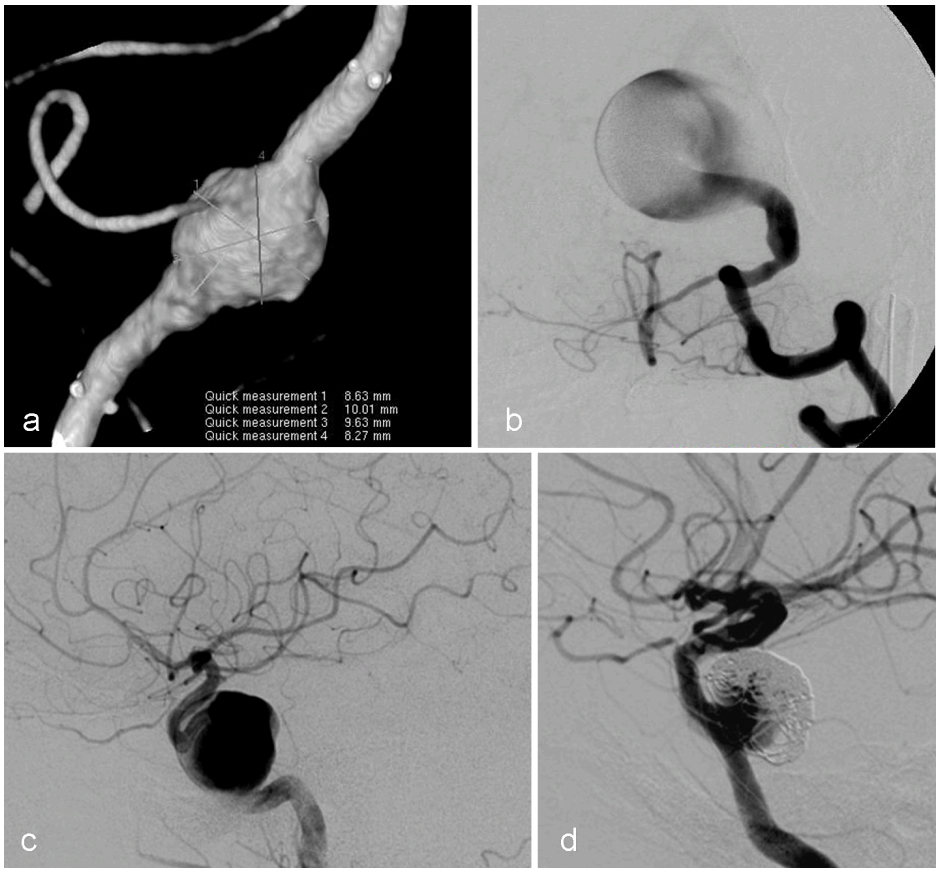


Figure 10.1: Representative angiograms of aneurysms treated with the SFD. Fusiform vertebral artery aneurysm (a); giant saccular aneurysm at the vertebrobasilar junction (b); large cavernous carotid artery saccular aneurysm (c); and a recurrent cavernous carotid artery aneurysm (d).

A standard description of the aneurysm to be treated was made. These details included: rupture status, location, saccular or fusiform shape, and sac dimensions (neck width, maximum diameter, and dome to neck length). Details of prophylactic anti-

thrombosis therapies were reported. These included: the dose and type of drugs used, and the duration of prescriptions.

10.3.1.3 Follow-up Protocols

A standard report of each patient's clinical status was requested at the time of follow-up imaging. In order to assess the effectiveness of the SFD at inducing thrombosis, it was requested that follow-up catheter angiography was performed 1 month after stopping antiplatelet therapy. The timing of interval imaging was therefore left to the centres. The follow-up period range was 9–528 days (median 119 days). Assessments of the degree of aneurysm thrombosis after SFD placement were rated as complete occlusion (OG1), neck remnant (OG2) and residual sac filling (OG3), at the end-of-treatment and follow-up (Raymond and Roy, 1997).

10.3.1.4 Statistical Analysis

Potential associations between the procedural and delayed complications and the variables related to aneurysm morphology, presentation, and use of adjuvant coils were explored using Fisher's exact test (aneurysm shape, use of coils, location, and previously ruptured vs unruptured aneurysms) and the Pearson's chi-square test (sac size).

10.3.2 Materials

10.3.2.1 Patients

Seventy patients were entered in the study. Patients' prior degrees of disability and symptoms due to the aneurysms were: mRS = 0 in 30, mRS = 1 in 19, mRS = 2 in 12, mRS = 3 in 2, mRS = 4 in 6 and mRS = 5 in 1 patients. Thus 30(43%) treatments were

performed for patients without symptoms, 31(44%) with symptoms but no or only mild disability and 9(13%) with moderate or significant disability i.e. mRS 3–5.

10.3.2.2 Aneurysms and SFD Sizing

Sixty target aneurysms were unruptured and 4 of the 10 ruptured aneurysms were treated within 30 days of haemorrhage. They comprised 44 (63%) saccular and 26 (37%) fusiform shapes. There were 15 (21%) giant (>25 mm), 37 (53%) large (10–25 mm) and 18 (26%) small (<10 mm) aneurysms. Details of target aneurysms are presented in table 10.1. Multiple aneurysms were identified in 5 patients (4 with 2 and 1 with 3 aneurysms). One patient with 2 aneurysms had both treated with the SFD in separate procedures (without complication) and another patient was treated for a co-incidental aneurysm with coils alone at the same procedure. These treatments have not been included in the analysis of primary treatment outcomes. The remaining co-incidental aneurysms were not treated during the study period.

10.3.2.3 Centres

The number of treatments performed in contributing centres varied from 1–9. Treatments per centre were: 1 in 2, 2 in 6, 3 in 2, 4 in 1, 5 in 3, 7 in 2, 8 in 1 and 9 in 1. Thus half the centres performed only 1–3 procedures and for most it was their first experience with SFD.

10.3.2.4 SFD Deployment Technique

Sixty treatments were performed with SFD alone and 10(14%) with adjuvant endosaccular coils. Additional coils were used for parent vessel occlusion during 1 treatment. During the study period many centres were supported by a proctor that was

introduced by the manufacturer, and treatments were performed under general anaesthesia according to the instructions-for-use of the SFD. Briefly, the technique involves positioning a delivery microcatheter (Vasco 21, Balt, Montmorency, France) with its tip distal to the aneurysm and then pushing the SFD, which is applied to a delivery microwire, to the tip of the delivery microcatheter. The system is then aligned with the aneurysm under x-ray fluoroscopy and the SFD deployed by unsheathing it from the constraint of the microcatheter. This involves a combination of pushing the delivery wire and retrieving the microcatheter to allow the SFD to expand and to compensate for any resulting foreshortening. The SFD can be retrieved into the microcatheter and removed or repositioned when less than 80% of its length has been extruded. No retrieval is possible thereafter.

10.3.2.5 Antiplatelet Regimens

All centres prescribed heparin and antiplatelets during treatments. Antiplatelet prescriptions in the majority of patients were a combination of aspirin and clopidogrel (46 pre-treatment and 49 post-treatment) or aspirin and dipyridamole (19 pre-treatment and 11 post-treatment). Single therapy with aspirin (2 pre-treatment and 3 post-treatment) or clopidigrel (3 pre-treatment and 7 post-treatment) was used in a minority. Reports of post-treatment prescriptions were incomplete. Reported intervals to stopping clopidigrel or dipyridamole after treatments were: after 2 months in 5 patients, after 3 months in 3 patients, after 4 months in 17 patients, after 5 months in 5 patients, and after 6 months in 9 patients.

10.4 Results

10.4.1 Procedures

Sixty-seven (96%) primary treatments were completed. In 3 (4%) treatments, an SFD could not be deployed for technical reasons and the procedures were abandoned. These were: failure to catheterise the aneurysm bearing artery, inability to open the SFD correctly and failure to advance a long SFD through the delivery catheter. In the last case, the patient was successfully treated with two shorter SFDs after the study period ended. Another 3 (4%) patients required repeat procedures because of suboptimal SFD deployment. In 2, the initial SFD shortened and another SFD was placed at a second procedure without complication. In the third, positioning 2 SFDs in a dolichectatic artery failed due to foreshortening and a second procedure was performed a few days later with an additional LEO stent (Balt Extrusion). Arterial patency was confirmed after 48 hours but the patient died from pneumonia 1 month later.

10.4.2 Untoward Procedural Events (UPEs)

One or more UPEs were reported in 20 patients. They were: 12(17%) poor SFD opening on deployment, 7(10%) partial or complete parent artery thrombosis (PAT), 6(8%) poor SFD positioning, 4(6%) SFD migration, 3(4%) post procedure extra-cranial haemorrhages and 1(1.5%) complication related to another device. No intracranial haemorrhage was reported.

Thus, the commonest UPE was poor SFD opening on deployment. In 4 procedures, poor SFD positioning and in 3 procedures SFD migrations were

concurrently reported. Thus overall in 15(21%) of procedures SFD deployment difficulties (DD) were reported and amalgamated for statistical analysis. The consequences of these events were that 3 patients required repeat procedures, as described above. In 1 other patient, the operator decided to occlude the parent artery with coils because of incomplete SFD opening. This was without clinical worsening.

The 7 reports of PAT occurred together with reports of SFD DD in 6 procedures (poor opening in 3, positioning in 1 and both in 2). At the remaining procedure, branch artery thrombosis was treated successfully with abciximab. Subsequent extracranial bleeding complicated 3 procedures. In 1 patient this occurred after endovascular access via the cervical carotid artery. A resulting neck haematoma was so serious that the patient required a week of intensive care treatment and the relevant internal carotid artery was occluded on follow-up angiography. A significant acute groin haematoma was reported in 1 further patient and 1 patient developed serious gastric bleeding 48 hours post-procedure and died of pneumonia 2 weeks later.

Table 10.1 Aneurysm locations presented as maximum sac size, neck width, and morphology

Aneurysm location	Saccular aneurysms (n=44)						Fusiform (n=26)			Total (n =)
	Maximum dimension (mm)			Neck width (mm)*			Maximum dimension (mm)			
	< 10	10 - 25	> 25	< 4	4 - 10	> 10	< 10	10 - 25	> 25	
ICA cavernous	1	6	2	1	5	3	2	7†	1	19
COA	5	8	3	2	12	2	2	1	0	19
PCoA	1	4	1	1	4	1	0	0	0	6
MCA	1	3	0	0	3	1	0	1	1	6
BA trunk	0	2	0	0	1	1	1	1†	1	5
SCA	0	1	0	0	1	0	0	0	0	1
AICA	0	1	1	0	2	0	0	0	0	2
PICA	1	0	0	0	1	0	0	1‡	0	2
VA	2‡	1*,†	0	1	1	0	2	0	5‡	10
Total (n =)	**11**	**26**	**7**	**5**	**30**	**8**	**7**	**11**	**8**	**70**

Abbreviations: n (numbers of aneurysms), mm (millimetres), AICA (anterior inferior cerebellar artery), BA (basilar artery), COA (carotid ophthalmic artery), ICA (internal carotid artery), MCA (middle cerebral artery), PCoA (posterior communicating artery), PICA (posterior inferior cerebellar artery), VA (vertebral artery).

* For one saccular aneurysm the neck width was not measured; † Procedure abandoned (failed treatments);

‡ Second procedures

Table 10.2 Clinical complications observed in patients treated with SFD

Aneurysm morphology			Complications	Cause or contributing events	Outcome
Location	*Size (mm)*	*Shape*			
			Procedure related:		
BA	13	S	Cerebral infarction	Thromboembolism attributed to the use of coils	Hemiparesis
BA	32	F	Pneumonia	Second procedure due to poor SFD positioning	Died
PcomA	32	S	Gastric bleeding followed by pneumonia	Antiplatelet drugs	Died
CCA	35	F	Neck hematoma	Carotid puncture for EVT and antiplatelets drugs	Prolonged ICU stay
MCA	30	F	Groin bleeding	Antiplatelet drugs	Resolved
			Delayed complications:		
AICA	11	S	Worsening brainstem compression symptoms	Aneurysm thrombosis and mass effect	Resolved
CCA	27	F	Worsening of cranial nerve palsy	Aneurysm thrombosis and mass effect	Resolved
COA	22	S	Worsening of cranial nerve palsy	Aneurysm thrombosis and mass effect	Resolved
CCA	10	S	Parent artery occlusion	Poor SFD deployment	Hemiparesis
BA	35	F	New cranial nerve palsy	Aneurysm thrombosis and mass effect	Died
MCA	24	F	Late increase in aneurysm size and bleeding	Uncertain; possible use of warfarin anti coagulation	Died

Abbreviations: BA (basilar artery), PcomA (posterior communicating artery), CCA (carotid cavernous artery), MCA (middle cerebral artery), AICA (anterior inferior cerebellar artery), COA (carotid ophthalmic artery), S (saccular), F (fusiform), EVT (endovascular therapy).

10.4.3 Procedural Morbidity

The GCS of patients immediately prior to treatment were: GCS 15 in 61 (plus 2 abandoned); GCS 10–14 in 5 (plus 1 abandoned); and GCS 10 in 1. In the 48 hours after treatment, 1 patient worsened (GCS 13 to 5) and 2 patients improved (GCS 14 to 15). The GCS worsening in the patient followed a thromboembolic complication, which caused a new permanent hemiparesis. This was attributed to thromboembolism caused by adjuvant endosaccular coils. Post-procedure MRI showed a new infarct in the temporal lobe and delayed angiography showed the SFD to be patent. There were no procedural deaths reported in the acute period. However, 2 patients whose treatments were complicated by UPEs, died of pneumonia within 1 month of the procedure. Thus the immediate procedural related morbidity was 1 new neurological deficit and 2 deaths.

10.4.4 Delayed Morbidity

Follow-up reports on clinical outcomes were returned on 50 (71%) patients. Delayed worsening of symptoms and/or new abnormal neurological signs were reported in 6 (12%) of these 50 patients. Transient events in 3 patients occurred within 30 days of treatment and were attributed to increased mass effect following aneurysm thrombosis. These included exacerbation of headaches, and in 2 patients (with aneurysms of the cavernous carotid artery) worsening opthalmoplegia. Permanent deficits developed in 3 patients and were attributed to delayed thrombosis of the SFD in the first patient (who developed hemiparesis 10 days post-procedure), increased mass effect in the second (who developed a new facial palsy a few days after treatment of a giant basilar

artery aneurysm and died 2 weeks later due to increased brainstem compression) and delayed aneurysm bleeding in the third patient. In this last case, follow-up angiography at 5 months showed residual aneurysm filling. Two months later the patient experienced increasing headache and acute hemiparesis. CT showed aneurysm enlargement and acute haemorrhage (figure 10.2). The patient died 4 weeks later despite surgical bypass. He had required long-term anticoagulation with warfarin because of a prosthetic heart valve and remained on aspirin after clopidigrel was stopped 2 months following SFD deployment. Thus the overall morbidity reported amongst 50 patients with follow-up was 2 permanent neurological deficits and 4 deaths, i.e. morbidity 2(4%) and mortality 4(8%). All clinical complications are summarized in table 10.2.

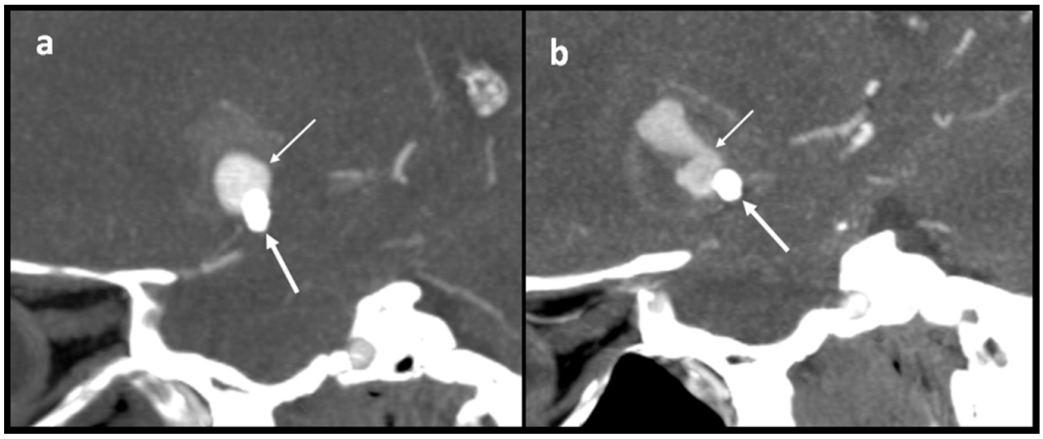


Figure 10.2: Partially thrombosed aneurysm after treatment with the flow diverter. CT angiograms showing a residual lumen within a large partially thrombosed fusiform aneurysm of the middle cerebral artery. Follow-up CTA (a) was performed 4 months and (b) 6 months after SFD (arrows) placement. The second follow-up study (b) shows enlargement of the residual aneurysm lumen (arrow heads) and was performed after a new haemorrhage (not shown).

10.4.5 Angiographic Outcomes

The end-of-treatment (EOT) assessments of the degree of aneurysm occlusion for 68 treated aneurysms (67 patients) were: OG1 in 7(10%), OG2 in 4(6%) and OG3 in 57(84%) aneurysms. Reports of follow-up angiograms were returned for 49(72%) aneurysms. The degrees of aneurysm occlusion on follow-up were: OG1 in 24(49%), OG2 in 13(26%) and OG3 in 12(25%). Thus all but 2 aneurysms were unchanged or improved on follow-up (1 OG1 and 1 OG2 dropped to OG3 on follow-up) (table 10.3). Follow-up imaging showed parent artery occlusion (PAO) in 7(14%) and a degree of arterial narrowing in 3(6%). Three PAOs were associated with UPEs (neck haematoma, DD, and deliberate PAO with coils), 1 was attributed to non-compliance with antiplatelet treatment and 3 occurred for no apparent reason. The degree of arterial narrowing reported in 3 cases was not graded but reported as severe in 1 patient. In 2 cases of arterial stenosis on follow-up imaging, UPEs had occurred during treatments (poor SDF opening and thrombosis requiring salvage abciximab).

The frequency of complete occlusion (i.e. OG1) and a possible effect of the timing of follow-up imaging was investigated by dividing the cohort at 20 week intervals post-treatment and comparing the within-group percentage occlusion grades. This analysis showed that the proportion of cured aneurysms increased with time intervals (table 10.3 and figure 10.3).

10.4.6 Statistical Analysis

No statistically significant relationship was found between the variables related to aneurysm morphology, rupture status, use of adjuvant coils and the occurrence of procedural and delayed complications (table 10.4).

Table 10.3 Angiographic outcomes for the aneurysms treated with SFD

Occlusion grade	Angiographic status at EOT	Follow-up available	Occlusion status of aneurysms at follow-up relative to EOT	Angiographic status at follow-up	Intervals (weeks) since treatment			
					0-20	*20-40*	*40-60*	*60-80*
OG1	7	5	OG1, 4; OG2, 0; OG3,1	24	17	3	2	2
OG2	4	4	OG1, 2; OG2, 1; OG3,1	13	13	0	0	0
OG3	57	40	OG1, 18; OG2, 12; OG3,10	12	9	3	0	0
OG1%	10%	10%		49%	44%	50%	100%	100%
95% CI	3-17%	3-17%		35-63%	28-60%	11-89%	-	-

Angiographic outcomes for the cohort of aneurysms with complete follow-up i.e. end of treatment and follow-up angiogram. Abbreviations: OG1 (complete occlusion); OG2 (neck remnant); OG3 (saccular filling).

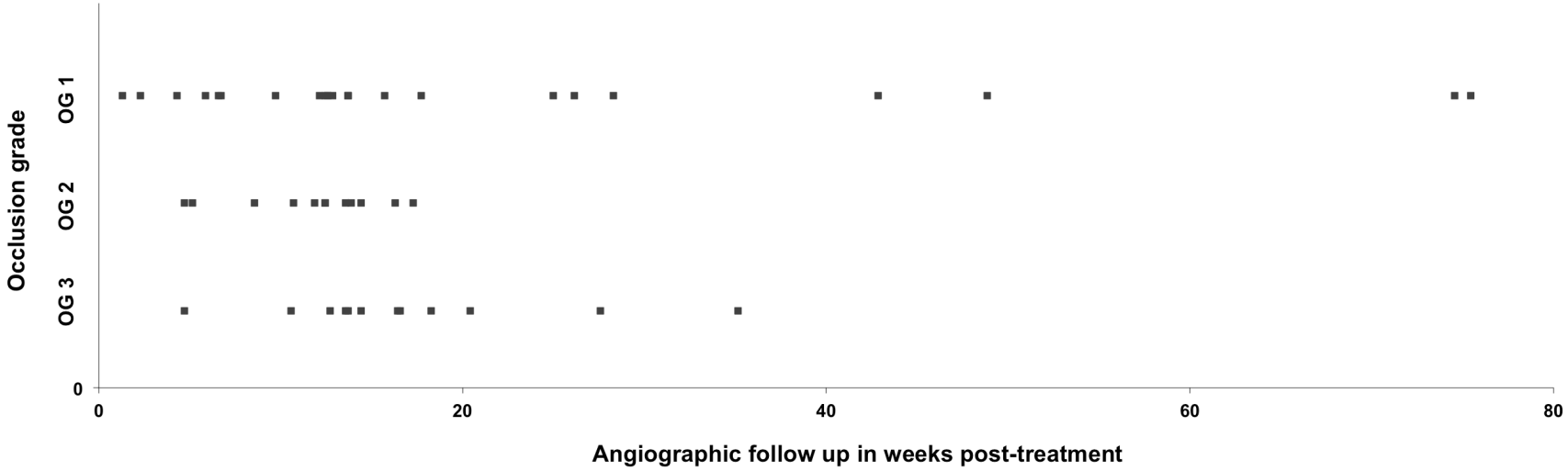


Figure 10.3: Timings and results of angiographic follow-up. Plot of angiographic outcomes against follow-up times in weeks.

Table 10.4 Effect of patient and procedure related variables on SFD deployment difficulty, flow disturbance, and delayed neurological complications

Procedural and patient variables		Deployment difficulty		Flow disturbance		Delayed neurological complications	
		Present	Absent	Present	Absent	Present	Absent
Sac morphology	Saccular	9	36	5	40	4	29
	Fusiform	6	19	2	23	2	16
		p-value 0.76		*p-value 1.0*		*p-value 1.0*	
Aneurysm size	Small	4	18	2	20	3	13
	Large	7	30	3	34	2	24
	Giant	4	7	2	9	1	8
		p-value 0.42		*p-value 0.61*		*p-value 0.56*	
Coils	Used	4	5	1	8	2	5
	Not used	11	50	6	55	4	40
		p-value 0.09		*p-value 1.0*		*p-value 0.18*	
Location	Anterior	12	36	5	43	4	31
	Posterior	3	19	2	21	2	14
		p-value 0.36		*p-value 1.0*		*p-value 1.0*	

Untoward events reported during and after treatments versus aneurysm shapes, sizes location, and use of coils. Deployment difficulty = poor opening, poor positioning, or migration of SFD. Flow disturbance = partial or complete thrombosis of parent artery.

10.5 Discussion

The concept of a stent capable of inducing thrombosis of intracranial aneurysms has stimulated the development of flow diverters over the last 15 years. Several researchers have demonstrated their potential to disrupt endosaccular blood flow in experimental aneurysms, and systematic haemodynamic studies have informed their design (Sadasivan et al., 2009). These established 70% porosity (defined as the proportion of open area to total area of the stent) as the optimum (Liou et al., 2007). Lower porosity covered stents have generally proved too inflexible for intracranial use and results of stent-alone treatments using conventional high porosity stents have been inconsistent (Szikora et al., 2006). Some operators have proposed the use of double or overlapping conventional stents to increase the effective stent porosity (Doerfler et al., 2004) and new covered devices are being tested (Li et al., 2009).

Against this background, FDs designed with low porosity and high flexibility were first used in humans in late 2006. To date, the few reports of their efficacy have been encouraging. Lylyk et al. reported a series of 53 patients treated in Buenos Aires using the pipeline embolisation device (Chestnut Medical Technologies, Inc., Menlo Park, CA) (Lylyk et al., 2009). The aneurysm types were predominantly saccular with only 12% fusiform and nearly half were small in size. Clinical experience with the same FD was collected on 31 patients treated in the 'Pipeline Embolization Device in the Intracranial Treatment of Aneurysms (PITA) Trial' conducted between January and November 2007 (Fiorella et al., 2009). One of the 4 contributing centres recently reported on 8 additional aneurysms (Szikora et al., 2010). Few procedure-related neurological

complications were reported; a new stroke rate of 6% in the PITA trial and none in the Buenos Aires report. The latter reported delayed exacerbation of aneurysm related cranial nerve palsies in 3 patients. Complication rates reported in this chapter are similar with only one acute new neurological deficit despite technical difficulties associated with SFD deployment in 21% of procedures. Like the Buenos Aires experience, a minority of our patients developed delayed neurological symptoms. The cause of transient worsening of symptoms after induced aneurysm thrombosis is generally attributed to aneurysm expansion. However, the low porosity of FDs theoretically increases their likelihood of occluding covered side branch arteries, which might also cause worsening of symptoms (Szikora et al., 2010).

In this registry, partial or complete parent artery thrombosis affected 7 procedures and was attributed to the SFD deployment difficulties rather than inadequate antithrombotic prophylaxes since these were given during all the procedures. However, in 1 case it was caused by the device covering a large branch artery. A cause of 1 delayed complication was parent artery occlusion found on follow-up imaging. The relative contribution of aneurysm expansion or branch artery occlusion in patients developing new neurological deficits is therefore difficult to assess. Our experience suggests a real vulnerability of parent artery blood flow after SFD deployment, perhaps due to a combination of its relatively low radial force and high metal density, which high dose antiplatelet therapy mitigates. In this regard, treatment using SFDs after acute SAH raises several concerns. Firstly, after SAH there is a natural reluctance to prescribe antiplatelets prior to securing the aneurysm against

rebleeding. In the minority of patients treated after acute SAH in this study, it was the usual practice to withhold prophylaxis with antiplatelet treatment until the SFD was deployed; accepting a small additional risk of thrombotic complications. The second issue is the longer delay to complete thrombosis of the aneurysm after SFD treatment than after clipping or coiling. During this period, the patient is at risk of more prolonged bleeding, should the aneurysm re-rupture, because of antiplatelet medication. One solution is to additionally pack the aneurysm sac with coils. In this cohort, adjuvant coils were only used in 1 of the 3 saccular aneurysms treated after acute SAH. Thus, when it proves difficult or impossible to place coils, treating physician have to assume that the alteration of local haemodynamics induced by the SFD reduces the risk of rebleeding. Currently, there is insufficient experience to prove this assumption. The relationship between complications and anti-thrombotic prophylaxis was clear in the patients who suffered haemorrhagic complications but its contribution to delayed events is complex. In this cohort, patient non-compliance caused delayed spontaneous artery occlusion and flow disturbances observed during treatments would probably have resulted in more frequent thrombotic events without the use of heparin or antiplatelets. Its contribution to the subsequent evolution of endosaccular thrombosis is unclear and needs further systematic study. It is tempting to attribute concurrent long-term anticoagulation and aspirin therapy as the cause of delayed aneurysm enlargement and haemorrhage, seen in one patient. On the same basis, antiplatelet therapy might contribute to symptomatic worsening attributed to sac swelling observed in the early post-procedure period. Another unanswered question raised by

our results, is whether it is a factor in the asymptomatic failure of sac occlusion, seen on follow-up imaging, in a minority of aneurysms.

Limitations to this study are incomplete follow-up imaging, no longitudinal data and the relatively short follow-up period. The 50% rate for complete occlusion up to 3 months is similar to the Buenos Aires experience (Lylyk et al., 2009). Their longitudinal follow-up suggested that induced thrombosis was progressive, with the 3-month 56% rate of complete occlusion rising to 95% at 12 months (Lylyk et al., 2009). Progressive improvement in occlusion rates were reported by Zentano et al. (Zenteno et al., 2008) and no recurrence was reported for Pipeline treated aneurysms (Szikora et al., 2010). Our findings are similar but because our data are based on a single follow-up time point, between-patients variations cannot be differentiated from variations over time. Thus the subsequent behaviour of those aneurysms followed-up early is unknown. The aneurysms reported here comprised a heterogeneous group, with a higher proportion of fusiform type and posterior circulation aneurysms than the series of Lylyk et al. or Szikora et al. (Lylyk et al., 2009; Szikora et al., 2010). A concern is two aneurysms whose occlusion grades dropped relative to the EOT grade and a large study of sufficient numbers will be needed to show the long-term stability of thrombosis of different aneurysm types. This concern has resulted in a recent change in the manufacturer's instructions for use and the SFD should now only be used to support embolisation with coils.

10.6 Conclusion

The conclusions that can be drawn from the results of this chapter need to be considered with reference to its objectives and methodology. The intention was to collect data on the use of the SFD during a period when it was being first used in a large number of hospitals, by experienced practitioners who had either not previously used the device or had only done so in very few patients. The centres contributed data on a voluntary basis and deserve our thanks. A registry can highlight early technical and clinical problems which would take much longer to identify without amalgamated data. Complete procedure reports allowed early recognition of deployment problems leading to a redesign of the SFD and an alteration in its instructions for use. The associations tested, though not statistically significant, should help to inform the design of future studies and devices. Several technical improvements have since been made to improve the SFD's visibility on x-ray fluoroscopy and deployment control. A new guide pusher has now been developed in addition to a new radio-opaque marker, which is more visible than the original version. However, conclusions about long-term efficacy must be tentative, because a possible bias to under reporting of poor outcomes cannot be excluded without complete follow-up data. Further studies are needed to define the place of flow diverters in the endovascular treatment of aneurysms and it is too early to predict their ultimate role.

10.7 Reception of the Work

Following publication of the work presented in this chapter, in 2010, the reported findings informed the neurointerventional community about the safety, efficacy, and

outcomes of flow diversion treatment. The work has since served as a reference for numerous subsequent clinical reports (over 145 citations of the total 230 publications indexed in pubmed that included the search term “flow diverter”) on the use of FDs for intracranial aneurysm treatment.

11

Assessment of Angiographic Outcomes after Flow Diversion Treatment of Intracranial Aneurysms: A New Grading Schema

11.1 Abstract

Background and purpose: Flow diverter (FD) devices have emerged as an alternative treatment for a subgroup of intracranial aneurysms. The principle of endovascular flow diversion is inherently different from endosaccular coil embolisation. To monitor the angiographic outcomes for FDs, a sensitive and reliable new measure is required. This chapter proposes a new grading schema and discusses its applicability and reproducibility.

Materials and methods: The grading schema was developed while conducting a registry to investigate outcomes of patients treated using a particular FD (SILK flow diverter; Balt Extrusion, France). The proposed schema is designed for both saccular and fusiform shaped aneurysms. For both morphologies, it documents the degree of aneurysm occlusion using a five-point scale and evaluates the parent artery patency on a three-point scale. Two neuroradiologists used the schema to independently rate 55 angiographic studies showing comparable treatment and follow-up angiograms of patients treated with a FD. Inter-observer agreement was calculated using the weighted kappa co-efficient.

Results: Both readers found the schema easy to apply. Overall, there were ten discordant readings for degree of aneurysm occlusion and two for parent artery patency. Inter-observer agreement was excellent for both the assessment of aneurysm occlusion (k = 0.89; C.I. = 0.81-0.99) and parent artery patency (k = 0.90; CI = 0.76-1.0).

Conclusion: The proposed schema is sufficiently sensitive to register gradual aneurysm

occlusion and parent artery patency on interval angiograms. The schema is reproducible, and applicable to both saccular and fusiform aneurysms. More data on follow-up of FD-treated aneurysms would establish its efficacy in predicting the long-term behaviour of treated aneurysms.

11.2 Introduction

Coil embolisation (CE) is an effective method for treating intracranial aneurysms, however, for a subgroup of aneurysms endosaccular packing with coils is either not feasible or not durable (Johnston et al., 2008; Murayama et al., 2003; Raymond et al., 2003). Such aneurysms include: (a) very large or giant, wide neck saccular aneurysms and (b) fusiform shape or circumferential aneurysms. Altering the blood flow into aneurysms using a stent placed in the parent vessel was proposed as a possible alternative treatment strategy for such aneurysms (Benndorf et al., 2001; Geremia et al., 1994). This concept was realised in clinical practice with the introduction of flow diverters (FDs), which are low porosity stents with a greater metal surface area than conventional stents and are designed to reconstruct the aneurysm-bearing artery to promote intrasaccular thrombosis and occlusion. Whereas CE aims to fill the aneurysm sac with coils and occlude it by promoting intra-aneurysmal thrombosis, FDs are deployed in the parent artery across the aneurysm neck to redirect blood flow in the parent artery away from the aneurysm sac. Disruption of both inflow and outflow of blood by the FD deployed at the *parent artery - aneurysm interface* creates an intra-aneurysmal environment favourable for thrombosis, which, over a period of time, leads to gradual aneurysm occlusion (Lylyk et al., 2009). The flow diversion treatment of intracranial aneurysm is relatively new and experience with this is limited (at the time of publication of this work). However, early reports identify it as an effective treatment technique, particularly for those aneurysms for which CE may not offer complete cure (Byrne et al., 2010; Lylyk et al., 2009; Szikora et al., 2010).

In order to assess the success of any treatment, an objective and reproducible measure of efficacy is required. For CE, a three-point scale is used, which describes the degree of aneurysm occlusion based on the angiographic appearance as complete, with residual neck, or with residual sac (Campi et al., 2007; Raymond and Roy, 1997). This grading scheme is simple, easy to administer, and triages anatomical outcomes, each of which is presumed to have different prognostic significance. For instance, it separates the completely or near-completely occluded aneurysms from the aneurysms with residual filling of sac, the latter being associated with higher risk of future rupture; and it separates the completely occluded aneurysm from the ones with neck remnant, the latter being associated with a higher incidence of subsequent recurrence (Raymond et al., 2007).

For flow diversion treatment of intracranial aneurysms, although the treatment goal remains the same i.e. complete obliteration of the aneurysm, the treatment principle is different from endosaccular CE. The differences are related to: the effect on the parent artery, coverage of the aneurysm neck, coverage of branch arteries, and delayed aneurysmal thrombosis. FD deployment potentially compromises blood flow in the parent artery and requires the use of prophylaxis with antiplatelet drugs. Coverage of the aneurysm neck and delayed progressive thrombosis changes the chronology of sac occlusion compared to CE. In the latter, occlusion is established in a few days and surveillance imaging is directed at monitoring for re-opening due to coil compaction. After FD treatment, monitoring in the short- and medium-term is aimed to document progressive sac thrombosis and remodelling of the parent artery. Once achieved, the

reconstruction of *parent artery – aneurysm complex* and the closure of aneurysmal neck is presumed to be permanent; contrary to CE, for which a modest degree of neck remnant may be an inevitable part of clot maturation and coil mass retraction (Friedman et al., 2003; Murayama et al., 2003). Thus, with CE, surveillance imaging is concerned with the long-term durability of the treatment and the detection of recurrence while the same is not true for FD treatment, where the intention is to monitor progression of aneurysm occlusion.

At Oxford Neurovascular and Neuroradiology Research Unit (ONNRU), we identified these issues when conducting a registry (discussed in chapter 10) to investigate outcomes of patients treated using a particular FD (SILK flow diverter; Balt International, Montmorency, France) (Byrne et al., 2010). It quickly became clear that the classification system in current use, designed to assess effectiveness of CE, was inadequate for defining the effects of the new FD devices. A new schema was therefore developed to assess the angiographic outcomes of aneurysms treated with FDs. The purpose of this chapter is to assess the feasibility and reproducibility of this new grading system.

11.3 Materials and Methods

Angiograms collected at 11 international centres, which contributed to the SILK registry were used to assess the new grading schema. The registry was conducted to assess the safety and efficacy of the SILK flow diverter (Balt Extrusion, Montmorency, France), used with or without endosaccular coils in a subgroup of aneurysms considered unsuitable for conventional endosaccular packing (chapter 10). Imaging data from

these treatments, submitted to ONNRU for central evaluation, were searched to identify two-dimensional digital subtraction angiograms (2D-DSA) showing comparable views of aneurysms at treatment and on follow-up. Fifty-five angiographic datasets, all of them acquired in 2008 and 2009, were extracted and independently reviewed by two experienced interventional neuroradiologists using the grading schema described below. Of the 55 angiograms reviewed, 39 showed saccular aneurysms while 16 angiograms were of fusiform aneurysms. The data sets had been anonymised prior to their entry in the registry and coded labels were used throughout the work discussed in chapters 10 and 11.

A trained researcher (MK) explained the grading schema to readers A (JVB) and B (IQG). Reader A had more than 20 years and reader B had ~10 years of experience in neuroradiology. Prior to presentation of the angiographic datasets to the readers, both were shown illustrations explaining the two axes and the respective categories on each axis of the grading schema, described in the following section. Subsequently, the 55 angiographic datasets, including end-of-treatment and follow-up angiograms, were presented to the readers in a random order and in separate sessions. The readers were asked to independently rate the presented angiograms for the degree of contrast filling of the aneurysm and for parent artery patency. Pre-treatment images were made available to the readers to obtain baseline dimensions of the treated aneurysm.

11.3.1 Grading Schema for the Assessment of Angiographic Outcomes Following Endovascular FD Deployment

The proposed grading schema documents the angiographic outcomes following endovascular FD deployment on two axes. Axis-I grades the degree of aneurysm occlusion (for both saccular and fusiform morphologies) on a five-point scale, assigning a higher score to greater aneurysm occlusion. Parent artery status following FD deployment is assessed on Axis-II using a simple three-point scale. Scores for the two axes are reported separately. Details of the grading system are discussed below with pictorial descriptions in figures 11.1 and 11.2, and illustrative case examples in figures 11.3 – 11.6.

11.3.1.1 Axis I: Degree of Aneurysm Occlusion

11.3.1.1.1 Saccular Aneurysms

Grade 0 No change in the endoaneurysmal flow

Grade 1 Residual contrast filling greater than 50% of the pre-treatment aneurysm volume (includes contrast medium stasis or a reduction in the contrast density inside the aneurysm sac)

Grade 2 Residual contrast filling less than 50% of the pre-treatment aneurysm volume

Grade 3 Residual filling confined to the neck region and not extending beyond the width of neck

Grade 4 No residual filling i.e. complete obliteration of the aneurysm

11.3.1.1.2 Fusiform or Circumferential Aneurysms

For the fusiform aneurysms, sac dimensions are recorded as the maximum width *(W)*, the maximum length *(L)*, and the width of the endovascular FD *(FD_w)*. Following treatment, width of the remnant sac *(w)* is measured on either side of the deployed FD *(w_1 and w_2)* and the two measurements are added to obtain an overall estimate of the width of the remnant sac *($w = w_1 + w_2$)*; residual sac length *(l)* at the point of maximum contrast filling is also measured. *W-FD_w* and *L* are used as denominators for comparing the dimensions of the remnant sac *(w and l)* on subsequent angiograms (figure 11.2).

Grade 0 No change in the endoaneurysmal flow

Grade 1 Residual contrast filling >50% the pre-treatment length *and* >50% the pre-treatment width of the aneurysm *($l > 50\%$ L and $w > 50\%$ W-FD_w)*

Grade 2 Residual contrast filling either <50% the pre-treatment length *or* <50% pre-treatment width *($l < 50\%$ L or $w < 50\%$ W-FD_w)*

Grade 3 Residual contrast filling <50% pre-treatment length *and* <50% pre-treatment width *($l < 50\%$ L and $w < 50\%$ W-FD_w)*

Grade 4 No residual contrast filling i.e. complete obliteration of the aneurysm

($l = 0$ and $w = 0$)

11.3.1.2 Axis II: Patency Status of the Parent Artery

Grade a No change in the parent artery diameter

Grade b Narrowing of the parent artery

Grade c Parent artery occlusion

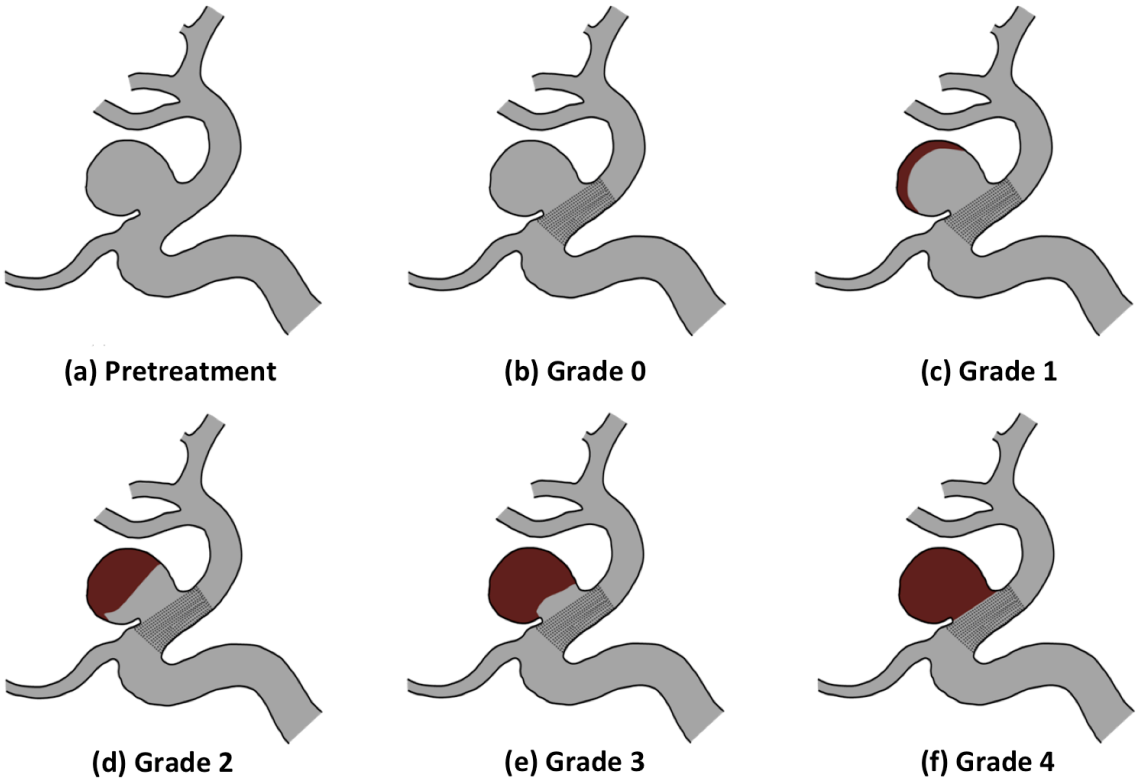


Figure. 11.1: Axis I grading for saccular aneurysms. Grading the degrees of aneurysm occlusion before (a) and after flow diverter treatment (b-f). Grade 0 (b) no change in sac filling despite device deployment; grade 1 (c) any change in endosaccular flow but with at least 50% of residual sac filing; grade 2 (d) less than 50% of residual sac filling, and grade 3 (e) similar to grade 2 but the filling is restricted to a region which is smaller than the width of the original neck. Grade 4 (f) represents complete sac occlusion with a patent parent artery. The effects of flow diverter device on the parent artery diameter are scored separately.

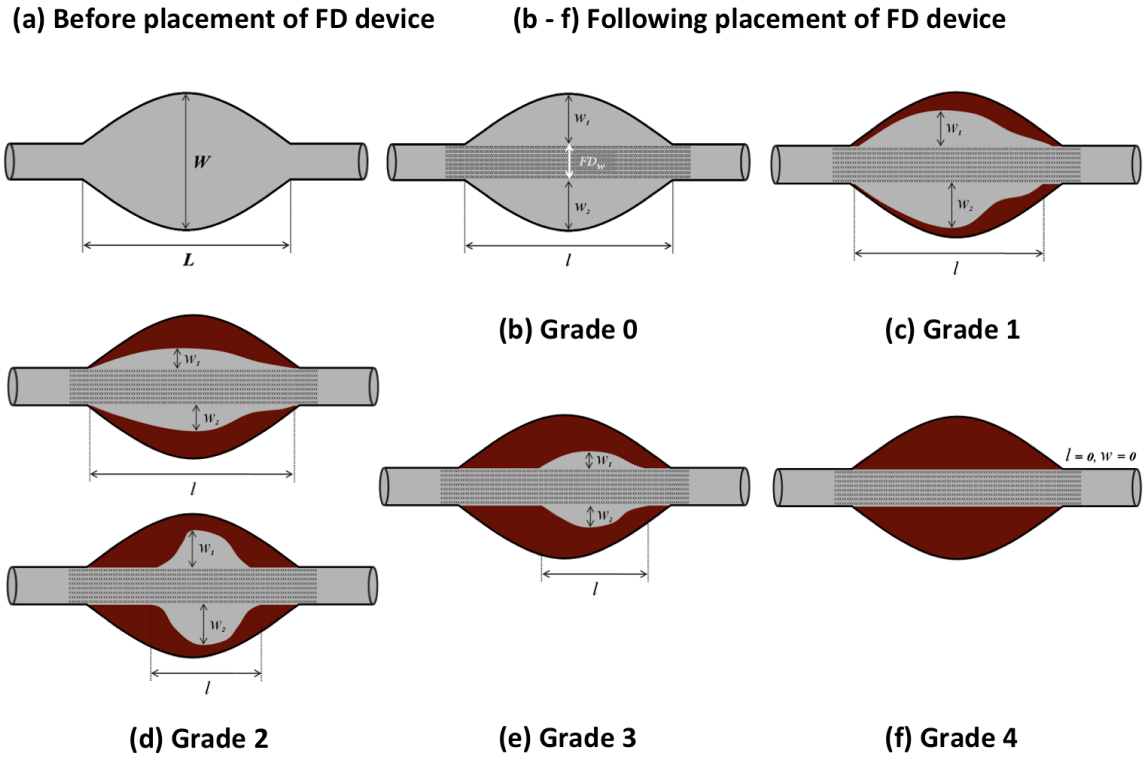


Figure 11.2: Axis II grading for fusiform aneurysms. Grading the degrees of aneurysm occlusion before (a) and after flow diverter treatment (b-f). Scoring is performed on 2-D angiograms and the sac dimensions are recorded as the maximum width *(W)*, the maximum length *(L)*, and the width of the endovascular FD *(FD_w)*. Following treatment, width of the remnant sac *(w)* is measured on either side of the deployed FD *(w_1 and w_2)* and the two measurements are added to obtain an overall estimate of the width of the remnant sac *($w = w_1 + w_2$)*; residual sac length *(l)* at the point of maximum contrast filling is also measured. *W-FD_w* and *L* are used as denominators for comparing the dimensions of the remnant sac *(w and l)* on subsequent angiograms. The degree of contrast filling after treatment is graded 0 (b) when there is no perceptible change in sac filling; grade 1 (c) when filling exceeds 50% of the denominator sac width *(W) and* 50% of the denominator sac length *(L)*; Grade 2 (d) when contrast fills less than 50% of the denominator sac width *(W) or* less than 50% of the denominator sac length *(L)*; Grade 3 (e) for contrast filling less than 50% of the denominator sac width *(W) and* less than 50% of the denominator sac length *(L)*, while grade 4 (f) is complete aneurysm occlusion with parent artery reconstruction.

11.3.2 Statistical Analysis

Cohen's kappa coefficient was calculated to assess the inter-observer agreement on the two axes of the proposed grading schema. When calculating the kappa statistic, the ordinal nature of the grading system and the size of categories on the two axes were taken into account by assigning proportional weights to individual categories. Quadratic weights were found appropriate for the axis I (5 degrees of residual sac filling), while linear weights were assigned to the axis II (3 degrees of parent artery patency). The resulting kappa statistic was interpreted for the inter-observer agreement using the following criteria: ≤ 0.40 poor agreement, 0.40 – 0.75 fair to good agreement, and ≥ 0.75 excellent agreement (Fleiss, 1981). The statistical analysis was performed using SPSS software (SPSS v 18.0, SPSS Inc., Chicago, IL).

11.4 Results

Both readers found the grading schema easy to administer, following a short tutorial by the researcher. Compared with axis I (degree of aneurysm occlusion on a five-point scale), the inter-observer agreement was better for axis II (assessment of parent artery status on a three-point scale). Observer's ratings on the two axes are summarised in tables 11.1 and 11.2.

Inter-observer agreements were excellent both for the assessment of degree of aneurysm occlusion (kappa statistic 0.89; 95% CI 0.81-0.99) and the parent artery patency status (kappa statistic 0.90; 95% CI 0.76-1.0). Overall, there were ten discordant readings for the assessment of aneurysm occlusion and two for the assessment of the parent artery patency.

Table 11.1: Axis I: Grading of the saccular occlusions following deployment of the FD devices

		Evaluator A				
	Grades	**0**	**1**	**2**	**3**	**4**
Evaluator B	**0**	13	0	0	0	0
	1	5	10	0	0	0
	2	1	1	9	0	0
	3	0	0	1	7	0
	4	0	0	0	2	6

Table 11.2: Axis II: Grading of the parent artery patency following deployment of the FD devices

		Evaluator A*		
	Grade	**a**	**b**	**c**
Evaluator B*	**a**	43	2	0
	b	0	7	0
	c	0	0	2

* For one angiogram, parent artery patency could not be assessed

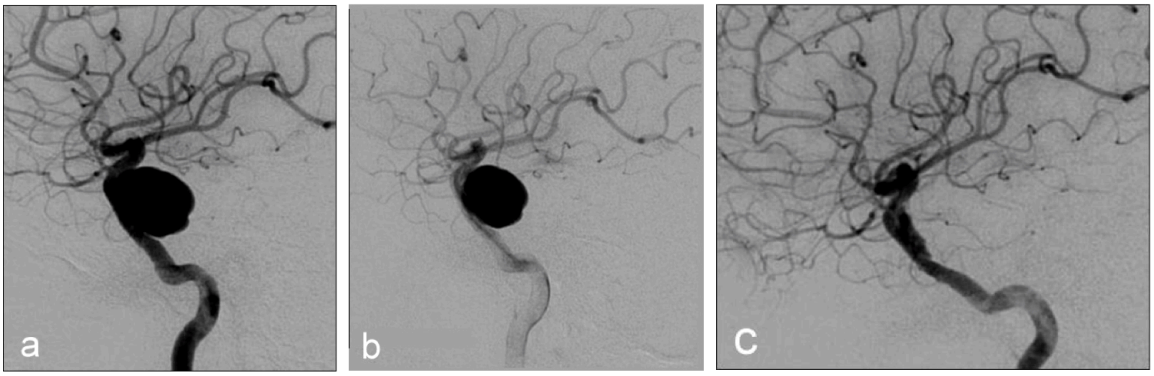


Figure 11.3: Illustrative case 1. Angiographic images for a patient treated with flow diversion**:** (a) Pre-treatment 2D-DSA; (b) end-of-treatment control angiogram showing no reduction in flow *(grade 0 on axis-I)*; (c) 3-months follow-up angiogram showing neck remnant *(grade 3 on axis-I)* and a patent parent artery *(grade a on axis-II)*.

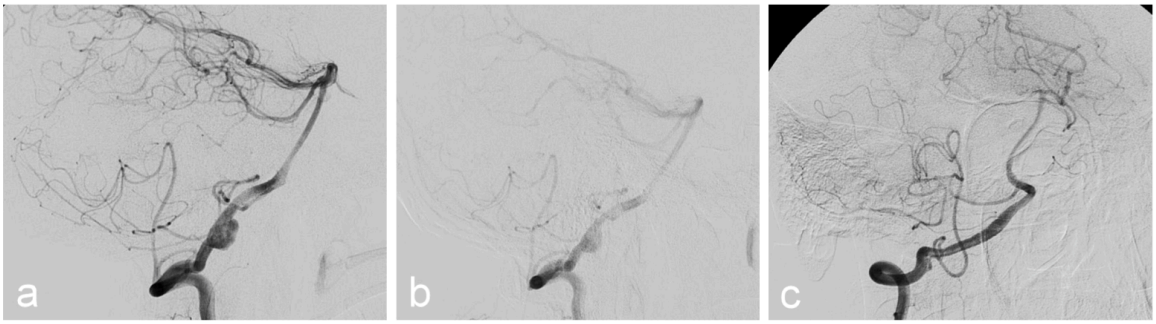


Figure 11.4: Illustrative case 2. Angiographic images for a patient treated with flow diversion**:** (a) Pre-treatment 2D-DSA; (b) end-of-treatment control angiogram showing flow reduction with contrast filling greater than 50% of the denominator width and length of the aneurysm *(grade 1 on axis-I)*; and (c) 6-months follow-up angiogram showing complete obliteration of the aneurysm *(grade 4 on axis-I)* with a patent parent artery *(grade a on axis-II).*

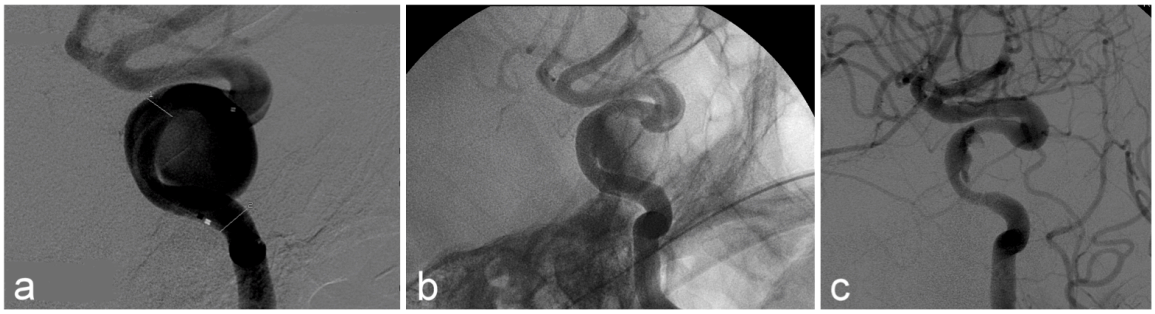


Figure 11.5: Illustrative case 3. Angiographic images for a patient treated with flow diversion**:** (a) Pre-treatment 2D-DSA; (b) end-of-treatment control angiogram showing flow reduction with contrast filling greater than 50% of the pre-treatment aneurysm volume *(grade 1 on axis-I)* and a patent parent artery *(grade a on axis-II)*; (c) 3-months follow-up angiogram showing contrast filling less than 50% of pre-treatment aneurysm volume; residual contrast filling is mainly in the neck region but extends beyond the width of aneurysm neck *(grade 2 on axis-I)* and narrowing of the parent artery *(grade b on axis-II)*.

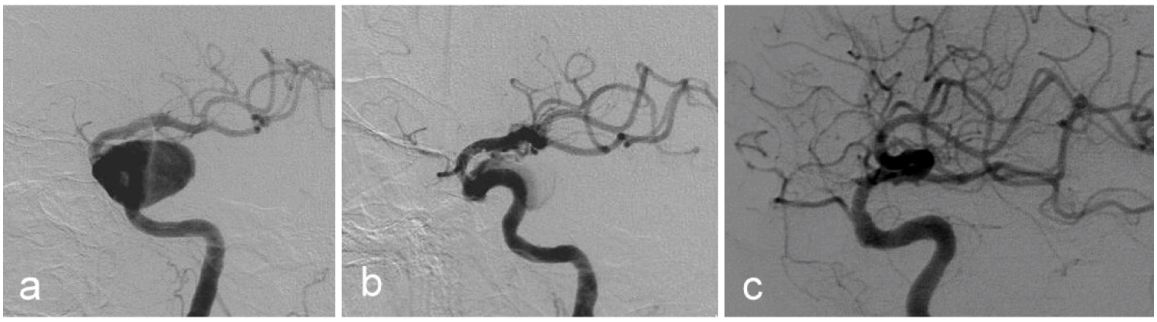


Figure 11.6: Illustrative case 4. Angiographic images for a patient treated with flow diversion**:** (a) Pre-treatment 2D-DSA; (b) end-of-treatment control angiogram showing flow reduction with contrast filling less than 50% of the pre-treatment aneurysm volume *(grade 2 on axis-I)* and a patent parent artery *(grade a on axis-II)*; (c) 3-months follow-up angiogram showing complete obliteration of the aneurysm *(grade 4 on axis-I)* with a patent parent artery *(grade a on axis-II).*

11.5 Discussion

This chapter proposes a new grading system to assess the angiographic outcomes following endovascular flow diversion treatment. The grading schema is easy to administer for clinical use and has excellent inter-rater reliability.

In proposing a new grading scale for clinical use, one must first recognise why a precedent scale may not be sufficient and how implementing the new system would be beneficial. Classification schemes commonly used for the assessment of angiographic outcomes following conventional CE treatment rely on either a three- or a four-point grading (Raymond and Roy, 1997). The most widely used three-point scale for CE describes treated intracranial aneurysms as completely occluded, with neck remnant, or with saccular filling. Proposed by Jean Raymond and colleagues, it primarily separates the aneurysms with a patent-sac from those completely or near-completely occluded (neck-remnant). The distinction is important as the patent-sac category has a worse prognosis in terms of higher risk of future growth or bleeding, compared with the other two categories (Fleiss, 1981; Raymond et al., 2007). With CE treatment, concern regarding the durability of aneurysm occlusion drives the need to achieve high packing density and complete sac occlusion, a practice supported by observations of lower recurrence rates in the densely packed, completely occluded aneurysms compared with the loosely packed, incompletely occluded aneurysms (Campi et al., 2007; Henkes et al., 2006; Pierot et al., 2006; Ries et al., 2007). Delayed recurrence may occur despite an apparently complete occlusion post-treatment, since the haemodynamic stresses acting on the coil-thrombus complex at the aneurysm neck

remain unaltered (Birchall et al., 2001; Cognard et al., 1999). A grading scale used for surveillance imaging after CE ought to identify any such change in its initial stage, hence the neck-remnant category to capture this angiographic outcome as a distinct entity.

For FD treatment, the underlying principle and the sequence of events following their deployment are inherently different from those concerning CE treatment. FDs disrupt both aneurysm inflow and outflow, and redirect the blood flow vector along the normal anatomical course of the parent artery. Resulting intra-aneurysmal blood stasis promotes thrombosis. Once initiated, successful aneurysm occlusion depends on a growing thrombus extending to fill the sac, a gradual process, which may take weeks depending upon the effective reduction in aneurysmal blood flow. Among the several determinants of this process are: porosity of FD device, size and location of the aneurysm, and the haematological status of the patient. Growth of an endothelial tissue lining on the FD, with neointima formation across the aneurysm neck, and incorporation of FD prosthesis in the vessel wall completes the healing process forming a seal across the *parent artery – aneurysm neck interface* (Fiorella, David et al., 2009). The FD treatment is new with relatively incomplete understanding of the associated biological effects. The process of aneurysm occlusion is assumed to be unidirectional (progressive thrombosis and occlusion of the aneurysm) and recanalisation with FD treatment is generally not a concern once the complete aneurysm occlusion has been achieved. In the SILK registry, however, we observed one case where a patient developed delayed recanalisation and rupture of a previously partially occluded aneurysm sac (Byrne et al., 2010).

The mechanism and time-course of FD action requires a grading scale that is able to document different degrees of aneurysmal occlusion. Since the occlusion evolves over time, any new grading scale needs to be sufficiently sensitive to register changes on interval examinations. One solution would be to use a linear scale, based simply on the percentage occlusion of the native aneurysm volume. This approach has proven difficult in practice when applied to endosaccular CE because aneurysm volume measurements are variable depending upon the methodology used, with no widely accepted standardization, making serial comparisons difficult. Accurate volume measurements require 3D imaging and cannot reliably be performed with 2D-DSA. Furthermore, remodelling and shrinkage of the aneurysm in response to reduced blood flow over time that follows successful aneurysmal thrombosis induced by parent artery occlusion or FD devices, makes it difficult to compare absolute volumes in such a system. The alternative of using an ordinal scale avoids these difficulties to some extent but needs to be responsive to varying aneurysm size, morphology, and the degree of any residual filling. A grading scheme for FD treatment also needs to recognize the possibility of recanalisation, even though recanalisation of a completely occluded aneurysm with a remodelled *parent vessel – aneurysm complex* is considered unlikely. Furthermore, in the SILK registry (chapter 10) we observed that endovascular placement of a FD device may be associated with narrowing or occlusion of the parent artery, and may affect the branch arteries whose origins are covered by the device. An evaluation scale should allow for these possibilities too, in addition to being applicable to the more complex morphologies and larger aneurysms that are currently the subject

of the new treatment. The three-point grading system was originally designed for endosaccular CE; it fails for fusiform aneurysms and cannot address the effects of FD device on parent or branch vessels. Its limitations became obvious during the evaluation of angiograms submitted as part of the SILK registry when the need for a more sensitive and more widely applicable grading approach became apparent.

For the new schema, the aneurysm occlusion and the change in parent vessel patency following endovascular deployment of the FD are identified as two distinct processes and are therefore independently graded. Although the scores on the two axes can be combined into a single score, we consider that it would be clinically more relevant to report the scores separately. The number of categories on axis-I was kept enough to register clinically meaningful serial changes in flow following the placement of FD. The five major categories i.e. no reduction in flow (grade 0), less than 50 percent flow reduction (grade 1), more than 50 percent flow reduction (grade 2), almost complete occlusion (grade 3), and complete occlusion (grades 4), were found sufficient in evaluating the effectiveness of FD in treating the target aneurysm and documenting any changes in contrast filling at multiple time-points which may have prognostic significance. Although it appears intuitive to have a larger number of categories than five to allow detection of minor changes in flow, such a strategy might reduce the reproducibility of scores and the smaller differences between adjacent categories on the scale may not have any prognostic significance.

A subjective component to our definitions and the need for proof-in-practice cannot be denied. The neck-remnant category (grade 3 on both axes) was included to

accept the possibility of recanalisation of a previously completely or near-completely occluded aneurysm and was informed by the initial reports on SAH occurring in FD treated aneurysms; even though from a theoretical stand-point, once the endovascular remodelling and curative anatomical reconstruction of the *parent artery - aneurysm complex* is achieved with FD, the haemodynamic factors have been so altered that recurrence is considered unlikely. The number of categories and their respective percentage cut-offs may need revision once more data on the follow-up of FD-treated aneurysms becomes available to inform on the prognostic significance of various degrees of aneurysm occlusion at various post-treatment follow-up durations. Axis-II was introduced to identify changes in parent artery status, and takes into account that the endoluminal flow-diversion principle treats the *parent artery - aneurysm complex* as a unit unlike the endosaccular treatment approach. The three-point categorisation of axis II is intuitive and recognises parent artery narrowing or occlusion. We considered adding an evaluation of branch artery patency; however, since it does not directly or indirectly affect the process of aneurysm occlusion, it was decided that it would unnecessarily add to the complexity of the schema. The clinical utility of this schema will be decided by the end user i.e. the interventional neuroradiologist using FD treatment to treat intracranial aneurysms; however, in its current form the scale is easy to administer and is reproducible enough for clinical use.

11.6 Conclusion

We acknowledge that the choice of categories for the new grading schema is arbitrary. The various parameters defining the proposed schema e.g. number of intervals, their

size, and break-points are kept broad in order to accommodate the relatively subjective nature of angiogram reading. For a scale to be clinically useful, it should be (1) simple and easy to administer, (2) sensitive to detect meaningful changes, (3) reproducible, and (4) able to distinguish outcomes which may have different prognosis. These aims served as the guidelines in adjusting the parameters while developing the grading schema reported here. For instance, increasing the number of intervals could have made the scale very sensitive in detecting very small changes in flow reduction or parent artery calibre but would have inevitably increased the inter-observer variability and risked over-splitting error which might adversely affect its prognostic power. Such trade offs were recognised and the chosen categories appeared intuitive and with a practical meaning.

11.7 Reception of the grading schema

Following its publication in 2011, the grading schema has received appraisal in the academic neurointerventionsit community as evidenced by its use in the clinical and experimental FD studies. It is being used in the EVIDENCE trial (Flow Diverter Stent for Endovascular Treatment of Unruptured Saccular Wide-necked Intracranial Aneurysms) to grade aneurysm occlusion following the FD treatment (Turjman et al., 2014). Raymond and colleagues, the authors of widely used three-point grading system for ECE, have adopted the schema for their work (Darsaut et al., 2013, 2012, 2011; Gentric et al., 2014). The work has been cited in numerous publications on the subject of flow diversion, including the experimental, clinical, and review articles (Alderazi et al., 2014; Attali et al., 2014; Benaissa et al., 2014; Byrne and Szikora, 2012; Chalouhi et al., 2012;

Darsaut et al., 2013, 2012, 2011; Delgado et al., 2014a, 2014b; Gentric et al., 2014; Gölitz et al., 2014; Gory et al., 2014; Grunwald et al., 2014; Jeon et al., 2012; Joshi et al., 2013; Kizilkilic et al., 2012; Lubicz et al., 2014; Mallik et al., 2014; McAuliffe et al., 2012; McAuliffe and Wenderoth, 2012; Pereira et al., 2013; Pierot, 2011; Saake et al., 2012; Siddiqui et al., 2012; Simgen et al., 2014; Struffert et al., 2013, 2011; Turjman et al., 2014; Wang et al., 2013; Weichert et al., 2013; Wong et al., 2011). Another similar scale with an aim to grade outcomes of FD treatment exists. This classification system attempts to evaluate the degree of aneurysm occlusion in four grades on three phases of a catheter angiogram (O'kelly et al., 2010). Using a total of 12 possible grades to assess the treatment outcomes, in our opinion, adds complexity to this classification system. As discussed above, for a scale to be clinically useful, it ought to be simple and easy to administer. Increasing the number of grades renders any grading system prone to over-splitting error. Also, at the time of its proposal, the authors did not provide any data on its applicability, reproducibility, or inter-rater reliability in clinical practice. Additionally, the grading schema was illustrated for its use in saccular aneurysms only. It is not clear how this grading system would be used for the fusiform aneurysms, which constitute a major subgroup of aneurysms treated with FDs, and evaluating outcomes for which, the Raymond grading scale (three-point scale used for ECE) had limited applicability.

12

Conclusions

12.1 Conclusions

(1) C-arm CT PBV is a composite parameter with both blood-volume (40%) and blood-flow (60%) weightings (chapter 04). The agreement between C-arm CT and MR-CBF is stronger relative to its agreement with MR-CBV, and includes clinically significant PBV discrepancies. That PBV has preferential blood-flow weighting is an important finding. At respective extremes, blood-flow or blood-volume weightings represent different perfusion parameters (CBF or CBV respectively), abnormal measurements of which denote different types of underlying tissue injury with unique prognostic significance. While interpreting the C-arm FDCT PBV maps, this distinction has important implications for patient management e.g. presuming a strong blood-volume weighting to PBV (an equivalence to CBV) can underestimate potentially salvageable parenchyma and can lead to under-selection of patients for revascularisation treatment in acute brain ischaemia.

(2) C-arm CT PBV imaging is feasible in DCI patients following aneurysmal SAH (chapter 04). Given its agreement with MR-PWI and its ability to provide whole brain physiological information, angiographic data, and parenchymal soft-tissue information, the C-arm CT examination can be incorporated in the imaging of patients receiving endovascular therapies for stroke, after SAH, and in situations of chronic cerebrovascular ischaemia. Apart from combining the diagnostic and interventional capabilities into a single environment, additional benefits include avoiding the repeat examinations and consequent reductions in contrast and radiation doses.

(3) Using the optimal thresholds, C-arm CT PBV allows reliable demarcation of irreversibly infarcted parenchyma (chapter 05). An accurate assessment of the brain viability and identification of irreversibly infarcted parenchyma in the interventional suite has implications for guiding the revascularisation procedures in acute brain ischaemia.

(4) C-arm CT PBV measurements allow reliable identification of moderate to severe ischaemia (chapter 05). In the setting of mild to moderate ischaemia, however, the PBV values may not be reliable when the autoregulatory mechanisms are intact and effective in maintaining a normal or elevated CBV. Thus, overall, the C-arm CT PBV may underestimate the ischaemic parenchyma which is related to its composite nature incorporating both blood-volume and blood-flow weightings.

(5) A catalogue of reference PBV measurements for various brain regions encompassing the whole brain is created, after excluding the locations with ongoing ischaemia or established infarcts (chapter 06). While these values may not be truly representative of PBV values in a normal population, they represent the best approximation given the ethical and logistical constraints to performing such measurements in normal healthy subjects using a technique that involves iodinated contrast and ionising radiation exposures. No such reference values for the C-arm CT PBV have been previously reported. The presented catalogue of reference PBV values is expected to inform the future studies and would be of value in clinical practice when interpreting PBV maps.

(6) While the steady-state contrast assumption is not fully met for C-arm CT PBV scans, the TDCs for most scans closely approximate the expected steady-state (chapter 07). The degree to which the TDC for a particular C-arm CT PBV examination approximates the expected steady-state, influences the agreement of resulting C-arm CT PBV measurements with CBV. The finding is of vital clinical significance because interpreting all C-arm CT PBV maps as equivalent to CBV maps, particularly when the TDC deviates markedly from steady-state, can potentially overestimate infarction and lead to under-selection of patients for revascularisation treatment.

(7) Despite similar scan parameters and identical contrast material injection protocols, the measured TDCs vary among patients undergoing C-arm CT PBV scanning (chapter 07). Given the calculation of PBV maps is based on the presence of contrast in the cerebral vasculature and the PBV parameter has combined blood-flow and blood-volume weightings, these inter-subject differences in the TDCs can lead to differences in the resulting PBV measurements.

Implementation of a quality control step is thus warranted in the workflow of C-arm CT PBV examinations which could be based on a simple ROI-based TDC analysis of the raw C-arm CT projection data at the scanner. It would provide an estimate of how adequately the steady-state contrast concentration was achieved in the cerebral vasculature during a particular C-arm CT study. This estimate of steady-state adequacy would inform the clinician interpreting the PBV maps on how closely the abnormality detected on PBV maps might correlate to a similar CBV (surrogate for infarction) or a CBF (surrogate for ischaemia) abnormality.

(8) Cross-sectional C-arm CT soft-tissues images are of adequate quality to allow a reliable assessment of the ventricular system and detection of suspected procedural vessel rupture in the interventional suite (chapter 08). In this regard, application-related advantages of C-arm CT outweigh its performance related disadvantages compared with conventional CT, and define it as a valuable tool in the angio-room.

(9) In the initial clinical experience with the flow diversion treatment of intracranial aneurysms, the procedural, angiographic, and clinical outcomes are reported (chapter 10). Several technical and clinical issues related to this new treatment approach are highlighted including FD deployment difficulties, parent artery thrombosis, delayed aneurysm rupture, challenges related to antiplatelet regimen, angiographic outcomes, and the procedural and delayed morbidity. This work (largest multi-centre series at the time of its publication) informed the wider community of interventional neuroradiologists about the safety, efficacy, and outcomes of flow diversion treatment; and has been cited in numerous subsequent clinical reports on the use of FDs for intracranial aneurysm treatment.

(10) A new grading schema to monitor angiographic outcomes after FD treatment is proposed (chapter 11). This grading schema documents the degree of aneurysm occlusion (on a five-point scale) and evaluates the parent artery patency (on a three-point). In a simulated clinical setting, the schema was found to be sufficiently sensitive to register gradual aneurysm occlusion and parent artery patency on interval angiograms. The system was found to be simple and easy to administer, was applicable to both saccular and fusiform morphologies, and had excellent inter-rater reliability.

Since its publication, the schema has been used to evaluate angiographic outcomes of FD treatment in numerous clinical studies, clinical trials, and in experimental studies.

12.2 Future directions

In regards to the C-arm CT PBV imaging, the work in this thesis has highlighted the value and limitations of the technique for its use in the neurointerventional suite. The issue of blood-flow and blood-volume weighting to PBV, optimal thresholds for PBV to demarcate infarction, reference PBV measurements, TDC analysis, and the effect of the temporal characteristics of TDCs on the final PBV measurements were previously unexplored. Published studies on C-arm CT PBV imaging are relatively few, related to its recent introduction for clinical use. The quantitative analyses that lead to the findings we observed were carefully constructed and executed. However, our results would need further validation by larger studies and in different clinical settings.

The work on defining optimal PBV thresholds for infarction needs further investigation to identify the tissue and region specific viability thresholds, which was not possible in the current study due to limited number of subjects and infarct locations. Differences between the grey and white matter are known to exist regarding cellular composition, metabolism, the normal perfusion parameter values, and their neurochemical response to ischaemia (Dohmen et al., 2001; Helenius et al., 2003; Stys et al., 1990). Tissue-specific infraction thresholds would thus be more informative in predicting the tissue outcomes in the setting of cerebrovascular ischaemia. Future studies recruiting larger number of patients with cerebral ischaemia may help in

addressing this issue. Validation of the reported optimal thresholds in predicting the final infarct volume for acute ischaemic stroke is another area that needs exploration.

We studied the TDCs in patients with DCI following SAH. It is possible that the temporal characteristics of TDCs we observed were partly reflective of the impaired cerebrovascular responses related to DCI. A similar analysis in different patient populations is warranted, in order to better understand the individual contributions of injection parameters and the possible underlying impaired cerebrovascular responses towards the inter-subject variations and the deviation of TDC temporal characteristics from the steady-state. The scan parameters may need refinement based on the results of future work. Similarly the issue of blood-flow and blood-volume weighting to PBV needs further study in patients with acute brain ischaemia who undergo revascularisation treatment to document the procedural significance of the relative weightings. PBV measurements in various brain regions would require further confirmation in larger studies preferably including patients with no ongoing cerebral ischaemia or infarction, which would be a challenging task.

Although measurement of a physiological parameter (PBV) of potential prognostic significance is an important step towards functional imaging in the neurointerventional suite, mechanical constraints still prevent dynamic perfusion imaging with C-arm systems in current clinical use. Implementation of interleaved scanning to augment the temporal resolution of new generation multi-axis C-arm angiographic systems has shown promising results in animal models to allow estimation of dynamic perfusion parameters i.e. CBF and MTT (Fieselmann et al., 2012;

Royalty et al., 2013). These new protocols, which are still under investigation and not available for use in human subjects, employ multiple (up to 7) bidirectional high-speed C-arm rotations and higher contrast injection rates to improve the temporal resolution and the contrast-to-noise ratio, respectively. Ongoing developments in multiple areas including the flat detector technology to improve their read out speed and sensitivity, reconstruction algorithms and image processing techniques such as iterative reconstruction and compressed sensing algorithms, and mechanical properties of the C-arm systems lend great optimism to the future of dynamic perfusion imaging with C-arm angiographic systems. While PBV measurements offer a window into the cerebral haemodynamics, these engineering developments would be crucial to bring the dynamic perfusion imaging capability to the neurointerventional suite of future. An ability to evaluate the brain parenchyma, vessels, and the haemodynamic status of the brain in the angiography suite, with an accuracy and reliability of conventional CT, would truly redefine the technique and its role in diagnosis, triage, and treatment of acute cerebrovascular ischaemic disease.

Bibliography

Ahmed, A.S., Zellerhoff, M., Strother, C.M., Pulfer, K.A., Redel, T., Deuerling-Zheng, Y., Royalty, K., Consigny, D., Niemann, D.B., 2009. C-Arm CT Measurement of Cerebral Blood Volume: An Experimental Study in Canines. AJNR Am J Neuroradiol 30, 917–922. doi:10.3174/ajnr.A1513

Akpek, S., Arat, A., Morsi, H., Klucznick, R.P., Strother, C.M., Mawad, M.E., 2005a. Self-expandable stent-assisted coiling of wide-necked intracranial aneurysms: a single-center experience. AJNR Am J Neuroradiol 26, 1223–1231.

Akpek, S., Brunner, T., Benndorf, G., Strother, C., 2005b. Three-dimensional imaging and cone beam volume CT in C-arm angiography with flat panel detector. Diagn Interv Radiol 11, 10–13.

Alderazi, Y.J., Shastri, D., Kass-Hout, T., Prestigiacomo, C.J., Gandhi, C.D., 2014. Flow Diverters for Intracranial Aneurysms. Stroke Research and Treatment 2014.

Allmendinger, A.M., Tang, E.R., Lui, Y.W., Spektor, V., 2012. Imaging of Stroke: Part 1, Perfusion CT—Overview of Imaging Technique, Interpretation Pearls, and Common Pitfalls. American Journal of Roentgenology 198, 52–62. doi:10.2214/AJR.10.7255

Arakawa, H., Marks, M.P., Do, H.M., Bouley, D.M., Strobel, N., Moore, T., Fahrig, R., 2008. Experimental Study of Intracranial Hematoma Detection with Flat Panel Detector C-Arm CT. AJNR Am J Neuroradiol 29, 766–772. doi:10.3174/ajnr.A0898

Arakawa, S., Wright, P.M., Koga, M., Phan, T.G., Reutens, D.C., Lim, I., Gunawan, M.R., Ma, H., Perera, N., Ly, J., Zavala, J., Fitt, G., Donnan, G.A., 2006. Ischemic thresholds for gray and white matter: a diffusion and perfusion magnetic resonance study. Stroke 37, 1211–1216. doi:10.1161/01.STR.0000217258.63925.6b

Arrese, I., Sarabia, R., Pintado, R., Delgado-Rodriguez, M., 2013. Flow-Diverter Devices for Intracranial Aneurysms: Systematic Review and Meta-analysis. Neurosurgery 73, 193–200. doi:10.1227/01.neu.0000430297.17961.f1

Attali, J., Benaissa, A., Soize, S., Kadziolka, K., Portefaix, C., Pierot, L., 2014. Follow-up of intracranial aneurysms treated by flow diverter: comparison of three-dimensional time-of-flight MR angiography (3D-TOF-MRA) and contrast-enhanced MR angiography (CE-MRA) sequences with digital subtraction angiography as the gold standard. Journal of neurointerventional surgery neurintsurg–2014.

Axel, L., 1980. Cerebral blood flow determination by rapid-sequence computed tomography: theoretical analysis. Radiology 137, 679–686. doi:10.1148/radiology.137.3.7003648

Axel, L., 2004. Cerebral Perfusion CT Techniques. Radiology 233, 935–935. doi:10.1148/radiol.2333040946

Bae, K.T., 2010. Intravenous contrast medium administration and scan timing at CT: considerations and approaches. Radiology 256, 32–61. doi:10.1148/radiol.10090908

Bae, K.T., Heiken, J.P., 2005. Scan and contrast administration principles of MDCT. Eur Radiol 15 Suppl 5, E46–59.

Becske, T., Kallmes, D.F., Saatci, I., McDougall, C.G., Szikora, I., Lanzino, G., Moran, C.J., Woo, H.H., Lopes, D.K., Berez, A.L., Cher, D.J., Siddiqui, A.H., Levy, E.I., Albuquerque, F.C., Fiorella, D.J., Berentei, Z., Marosfoi, M., Cekirge, S.H., Nelson, P.K., 2013. Pipeline for uncoilable or failed aneurysms: results from a multicenter clinical trial. Radiology 267, 858–868. doi:10.1148/radiol.13120099

Benaissa, A., Januel, A.-C., Herbreteau, D., Berge, J., Aggour, M., Kadziolka, K., Cognard, C., Pierot, L., 2014. Endovascular treatment with flow diverters of recanalized and multitreated aneurysms initially treated by endovascular approach. Journal of neurointerventional surgery neurintsurg–2013.

Benndorf, G., Herbon, U., Sollmann, W.P., Campi, A., 2001. Treatment of a ruptured dissecting vertebral artery aneurysm with double stent placement: case report. AJNR Am J Neuroradiol 22, 1844–1848.

Benndorf, G., Strother, C.M., Claus, B., Naeini, R., Morsi, H., Klucznik, R., Mawad, M.E., 2005. Angiographic CT in Cerebrovascular Stenting. AJNR Am J Neuroradiol 26, 1813–1818.

Berge, J., Biondi, A., Machi, P., Brunel, H., Pierot, L., Gabrillargues, J., Kadziolka, K., Barreau, X., Dousset, V., Bonafé, A., 2012. Flow-Diverter Silk Stent for the Treatment of Intracranial Aneurysms: 1-year Follow-Up in a Multicenter Study. AJNR Am J Neuroradiol 33, 1150–1155. doi:10.3174/ajnr.A2907

Berge, J., Tourdias, T., Moreau, J.-F., Barreau, X., Dousset, V., 2011. Perianeurysmal Brain Inflammation after Flow-Diversion Treatment. AJNR Am J Neuroradiol 32, 1930–1934. doi:10.3174/ajnr.A2710

Berkhemer, O.A., Fransen, P.S.S., Beumer, D., van den Berg, L.A., Lingsma, H.F., Yoo, A.J., Schonewille, W.J., Vos, J.A., Nederkoorn, P.J., Wermer, M.J.H., van Walderveen, M.A.A., Staals, J., Hofmeijer, J., van Oostayen, J.A., Lycklama à Nijeholt, G.J., Boiten, J., Brouwer, P.A., Emmer, B.J., de Bruijn, S.F., van Dijk, L.C., Kappelle, L.J., Lo, R.H., van Dijk, E.J., de Vries, J., de Kort, P.L.M., van Rooij, W.J.J., van den Berg, J.S.P., van Hasselt, B.A.A.M., Aerden, L.A.M., Dallinga, R.J., Visser, M.C., Bot, J.C.J., Vroomen, P.C., Eshghi, O., Schreuder, T.H.C.M.L., Heijboer, R.J.J., Keizer, K., Tielbeek, A.V., den Hertog, H.M., Gerrits, D.G., van den Berg-Vos, R.M., Karas, G.B., Steyerberg, E.W., Flach, H.Z., Marquering, H.A., Sprengers, M.E.S., Jenniskens, S.F.M., Beenen, L.F.M., van den Berg, R., Koudstaal, P.J., van Zwam, W.H., Roos, Y.B.W.E.M., van der Lugt, A., van Oostenbrugge, R.J., Majoie, C.B.L.M., Dippel, D.W.J., 2015. A Randomized Trial of Intraarterial Treatment for Acute Ischemic Stroke. New England Journal of Medicine 372, 11–20. doi:10.1056/NEJMoa1411587

Birchall, D., Khangure, M.S., McAuliffe, W., Thomas, W., 2001. Delayed aneurysm rerupture following total endovascular occlusion. Br J Neurosurg 15, 269–272. doi:10.1080/02688690175035374 6

Bley, T., Strother, C.M., Pulfer, K., Royalty, K., Zellerhoff, M., Deuerling-Zheng, Y., Bender, F., Consigny, D., Yasuda, R., Niemann, D., 2010. C-Arm CT Measurement of Cerebral Blood Volume in Ischemic Stroke: An Experimental Study in Canines. AJNR Am J Neuroradiol 31, 536–540. doi:10.3174/ajnr.A1851

Blomley, M.M., Dawson, D.P., Miles, D.K.A., 1997. Functional Computed Tomography. CRC Press, Oxford.

Briganti, F., Napoli, M., Tortora, F., Solari, D., Bergui, M., Boccardi, E., Cagliari, E., Castellan, L., Causin, F., Ciceri, E., Cirillo, L., De Blasi, R., Delehaye, L., Di Paola, F., Fontana, A., Gasparotti, R., Guidetti, G., Divenuto, I., Iannucci, G., Isalberti, M., Leonardi, M., Lupo, F., Mangiafico, S., Manto, A., Menozzi, R., Muto, M., Nuzzi, N.P., Papa, R., Petralia, B., Piano, M., Resta, M., Padolecchia, R., Saletti, A., Sirabella, G., Bolgè, L.P.V., 2012. Italian multicenter experience with flow-diverter devices for intracranial unruptured aneurysm treatment with periprocedural complications--a retrospective data analysis. Neuroradiology 54, 1145–1152. doi:10.1007/s00234-012-1047-3

Brinjikji, W., Murad, M.H., Lanzino, G., Cloft, H.J., Kallmes, D.F., 2013. Endovascular treatment of intracranial aneurysms with flow diverters: a meta-analysis. Stroke 44, 442–447. doi:10.1161/STROKEAHA.112.678151

Broderick, J.P., Palesch, Y.Y., Demchuk, A.M., Yeatts, S.D., Khatri, P., Hill, M.D., Jauch, E.C., Jovin, T.G., Yan, B., Silver, F.L., von Kummer, R., Molina, C.A., Demaerschalk, B.M., Budzik, R., Clark, W.M., Zaidat, O.O., Malisch, T.W., Goyal, M., Schonewille, W.J., Mazighi, M., Engelter, S.T., Anderson, C., Spilker, J., Carrozzella, J., Ryckborst, K.J., Janis, L.S., Martin, R.H., Foster, L.D., Tomsick, T.A., Interventional Management of Stroke (IMS) III Investigators, 2013. Endovascular therapy after intravenous t-PA versus t-PA alone for stroke. N. Engl. J. Med. 368, 893–903. doi:10.1056/NEJMoa1214300

Buhk, J.-H., Kallenberg, K., Mohr, A., Dechent, P., Knauth, M., 2009. Evaluation of angiographic computed tomography in the follow-up after endovascular treatment of cerebral aneurysms—a comparative study with DSA and TOF-MRA. Eur Radiol 19, 430–436. doi:10.1007/s00330-008-1171-y

Buhk, J.-H., Lingor, P., Knauth, M., 2008. Angiographic CT with intravenous administration of contrast medium is a noninvasive option for follow-up after intracranial stenting. Neuroradiology 50, 349–354. doi:10.1007/s00234-007-0342-x

Byrne, J.V., Beltechi, R., Yarnold, J.A., Birks, J., Kamran, M., 2010. Early Experience in the Treatment of Intra-Cranial Aneurysms by Endovascular Flow Diversion: A Multicentre Prospective Study. PLoS ONE 5, e12492. doi:10.1371/journal.pone.0012492

Byrne, J.V., Szikora, I., 2012. Flow diverters in the management of intracranial aneurysms: a review. EJMINT Orig Artic 1225000057, 1–22.

Cahill, J., Zhang, J.H., 2009. Subarachnoid Hemorrhage Is It Time for a New Direction? Stroke 40, S86–S87. doi:10.1161/STROKEAHA.108.533315

Campbell, B.C.V., Christensen, S., Levi, C.R., Desmond, P.M., Donnan, G.A., Davis, S.M., Parsons, M.W., 2011. Cerebral blood flow is the optimal CT perfusion parameter for assessing infarct core. Stroke 42, 3435–3440. doi:10.1161/STROKEAHA.111.618355

Campi, A., Ramzi, N., Molyneux, A.J., Summers, P.E., Kerr, R.S.C., Sneade, M., Yarnold, J.A., Rischmiller, J., Byrne, J.V., 2007a. Retreatment of ruptured cerebral aneurysms in patients randomized by coiling or clipping in the International Subarachnoid Aneurysm Trial (ISAT). Stroke 38, 1538–1544. doi:10.1161/STROKEAHA.106.466987

Campi, A., Ramzi, N., Molyneux, A.J., Summers, P.E., Kerr, R.S.C., Sneade, M., Yarnold, J.A., Rischmiller, J., Byrne, J.V., 2007b. Retreatment of Ruptured Cerebral Aneurysms in Patients Randomized by Coiling or Clipping in the International Subarachnoid Aneurysm Trial (ISAT). Stroke 38, 1538–1544. doi:10.1161/STROKEAHA.106.466987

Chalouhi, N., Campbell, P., Makke, Y., Yadla, S., Dumont, A.S., Gonzalez, L.F., Tjoumakaris, S., Albani, B., Rosenwasser, R.H., Jabbour, P., 2012. Treatment of complex intracranial aneurysms with a telescoping stent technique. Journal of Neurological Surgery Part A: Central European Neurosurgery 73, 281–288.

Chalouhi, N., Tjoumakaris, S., Phillips, J.L.H., Starke, R.M., Hasan, D., Wu, C., Zanaty, M., Kung, D., Gonzalez, L.F., Rosenwasser, R., Jabbour, P., 2014. A Single Pipeline Embolization Device is Sufficient for Treatment of Intracranial Aneurysms. AJNR Am J Neuroradiol. doi:10.3174/ajnr.A3957

Christensen, S., Mouridsen, K., Wu, O., Hjort, N., Karstoft, H., Thomalla, G., Röther, J., Fiehler, J., Kucinski, T., Østergaard, L., 2009. Comparison of 10 perfusion MRI parameters in 97 sub-6-hour stroke patients using voxel-based receiver operating characteristics analysis. Stroke 40, 2055–2061. doi:10.1161/STROKEAHA.108.546069

Ciccone, A., Valvassori, L., Nichelatti, M., Sgoifo, A., Ponzio, M., Sterzi, R., Boccardi, E., 2013. Endovascular Treatment for Acute Ischemic Stroke. New England Journal of Medicine 368, 904–913. doi:10.1056/NEJMoa1213701

Cloft, H.J., Kallmes, D.F., 2002. Cerebral aneurysm perforations complicating therapy with Guglielmi detachable coils: a meta-analysis. AJNR Am J Neuroradiol 23, 1706–1709.

Cloft, H.J., Tomsick, T.A., Kallmes, D.F., Goldstein, J.H., Connors, J.J., 2002. Assessment of the Interventional Neuroradiology Workforce in the United States: A Review of the Existing Data. AJNR Am J Neuroradiol 23, 1700–1705.

Cognard, C., Pierot, L., Anxionnat, R., Ricolfi, F., Clarity Study Group, 2011. Results of embolization used as the first treatment choice in a consecutive nonselected population of ruptured aneurysms: clinical results of the Clarity GDC study. Neurosurgery 69, 837–841; discussion 842. doi:10.1227/NEU.0b013e3182257b30

Cognard, C., Weill, A., Spelle, L., Piotin, M., Castaings, L., Rey, A., Moret, J., 1999. Long-term angiographic follow-up of 169 intracranial berry aneurysms occluded with detachable coils. Radiology 212, 348–356. doi:10.1148/radiology.212.2.r99jl47348

Cohen, J., 1960. A coefficient of agreement for nominal scales. Educational and Psychological Measurement 20, 37–46. doi:10.1177/001316446002000104

Cowen, A.R., Davies, A.G., Sivananthan, M.U., 2008. The design and imaging characteristics of dynamic, solid-state, flat-panel x-ray image detectors for digital fluoroscopy and fluorography. Clin Radiol 63, 1073–1085. doi:10.1016/j.crad.2008.06.002

Cruz, J.P., Chow, M., O'Kelly, C., Marotta, B., Spears, J., Montanera, W., Fiorella, D., Marotta, T., 2012. Delayed Ipsilateral Parenchymal Hemorrhage Following Flow Diversion for the Treatment of Anterior Circulation Aneurysms. AJNR Am J Neuroradiol 33, 603–608. doi:10.3174/ajnr.A3065

Dankbaar, J.W., Rijsdijk, M., van der Schaaf, I.C., Velthuis, B.K., Wermer, M.J.H., Rinkel, G.J.E., 2009. Relationship between vasospasm, cerebral perfusion, and delayed cerebral ischemia after aneurysmal subarachnoid hemorrhage. Neuroradiology 51, 813–819. doi:10.1007/s00234-009-0575-y

Dankbaar, J.W., Rooij, N.K. de, Rijsdijk, M., Velthuis, B.K., Frijns, C.J.M., Rinkel, G.J.E., Schaaf, I.C. van der, 2010. Diagnostic Threshold Values of Cerebral Perfusion Measured With Computed Tomography for Delayed Cerebral Ischemia After Aneurysmal Subarachnoid Hemorrhage. Stroke 41, 1927–1932. doi:10.1161/STROKEAHA.109.574392

Darsaut, T.E., Bing, F., Makoyeva, A., Gevry, G., Salazkin, I., Raymond, J., 2013. Flow Diversion of Giant Curved Sidewall and Bifurcation Experimental Aneurysms with Very-Low-Porosity Devices. World neurosurgery.

Darsaut, T.E., Bing, F., Salazkin, I., Gevry, G., Raymond, J., 2011. Testing flow diverters in giant fusiform aneurysms: a new experimental model can show leaks responsible for failures. American Journal of Neuroradiology 32, 2175–2179.

Darsaut, T.E., Bing, F., Salazkin, I., Gevry, G., Raymond, J., 2012. Flow diverters can occlude

aneurysms and preserve arterial branches: a new experimental model. American Journal of Neuroradiology 33, 2004–2009.

Delgado, F., Saiz, A., Hilario, A., Murias, E., San Román Manzanera, L., Lagares Gomez-Abascal, A., Gabarrós, A., González García, A., 2014a. Neuroimaging follow-up of cerebral aneurysms treated with endovascular techniques. Radiología (English Edition) 56, 118–128.

Delgado, F., Saiz, A., Hilario, A., Murias, E., San Román Manzanera, L., Lagares Gomez-Abascal, A., Gabarrós, A., González García, A., 2014b. Seguimiento mediante técnicas de neuroimagen de los aneurismas cerebrales tratados por vía endovascular. Radiología 56, 118–128.

Diringer, M.N., Bleck, T.P., Claude Hemphill, J., 3rd, Menon, D., Shutter, L., Vespa, P., Bruder, N., Connolly, E.S., Jr, Citerio, G., Gress, D., Hänggi, D., Hoh, B.L., Lanzino, G., Le Roux, P., Rabinstein, A., Schmutzhard, E., Stocchetti, N., Suarez, J.I., Treggiari, M., Tseng, M.-Y., Vergouwen, M.D.I., Wolf, S., Zipfel, G., Neurocritical Care Society, 2011. Critical care management of patients following aneurysmal subarachnoid hemorrhage: recommendations from the Neurocritical Care Society's Multidisciplinary Consensus Conference. Neurocrit Care 15, 211–240. doi:10.1007/s12028-011-9605-9

Doelken, M., Struffert, T., Richter, G., Engelhorn, T., Nimsky, C., Ganslandt, O., Hammen, T., Doerfler, A., 2008. Flat-panel detector volumetric CT for visualization of subarachnoid hemorrhage and ventricles: preliminary results compared to conventional CT. Neuroradiology 50, 517–523. doi:10.1007/s00234-008-0372-z

Doerfler, A., Wanke, I., Egelhof, T., Dietrich, U., Asgari, S., Stolke, D., Forsting, M., 2001. Aneurysmal rupture during embolization with Guglielmi detachable coils: causes, management, and outcome. AJNR Am J Neuroradiol 22, 1825–1832.

Doerfler, A., Wanke, I., Egelhof, T., Stolke, D., Forsting, M., 2004. Double-stent method: therapeutic alternative for small wide-necked aneurysms. Technical note. J. Neurosurg. 100, 150–154. doi:10.3171/jns.2004.100.1.0150

Dohmen, C., Kumura, E., Rosner, G., Heiss, W.D., Graf, R., 2001. Adenosine in relation to calcium homeostasis: comparison between gray and white matter ischemia. J. Cereb. Blood Flow Metab. 21, 503–510. doi:10.1097/00004647-200105000-00004

D'Urso, P.I., Lanzino, G., Cloft, H.J., Kallmes, D.F., 2011. Flow Diversion for Intracranial Aneurysms A Review. Stroke 42, 2363–2368. doi:10.1161/STROKEAHA.111.620328

Ebrahimi, N., Claus, B., Lee, C.-Y., Biondi, A., Benndorf, G., 2007. Stent conformity in curved vascular models with simulated aneurysm necks using flat-panel CT: an in vitro study. AJNR Am J Neuroradiol 28, 823–829.

Engelhorn, T., Struffert, T., Richter, G., Doelken, M., Ganslandt, O., Kalender, W., Doerfler, A., 2008. Flat Panel Detector Angiographic CT in the Management of Aneurysmal Rupture During Coil Embolization. AJNR Am J Neuroradiol 29, 1581–1584. doi:10.3174/ajnr.A1119

Ernemann, U.U., Grönewäller, E., Duffner, F.B., Guervit, O., Claassen, J., Skalej, M.D., 2003. Influence of geometric and hemodynamic parameters on aneurysm visualization during three-dimensional rotational angiography: an in vitro study. AJNR Am J Neuroradiol 24, 597–603.

Essig, M., Shiroishi, M.S., Nguyen, T.B., Saake, M., Provenzale, J.M., Enterline, D., Anzalone, N., Dorfler, A., Rovira, A., Wintermark, M., Law, M., 2013. Perfusion MRI: The Five Most

Frequently Asked Technical Questions. AJR Am J Roentgenol 200, 24–34. doi:10.2214/AJR.12.9543

Etminan, N., Beseoglu, K., Heiroth, H.-J., Turowski, B., Steiger, H.J., Hänggi, D., 2013. Early Perfusion Computerized Tomography Imaging as a Radiographic Surrogate for Delayed Cerebral Ischemia and Functional Outcome After Subarachnoid Hemorrhage. Stroke 44, 1260–1266. doi:10.1161/STROKEAHA.111.675975

Fahrig, R., Fox, A.J., Lownie, S., Holdsworth, D.W., 1997. Use of a C-arm system to generate true three-dimensional computed rotational angiograms: preliminary in vitro and in vivo results. AJNR Am J Neuroradiol 18, 1507–1514.

Ferns, S.P., Sprengers, M.E.S., Rooij, W.J. van, Rinkel, G.J.E., Rijn, J.C. van, Bipat, S., Sluzewski, M., Majoie, C.B.L.M., 2009. Coiling of Intracranial Aneurysms A Systematic Review on Initial Occlusion and Reopening and Retreatment Rates. Stroke 40, e523–e529. doi:10.1161/STROKEAHA.109.553099

Fieselmann, A., Ganguly, A., Deuerling-Zheng, Y., Zellerhoff, M., Boese, J., Hornegger, J., Fahrig, R., 2010. A dynamic reconstruction approach for cerebral blood flow quantification with an interventional C-arm CT, in: 2010 IEEE International Symposium on Biomedical Imaging: From Nano to Macro. Presented at the 2010 IEEE International Symposium on Biomedical Imaging: From Nano to Macro, pp. 53–56. doi:10.1109/ISBI.2010.5490417

Fieselmann, A., Ganguly, A., Deuerling-Zheng, Y., Zellerhoff, M., Rohkohl, C., Boese, J., Hornegger, J., Fahrig, R., 2012. Interventional 4-D C-Arm CT Perfusion Imaging Using Interleaved Scanning and Partial Reconstruction Interpolation. IEEE Transactions on Medical Imaging 31, 892–906. doi:10.1109/TMI.2011.2181531

Fieselmann, A., Kowarschik, M., Ganguly, A., Hornegger, J., Fahrig, R., 2011. Deconvolution-Based CT and MR Brain Perfusion Measurement: Theoretical Model Revisited and Practical Implementation Details. International Journal of Biomedical Imaging 2011, e467563. doi:10.1155/2011/467563

Fiorella, David, Kelly, Michael, Woo, Henry, 2009. Flow Diversion for Intracranial Aneurysm Treatment. Endovascular Today.

Fiorella, D., Chow, M.M., Anderson, M., Woo, H., Rasmussen, P.A., Masaryk, T.J., 2007. A 7-year experience with balloon-mounted coronary stents for the treatment of symptomatic vertebrobasilar intracranial atheromatous disease. Neurosurgery 61, 236–242; discussion 242–243. doi:10.1227/01.NEU.0000255521.42579.31

Fiorella, D., Lylyk, P., Szikora, I., Kelly, M.E., Albuquerque, F.C., McDougall, C.G., Nelson, P.K., 2009. Curative cerebrovascular reconstruction with the Pipeline embolization device: the emergence of definitive endovascular therapy for intracranial aneurysms. J Neurointerv Surg 1, 56–65. doi:10.1136/jnis.2009.000083

Fisher, C.M., Kistler, J.P., Davis, J.M., 1980. Relation of cerebral vasospasm to subarachnoid hemorrhage visualized by computerized tomographic scanning. Neurosurgery 6, 1–9.

Fisher, R.A., 1922. On the Interpretation of χ 2 from Contingency Tables, and the Calculation of P. Journal of the Royal Statistical Society 85, 87. doi:10.2307/2340521

Fleischmann, D., 2005. How to design injection protocols for multiple detector-row CT angiography (MDCTA). Eur Radiol 15 Suppl 5, E60–65.

Fleiss, J.L., 1981. Statistical Methods for Rates and Proportions. Wiley.

Friedman, J.A., Nichols, D.A., Meyer, F.B., Pichelmann, M.A., McIver, J.I., Toussaint, L.G., Axley, P.L., Brown, R.D., 2003. Guglielmi detachable coil treatment of ruptured saccular cerebral aneurysms: retrospective review of a 10-year single-center experience. AJNR Am J Neuroradiol 24, 526–533.

Gallas, S., Drouineau, J., Gabrillargues, J., Pasco, A., Cognard, C., Pierot, L., Herbreteau, D., 2008. Feasibility, Procedural Morbidity and Mortality, and Long-Term Follow-Up of Endovascular Treatment of 321 Unruptured Aneurysms. AJNR Am J Neuroradiol 29, 63–68. doi:10.3174/ajnr.A0757

Gentric, J.C., Darsaut, T.E., Makoyeva, A., Salazkin, I., Raymond, J., 2014. The Success of Flow Diversion in Large and Giant Sidewall Aneurysms May Depend on the Size of the Defect in the Parent Artery. American Journal of Neuroradiology 35, 2119–2124.

Geremia, G., Haklin, M., Brennecke, L., 1994. Embolization of experimentally created aneurysms with intravascular stent devices. AJNR Am J Neuroradiol 15, 1223–1231.

Go, A.S., Mozaffarian, D., Roger, V.L., Benjamin, E.J., Berry, J.D., Blaha, M.J., Dai, S., Ford, E.S., Fox, C.S., Franco, S., Fullerton, H.J., Gillespie, C., Hailpern, S.M., Heit, J.A., Howard, V.J., Huffman, M.D., Judd, S.E., Kissela, B.M., Kittner, S.J., Lackland, D.T., Lichtman, J.H., Lisabeth, L.D., Mackey, R.H., Magid, D.J., Marcus, G.M., Marelli, A., Matchar, D.B., McGuire, D.K., Mohler, E.R., Moy, C.S., Mussolino, M.E., Neumar, R.W., Nichol, G., Pandey, D.K., Paynter, N.P., Reeves, M.J., Sorlie, P.D., Stein, J., Towfighi, A., Turan, T.N., Virani, S.S., Wong, N.D., Woo, D., Turner, M.B., 2014. Heart Disease and Stroke Statistics—2014 Update A Report From the American Heart Association. Circulation 129, e28–e292. doi:10.1161/01.cir.0000441139.02102.80

Gobbel, G.T., Cann, C.E., Iwamoto, H.S., Fike, J.R., 1991. Measurement of regional cerebral blood flow in the dog using ultrafast computed tomography. Experimental validation. Stroke 22, 772–779.

Gölitz, P., Struffert, T., Rösch, J., Ganslandt, O., Knossalla, F., Doerfler, A., 2014. Cerebral aneurysm treatment using flow-diverting stents: in-vivo visualization of flow alterations by parametric colour coding to predict aneurysmal occlusion: preliminary results. European radiology 1–8.

Gory, B., Bonafé, A., Pierot, L., Spelle, L., Berge, J., Piotin, M., Mounayer, C., Biondi, A., Courtheoux, P., Cognard, C., others, 2014. Safety and efficacy of flow-diverter stents in endovascular treatment of intracranial aneurysm: Interest of the prospective DIVERSION observational study. Journal of neuroradiology. Journal de neuroradiologie 41, 93.

Grass, M., Koppe, R., Klotz, E., Proksa, R., Kuhn, M.H., Aerts, H., Op de Beek, J., Kemkers, R., 1999. Three-dimensional reconstruction of high contrast objects using C-arm image intensifier projection data. Comput Med Imaging Graph 23, 311–321.

Gröschel, K., Schnaudigel, S., Pilgram, S.M., Wasser, K., Kastrup, A., 2009. A Systematic Review on Outcome After Stenting for Intracranial Atherosclerosis. Stroke 40, e340–e347. doi:10.1161/STROKEAHA.108.532713

Grunwald, I.Q., Kühn, A.L., Schmitt, A.J., Balami, J.S., 2014. Aneurysmal SAH: Current Management and Complications Associated With Treatment and Disease. J INVASIVE CARDIOL 26, 30–37.

Guglielmi, G., Viñuela, F., Dion, J., Duckwiler, G., 1991. Electrothrombosis of saccular aneurysms via endovascular approach. Part 2: Preliminary clinical experience. J. Neurosurg. 75, 8–

14. doi:10.3171/jns.1991.75.1.0008

Gupta, R., Grasruck, M., Suess, C., Bartling, S.H., Schmidt, B., Stierstorfer, K., Popescu, S., Brady, T., Flohr, T., 2006. Ultra-high resolution flat-panel volume CT: fundamental principles, design architecture, and system characterization. Eur Radiol 16, 1191–1205. doi:10.1007/s00330-006-0156-y

Gupta, V., Chugh, M., Walia, B., Vaishya, S., Jha, A., 2008. Digital subtraction angiography laboratory with inbuilt CT (DynaCT): Application during intracranial anurysm embolization. Neurology India 56, 90. doi:10.4103/0028-3886.39325

Hamberg, L.M., Hunter, G.J., Kierstead, D., Lo, E.H., González, R.G., Wolf, G.L., 1996. Measurement of cerebral blood volume with subtraction three-dimensional functional CT. AJNR Am J Neuroradiol 17, 1861–1869.

Hatazawa, J., Fujita, H., Kanno, I., Satoh, T., Iida, H., Miura, S., Murakami, M., Okudera, T., Inugami, A., Ogawa, T., 1995. Regional cerebral blood flow, blood volume, oxygen extraction fraction, and oxygen utilization rate in normal volunteers measured by the autoradiographic technique and the single breath inhalation method. Ann Nucl Med 9, 15–21.

Helenius, J., Perkiö, J., Soinne, L., Østergaard, L., Carano, R. a. D., Salonen, O., Savolainen, S., Kaste, M., Aronen, H.J., Tatlisumak, T., 2003. Cerebral hemodynamics in a healthy population measured by dynamic susceptibility contrast MR imaging. Acta Radiol 44, 538–546.

Henkes, H., Fischer, S., Liebig, T., Weber, W., Reinartz, J., Miloslavski, E., Kühne, D., 2006. Repeated endovascular coil occlusion in 350 of 2759 intracranial aneurysms: safety and effectiveness aspects. Neurosurgery 58, 224–232; discussion 224–232. doi:10.1227/01.NEU.0000194831.54183.3F

Heran, N.S., Song, J.K., Namba, K., Smith, W., Niimi, Y., Berenstein, A., 2006. The utility of DynaCT in neuroendovascular procedures. AJNR Am J Neuroradiol 27, 330–332.

Higashida, R.T., Smith, W., Gress, D., Urwin, R., Dowd, C.F., Balousek, P.A., Halbach, V.V., 1997. Intravascular stent and endovascular coil placement for a ruptured fusiform aneurysm of the basilar artery. Case report and review of the literature. J. Neurosurg. 87, 944–949. doi:10.3171/jns.1997.87.6.0944

Hoeffner, E.G., Case, I., Jain, R., Gujar, S.K., Shah, G.V., Deveikis, J.P., Carlos, R.C., Thompson, B.G., Harrigan, M.R., Mukherji, S.K., 2004. Cerebral Perfusion CT: Technique and Clinical Applications. Radiology 231, 632–644. doi:10.1148/radiol.2313021488

Honda, Y., Fitzgerald, P.J., 2003. Stent Thrombosis An Issue Revisited in a Changing World. Circulation 108, 2–5. doi:10.1161/01.CIR.0000075929.79964.D8

Hunter, G.J., Hamberg, L.M., Ponzo, J.A., Huang-Hellinger, F.R., Morris, P.P., Rabinov, J., Farkas, J., Lev, M.H., Schaefer, P.W., Ogilvy, C.S., Schwamm, L., Buonanno, F.S., Koroshetz, W.J., Wolf, G.L., González, R.G., 1998. Assessment of cerebral perfusion and arterial anatomy in hyperacute stroke with three-dimensional functional CT: early clinical results. AJNR Am J Neuroradiol 19, 29–37.

Jenkinson, M., Bannister, P., Brady, M., Smith, S., 2002. Improved optimization for the robust and accurate linear registration and motion correction of brain images. Neuroimage 17, 825–841.

Jenkinson, M., Beckmann, C.F., Behrens, T.E.J., Woolrich, M.W., Smith, S.M., 2012. FSL.

Neuroimage 62, 782–790. doi:10.1016/j.neuroimage.2011.09.015

Jeon, P., Kim, B.M., Kim, D.I., Park, S.I., Kim, K.H., Kim, D.J., Suh, S.H., Huh, S.K., Kim, Y.B., 2012. Reconstructive endovascular treatment of fusiform or ultrawide-neck circumferential aneurysms with multiple overlapping enterprise stents and coiling. American Journal of Neuroradiology 33, 965–971.

Johnston, S.C., Dowd, C.F., Higashida, R.T., Lawton, M.T., Duckwiler, G.R., Gress, D.R., 2008. Predictors of Rehemorrhage After Treatment of Ruptured Intracranial Aneurysms The Cerebral Aneurysm Rerupture After Treatment (CARAT) Study. Stroke 39, 120–125. doi:10.1161/STROKEAHA.107.495747

Johnston, S.C., Higashida, R.T., Barrow, D.L., Caplan, L.R., Dion, J.E., Hademenos, G., Hopkins, L.N., Molyneux, A., Rosenwasser, R.H., Vinuela, F., Wilson, C.B., Committee on Cerebrovascular Imaging of the American Heart Association Council on Cardiovascular Radiology, 2002. Recommendations for the endovascular treatment of intracranial aneurysms: a statement for healthcare professionals from the Committee on Cerebrovascular Imaging of the American Heart Association Council on Cardiovascular Radiology. Stroke 33, 2536–2544.

Joshi, M.D., O'Kelly, C.J., Krings, T., Fiorella, D., Marotta, T.R., 2013. Observer Variability of an Angiographic Grading Scale Used for the Assessment of Intracranial Aneurysms Treated with Flow-Diverting Stents. American Journal of Neuroradiology 34, 1589–1592.

Jou, L.-D., Mohamed, A., Lee, D.H., Mawad, M.E., 2007. 3D Rotational Digital Subtraction Angiography May Underestimate Intracranial Aneurysms: Findings from Two Basilar Aneurysms. AJNR Am J Neuroradiol 28, 1690–1692. doi:10.3174/ajnr.A0652

Kalender, W.A., Kyriakou, Y., 2007. Flat-detector computed tomography (FD-CT). Eur Radiol 17, 2767–2779. doi:10.1007/s00330-007-0651-9

Kallmes, D.F., Ding, Y.H., Dai, D., Kadirvel, R., Lewis, D.A., Cloft, H.J., 2007. A New Endoluminal, Flow-Disrupting Device for Treatment of Saccular Aneurysms. Stroke 38, 2346–2352. doi:10.1161/STROKEAHA.106.479576

Kallmes, D.F., Hanel, R., Lopes, D., Boccardi, E., Bonafé, A., Cekirge, S., Fiorella, D., Jabbour, P., Levy, E., McDougall, C., Siddiqui, A., Szikora, I., Woo, H., Albuquerque, F., Bozorgchami, H., Dashti, S.R., Almandoz, J.D., Kelly, M.E., Turner, R., Woodward, B.K., Brinjikji, W., Lanzino, G., Lylyk, P., 2014. International Retrospective Study of the Pipeline Embolization Device: A Multicenter Aneurysm Treatment Study. AJNR Am J Neuroradiol. doi:10.3174/ajnr.A4111

Kamalian, S., Kamalian, S., Konstas, A.A., Maas, M.B., Payabvash, S., Pomerantz, S.R., Schaefer, P.W., Furie, K.L., González, R.G., Lev, M.H., 2012. CT perfusion mean transit time maps optimally distinguish benign oligemia from true "at-risk" ischemic penumbra, but thresholds vary by postprocessing technique. AJNR Am J Neuroradiol 33, 545–549. doi:10.3174/ajnr.A2809

Kamalian, S., Kamalian, S., Maas, M.B., Goldmacher, G.V., Payabvash, S., Akbar, A., Schaefer, P.W., Furie, K.L., Gonzalez, R.G., Lev, M.H., 2011. CT cerebral blood flow maps optimally correlate with admission diffusion-weighted imaging in acute stroke but thresholds vary by postprocessing platform. Stroke 42, 1923–1928. doi:10.1161/STROKEAHA.110.610618

Kamran, M., Nagaraja, S., Byrne, J.V., 2010. C-arm flat detector computed tomography: the

technique and its applications in interventional neuro-radiology. Neuroradiology 52, 319–327. doi:10.1007/s00234-009-0609-5

Kamran, M., Yarnold, J., Grunwald, I.Q., Byrne, J.V., 2011. Assessment of angiographic outcomes after flow diversion treatment of intracranial aneurysms: a new grading schema. Neuroradiology 53, 501–508. doi:10.1007/s00234-010-0767-5

Keedy, A., 2006. An overview of intracranial aneurysms. Mcgill J Med 9, 141–146.

Khalessi, A.A., Natarajan, S.K., Orion, D., Binning, M.J., Siddiqui, A., Levy, E.I., Hopkins, L.N., 2011. Acute Stroke Intervention. JACC: Cardiovascular Interventions 4, 261–269. doi:10.1016/j.jcin.2010.11.015

Khandelwal, N., 2008. CT perfusion in acute stroke. Indian J Radiol Imaging 18, 281–286. doi:10.4103/0971-3026.43837

Kidwell, C.S., Jahan, R., Gornbein, J., Alger, J.R., Nenov, V., Ajani, Z., Feng, L., Meyer, B.C., Olson, S., Schwamm, L.H., Yoo, A.J., Marshall, R.S., Meyers, P.M., Yavagal, D.R., Wintermark, M., Guzy, J., Starkman, S., Saver, J.L., MR RESCUE Investigators, 2013. A trial of imaging selection and endovascular treatment for ischemic stroke. N. Engl. J. Med. 368, 914–923. doi:10.1056/NEJMoa1212793

Kizilkilic, O., Kocer, N., Metaxas, G.E., Babic, D., Homan, R., Islak, C., 2012. Utility of VasoCT in the treatment of intracranial aneurysm with flow-diverter stents: Clinical article. Journal of neurosurgery 117, 45–49.

Kloska, S.P., Fischer, T., Nabavi, D.G., Dittrich, R., Ditt, H., Klotz, E., Fischbach, R., Ringelstein, E.B., Heindel, W., 2007. Color-coded perfused blood volume imaging using multidetector CT: initial results of whole-brain perfusion analysis in acute cerebral ischemia. Eur Radiol 17, 2352–2358. doi:10.1007/s00330-007-0580-7

Kocer, N., Islak, C., Kizilkilic, O., Kocak, B., Saglam, M., Tureci, E., 2014. Flow Re-direction Endoluminal Device in treatment of cerebral aneurysms: initial experience with short-term follow-up results. Journal of Neurosurgery 120, 1158–1171. doi:10.3171/2014.1.JNS131442

Konstas, A.A., Goldmakher, G.V., Lee, T.-Y., Lev, M.H., 2009a. Theoretic Basis and Technical Implementations of CT Perfusion in Acute Ischemic Stroke, Part 2: Technical Implementations. AJNR Am J Neuroradiol 30, 885–892. doi:10.3174/ajnr.A1492

Konstas, A.A., Goldmakher, G.V., Lee, T.-Y., Lev, M.H., 2009b. Theoretic Basis and Technical Implementations of CT Perfusion in Acute Ischemic Stroke, Part 1: Theoretic Basis. AJNR Am J Neuroradiol 30, 662–668. doi:10.3174/ajnr.A1487

Krings, T., Mandell, D.M., Kiehl, T.-R., Geibprasert, S., Tymianski, M., Alvarez, H., terBrugge, K.G., Hans, F.-J., 2011. Intracranial aneurysms: from vessel wall pathology to therapeutic approach. Nat Rev Neurol 7, 547–559. doi:10.1038/nrneurol.2011.136

Kudo, K., Sasaki, M., Yamada, K., Momoshima, S., Utsunomiya, H., Shirato, H., Ogasawara, K., 2009. Differences in CT Perfusion Maps Generated by Different Commercial Software: Quantitative Analysis by Using Identical Source Data of Acute Stroke Patients. Radiology 254, 200–209. doi:10.1148/radiol.254082000

Kuker, W., Downer, J., Cellerini, M., Schulz, U., 2011. Dissecting aneurysm of a dominant intracranial vertebral artery in fibromuscular dysplasia: flow diversion using multiple conventional stents. Neuroradiology 53, 193–195. doi:10.1007/s00234-010-0810-6

Kulcsár, Z., Ernemann, U., Wetzel, S.G., Bock, A., Goericke, S., Panagiotopoulos, V., Forsting, M., Ruefenacht, D.A., Wanke, I., 2010. High-profile flow diverter (silk) implantation in the basilar artery: efficacy in the treatment of aneurysms and the role of the perforators. Stroke 41, 1690–1696. doi:10.1161/STROKEAHA.110.580308

Kulcsár, Z., Houdart, E., Bonafé, A., Parker, G., Millar, J., Goddard, A.J.P., Renowden, S., Gál, G., Turowski, B., Mitchell, K., Gray, F., Rodriguez, M., van den Berg, R., Gruber, A., Desal, H., Wanke, I., Rüfenacht, D.A., 2011. Intra-Aneurysmal Thrombosis as a Possible Cause of Delayed Aneurysm Rupture after Flow-Diversion Treatment. American Journal of Neuroradiology 32, 20 –25. doi:10.3174/ajnr.A2370

Kyriakou, Y., Kalender, W.A., 2007. X-ray scatter data for flat-panel detector CT. Phys Med 23, 3–15. doi:10.1016/j.ejmp.2006.12.004

Lakhan, S.E., Kaplan, A., Laird, C., Leiter, Y., 2009. The interventionalism of medicine: interventional radiology, cardiology, and neuroradiology. Int Arch Med 2, 27. doi:10.1186/1755-7682-2-27

Landis, J.R., Koch, G.G., 1977. The measurement of observer agreement for categorical data. Biometrics 33, 159–174.

Latchaw, R.E., Alberts, M.J., Lev, M.H., Connors, J.J., Harbaugh, R.E., Higashida, R.T., Hobson, R., Kidwell, C.S., Koroshetz, W.J., Mathews, V., Villablanca, P., Warach, S., Walters, B., 2009. Recommendations for Imaging of Acute Ischemic Stroke A Scientific Statement From the American Heart Association. Stroke 40, 3646–3678. doi:10.1161/STROKEAHA.108.192616

Latchaw, R.E., Yonas, H., Hunter, G.J., Yuh, W.T.C., Ueda, T., Sorensen, A.G., Sunshine, J.L., Biller, J., Wechsler, L., Higashida, R., Hademenos, G., Council on Cardiovascular Radiology of the American Heart Association, 2003. Guidelines and recommendations for perfusion imaging in cerebral ischemia: A scientific statement for healthcare professionals by the writing group on perfusion imaging, from the Council on Cardiovascular Radiology of the American Heart Association. Stroke 34, 1084–1104. doi:10.1161/01.STR.0000064840.99271.9E

Leenders, K.L., Perani, D., Lammertsma, A.A., Heather, J.D., Buckingham, P., Jones, T., Healy, M.J.R., Gibbs, J.M., Wise, R.J.S., Hatazawa, J., Herold, S., Beaney, R.P., Brooks, D.J., Spinks, T., Rhodes, C., Frackowiak, R.S.J., 1990. Cerebral Blood Flow, Blood Volume and Oxygen Utilization Normal Values and Effect of Age. Brain 113, 27–47. doi:10.1093/brain/113.1.27

Leung, G.K.K., Tsang, A.C.O., Lui, W.M., 2012. Pipeline embolization device for intracranial aneurysm: a systematic review. Clin Neuroradiol 22, 295–303. doi:10.1007/s00062-012-0178-6

Levy, E.I., Mehta, R., Gupta, R., Hanel, R.A., Chamczuk, A.J., Fiorella, D., Woo, H.H., Albuquerque, F.C., Jovin, T.G., Horowitz, M.B., Hopkins, L.N., 2007. Self-expanding stents for recanalization of acute cerebrovascular occlusions. AJNR Am J Neuroradiol 28, 816–822.

Levy, E., Koebbe, C.J., Horowitz, M.B., Jungreis, C.A., Pride, G.L., Dutton, K., Kassam, A., Purdy, P.D., 2001. Rupture of intracranial aneurysms during endovascular coiling: management and outcomes. Neurosurgery 49, 807–811; discussion 811–813.

Li, M.-H., Gao, B.-L., Fang, C., Cheng, Y.-S., Li, Y.-D., Wang, J., Xu, G.-P., 2006. Prevention and management of intraprocedural rupture of intracranial aneurysm with detachable coils

during embolization. Neuroradiology 48, 907–915. doi:10.1007/s00234-006-0147-3

Li, M.-H., Gao, B.-L., Fang, C., Gu, B.-X., Cheng, Y.-S., Wang, W., Scotti, G., 2006. Angiographic follow-up of cerebral aneurysms treated with Guglielmi detachable coils: an analysis of 162 cases with 173 aneurysms. AJNR Am J Neuroradiol 27, 1107–1112.

Li, M.-H., Li, Y.-D., Tan, H.-Q., Luo, Q.-Y., Cheng, Y.-S., 2009. Treatment of distal internal carotid artery aneurysm with the willis covered stent: a prospective pilot study. Radiology 253, 470–477. doi:10.1148/radiol.2532090037

Linsenmaier, U., Rock, C., Euler, E., Wirth, S., Brandl, R., Kotsianos, D., Mutschler, W., Pfeifer, K.J., 2002. Three-dimensional CT with a modified C-arm image intensifier: feasibility. Radiology 224, 286–292. doi:10.1148/radiol.2241010646

Liou, T.-M., Li, Y.-C., Juan, W.-C., 2007. Numerical and experimental studies on pulsatile flow in aneurysms arising laterally from a curved parent vessel at various angles. J Biomech 40, 1268–1275. doi:10.1016/j.jbiomech.2006.05.024

Liu, A.Y., 2006. Update on Interventional Neuroradiology. Perm J 10, 42–46.

Lubicz, B., Collignon, L., Raphaeli, G., Pruvo, J.-P., Bruneau, M., De Witte, O., Leclerc, X., 2010. Flow-diverter stent for the endovascular treatment of intracranial aneurysms: a prospective study in 29 patients with 34 aneurysms. Stroke 41, 2247–2253. doi:10.1161/STROKEAHA.110.589911

Lubicz, B., Van der Elst, O., Collignon, L., Mine, B., Alghamdi, F., 2014. Silk Flow-Diverter Stent for the Treatment of Intracranial Aneurysms: A Series of 58 Patients with Emphasis on Long-Term Results. American Journal of Neuroradiology.

Luessenhop AJ, Spence WT, 1960. Artificial embolization of cerebral arteries: Report of use in a case of arteriovenous malformation. JAMA 172, 1153–1155. doi:10.1001/jama.1960.63020110001009

Lu, J., Zhang, M., Cao, Y., Ma, Q., Chen, J., Ji, X., Li, K., 2011. Three-dimensional whole-brain perfused blood volume imaging with multimodal CT for evaluation of acute ischaemic stroke. Clinical Radiology 66, 517–525. doi:10.1016/j.crad.2011.01.003

Lylyk, P., Cohen, J.E., Ceratto, R., Ferrario, A., Miranda, C., 2002. Endovascular reconstruction of intracranial arteries by stent placement and combined techniques. J. Neurosurg. 97, 1306–1313. doi:10.3171/jns.2002.97.6.1306

Lylyk, P., Miranda, C., Ceratto, R., Ferrario, A., Scrivano, E., Luna, H.R., Berez, A.L., Tran, Q., Nelson, P.K., Fiorella, D., 2009. Curative endovascular reconstruction of cerebral aneurysms with the pipeline embolization device: the Buenos Aires experience. Neurosurgery 64, 632–642; discussion 642–643; quiz N6. doi:10.1227/01.NEU.0000339109.98070.65

Mallik, A.S., Nuss, K., Kronen, P.W., Klein, K., Karol, A., von Rechenberg, B., Rüfenacht, D.A., Wanke, I., Kulcsár, Z., 2014. A new-generation, low-permeability flow diverting device for treatment of saccular aneurysms. European radiology 24, 12–18.

Martin Bland, J., Altman, D., 1986. STATISTICAL METHODS FOR ASSESSING AGREEMENT BETWEEN TWO METHODS OF CLINICAL MEASUREMENT. The Lancet 327, 307–310. doi:10.1016/S0140-6736(86)90837-8

Masuo, O., Terada, T., Walker, G., Tsuura, M., Matsumoto, H., Tohya, K., Kimura, M., Nakai, K., Itakura, T., 2002. Study of the patency of small arterial branches after stent

placement with an experimental in vivo model. AJNR Am J Neuroradiol 23, 706–710.

Maulaz, A., Piechowski-Józwiak, B., Michel, P., Bogousslavsky, J., 2005. Selecting patients for early stroke treatment with penumbra images. Cerebrovasc. Dis. 20 Suppl 2, 19–24. doi:10.1159/000089353

McAuliffe, W., Wenderoth, J.D., 2012. Immediate and midterm results following treatment of recently ruptured intracranial aneurysms with the pipeline embolization device. American Journal of Neuroradiology 33, 487–493.

McAuliffe, W., Wycoco, V., Rice, H., Phatouros, C., Singh, T.J., Wenderoth, J., 2012. Immediate and midterm results following treatment of unruptured intracranial aneurysms with the pipeline embolization device. American Journal of Neuroradiology 33, 164–170.

Menghini, V.V., Brown, R.D., Sicks, J.D., O'Fallon, W.M., Wiebers, D.O., 1998. Incidence and prevalence of intracranial aneurysms and hemorrhage in Olmsted County, Minnesota, 1965 to 1995. Neurology 51, 405–411. doi:10.1212/WNL.51.2.405

Meyers, P.M., Schumacher, H.C., Connolly, E.S., Heyer, E.J., Gray, W.A., Higashida, R.T., 2011. Current Status of Endovascular Stroke Treatment. Circulation 123, 2591–2601. doi:10.1161/CIRCULATIONAHA.110.971564

Mills, J.N., Mehta, V., Russin, J., Amar, A.P., Rajamohan, A., Mack, W.J., 2013. Advanced Imaging Modalities in the Detection of Cerebral Vasospasm. Neurology Research International 2013, e415960. doi:10.1155/2013/415960

Mir, D.I.A., Gupta, A., Dunning, A., Puchi, L., Robinson, C.L., Epstein, H. -a. B., Sanelli, P.C., 2013. CT Perfusion for Detection of Delayed Cerebral Ischemia in Aneurysmal Subarachnoid Hemorrhage: A Systematic Review and Meta-Analysis. AJNR Am J Neuroradiol. doi:10.3174/ajnr.A3787

Molyneux, A., 2002. International Subarachnoid Aneurysm Trial (ISAT) of neurosurgical clipping versus endovascular coiling in 2143 patients with ruptured intracranial aneurysms: a randomised trial. The Lancet 360, 1267–1274. doi:10.1016/S0140-6736(02)11314-6

Mordasini, P., El-Koussy, M., Brekenfeld, C., Schroth, G., Fischer, U., Beck, J., Gralla, J., 2012. Applicability of Tableside Flat Panel Detector CT Parenchymal Cerebral Blood Volume Measurement in Neurovascular Interventions: Preliminary Clinical Experience. AJNR Am J Neuroradiol 33, 154–158. doi:10.3174/ajnr.A2715

Murayama, Y., Nien, Y.L., Duckwiler, G., Gobin, Y.P., Jahan, R., Frazee, J., Martin, N., Viñuela, F., 2003. Guglielmi Detachable Coil embolization of cerebral aneurysms: 11 years' experience. Journal of Neurosurgery 98, 959–966. doi:10.3171/jns.2003.98.5.0959

Murphy, B.D., Fox, A.J., Lee, D.H., Sahlas, D.J., Black, S.E., Hogan, M.J., Coutts, S.B., Demchuk, A.M., Goyal, M., Aviv, R.I., Symons, S., Gulka, I.B., Beletsky, V., Pelz, D., Hachinski, V., Chan, R., Lee, T.-Y., 2006. Identification of penumbra and infarct in acute ischemic stroke using computed tomography perfusion-derived blood flow and blood volume measurements. Stroke 37, 1771–1777. doi:10.1161/01.STR.0000227243.96808.53

Murthy, S.B., Shah, S., Shastri, A., Venkatasubba Rao, C.P., Bershad, E.M., Suarez, J.I., 2014. The SILK flow diverter in the treatment of intracranial aneurysms. Journal of Clinical Neuroscience 21, 203–206. doi:10.1016/j.jocn.2013.07.006

Neitzel, U., 2005. Status and prospects of digital detector technology for CR and DR. Radiat Prot

Dosimetry 114, 32–38. doi:10.1093/rpd/nch532

Nelson, P.K., Lylyk, P., Szikora, I., Wetzel, S.G., Wanke, I., Fiorella, D., 2011. The pipeline embolization device for the intracranial treatment of aneurysms trial. AJNR Am J Neuroradiol 32, 34–40. doi:10.3174/ajnr.A2421

O'kelly, C.J., Krings, T., Fiorella, D., Marotta, T.R., 2010. A novel grading scale for the angiographic assessment of intracranial aneurysms treated using flow diverting stents. Interv Neuroradiol 16, 133–137.

Orth, R.C., Wallace, M.J., Kuo, M.D., Technology Assessment Committee of the Society of Interventional Radiology, 2008. C-arm cone-beam CT: general principles and technical considerations for use in interventional radiology. J Vasc Interv Radiol 19, 814–820. doi:10.1016/j.jvir.2008.02.002

Pereira, V.M., Bonnefous, O., Ouared, R., Brina, O., Stawiaski, J., Aerts, H., Ruijters, D., Narata, A.P., Bijlenga, P., Schaller, K., others, 2013. A DSA-based method using contrast-motion estimation for the assessment of the intra-aneurysmal flow changes induced by flow-diverter stents. American Journal of Neuroradiology 34, 808–815.

Phillips, T.J., Wenderoth, J.D., Phatouros, C.C., Rice, H., Singh, T.P., Devilliers, L., Wycoco, V., Meckel, S., McAuliffe, W., 2012. Safety of the Pipeline Embolization Device in Treatment of Posterior Circulation Aneurysms. AJNR Am J Neuroradiol 33, 1225–1231. doi:10.3174/ajnr.A3166

Pierot, L., 2011. Flow diverter stents in the treatment of intracranial aneurysms: Where are we? Journal of Neuroradiology 38, 40–46.

Pierot, L., Bonafé, A., Bracard, S., Leclerc, X., 2006. Endovascular Treatment of Intracranial Aneurysms with Matrix Detachable Coils: Immediate Posttreatment Results from a Prospective Multicenter Registry. AJNR Am J Neuroradiol 27, 1693–1699.

Pierot, L., Spelle, L., Vitry, F., 2008. Immediate Clinical Outcome of Patients Harboring Unruptured Intracranial Aneurysms Treated by Endovascular Approach Results of the ATENA Study. Stroke 39, 2497–2504. doi:10.1161/STROKEAHA.107.512756

Piotin, M., Spelle, L., Mounayer, C., Salles-Rezende, M.T., Giansante-Abud, D., Vanzin-Santos, R., Moret, J., 2007. Intracranial Aneurysms: Treatment with Bare Platinum Coils—Aneurysm Packing, Complex Coils, and Angiographic Recurrence. Radiology 243, 500–508. doi:10.1148/radiol.2431060006

Powers, W.J., Grubb, R.L., Raichle, M.E., 1984. Physiological responses to focal cerebral ischemia in humans. Ann. Neurol. 16, 546–552. doi:10.1002/ana.410160504

Puffer, R.C., Kallmes, D.F., Cloft, H.J., Lanzino, G., 2012. Patency of the ophthalmic artery after flow diversion treatment of paraclinoid aneurysms. J. Neurosurg. 116, 892–896. doi:10.3171/2011.11.JNS111612

Qureshi, A.I., 2004. Endovascular treatment of cerebrovascular diseases and intracranial neoplasms. Lancet 363, 804–813. doi:10.1016/S0140-6736(04)15697-3

Raymond, J., Guilbert, F., Weill, A., Georganos, S.A., Juravsky, L., Lambert, A., Lamoureux, J., Chagnon, M., Roy, D., 2003. Long-Term Angiographic Recurrences After Selective Endovascular Treatment of Aneurysms With Detachable Coils. Stroke 34, 1398–1403. doi:10.1161/01.STR.0000073841.88563.E9

Raymond, J., Roy, D., 1997. Safety and efficacy of endovascular treatment of acutely ruptured aneurysms. Neurosurgery 41, 1235–1245; discussion 1245–1246.

Raymond, J., White, P.M., Molyneux, A.J., 2007. Scales, Agreement, Outcome Measures, and Progress in Aneurysm Therapy. AJNR Am J Neuroradiol 28, 501–502.

Renowden, S., 2005. Interventional neuroradiology. J Neurol Neurosurg Psychiatry 76, iii48–iii63. doi:10.1136/jnnp.2005.075226

Richter, G., Engelhorn, T., Struffert, T., Doelken, M., Ganslandt, O., Hornegger, J., Kalender, W.A., Doerfler, A., 2007. Flat Panel Detector Angiographic CT for Stent-Assisted Coil Embolization of Broad-Based Cerebral Aneurysms. AJNR Am J Neuroradiol 28, 1902–1908. doi:10.3174/ajnr.A0697

Riedel, C.H., Tietke, M., Alfke, K., Stingele, R., Jansen, O., 2009. Subacute stent thrombosis in intracranial stenting. Stroke 40, 1310–1314. doi:10.1161/STROKEAHA.108.531400

Ries, T., Siemonsen, S., Thomalla, G., Grzyska, U., Zeumer, H., Fiehler, J., 2007. Long-term follow-up of cerebral aneurysms after endovascular therapy prediction and outcome of retreatment. AJNR Am J Neuroradiol 28, 1755–1761. doi:10.3174/ajnr.A0649

Rijsdijk, M., Schaaf, I.C. van der, Velthuis, B.K., Wermer, M.J., Rinkel, G.J.E., 2008. Global and focal cerebral perfusion after aneurysmal subarachnoid hemorrhage in relation with delayed cerebral ischemia. Neuroradiology 50, 813–820. doi:10.1007/s00234-008-0416-4

Rinkel, G.J., Djibuti, M., Algra, A., van Gijn, J., 1998. Prevalence and risk of rupture of intracranial aneurysms: a systematic review. Stroke 29, 251–256.

Rorden, C., Brett, M., 2000. Stereotaxic display of brain lesions. Behav Neurol 12, 191–200.

Royalty, K., Manhart, M., Pulfer, K., Deuerling-Zheng, Y., Strother, C., Fieselmann, A., Consigny, D., 2013. C-Arm CT Measurement of Cerebral Blood Volume and Cerebral Blood Flow Using a Novel High-Speed Acquisition and a Single Intravenous Contrast Injection. AJNR Am J Neuroradiol 34, 2131–2138. doi:10.3174/ajnr.A3536

Ruff, J., Froehler, M.T., 2013. Status of endovascular interventions to treat acute ischemic stroke. Curr Treat Options Neurol 15, 557–566. doi:10.1007/s11940-013-0250-9

Saake, M., Struffert, T., Goelitz, P., Ott, S., Seifert, F., Ganslandt, O., Doerfler, A., 2012. Angiographic CT with intravenous contrast agent application for monitoring of intracranial flow diverting stents. Neuroradiology 54, 727–735.

Saatci, I., Yavuz, K., Ozer, C., Geyik, S., Cekirge, H.S., 2012. Treatment of intracranial aneurysms using the pipeline flow-diverter embolization device: a single-center experience with long-term follow-up results. AJNR Am J Neuroradiol 33, 1436–1446. doi:10.3174/ajnr.A3246

Sadasivan, C., Cesar, L., Seong, J., Rakian, A., Hao, Q., Tio, F.O., Wakhloo, A.K., Lieber, B.B., 2009. An original flow diversion device for the treatment of intracranial aneurysms: evaluation in the rabbit elastase-induced model. Stroke 40, 952–958. doi:10.1161/STROKEAHA.108.533760

Sa de Camargo, E.C., Koroshetz, W.J., 2005. Neuroimaging of Ischemia and Infarction. NeuroRx 2, 265–276.

Sanelli, P.C., Ugorec, I., Johnson, C.E., Tan, J., Segal, A.Z., Fink, M., Heier, L.A., Tsiouris, A.J., Comunale, J.P., John, M., Stieg, P.E., Zimmerman, R.D., Mushlin, A.I., 2011. Using

Quantitative CT Perfusion for Evaluation of Delayed Cerebral Ischemia Following Aneurysmal Subarachnoid Hemorrhage. AJNR Am J Neuroradiol 32, 2047–2053. doi:10.3174/ajnr.A2693

Schaefer, P.W., Barak, E.R., Kamalian, S., Gharai, L.R., Schwamm, L., Gonzalez, R.G., Lev, M.H., 2008. Quantitative assessment of core/penumbra mismatch in acute stroke: CT and MR perfusion imaging are strongly correlated when sufficient brain volume is imaged. Stroke 39, 2986–2992. doi:10.1161/STROKEAHA.107.513358

Schellinger, P.D., Bryan, R.N., Caplan, L.R., Detre, J.A., Edelman, R.R., Jaigobin, C., Kidwell, C.S., Mohr, J.P., Sloan, M., Sorensen, A.G., Warach, S., Therapeutics and Technology Assessment Subcommittee of the American Academy of Neurology, 2010. Evidence-based guideline: The role of diffusion and perfusion MRI for the diagnosis of acute ischemic stroke: report of the Therapeutics and Technology Assessment Subcommittee of the American Academy of Neurology. Neurology 75, 177–185. doi:10.1212/WNL.0b013e3181e7c9dd

Serbinenko, F.A., 1971. Balloon occlusion of cavernous portion of the carotid artery as a method of treating carotid-cavernous fistulae. Zh Vopr Neirokhir 6, 3–9.

Shankar, J.J.S., Vandorpe, R., Pickett, G., Maloney, W., 2013. SILK flow diverter for treatment of intracranial aneurysms: initial experience and cost analysis. J Neurointerv Surg 5 Suppl 3, iii11–15. doi:10.1136/neurintsurg-2012-010590

Sharma, M., Fox, A.J., Symons, S., Jairath, A., Aviv, R.I., 2011. CT Angiographic Source Images: Flow- or Volume-Weighted? AJNR Am J Neuroradiol 32, 359–364. doi:10.3174/ajnr.A2282

Siddiqui, A.H., Abla, A.A., Kan, P., Dumont, T.M., Jahshan, S., Britz, G.W., Hopkins, L.N., Levy, E.I., 2012. Panacea or problem: flow diverters in the treatment of symptomatic large or giant fusiform vertebrobasilar aneurysms: Clinical article. Journal of neurosurgery 116, 1258–1266.

Simgen, A., Ley, D., Roth, C., Yilmaz, U., Körner, H., Mühl-Benninghaus, R., Kim, Y.-J., Scheller, B., Reith, W., 2014. Evaluation of a newly designed flow diverter for the treatment of intracranial aneurysms in an elastase-induced aneurysm model, in New Zealand white rabbits. Neuroradiology 56, 129–137.

Smith, S.M., 2002. Fast robust automated brain extraction. Human Brain Mapping 17, 143–155. doi:10.1002/hbm.10062

Smyth, J., Sutton, D., Houston, J., 2006. Evaluation of the quality of CT-like images obtained using a commercial flat panel detector system. Biomed Imaging Interv J 2. doi:10.2349/biij.2.4.e48

Söderman, M., Babic, D., Holmin, S., Andersson, T., 2008. Brain imaging with a flat detector C-arm. Neuroradiology 50, 863–868. doi:10.1007/s00234-008-0419-1

Spetzler, R.F., McDougall, C.G., Albuquerque, F.C., Zabramski, J.M., Hills, N.K., Partovi, S., Nakaji, P., Wallace, R.C., 2013. The Barrow Ruptured Aneurysm Trial: 3-year results. J. Neurosurg. 119, 146–157. doi:10.3171/2013.3.JNS12683

Strother, C., 2012. The Neurointerventional Suite as an Acute Stroke Intervention Unit. Endovascular Today.

Strother, C.M., 2000. Interventional Neuroradiology. AJNR Am J Neuroradiol 21, 19–24.

Struffert, T., Deuerling-Zheng, Y., Engelhorn, T., Kloska, S., Gölitz, P., Köhrmann, M., Schwab, S., Strother, C.M., Doerfler, A., 2012. Feasibility of Cerebral Blood Volume Mapping by Flat Panel Detector CT in the Angiography Suite: First Experience in Patients with Acute Middle Cerebral Artery Occlusions. AJNR Am J Neuroradiol 33, 618–625. doi:10.3174/ajnr.A2839

Struffert, T., Deuerling-Zheng, Y., Kloska, S., Engelhorn, T., Boese, J., Zellerhoff, M., Schwab, S., Doerfler, A., 2011a. Cerebral blood volume imaging by flat detector computed tomography in comparison to conventional multislice perfusion CT. Eur Radiol 21, 882–889. doi:10.1007/s00330-010-1957-6

Struffert, T., Deuerling-Zheng, Y., Kloska, S., Engelhorn, T., Strother, C.M., Kalender, W.A., Köhrmann, M., Schwab, S., Doerfler, A., 2010. Flat Detector CT in the Evaluation of Brain Parenchyma, Intracranial Vasculature, and Cerebral Blood Volume: A Pilot Study in Patients with Acute Symptoms of Cerebral Ischemia. AJNR Am J Neuroradiol 31, 1462–1469. doi:10.3174/ajnr.A2083

Struffert, T., Ott, S., Kowarschik, M., Bender, F., Adamek, E., Engelhorn, T., Gölitz, P., Lang, S., Strother, C.M., Doerfler, A., 2013. Measurement of quantifiable parameters by time-density curves in the elastase-induced aneurysm model: first results in the comparison of a flow diverter and a conventional aneurysm stent. European radiology 23, 521–527.

Struffert, T., Richter, G., Engelhorn, T., Doelken, M., Goelitz, P., Kalender, W.A., Ganslandt, O., Doerfler, A., 2009. Visualisation of intracerebral haemorrhage with flat-detector CT compared to multislice CT: results in 44 cases. Eur Radiol 19, 619–625. doi:10.1007/s00330-008-1183-7

Struffert, T., Saake, M., Ott, S., Engelhorn, T., Gölitz, P., Kloska, S., Doelken, M., Doerfler, A., 2011b. Intravenous flat detector CT angiography for non-invasive visualisation of intracranial flow diverter: technical feasibility. European radiology 21, 1797–1801.

Stys, P.K., Ransom, B.R., Waxman, S.G., Davis, P.K., 1990. Role of extracellular calcium in anoxic injury of mammalian central white matter. Proc. Natl. Acad. Sci. U.S.A. 87, 4212–4216.

Suh, D.C., Kim, J.K., Choi, J.W., Choi, B.S., Pyun, H.W., Choi, Y.J., Kim, M.-H., Yang, H.R., Ha, H.I., Kim, S.J., Lee, D.H., Choi, C.G., Hahm, K.D., Kim, J.S., 2008. Intracranial stenting of severe symptomatic intracranial stenosis: results of 100 consecutive patients. AJNR Am J Neuroradiol 29, 781–785. doi:10.3174/ajnr.A0922

Szikora, I., Berentei, Z., Kulcsar, Z., Barath, K., Berez, A., Bose, A., Nyary, I., 2006. Endovascular treatment of intracranial aneurysms with parent vessel reconstruction using balloon and self expandable stents. Acta Neurochir (Wien) 148, 711–723; discussion 723. doi:10.1007/s00701-006-0785-6

Szikora, I., Berentei, Z., Kulcsar, Z., Marosfoi, M., Vajda, Z.S., Lee, W., Berez, A., Nelson, P.K., 2010. Treatment of intracranial aneurysms by functional reconstruction of the parent artery: the Budapest experience with the pipeline embolization device. AJNR Am J Neuroradiol 31, 1139–1147. doi:10.3174/ajnr.A2023

Tähtinen, O.I., Manninen, H.I., Vanninen, R.L., Seppänen, J., Niskakangas, T., Rinne, J., Keski-Nisula, L., 2012. The silk flow-diverting stent in the endovascular treatment of complex intracranial aneurysms: technical aspects and midterm results in 24 consecutive patients. Neurosurgery 70, 617–623; discussion 623–624. doi:10.1227/NEU.0b013e31823387d4

Taveras, J.M., 1990. Diamond Jubilee lecture. Neuroradiology: past, present, future. Radiology 175, 593–602. doi:10.1148/radiology.175.3.2188291

Thornton, J., Debrun, G.M., Aletich, V.A., Bashir, Q., Charbel, F.T., Ausman, J., 2002. Follow-up angiography of intracranial aneurysms treated with endovascular placement of Guglielmi detachable coils. Neurosurgery 50, 239–249; discussion 249–250.

Trossbach, M., Hartmann, M., Braun, C., Sartor, K., Hähnel, S., 2004. Small vessel stents for intracranial angioplasty: in vitro evaluation of in-stent stenoses using CT angiography. Neuroradiology 46, 459–463. doi:10.1007/s00234-004-1205-3

Tummala, R.P., Chu, R.M., Madison, M.T., Myers, M., Tubman, D., Nussbaum, E.S., 2001. Outcomes after aneurysm rupture during endovascular coil embolization. Neurosurgery 49, 1059–1066; discussion 1066–1067.

Turjman, F., Levrier, O., Combaz, X., Bonafé, A., Biondi, A., Desal, H., Bracard, S., Mounayer, C., Riva, R., Chapuis, F., others, 2014. EVIDENCE Trial: design of a phase 2, randomized, controlled, multicenter study comparing flow diversion and traditional endovascular strategy in unruptured saccular wide-necked intracranial aneurysms. Neuroradiology 1–6.

Turowski, B., Macht, S., Kulcsár, Z., Hänggi, D., Stummer, W., 2011. Early fatal hemorrhage after endovascular cerebral aneurysm treatment with a flow diverter (SILK-Stent): do we need to rethink our concepts? Neuroradiology 53, 37–41. doi:10.1007/s00234-010-0676-7

Van Rooij, W.J., Sluzewski, M., Beute, G.N., Nijssen, P.C., 2006. Procedural complications of coiling of ruptured intracranial aneurysms: incidence and risk factors in a consecutive series of 681 patients. AJNR Am J Neuroradiol 27, 1498–1501.

Vlak, M.H., Algra, A., Brandenburg, R., Rinkel, G.J., 2011. Prevalence of unruptured intracranial aneurysms, with emphasis on sex, age, comorbidity, country, and time period: a systematic review and meta-analysis. Lancet Neurol 10, 626–636. doi:10.1016/S1474-4422(11)70109-0

Vries, J.D., Boogaarts, J., Norden, A.V., Wakhloo, A.K., 2013. New Generation of Flow Diverter (Surpass) for Unruptured Intracranial Aneurysms A Prospective Single-Center Study in 37 Patients. Stroke 44, 1567–1577. doi:10.1161/STROKEAHA.111.000434

Wajnberg, E., Silva, T.S., Johnson, A.K., Lopes, D.K., 2014. Progressive Deconstruction: A Novel Aneurysm Treatment Using the Pipeline Embolization Device for Competitive Flow Diversion. Neurosurgery 10, E161–E166. doi:10.1227/NEU.0000000000000029

Wakhloo, A.K., Mandell, J., Gounis, M.J., Brooks, C., Linfante, I., Winer, J., Weaver, J.P., 2008. Stent-assisted reconstructive endovascular repair of cranial fusiform atherosclerotic and dissecting aneurysms: long-term clinical and angiographic follow-up. Stroke 39, 3288–3296. doi:10.1161/STROKEAHA.107.512996

Wallace, M.J., Kuo, M.D., Glaiberman, C., Binkert, C.A., Orth, R.C., Soulez, G., Technology Assessment Committee of the Society of Interventional Radiology, 2008. Three-dimensional C-arm cone-beam CT: applications in the interventional suite. J Vasc Interv Radiol 19, 799–813. doi:10.1016/j.jvir.2008.02.018

Wallace, M.J., Kuo, M.D., Glaiberman, C., Binkert, C.A., Orth, R.C., Soulez, G., Technology Assessment Committee of the Society of Interventional Radiology, 2009. Three-

dimensional C-arm cone-beam CT: applications in the interventional suite. J Vasc Interv Radiol 20, S523–537. doi:10.1016/j.jvir.2009.04.059

Wang, K., Yuan, S., Zhang, X., Liu, Q., Zhong, Q., Zhang, R., Lu, P., Li, J., 2013. Biodegradable flow-diverting device for the treatment of intracranial aneurysm: short-term results of a rabbit experiment. Neuroradiology 55, 621–628.

Weichert, F., Walczak, L., Fisseler, D., Opfermann, T., Razzaq, M., Münster, R., Turek, S., Grunwald, I., Roth, C., Veith, C., others, 2013. Simulation of Intra-Aneurysmal Blood Flow by Different Numerical Methods. Computational and mathematical methods in medicine 2013.

Wermer, M.J.H., Schaaf, I.C. van der, Algra, A., Rinkel, G.J.E., 2007. Risk of Rupture of Unruptured Intracranial Aneurysms in Relation to Patient and Aneurysm Characteristics An Updated Meta-Analysis. Stroke 38, 1404–1410. doi:10.1161/01.STR.0000260955.51401.cd

White, P.M., Gilmour, J.N., Weir, N.W., Innes, B., Sellar, R.J., 2008. AngioCT in the management of neurointerventional patients: a prospective, consecutive series with associated dosimetry and resolution data. Neuroradiology 50, 321–330. doi:10.1007/s00234-007-0339-5

Willinsky, R.A., Taylor, S.M., terBrugge, K., Farb, R.I., Tomlinson, G., Montanera, W., 2003. Neurologic Complications of Cerebral Angiography: Prospective Analysis of 2,899 Procedures and Review of the Literature. Radiology 227, 522–528. doi:10.1148/radiol.2272012071

Wintermark, M., Albers, G.W., Alexandrov, A.V., Alger, J.R., Bammer, R., Baron, J.-C., Davis, S., Demaerschalk, B.M., Derdeyn, C.P., Donnan, G.A., Eastwood, J.D., Fiebach, J.B., Fisher, M., Furie, K.L., Goldmakher, G.V., Hacke, W., Kidwell, C.S., Kloska, S.P., Kohrmann, M., Koroshetz, W., Lee, T.-Y., Lees, K.R., Lev, M.H., Liebeskind, D.S., Ostergaard, L., Powers, W.J., Provenzale, J., Schellinger, P., Silbergleit, R., Sorensen, A.G., Wardlaw, J., Wu, O., Warach, S., 2008. Acute Stroke Imaging Research Roadmap. AJNR Am J Neuroradiol 29, e23–e30. doi:10.1161/STROKEAHA.107.512319

Wintermark, M., Albers, G.W., Broderick, J.P., Demchuk, A.M., Fiebach, J.B., Fiehler, J., Grotta, J.C., Houser, G., Jovin, T.G., Lees, K.R., Lev, M.H., Liebeskind, D.S., Luby, M., Muir, K.W., Parsons, M.W., von Kummer, R., Wardlaw, J.M., Wu, O., Yoo, A.J., Alexandrov, A.V., Alger, J.R., Aviv, R.I., Bammer, R., Baron, J.-C., Calamante, F., Campbell, B.C.V., Carpenter, T.C., Christensen, S., Copen, W.A., Derdeyn, C.P., Haley, E.C., Khatri, P., Kudo, K., Lansberg, M.G., Latour, L.L., Lee, T.-Y., Leigh, R., Lin, W., Lyden, P., Mair, G., Menon, B.K., Michel, P., Mikulik, R., Nogueira, R.G., Ostergaard, L., Pedraza, S., Riedel, C.H., Rowley, H.A., Sanelli, P.C., Sasaki, M., Saver, J.L., Schaefer, P.W., Schellinger, P.D., Tsivgoulis, G., Wechsler, L.R., White, P.M., Zaharchuk, G., Zaidat, O.O., Davis, S.M., Donnan, G.A., Furlan, A.J., Hacke, W., Kang, D.-W., Kidwell, C., Thijs, V.N., Thomalla, G., Warach, S.J., Stroke Imaging Research (STIR) and Virtual International Stroke Trials Archive (VISTA)-Imaging Investigators, 2013. Acute Stroke Imaging Research Roadmap II. Stroke 44, 2628–2639. doi:10.1161/STROKEAHA.113.002015

Wintermark, M., Reichhart, M., Thiran, J.-P., Maeder, P., Chalaron, M., Schnyder, P., Bogousslavsky, J., Meuli, R., 2002. Prognostic accuracy of cerebral blood flow measurement by perfusion computed tomography, at the time of emergency room admission, in acute stroke patients. Ann. Neurol. 51, 417–432.

Wintermark, M., Sesay, M., Barbier, E., Borbély, K., Dillon, W.P., Eastwood, J.D., Glenn, T.C.,

Grandin, C.B., Pedraza, S., Soustiel, J.-F., Nariai, T., Zaharchuk, G., Caillé, J.-M., Dousset, V., Yonas, H., 2005. Comparative Overview of Brain Perfusion Imaging Techniques. Stroke 36, e83–e99. doi:10.1161/01.STR.0000177884.72657.8b

Wittkamp, G., Buerke, B., Dziewas, R., Ditt, H., Seidensticker, P., Heindel, W., Kloska, S.P., 2010. Whole Brain Perfused Blood Volume CT: Visualization of Infarcted Tissue Compared to Quantitative Perfusion CT. Academic Radiology 17, 427–432. doi:10.1016/j.acra.2009.11.005

Wolpert, S.M., 1999. Neuroradiology Classics. AJNR Am J Neuroradiol 20, 1752–1753.

Wong, G.K., Kwan, M.C., Ng, R.Y., Yu, S.C., Poon, W.S., 2011. Flow diverters for treatment of intracranial aneurysms: current status and ongoing clinical trials. Journal of Clinical Neuroscience 18, 737–740.

Yamaguchi, T., Kanno, I., Uemura, K., Shishido, F., Inugami, A., Ogawa, T., Murakami, M., Suzuki, K., 1986. Reduction in regional cerebral metabolic rate of oxygen during human aging. Stroke 17, 1220–1228. doi:10.1161/01.STR.17.6.1220

Yoo, E., Kim, D.J., Kim, D.I., Lee, J.-W., Suh, S.H., 2009. Bailout stent deployment during coil embolization of intracranial aneurysms. AJNR Am J Neuroradiol 30, 1028–1034. doi:10.3174/ajnr.A1482

Zaidat, O.O., Klucznik, R., Alexander, M.J., Chaloupka, J., Lutsep, H., Barnwell, S., Mawad, M., Lane, B., Lynn, M.J., Chimowitz, M., NIH Multi-center Wingspan Intracranial Stent Registry Study Group, 2008. The NIH registry on use of the Wingspan stent for symptomatic 70-99% intracranial arterial stenosis. Neurology 70, 1518–1524. doi:10.1212/01.wnl.0000306308.08229.a3

Zanaty, M., Chalouhi, N., Tjoumakaris, S.I., Rosenwasser, R.H., Gonzalez, L.F., Jabbour, P., 2014. Flow-diversion panacea or poison? Front. Neurol. 5, 21. doi:10.3389/fneur.2014.00021

Zellerhoff, M., Deuerling-Zheng, Y., Strother, C.M., Ahmed, A., Pulfer, K., Redel, T., Royalty, K., Grinde, J., Consigny, D., 2009. Measurement of cerebral blood volume using angiographic C-arm systems. p. 72620H–72620H–8. doi:10.1117/12.812097

Zenteno, M.A., Santos-Franco, J.A., Freitas-Modenesi, J.M., Gómez, C., Murillo-Bonilla, L., Aburto-Murrieta, Y., Díaz-Romero, R., Nathal, E., Gómez-Llata, S., Lee, A., 2008. Use of the sole stenting technique for the management of aneurysms in the posterior circulation in a prospective series of 20 patients. J. Neurosurg. 108, 1104–1118. doi:10.3171/JNS/2008/108/6/1104

Zussman, B.M., Boghosian, G., Gorniak, R.J., Olszewski, M.E., Read, K.M., Siddiqui, K.M., Flanders, A.E., 2011. The relative effect of vendor variability in CT perfusion results: a method comparison study. AJR Am J Roentgenol 197, 468–473. doi:10.2214/AJR.10.6058